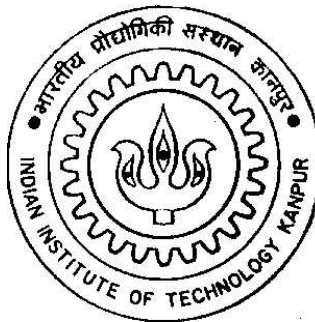# FORMULATION OF A COMPUTATIONAL AEROELASTIC MODEL FOR THE PREDICTION OF TRIM AND RESPONSE OF A HELICOPTER ROTOR SYSTEM IN FORWARD FLIGHT

by

VAITLA LAXMAN

DEPARTMENT OF AEROSPACE ENGINEERING

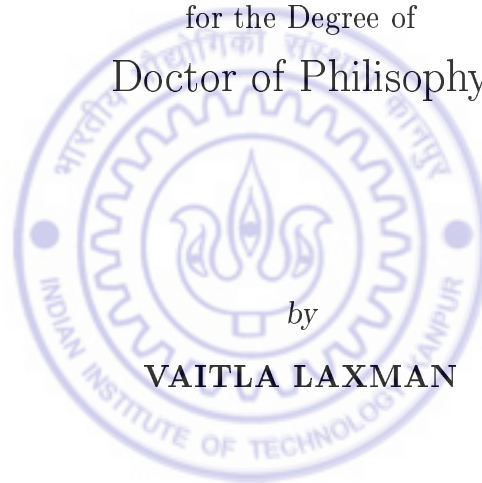INDIAN INSTITUTE OF TECHNOLOGY, KANPUR

April, 2008

FORMULATION OF A COMPUTATIONAL AEROELASTIC MODEL FOR THE PREDICTION OF TRIM AND RESPONSE OF A HELICOPTER ROTOR SYSTEM IN FORWARD FLIGHT

A Thesis Submitted
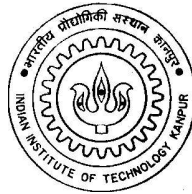
in Partial Fulfillment of the Requirements
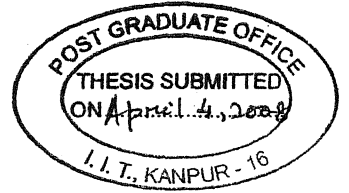
for the Degree of

Doctor of Philisophy

by

VAITLA LAXMAN

to the

DEPARTMENT OF AEROSPACE ENGINEERING

INDIAN INSTITUTE OF TECHNOLOGY, KANPUR

April, 2008

CERTIFICATE

This is to certify that the work contained in the thesis entitled *"Formulation of a Computational Aeroelastic Model For the Prediction of Trim and Response of a Helicopter Rotor System In Forward Flight"* by Laxman Vaitla, has been carried out under my supervision and that this work has not been submitted elsewhere for a degree.

April, 2008

Prof. C. Venkatesan

Department of Aerospace Engineering

Indian Institute of Technology Kanpur

SYNOPSIS

Rotary wing aeroelasticity is a highly complex phenomenon involving coupling between flexible blade dynamics, unsteady aerodynamics including stall and unsteady wake effects. It has progressed considerably in the past four decades. However, because of the complexities, still there are several unresolved issues related to blade loads, blade response and vibration of helicopter in forward flight. One such problem is related to the presence of wide spectrum of frequencies including N_b/rev and its integer multiples (where N_b is the number of blades in the rotor system) in the vibratory response of the fuselage. Several studies on helicopter vibration and its control have essentially focused on N_b/rev vibrations. One of the possible reasons for the presence of frequencies below N_b/rev in the vibratory signal can be due to unsymmetric structural/mass properties of the rotor blade system. However, even when the rotor blades are identical, it is possible that asymmetry in the aerodynamic environment (due to unsteady nonlinear effects) of the rotor blade as it goes around the azimuth can lead to a vibratory signal which can have frequencies below N_b/rev. The nonlinearities in the rotor blade aeroelasticity can arise due to: (a) moderate deformation of coupled flap (out-of-plane bending)-lag (in-plane bending)-torsion-axial modes (structural nonlinearity) and (b) unsteady aerodynamics including dynamic stall and wake effects (aerodynamic nonlinearity).

Structural dynamic modeling of the rotor blade incorporating all the geometric complexities of the rotor system and flap-lag-axial-torsion deformations of the blade has reached a high level of sophistication. While formulating the aerodynamic operator, one should consider: (a) unsteady aerodynamics of a rotor blade undergoing coupled pitching-plunging motion in a time varying oncoming flow, (b) induced flow (or inflow) at the rotor disc due to rotor blade wake and (c) dynamic stall.

In the absence of a suitable three-dimensional (3-D) aerodynamic model, only two-dimensional (2-D) models are used in the aeroelastic analysis of rotor blades. The

classical two-dimensional unsteady aerodynamic models for unstalled flow (attached flow) condition are: (1) Theodorsen's model applicable for a pitching and plunging airfoil with zero mean angle of attack; (2) Greenberg's theory for a pitching and plunging airfoil having non-zero mean angle of attack in a time varying on-coming flow; and (3) Loewy's model applicable for a pitching and plunging airfoil including cascade effects (rotor wake is treated in an approximate manner for a hovering rotor). Because of simplicity in application, most of the aeroelastic studies use Greenberg's theory, taking into consideration the wake induced inflow effects.

The wake induced inflow at the rotor disk can be obtained by either prescribed wake or free wake model. These models are computationally expensive. On the other hand, dynamic inflow models are global models, which represent the unsteady wake effects of the rotor system in a simple form. In these models, the unsteady wake-induced flow through the rotor disk is defined by a set of inflow variables and these variables essentially provide a correction to the mean inflow. Extending the dynamic inflow model, Peters and He have developed a generalized wake model. In this model, the inflow distribution is represented by a set of harmonic functions and Legendre polynomials (radial shape functions).

The most complicated phenomenon of unsteady aerodynamics is dynamic stall. During forward flight, the helicopter rotor blades are subjected to time varying on-coming flow. In order to compensate for this asymmetry in the relative airspeed between advancing and retreating sides, a time varying (once per revolution) pitch input is provided to the rotor blades. Since rotor blades are long slender beams, under time varying aerodynamic loads, these blades undergo coupled flap bending, lag bending, elastic torsion and axial deformations. In addition, the unsteady wake of the rotor system induces a time varying inflow through the rotor disc. The influence of this inflow is to modify the effective angle of attack of the blade cross-section. As a result of these complicated flow conditions and blade motions, some sections

iv

of the blade undergo dynamic stall in the retreating side of the rotor disc. It is difficult to predict stall and its effect using theoretical unsteady aerodynamic tools. So researchers depend on empirical or semi-empirical models. Several mathematical models that attempt to predict the effects of dynamic stall are available in the literature. ONERA dynamic stall model is a relatively simple and efficient model, which can be easily incorporated in any aeroelastic analysis. Recently CFD methods are applied to predict dynamic stall in airfoils.

In the recent years, several aeroelastic studies were undertaken by combining different aerodynamic models representing the rotor wake effects and the unsteady aerodynamic loads on a typical section of a rotor blade. In the present study, five different combinations of aerodynamic models have been proposed and the influence of each one of these models on the trim and response characteristics of helicopter rotor in forward flight is analysed systematically.

The objectives of the present study are:

- Development of a structural dynamic model for a flexible rotor blade with and without pretwist.

- Detailed analysis of ONERA dynamic stall model. Based on this study, an improved dynamic stall model is proposed in this thesis.

- Formulation of a time domain computational aeroelastic model by integrating the structural model, the inflow model, and the dynamic stall model for the prediction of trim and response of a helicopter rotor system in forward flight.

- Study the influence of nonlinearity due to dynamic stall and aeroelastic coupling on the response of 2-D airfoil undergoing pitching and plunging motion in a time varying oncoming flow, simulating the dynamics of a typical section of a rotor blade in forward flight.

- Formulation of a suitable computational technique for the evaluation of trim and response of a multi-bladed helicopter rotor system in forward flight. Perform a systematic analysis to identify the effects of aerodynamic modeling on trim and rotor loads in forward flight.

- Study the effects of structural couplings due to blade pretwist on trim, blade response and rotor loads of a helicopter.

The results of the study are presented in two major sections. The first part of the work addresses the effect of dynamic stall and aeroelastic couplings on the response of a 2-D airfoil. The important observations of this study can be summarised as:

1. ONERA(EDLin) dynamic stall model has been analysed in relation to Theodorsen's and Greenberg's unsteady aerodynamic theory. It is shown that ONERA(EDLin) dynamic stall model in the unstalled region is identical to Theodorsen's model except that the lift deficiency function $C(k)$ is approximated by a first order rational approximation. Replacing the first order rational approximation by a more accurate second order rational approximation, a *modified* dynamic stall model is proposed. This *modified* stall model is shown to provide a better correlation with experimental stall data.

2. Using the *modified* stall model, the response characteristics of a 2-D airfoil undergoing pitching and plunging motion in a pulsating oncoming flow are analysed to study the effects of dynamic stall. The results of this study show that dynamic stall in association with aeroelastic couplings above a certain level leads to bounded chaotic motion of the airfoil.

In the second part of the thesis, a systematic approach is undertaken to analyse the influence of various aerodynamic models, representing rotor inflow and sectional aerodynamic loads, on the helicopter trim and response of the rotor blades. The aerodynamic loads acting on the blade are evaluated at 15 radial stations (starting

from 0.25R to 0.95R with an increment of 0.05R) for each blade. The total number of state variables representing the sectional aerodynamic coefficients (lift, drag and moment) for one blade is 120 (15 radial stations * 8 state variables per stations). The rotor blade structural model is represented by eight modes consisting of four flap modes, two lag modes, one torsion mode, and one axial mode. The total number of state variables representing structural modes per blade is 16. The time varying inflow is given by three state variables. Therefore, for a four bladed rotor system, there are in total 547 state variables (480 aerodynamic state variables + 64 structural state variables + 3 state variables for dynamic wake effects). In the present study, a four bladed system with proper spacing in the azimuth angle is considered for the analysis. By solving simultaneously the response of all the blades, one can identify the difference in the response of the blades as they go around the azimuth. Since the response and loads of all the blades are solved at every instant of time, the time varying hub loads and time varying inflow (dynamic wake effects) can be captured.

The most important observations of this study can be summarised as follows:

1. The lateral cyclic pitch setting (θ_{1c}) required for trim is significantly affected by rotor inflow at low forward speeds, and by dynamic stall effects at high forward speeds. It is also found that the aerodynamic model, incorporating dynamic wake and dynamic stall effects, predicts the trim parameter (θ_{1c}) whose variation with forward speed resembles closely to those obtained in flight test.

2. At high forward speeds, the azimuthal location in the advancing side where the minimum value of the sectional lift occurs, is influenced by dynamic stall effects.

3. At high forward speeds, dynamic stall effects significantly increase the torsional response of the rotor blade.

4. The results of the present study clearly show that dynamic stall and dynamic

wake effects introduce large number of harmonics in the hub loads, including those below the blade passage frequency and its integer multiples.

5. The structural coupling due to blade pretwist is observed to significantly alter the time variation of the sectional loads as compared to the loads obtained for a straight untwisted blade. This result indicates that aeroelastic couplings have a significant influence on the rotor loads.

The thesis is organised in several chapters and each one is addressing a specific aspect of the problem. Chapter 1 contains the introduction of the problem, literature survey and objectives. In Chapter 2, structural modeling of the rotor blade has been developed using Hamilton's principle. This model considers the moderate deformations in flap, lag, torsion and axial modes. The coupled rotating natural frequencies and mode shapes of helicopter rotor blade are evaluated. Chapter 3 provides a description on inflow modeling and a detailed study of ONERA dynamic stall model. An improved dynamic dynamic stall is proposed in this thesis, which is refered as "*modified* stall model". Chapter 4 deals with the aeroelastic response analysis of an airfoil operating under dynamic stall conditions. It is shown that the dynamic stall in association with aeroelastic coupling can lead to bounded chaotic motion of the airfoil. Chapter 5 presents the formulation of a time domain computational model and the solution technique, for the aeroelastic response analysis of a helicopter rotor system in forward flight. The results of the aeroelastic study are presented in Chapter 6. Concluding remarks of this study are presented in Chapter 7.

ACKNOWLEDGEMENT

Contents

List of Tables

List of Figures

NOMENCLATURE

a	torque offset or lift curve slope
a_d, a_l, a_m	parameters used in dynamic stall model
$A.C$	aerodynamic centre
b	blade semi-chord
b_l, b_m	parameters used to define static aerodynamic coefficients
c	blade chord $(= 2\,b)$
$C(k)$	Theodorsen's lift deficiency function
C_D	unsteady drag coefficient
C_{d_L}	linear static drag coefficient extrapolated to the stall region
$C.G$	centre of mass
C_M	unsteady moment coefficient
C_{m_L}	linear static moment coefficient extrapolated to the stall region
C_t	chord of the tail rotor
C_T	main rotor thrust coefficient
C_{T_t}	tail rotor thrust coefficient
C_Z	unsteady lift coefficient
C_{z_L}	linear static lift coefficient extrapolated to the stall region
C_0	zero-lift drag coefficient
$[\overline{C}]$	damping matrix in modal space
d, d_m	parameters used in dynamic stall model
D	drag on airfoil or fuselage drag
dA	an elemental area of the disk
e_1, e_2	root offset
$\hat{e}_x, \hat{e}_y, \hat{e}_z$	unit vectors along x, y, z axes
E	modulus of elasticity
E_d, E_l, E_m	parameters used in dynamic stall model

E_0	reference modulus
$E.A$	elastic axis
EA	axial stiffness
$EI_{\eta\eta}$, $EI_{\zeta\zeta}$	bending stiffnesses of the blade
f	fuselage frontal area
$\{\overline{F}\}$	generalized aerodynamic load vector
G	shear modulus
GJ	torsional stiffness
h	heaving motion of an airfoil
h_l, h_m	parameters used to define static aerodynamic coefficients
H	longitudinal force
H_n^m	parameter used in dynamic wake model
$Im_{\eta\eta}, Im_{\zeta\zeta}, Im_{\eta\zeta}$	mass moment of inertia of the blade cross-section
I_{xx}	moment of inertia about x-axis
I_{yy}	moment of inertia about y-axis
I_{zz}	moment of inertia about z-axis
I_ϕ	moment of inertia about elastic axis
k	reduced frequency, $\frac{\omega b}{V}$
k_x, k_y	inflow parameters in Drees model
$[K^{cf}]$	centrifugal stiffness matrix
$[K^E]$	linear stiffness matrix
K_h	linear spring constant in heaving motion
K_n^m	parameter used in dynamic wake model, $\frac{2}{\pi} H_n^m$
K_ϕ	linear torsional spring constant in pitching motion
$[\overline{K}]$	stiffness matrix in modal space
l	length of the blade
l_e	length of finite element

L	lift on airfoil
L_C	circulatory lift
L_{NC}	noncirculatory lift
$[L]$	coupling or gain matrix
$[\tilde{\mathbf{L}}^{\mathbf{c}}], [\tilde{\mathbf{L}}^{\mathbf{s}}]$	cosine and sine influence coefficient matrices
m	mass of airfoil
m, p	harmonic number
m_0	reference mass
$\dot{m}$	mass flow rate
M	moment on airfoil about elastic axis or Mach number
M_b	mass of the blade
M_C	circulatory moment
M_{NC}	noncirculatory moment
M_x, M_y, M_z	rolling, pitching and yawing moment
$[M]$	mass matrix or apparent mass matrix in inflow model
$[M^C]$	Coriolis damping matrix
$[M^1], [M^2]$	matrices related to perturbational hub motion (translations)
$[M^3], [M^4]$	matrices related to perturbational hub motion (rotations)
$m\eta_m, m\zeta_m$	first moment of inertia of the beam cross-section
M_∞	Mach number
$[\overline{M}]$	mass matrix in modal space
n, j	polynomial number
N	number of finite elements
N_b	number of blades
O_H	hub center
p_0, p_1	parameters used to define static lift coefficient
$P_j^p(\overline{\nu})$	Legendre polynomial functions

$\bar{P}_j^p(\bar{\nu})$	normalised Legendre polynomial functions, $(-1)^p \ P_j^p \ (\bar{\nu})/\rho_j^p$
$\{q\}$	finite element nodal displacements
r	radial distance
$\bar{r}$	nondimensional radial coordinate, $\frac{r}{R}$
$r_d, \ r_l, \ r_m$	parameters used in dynamic stall model
R	rotor blade radius
R_t	radius of the tail rotor
$R_x, \ R_y, \ R_z$	components of perturbational hub motion
$\overrightarrow{r_p}$	position vector of a point 'p' on the blade
$s, \ s_m$	parameters used in dynamic stall model
$\tilde{S}$	area of airfoil
s_h	horizontal tail area
s_v	vertical tail area
S_ϕ	static moment about elastic axis
t	time
T	main rotor thrust force or kinetic energy
T_t	tail rotor thrust force
$[T_{ij}]$	transformation matrix between orthogonal coordinate systems i and j
u_k	axial deformation of kth blade
U	strain energy
$u_1, \ v_1, \ w_1, \ \phi_1,$	
$u_2, \ v_2, \ w_2, \ \phi_2,$	
$v_1', \ w_1', \ v_2', \ w_2',$	
$u_{12}, \ \phi_{12}$	element nodal degrees of freedom
$\{U\},\{V\},\{W\},\{\Phi\}$	vectors of element nodal degrees of freedom
v_k	lead-lag deformation of kth blade
V	oncoming velocity

V_F	velocity at helicopter centre of mass
V_H	velocity of the hub
V_T, V_R	velocity terms used in inflow models
V_x, V_y, V_z	components of $\overrightarrow{V}$ in x, y and z direction
V_0	mean value of oncoming velocity
$\tilde{V}$	amplitude of time varying part of oncoming velocity
$\{V^L\}$	linear vector defined in the expression of kinetic energy variation
$\{V^{NL}\}$	nonlinear vector defined in the expression of kinetic energy variation
$\{V^I\}$	inertia vector defined in the expression of kinetic energy variation
$[V], [V_c], [V_s]$	velocity matrices used in dynamic inflow models
w_k	flap deformation of kth blade
W	weight of the helicopter
W_e	external work due to nonconservative forces
x_k	coordinate along k^{th} blade axis
x, y, z	coordinate of a point in the $\widehat{e}_x - \widehat{e}_y - \widehat{e}_z$ system
x, η, ζ	coordinate of a point in the $\widehat{e}_x - \widehat{e}_\eta - \widehat{e}_\zeta$ system
X, l	parameters defined in dynamic wake model
Y	lateral force
$\overline{Z}_u, \overline{Z}_v, \overline{Z}_w$	the coefficients of δu_k, δv_k and δw_k used in
	the variation of kinetic energy expression
$\overline{Z}_{v'}, \overline{Z}_{w'}, \overline{Z}_\phi$	the coefficients of $\delta v_k'$, $\delta w_k'$ and $\delta \phi_k$, used in
	the variation of kinetic energy expression
α	warping amplitude
α	rotor shaft tilt angle $w.r.t.$ helicopter forward velocity
$\tilde{\alpha}, \tilde{k}$	parameters used in dynamic stall model
α_j^p, β_j^p	induced flow coefficients
β_d	blade predroop angle

β_k	local slope in flap bending of kth blade
β_p	blade precone angle
β_s	blade presweep angle
χ	wake skew angle
$\delta\lambda$	time varying part of inflow
Δt	time step
ε	non-dimensional parameter representing the order of magnitude of typical elastic blade bending slope
ϵ_{xx}	normal strain component
ϕ	elastic twist of airfoil
ϕ_k	elastic twist of kth blade
ϕ_j^p	radial shape functions
Φ	fuselage attitude in roll
Φ	phase angle between oncoming flow and pitching motion
$\{\Phi_c\}$	Hermite cubic interpolation function
$\{\Phi_q\}$	quadratic interpolation function
$\gamma_{x\eta}, \gamma_{x\zeta}$	transverse shear strain components
$\overline{\gamma}_{x\eta}, \overline{\gamma}_{x\zeta}$	transverse shear strain at the elastic axis
Γ_1	aerodynamic state in unstalled region in lift equation
Γ_2	aerodynamic state in stalled region in lift equation
Γ_{d_2}	aerodynamic state in stalled region in drag equation
Γ_{m_2}	aerodynamic state in stalled region in moment equation
λ	total inflow ratio
λ_i	induced inflow ratio
λ_u, λ_0	uniform inflow ratio
λ_1	time varying inflow
$\lambda_{1c}, \lambda_{1s}$	cyclic inflow

λ_t	tail rotor inflow
Λ_a	tip anhedral angle
Λ_s	tip sweep angle
η, ζ	blade cross-sectional principal axes coordinates
$\{\eta\}$	vector of modal degrees of freedom
μ	advance ratio
ν	rotor induced velocity
$\overline{\nu}$	ellipsoidal coordinate on the disk, $\sqrt{1 - \bar{r}^2}$
θ	pitch angle in degree
θ_d	static stall angle
θ_{FP}	flight path angle
θ_G	geometric pitch angle
θ_I	control pitch angle
$\theta_{max}, \theta_{Mach}, u$	parameters used to define static drag coefficient
θ_{tw}	blade pretwist angle
$\theta_x, \theta_y, \theta_z$	rigid body perturbational rotation in roll-pitch-yaw
θ_0	mean value of pitch angle or main rotor collective pitch angle
θ_{0T}	tail rotor collective pitch angle
θ_{1c}, θ_{1s}	cyclic pitch angles
$\tilde{\theta}$	amplitude of time varying pitch angle
Θ	fuselage attitude pitch
ρ	density of air
ρ_j^p	normalised factor used in dynamic wake model, $\sqrt{\frac{(j+p)!!}{(2\,j+1)!!(j-p)!!}}$
$\sigma, \sigma_d, \sigma_m, \overline{\sigma_m}$	parameters used in dynamic stall model
σ_t	tail rotor solidity ratio
$\sigma_{xx}, \sigma_{x\eta}, \sigma_{x\zeta}$	stress components
τ	nondimensional time, $\frac{Vt}{b}$

τ_0	initial twist rate of the blade
τ_n^{mc}, τ_n^{ms}	coefficients of pressure expansion
ω	excitation frequency
$\overrightarrow{\omega}$	angular velocity vector
ω_h	natural frequency of the heaving motion
$\omega_x, \omega_y, \omega_z$	components of $\overrightarrow{\omega}_k$ in x, y, and z direction
$\overrightarrow{\omega}_{rigid}$	rigid body angular velocity
ω_ϕ	natural frequency of the pitching motion of 2-D airfoil
Ω	rotational speed (frequency) of the rotor
Ω	input excitation frequency in 2-D airfoil response calculation
Ω_t	tail rotor rotating speed
ψ	azimuthal angle or nondimentional time, Ωt
ψ_k	azimuthal angle of the kth blade
Ψ	cross-sectional warping function
ζ_k	local slope in lag bending of kth blade
$(\ )_{,\eta}$	derivative of $(\ )$ $w.r.t.$ η
$(\ )_{,\eta\eta}$	double derivative of $(\ )$ $w.r.t.$ η
$(\ )'$	derivative $w.r.t.$ x
$\delta(\ )$	variation of $(\ )$
$(\ )_{HT}$	quantities related to horizontal tail
$(\ )_{PA}$	quantities related to perturbational aerodynamics
$(\ )_R$	quantities in nonrotating R coordinate system
$(\ )_{VT}$	quantities related to vertical tail
$(\ )_H$	quantities in nonrotating H coordinate system
$(\ )_{1k}$	quantities in rotating $1k$ coordinate system
$(\ )_{2k}$	quantities in rotating $2k$ coordinate system
$(\ )_{3k}$	quantities in rotating $3k$ coordinate system

$(\quad)_{4k}$	quantities in rotating $4k$ coordinate system
$(\quad)_{e}$	quantities in rotating e coordinate system
$(\quad)_{5k}$	quantities in rotating $5k$ coordinate system
$(\quad)_{6k}$	quantities in rotating $6k$ coordinate system
$(\dot{\ })$	derivative $w.r.t.$ time
$(\ n\ )!!$	double factorial of n

$$= n(n-2)(n-4)\ldots(2) \text{ for even } n$$

$$= n(n-2)(n-4)\ldots(3)(1) \text{ for odd } n$$

Chapter 1

INTRODUCTION

1.1 Introduction

Formulation and analysis of rotary-wing aeroelastic/aeromechanical problems require an understanding of wide range of disciplines like, continuum mechanics, unsteady aerodynamics including stall effects, and control techniques. It is well known that helicopter rotor blades are long slender beams undergoing moderate structural deformations involving coupled flap (out-of-plane bending), lag (in-plane bending), torsion and axial modes. Therefore, a thorough knowledge of continuum mechanics is necessary for the development of structural models for rotor blades. Unlike aircraft wings, the helicopter rotor blades operate in a highly complex aerodynamic environment where different cross-sections of the blade undergo different adverse aerodynamic phenomena, like, dynamic stall, reverse flow, compressibility effects, radial flow and blade-vortex interaction (Fig. 1.1).

The field of rotary-wing aeroelasticity has progressed considerably in the past four decades (Refs. [1]-[3]). However because of the complexities, still there are several unresolved issues related to blade loads, blade response and vibrations exist (Refs. [4]-[6]). In Ref. [4], it is reported that divergence vertical oscillations are observed on most helicopter configurations and the frequencies of these oscillations are found to be in the range $3 \sim 4$ Hz which is close to the rotor rpm. Bousman in Ref. [5] has observed

that at high forward speed the vibration in the helicopter is significantly influenced by frequencies other than blade passage frequency and its integer multiples (bN_b/rev, b = 1,2,3,..., where N_b is the number of blades in the rotor system). In a recent study reported in Ref. [6], the authors have shown that there is a good correlation between rotor noise and vibration measured at the floor of the cockpit. The vibratory signals are observed to have a wide spectrum of frequency contents including those below N_b/rev. There is no published open literature available on theoretical studies addressing the issue of frequencies below N_b/rev on the rotor vibratory loads. One of the possible reasons for the presence of frequencies below N_b/rev in the vibratory signal can be due to asymmetric structural/mass properties of the rotor blade system [7]. However, even when the rotor blades are identical, it is possible that asymmetry in the aerodynamic environment (due to unsteady nonlinear effects) of the rotor blades as it goes around the azimuth can lead to a vibratory signal which can have frequencies below N_b/rev. The nonlinearities in the rotor blade aeroelasticity can arise due to: (a) moderate deformation of coupled flap-lag-torsion-axial modes (structural nonlinearity) and (b) unsteady aerodynamics including dynamic stall and wake effects (aerodynamic nonlinearity).

Structural dynamic modeling of the rotor blade representing all the geometric complexities of the rotor system and the coupled flap-lag-axial-torsion motions of the blade has reached a high level of sophistication (Refs. [8] - [10]). While formulating the aerodynamic operator, one should consider (a) unsteady aerodynamics of a rotor blade undergoing coupled pitching-plunging motion in a time varying oncoming flow, (b) induced flow (or inflow) at the rotor disc due to rotor blade wake, and (c) dynamic stall.

In the absence of a suitable three-dimensional (3-D) aerodynamic model, only two-dimensional (2-D) models are used in the aeroelastic analysis of rotor blades.

The classical two-dimensional unsteady aerodynamic models for unstalled flow (attached flow) condition are: (1) Theodorsen's model [11] applicable for a pitching and plunging airfoil with zero mean angle of attack; (2) Greenberg's theory [12] for a pitching and plunging airfoil having non-zero mean angle of attack in a time varying on-coming flow; and (3) Loewy's model [13] applicable for a pitching and plunging airfoil including cascade effects (rotor wake is treated in an approximate manner for a hovering condition). Because of the simplicity for application, most of the aeroelastic studies use Greenberg's theory, taking into consideration the wake induced inflow effects (Refs. [14]-[17]).

The wake induced inflow at the rotor disc can be obtained by either prescribed wake or free wake model. These models are computationally expensive. On the other hand, dynamic inflow models are global models, which represent the unsteady wake effects of the rotor system in a simple form. In these models, the unsteady wake-induced flow through the rotor disc is defined by a set of inflow variables and these variables essentially provide a correction to the mean inflow (Ref. [18]). Extending the dynamic inflow model, Peters *et al*. (Ref. [19]) have developed a generalised wake model. In this model, the inflow distribution is represented by a set of harmonic functions and Legendre polynomials (radial shape functions).

The most complicated phenomenon of unsteady aerodynamics is dynamic stall. It is difficult to predict stall and its effect using theoretical unsteady aerodynamic tools. Hence, most of the researchers depend on empirical or semi-empirical models. Several mathematical models that attempt to predict the effects of dynamic stall are available in the literature (Refs. [20]-[24]). ONERA dynamic stall model (Ref. [23]) is a relatively simple and efficient model, which can be easily incorporated in any aeroelastic analysis. Recently, CFD methods are applied to predict aerodynamic loads on rotors and airfoils (Refs. [25] and [26]).

1.2 Literature Review

The literature review is divided into three subsections, with each one addressing a specific aspect of mathematical modeling relevent for the study of aeroelastic problems in helicopters.

- Section 1 provides a description on structural modeling of rotor blades.

- Section 2 covers the literature on modeling of wake induced inflow at the rotor disc and sectional aerodynamics in attached (classical unsteady aerodynamic theories) and separated (2-D dynamic stall) flow regions.

- Section 3 describes the comprehensive aeroelastic models available in the literature and their contribution towards the study of rotary-wing aeroelasticity.

1.2.1 Structural Modeling of Rotor Blades

Helicopter rotor blades are long slender beams undergoing moderate deformations in flap, lag, torsion and axial modes. Over the years, several researchers have developed structural models for the rotor blade undergoing axial, bending and torsional deformations. Earlier models were restricted to the treatment of isotropic blades. With increase in the usage of composite materials in the construction of rotor blades, structural models suitable for composite rotor blades have been developed in the past two decades. Today, the structural modeling of rotor blades has reached a high level of maturity.

Since helicopter rotor blades are long slender beams undergoing moderate deformations, a nonlinear strain-displacement model is used to describe the coupling effects between axial, bending and torsional modes. Generally, the strains are assumed to be very small in comparison to unity. Such an assumption is consistent with the design requirement based on the fatigue life consideration which requires that the rotor

blades must have an operating strain level well below the elastic limit of the rotor blades.

A structural model for a rotor blade undergoing flap-lag-torsional deformations is developed by Houbolt and Brooks [27]. This model has not included the nonlinear coupling effects between bending and torsion, which are shown to be important by later researchers for the dynamic and aeroelastic analysis of helicopter rotor blades. The importance of these nonlinear coupling effects has been discussed in a review article by Friedmann [28].

Nonlinear beam theories applicable for moderate deformation of an isotropic beam, have been developed by several researchers (Refs. [29]-[32]). In these theories, the rotor blade is modeled as a one-dimensional Euler-Bernoulli beam and its sectional properties are evaluated from 2-D sectional analysis. These theories assume small strain and moderate rotation. In developing the final beam equations, higher order terms are eliminated using an ordering scheme. These moderate deformation beam theories are validated by comparing the theoretical results with the experimental data obtained for the static deformation of a cantilever beam [33]. These formulations laid the foundation of nonlinear structural dynamics of coupled bending, torsion and axial deformation of twisted nonuniform rotor blades. It may be noted that these models did not include the effects of cross-sectional warping and transverse shear. These beam models are later widely used to formulate the inertia and aerodynamic operators for aeroelastic analysis of helicopter rotor blades.

With the development of composite rotor blades, several researchers proposed structural models applicable for the analysis of composite beams having arbitrary/thin walled cross-sections (Refs. [34]-[42]). A detailed review of structural models suitable for composite rotor blades can be found in Refs. [8] and [43]-[45]. While developing the theories for composite rotor blades, the importance of cross-sectional warping and

shear effects have been identified and hence these effects are included in the formulation of beam equations. The significance of cross-sectional warping and bending-shear coupling have been studied in detail in Refs. [46]-[49]. Using a 3-D elasticity formulation, the cross-sectional properties and one-dimensional beam model are extracted in a systematic approach in Ref. [50]. This approach is denoted by the authors as "dimensional reduction".

The structural models suitable for advanced geometry tip shapes (tip sweep and anhedral) have been developed in Refs. [51]-[55]. These structural models developed for isotropic as well as composite beams are widely used in the aeroelastic analysis of rotor blade stability and response.

1.2.2 Aerodynamic Modeling

The aerodynamic modeling essentially has to address two important aspects. One is related to the evaluation of inflow through the rotor disc and other is the estimation of sectional aerodynamic loads on the rotor blade. A hierarchy of models have been developed, starting from simple to computationally intensive mathematical approaches. In the following two sections, a survey of literature on inflow modeling and sectional aerodynamic modeling is presented.

(i) Inflow Models

The induced flow through the rotor disc is generated by the shed and trailing wake vorticies from the rotor blade (Fig. 1.2). The shed vorticies are generated due to the time variation (function of azimuth angle) in lift at any cross section of the rotor blade. Trailing vorticies are formed due to variation of lift along the span-wise direction of the blade. The trailing vorticies curl up and form a strong helical tip vortex. The influence of the wake vorticies is to create an induced velocity (induced inflow) at the rotor disc. Most of the earlier vortex theories considered uniform loading along the span

of the blade and this assumption results in only a tip vortex. By assuming infinite number blades in the rotor system (actuator disc approximation), the structure of the tip vortex wake is represented as a semi-infinite vertical cylinder for hover and skewed cylinder for forward flight, as shown in Figs. 1.3 and 1.4, respectively. A brief historical description on the development of rotor inflow can be found in Ref. [56].

In hover, momentum theory (based on conservation of mass, momentum, and energy) and vortex theory (semi-infinite vertical cylindrical wake) provide identical expressions relating induced flow and rotor thrust. Using momentum theory in hover and fixed wing theory in forward flight as the two extreme conditions, Glauert provided a general expression relating the induced flow and rotor thrust, which is valid for all forward speeds starting from hover to horizontal flight. The expression for induced velocity matches exactly with momentum theory in hover and fixed wing theory in forward flight. However, at high forward speeds, the rotor disc treated as a circular wing (due to low aspect ratio) may result in considerable variation in inflow at the rotor disc.

Using skewed semi-infinite cylindrical wake and assuming uniform loading, Coleman, Feingold, and Stempin [57] obtained a closed form expression for inflow, which is varying linearly along the fore and aft diameter of the rotor disc. The linear variation is related to a constant, defined in terms of wake skew angle χ (Fig. 1.4). Drees assumed a radially constant and azimuthally varying (in sinusoidal form) circulation. This assumption leads to both tip and shed vortices. By equating the first harmonic flap moment to zero (valid for articulated blade), the expression for rotor inflow is obtained, as a function of both radial and azimuth. Mangler and Squire (Refs. [58] and [59]) obtained the expression for nonuniform inflow in the rotor disc by solving the Laplace equation of pressure field and using linearised Euler equation. The expression for the induced velocity is given in the form of a Fourier series. All the above theories consider the rotor as an actuator disc (with infinite number of blades).

For finite number of blades, the discrete vortex formation from each blade and their structure has to be properly considered in the inflow calculations. The wake geometry can be assumed to be prescribed or the sophisticated free wake (which considers the interaction between the vortices). In the prescribed wake analysis, the geometry of the vortex sheets from individual blades are prescribed in advance, which implies that the velocity field has been assumed. In this approach, the wake geometry is specified as a function of rotor configuration and thrust level, through simple analytical expressions. Landgrebe (Ref. [60]) demonstrated the practicality of this method by incorporating an experimentally derived generalised wake description in the UTRC prescribed wake hover performance analysis. Kocurek and Tangler (Ref. [61]) used a prescribed wake lifting surface model in their hover performance analysis. Prescribed vortex wake model suitable for forward flight condition is developed in Ref. [62]. In the free wake analysis, an initial distribution of the vortex sheets is assumed and the elements of the vortex sheets are allowed to convect in the velocity field they create. The vortex elements will move until they take up positions, which are consistent with the velocity field. This analysis is computationally more expensive than the prescribed wake. The application of the free-wake analysis can be found in the works of Johnson [63] and Bagai and Leishman [64]. Gray has discussed some of the aspects of vortex modeling for rotary wings in Ref. [65]. A detailed description about rotor wake and tip vortices and their modeling can be seen in Ref. [66].

The early studies (till 1950) have resulted in the formulation of nonuniform and time invariant inflow for a helicopter rotor. Sissingh was the first to develop a relation between perturbation in thrust to perturbation in inflow based on Glauert's theory (taken from Ref. [67], since original paper could not be obtained). In 1953, Carpenter and Fridovich [68] proposed a dynamic inflow model to investigate the transient rotor thrust and the inflow buildup during a jump takeoff maneuver. They extended the momentum theory in hover by including time varying inflow term involving the

apparent mass effect. It is shown that the theoretical results are in good agreement with the experimental data. It is interesting to note that no further research on the dynamic aspects of the induced velocity was pursued for the next two decades.

In 1971, extending the work of Sissingh, Curtiss and Shupe [69] developed a quasi-steady relation between perturbation in inflow to perturbation in rotor thrust, rolling and pitching moments. It is shown that incorporation of this model in rotor dynamics results in the definition of an equivalent Lock number. Ormiston and Peters [70] have expressed the perturbation in inflow to perturbation in rotor thrust, rolling and pitching moment in a compact matrix form. The perturbation inflow is given in three terms, representing the three coefficients of a truncated Fourier series upto first harmonics. Along the lines of Carpenter and Fridovich model, a time lag term is introduced in the perturbational inflow model by Crews *et al.* [71].

Using the concept of an apparent mass associated with inflow dynamics, Pitt and Peters [18] developed a dynamic inflow model consisting of three states representing the unsteady inflow through the rotor disc. This dynamic inflow model has been extensively used in rotor flight dynamics and aeromechanic problems (Refs. [72] - [75]). For detailed discussions of the dynamic inflow models, one can see the review paper given by Chen [76].

Further development in the inflow model resulted in the formulation of generalised dynamic wake model by Peters-He (Refs. [19] and [77]-[79]). This generalised wake model was derived using acceleration potential for an actuator disc. The inflow is expressed as a Fourier series in azimuth angle and by Legendre functions along the radial direction. The coefficients of each term in the series is determined by solving a set of first-order coupled differential equations with integrals of the blade loadings acting as forcing functions. The elements of the matrices representing the differential equations depend on the wake skew angle, forward speed, mean inflow, and apparent mass effects.

The dynamic wake model has been used to compute the induced-flow distribution of helicopter rotors in forward flight (Ref. [80]). The numerical results were compared with experimental inflow data and the correlation was found to be good in hover and forward flight. The dynamic wake model is extensively applied for various aeroelastic applications. To improve the observed discrepancy between theory and experiment in off-axis response of the helicopter under maneuver, wake distortion effects have been incorporated in dynamic wake model (Refs. [81] - [84]).

(ii) Sectional Aerodynamics

(a) **Attached Flow:** The earliest unsteady aerodynamic theory applicable for an airfoil oscillating in an incompressible flow was developed by Theodorsen's [11]. The airfoil is assumed to be executing simple harmonic pitching and heaving motions with mean pitch angle set at zero. Greenberg's theory [12], which is an extension of Theodorsen's theory, accounted for: (i) time varying on-coming velocity superimposed on a steady velocity, and (ii) a non-zero mean pitch angle. In these theories the unsteady wake effects are represented by a lift deficiency function $C(k)$, which is a complex quantity defined in terms of Hankel functions. While applying these theories to rotary-wing aeroelastic problem, rotor inflow has to be included suitably. In the application of the above described two-dimensional unsteady aerodynamic theories, it is often assumed that the lift deficiency function $C(k)$ is equal to unity, and this assumption implies that the unsteady wake effects are totally neglected. This assumption leads to a quasi-steady aerodynamic model. Quasi-steady Greenberg's theory has been extensively used in rotary-wing aeroleastic problems (Refs. [85]-[87]). In Lowey's theory [13], the helical wake of the rotor was considered by introducing layers of vorticity extending to infinity in both (fore and aft) directions beneath the airfoil. In this theory, a similar lift deficiency function was developed which incorporates the wake spacing. The limitation of Lowey's theory is that it is applicable only for hover

and axial flight conditions.

In all these methods, the theories are formulated in frequency domain and hence they are strictly valid only at the stability boundaries and not under sub or super critical conditions. Therefore, there is a need for the development of an unsteady aerodynamic theory valid for finite time arbitrary motion of the airfoil. Friedmann and Venkatesan [88] offered a useful method to extract finite state model from classical two dimensional unsteady aerodynamic theory with Bodè plot technique. These finite state unsteady aerodynamic models have potential application in aeroelastic systems with active control and transient response analysis. Another important unsteady aerodynamic theory is based on the work by Leishman (Refs. [89]-[92]). In this method, the attached flow aerodynamic loads are calculated using an indicial response method based on the principle of superposition. The indicial response determines the aerodynamic loading due to a step change in the airfoil downwash at the 3/4 chord position. This response is then convoluted over time to obtain the unsteady aerodynamic loads on the airfoil.

These classical 2D aerodynamic theories ignore compressibility, viscous effect, and most importantly separation and dynamic stall. Because of simplicity for application, most of the aeroelastic studies use Greenberg's theory, taking into consideration the wake induced inflow effects.

(b) **Separated Flow:** During forward flight, helicopter rotor blades are subjected to time varying oncoming flow. In order to compensate for this asymmetry in the relative airspeed between advancing and retreating sides, a time varying (once per revolution) pitch input is provided to the rotor blades. Since the rotor blades are long slender beams, under time varying aerodynamic loads, these blades undergo coupled flap bending, lag bending, elastic torsion and axial deformations. In addition, the unsteady wake of the rotor system induces a time varying inflow through the rotor disc. The influence of this inflow is to modify the effective angle of attack of the blade

11

cross-section. As a result of these complicated flow conditions and blade motions, some sections of the blade undergo dynamic stall in the retreating side of the rotor disc.

Dynamic stall is a strong nonlinear unsteady aerodynamic effect associated with flow separation and reattachment. Several experimental (Refs. [93]-[107]) and theoretical (Refs. [108]-[122]) studies are available in the open literature on dynamic stall of a 2-D airfoil undergoing pitching, plunging motion and time varying oncoming flow. Most of the experimental studies on dynamic stall phenomenon have focused on airfoils oscillating only in pitching motion (Refs. [94] and [95]). McCroskey et $al.$ [95] have shown that the dynamic stall effects depend on the amplitude of oscillation, mean angle of attack and frequency of motion. Compressibility effects on dynamic stall of a NACA 0012 airfoil undergoing pitching motion were studied by Chandrashekhara [97]. The results demonestrated that occurrence of deep stall is delayed to higher angles of attack with increased reduced frequency, but increasing Mach number alone has the opposite effect. A comparative study on the effect of pitching and plunging motions of an oscillating airfoil has been reported by Carta [101] and Ericsson et $al.$ (Refs. [102]-[104]). The experimental data show that for low angle of attack (about $\theta = 2$ deg.), pitching and plunging motions have similar effect on the lift and moment characteristics. However, for high angles of attack (about $\theta = 8$ deg.), considerable differences were observed. The combined effect of time varying oncoming velocity and pitching motion on the aerodynamic behavior of a NACA 0012 airfoil was investigated by Favier et $al.$ (Refs. [105]-[107]). It may be noted that, there is no experimental study available in the open literature on the combined effects of pitching, plunging and oncoming flow velocity variations on the aerodynamic characteristics of a 2-D airfoil.

Theoretical models that attempt to predict the effects of dynamic stall range from

relatively simple semi-empirical models to sophisticated computational fluid dynamics (CFD) methods. One of the earliest semi-empirical model for dynamic stall was developed by Beddoes [108]. In this model, aerodynamic lift and moment on an airfoil in attached flow regime is obtained from Duhamel superposition integral using the Wagner indicial response function. Corrections are applied to Wagner function to account for the effects of compressibility. Gangwani [109] has developed a synthesised airfoil method for the prediction of dynamic stall. To model the airloads in attached flow, a Mach-scaled Wagner function is used in the Duhamel superposition integral. In the separated flow regime, a set of algebraic equations with several empirical coefficients is used to represent the unsteady aerodynamic coefficients of the airfoil. Leishman and Beddoes [110] have developed a model capable of representing unsteady lift, moment and drag characteristics of an oscillating airfoil in pitching motion using Wagner function and flow separation point on the suction side of the airfoil, identified by Kirchoff flow idealisation. This model was later extended to include heaving motion [111] and pulsating motion [112]. ONERA (EDLin) model developed by Petot (Refs. [23], [113], and [114]) describes the unsteady airfoil behavior in both attached flow and separated flow of a pitching airfoil using a set of differential equations. Peters [115] modified Petot's model [23] by including the effects of heaving and pulsating oncoming flow in the lift expression and referred it as 'unified lift model'. Based on the observations of Peters [115], Petot (Refs. [116] and [117]) proposed an extended dynamic stall model including the effects of pitching, plunging and oncoming flow velocity variations. The coefficients of the differential equations of this extended model are determined by parameter identification using experimental measurements on oscillating airfoils. ONERA (BH) model developed by Troung (Refs. [118] and [119]), uses a Vander pol Duffing type nonlinear equation to represent the separated flow conditions. However, in the attached flow region, it

retains the equation developed by Petot [116]. Some of the above models are compared and well documented by Petot *et al.* [120]. Recently, CFD methods (Refs. [121] and [122]) are applied to predict dynamic stall in airfoils. Since, semi-empirical stall models can be easily integrated to aeroelastic analysis, ONERA and Leishman-Beddoes dynamic stall models are used in the literature for aeroelastic applications (Refs. [123]-[126]). Refs. [127]-[136] deal with the application of CFD approach to predict the rotor blade loads.

1.2.3 Aeroelastic Studies

Aeroelastic stability and response of rotor blade under hovering and forward flight conditions, has been studied extensively by several researchers. An excellent review on the developments of rotary-wing aeroelasticity is presented in Refs. [1]-[3]. Earlier studies used inflow models derived from momentum theory and quasi-steady aerodynamic models for the evaluation of sectional loads. With the development of perturbation inflow and dynamic inflow models, several studies employed these models in their analysis (Refs. [137]-[140]).

The application of dynamic wake model for rotor analysis was attempted for the first time by Ay Su and Peters (Refs. [141] and [142]). In this work, an isolated elastic rotor system with flapping motion was considered. The results showed that there is a significant effect of unsteady aerodynamics on the dampings of all the flap modes of the rotor. The results also showed that fairly good converged dampings can be obtained with a wake model having three radial shape functions for each harmonic of the inflow. Manjunath [67], applied dynamic wake model for his work on rotor stability in hover and forward flight. The results (Refs. [143] and [144]) indicated that analysis with dynamic wake model showed an improved correlation with the test data. The results also showed that for a better prediction of damping atleast three radial functions with each harmonic of the wake states are required

in dynamic wake model. The dynamic wake model was applied to investigate the aeromechanical stability of a rotor-fuselage system under hover and forward flight conditions (Ref. [145]). Authors validated their theoretical model with experimental data on ground resonance of a model helicopter. In all these studies, dynamic stall effects were not considered.

Tran and Falchero [146] have applied the ONERA stall model to study the stability and response of an isolated rotor blade in hover and forward flight. A nonuniform inflow model has been used for the induced inflow calculation. Rogers [147] has applied the simplified version of ONERA stall model to analyse stabilty and response of a single section model of a helicopter blade under-going flapping motion. Several other researchers (Refs. [148]-[150]) have also applied the dynamic stall model in the aeroelastic stability and response studies of rotor blades. None of the above models have used either dynamic inflow model or dynamic wake model. The effect of dynamic stall on flap-lag stability of rotor blade is analysed by Barwey *et al.* (Refs. [151] and [152]). The results of this study showed that the dynamic stall effects improve the correlation with experimental data as compared to quasi-steady aerodynamic model [153]. ONERA dynamic stall was applied to analyse the nonlinear stall flutter phenomenon of a 2-D airfoil (Ref. [154]). The mathematical analysis used Fourier decomposition, harmonic balance, and Newton-Raphson techniques to solve for the flutter boundary. The study showed that the analytical results compare well with the experimental data.

In recent years, several aeroelastic studies were undertaken by combining different aerodynamic models representing the rotor wake effects and the unsteady aerodynamic loads on a typical section of a rotor blade. These studies can be grouped into three distinct approaches. Peters *et al.* [155] have developed a suitable formulation by combining ONERA stall model and dynamic wake model for rotor blade aeroelastic and control analysis. Chunduru *et al.* [156] investigated the effects of dynamic

stall and 3-D wake on trim and lag damping of isolated bearingless rotors. They concluded that dynamic stall and wake effects appreciably improve the correlation between theory and experiment for lag damping which is given as a function of forward speed. In a subsequent study, Subramanian *et al.* [157] investigated a hierarchy of aerodynamic models. Their work mainly focused on the prediction of trim settings, regressive lag-mode damping, and root flap moment. A numerical [124] simulation was carried out to determine the transient response and lag damping of a hingeless rotor blade. The study showed that the results with dynamic wake model improve the correlation with experimental data in comparison to uniform inflow model. In a further study, the authors have shown that dynamic wake and dynamic stall model provides a better correlation with experimental data on lag damping and flap moment measured as function of forward speed (Ref. [158]).

In Refs. [159]-[161], the authors have combined rational function approximation and ONERA stall model to represent unsteady load in attached flow and separated flow regimes, respectively. Free wake model was used to predict the rotor inflow. Using this combination of stall and free wake model, they have studied vibration and noise in helicopters. Description of comprehensive codes for prediction of loads on helicopter can be found in Refs. [162]-[165]. In Refs. [166]-[174], a combination of computational fluid dynamics and computational structural dynamics has been developed to predict rotor loads and the blade response. These studies (Refs. [166]-[171]) essentially focused on predicting the blade loads for steady and level flight. Whereas, Bhagwat *et al.* (Refs. [172]-[174]) have focused on predicting the blade loads for the case of maneuvering flight. All these studies focused on correlating the theoretical results with the flight test data of UH-60A (Refs. [175]-[176]).

In general, nonlinear effects are often cited as possible reasons for any observed difference between theory and experiment (Refs. [177] and [178]). The effect of nonlinearity due to dynamic stall has been analysed by several researchers. In Ref.

[150], the authors have studied the effects of structural nonlinearity and ONERA dynamic stall model on the response of a rotor blade. In the reference [149], the semi-empirical ONERA aerodynamic model is applied to the study of nonlinear stall flutter and divergence of cantilevered wings with large amplitude and a high angle of attack. Based on the comparison of theoretical and experimental data, they concluded that the nonlinear aeroelastic analysis predicts reasonably the experimentally observed stall phenomena on the wings. The effect of dynamic stall nonlinearity in introducing chaotic behaviour of a 2-D airfoil and helicopter rotor blades have been analysed in Refs. [179] and [180]. They have shown that the necessary condition for the onset of chaotic response is that the system must be near flutter boundary. An excellent review on the nonlinear aeroelastic analysis of airfoils is presented in Ref. [181].

1.3   Objectives of the Present Study

The survey of literature clearly indicates that there is continued development in the theoretical modeling of rotor blade structural dynamics and aerodynamics. Comparison of theoretical and experimental data (Flight test data) reveals that still there is a gap between theory and experiment. Some of the observed phenomenon in flight test may be due to the nonlinearities associated with the aeroelastic problems and this thesis attempts to develop a theoretical formulation including the geometrical non-linearities associated with structural modeling and the aerodynamic nonlinearities associated with dynamic stall. The complexity of the unsteady aerodynamic model is categorised into two cases; namely (i) evaluation of rotor inflow, and (ii) evaluation of sectional aerodynamic loads (It may be noted that this study does not address issues related to blade vortex interaction, rotor/fuselage aerodynamic interaction and radial flow effects). Different levels of models are available in the literature for in-flow calculations. They are: (i) uniform inflow model based on momentum theory, (ii) Drees model, and (iii) dynamic wake model. The sectional aerodynamic loads

can be evaluated by: (i) quasi-steady approximation of Greenberg's theory applicable for only attached flow conditions, and (ii) dynamic stall model applicable for both attached and separated flow. In the present study, five different combinations of aerodynamic models have been proposed and the influence of each one of these models on the trim and response characteristics of helicopter rotor in forward flight is analysed systematically.

The objectives of the present study are:

- Development of a structural dynamic model for a flexible rotor blade with and without pretwist.

- Detailed analysis of ONERA dynamic stall model. Based on this study, an improved dynamic stall model is proposed in this thesis.

- Formulation of a time domain computational aeroelastic model by integrating the structural model, the inflow model, and the dynamic stall model for the prediction of trim and response of a helicopter rotor system in forward flight.

- Study the influence of nonlinearity due to dynamic stall and aeroelastic coupling on the response of 2-D airfoil undergoing pitching and plunging motion in a time varying oncoming flow, simulating the dynamics of a typical section of a rotor blade in forward flight.

- Formulation of a suitable computational technique for the evaluation of trim and response of a multi-bladed helicopter rotor system in forward flight. Perform a systematic analysis to identify the effects of aerodynamic modeling on the trim and rotor loads in forward flight.

- Study the effects of structural couplings due to blade pretwist on trim, blade response and rotor loads of a helicopter.

1.4   Organisation of the Thesis

The thesis is organised in several chapters and each one addresses a specific aspect of the problem.

Chapter 1 contains the introduction of the problem, literature survey and objectives.

In Chapter 2, structural modeling of the rotor blade has been developed using Hamilton's principle. This model includes the moderate deformations in flap bending, lag bending, torsion and axial modes. These equations are used to obtain the rotating natural frequencies and mode shapes of helicopter rotor blade.

Chapter 3 provides a description on inflow modeling and detailed study of ONERA dynamic stall model. An improved dynamic dynamic stall is proposed in this thesis, which is referred, as "$modified$ stall model". This stall model has been evaluated by comparing the theoretical results with experimental dynamic stall data available in the literature for pitching, plunging and fore-and-aft motion of an airfoil.

Chapter 4 deals with the aeroelastic response analysis of an airfoil operating under dynamic stall conditions. It is shown that dynamic stall in association with aeroelastic coupling can lead to bounded chaotic motion of the airfoil.

Chapter 5 presents the formulation of a time domain computational model and the solution technique, for the aeroelastic response analysis of a helicopter rotor system in forward flight. Five different combinations of aerodynamic models have been proposed in this thesis.

The influence of five aerodynamic models on the trim and response of a rotor system has been analysed systematically. The results of the aeroealstic study of straight and twisted blade configurations are presented in Chapter 6.

Conclusions of this study are presented in Chapter 7.
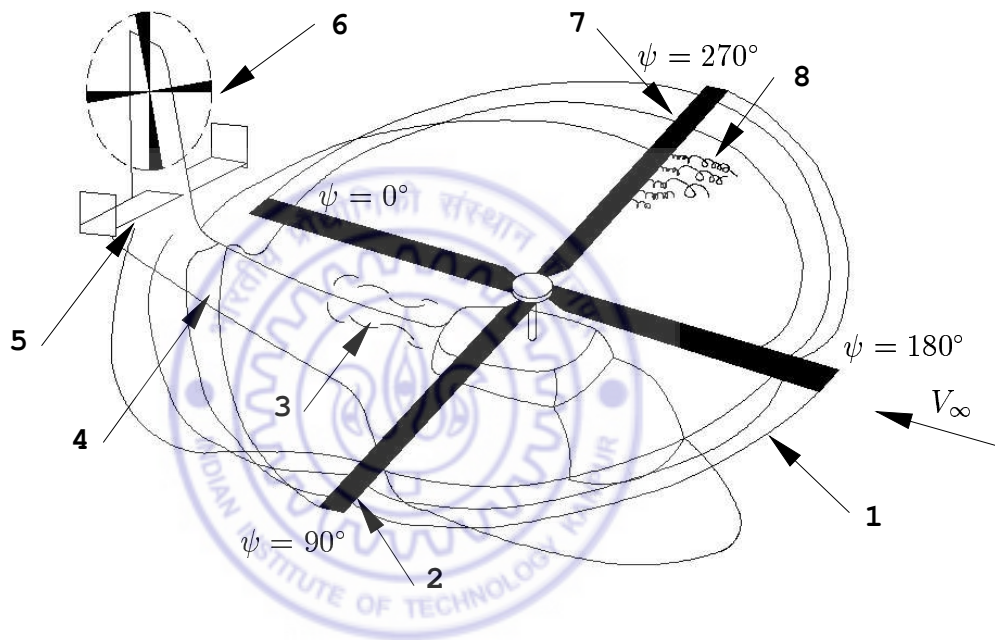
Figure 1.1: Schematic diagram of flow structure on a helicopter in forward flight
1. Tip vortices 2. Transonic flow 3. Hub wake 4. Wake and airframe interactions
5. Wake and empennage interactions 6. Wake and tail rotor interactions
7. Blade and tip vortex interactions 8. Blade stall
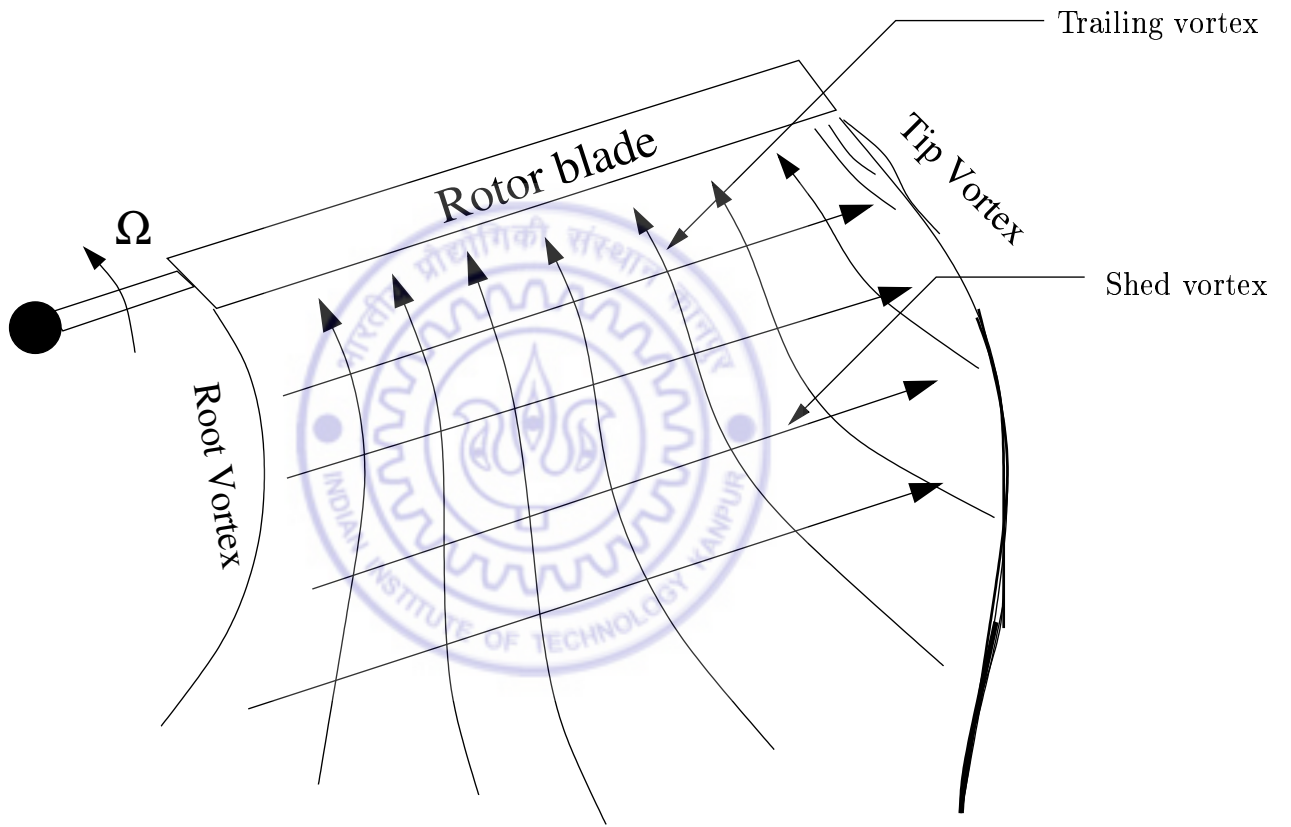
Figure 1.2: Rotor blade wake structure
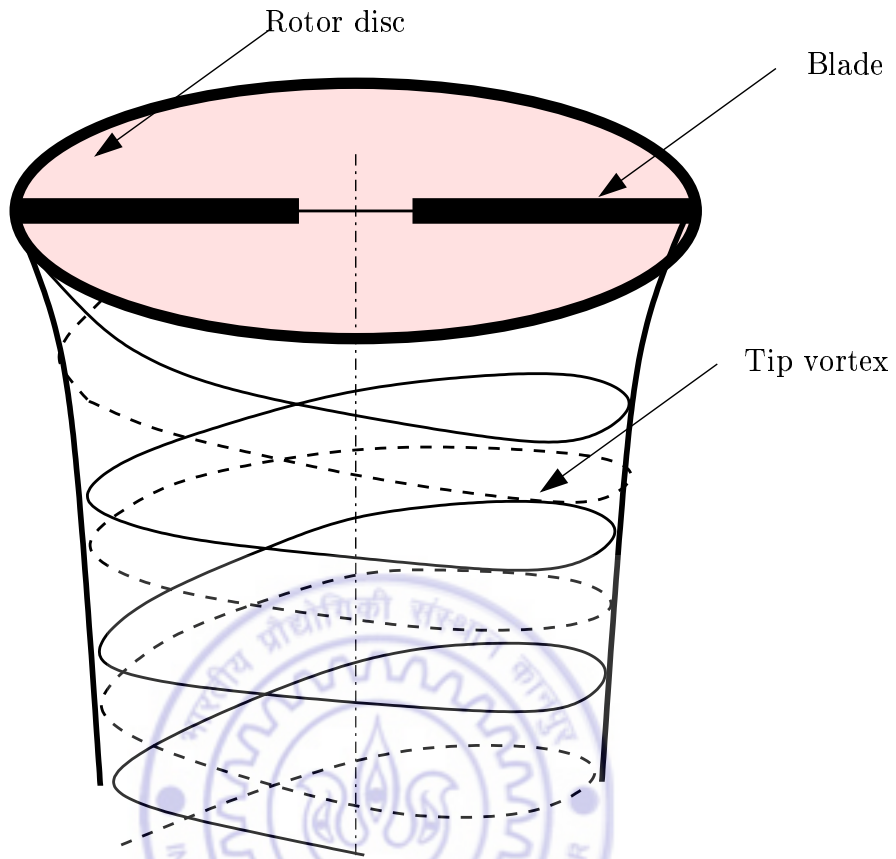
Figure 1.3: Vertical cylindrical wake structure of helicopter rotor in hover
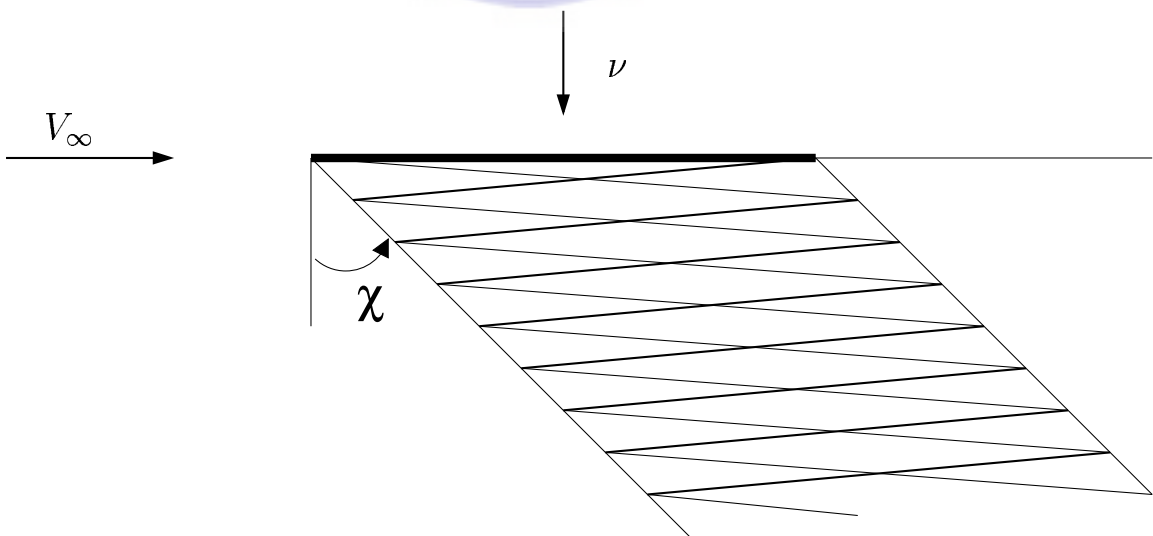
Figure 1.4: Skewed cylindrical wake structure of helicopter rotor in forward flight

Chapter 2

Structural Modeling of Rotor Blade

Helicopter rotor blades are long slender beams, undergoing moderate deformations in axial, bending and torsional modes. A nonlinear strain-displacement model is used to describe the coupling effects between axial, bending and torsional deformations. Generally, the strains are assumed to be small in comparison to unity. This assumption is consistent in satisfying the design requirement based on fatigue life consideration which states that the rotor blades must be designed to have an operating strain level well below the elastic limit of the blade material.

2.1   Rotor Blade Model

The rotor blades are attached to the hub through a complex geometrical and mechanical arrangement. The geometrical parameters describing the configuration of the rotor blade-hub system is shown in Fig. 2.1. The parameter a represents the torque offset, which is the distance from the center of rotation (hub center) to reference axis of the blade. The quantities e_1 and e_2 represent blade root offset distance from the hub. β_p stands for blade precone, describing the inclination of pitch axis with respect to ($w.r.t.$) hub plane. β_d and β_s correspond to predroop and presweep,

respectively representing the orientation of the longitudinal axis $w.r.t.$ pitch axis. Λ_a and Λ_s represent tip anhedral and sweep. The formulation represented in this section follows the approach adopted in Refs. [182]-[188].

2.1.1 Basic Assumptions

In the formulation of the dynamic model of the rotor blade with swept tip, following assumptions are made:

1. The blade is treated as an elastic beam.

2. The blade is modeled by beam type finite elements along the length of the blade.

3. The rotor shaft is rigid.

4. The blade cross section is treated as rigid in its plane but flexible for warping deformation.

5. The blade cross section has a general shape with distinct shear center, aerodynamic center and center of mass.

6. The blade undergoes moderate deformation in flap, lag, torsion and axial modes.

7. The blade has non-uniform properties along the span though it is made of isotropic material.

2.2 Ordering Scheme and Nondimensionalisation
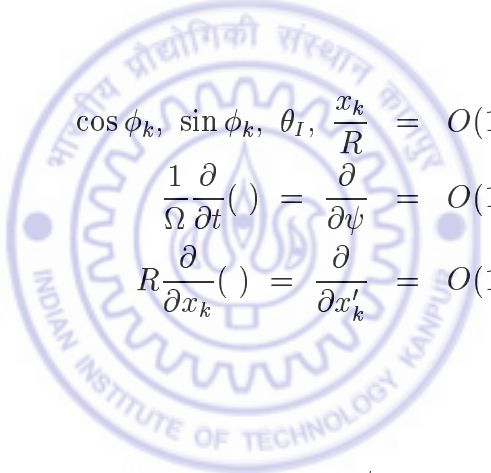
In the formulation of the equations of motion of a rotor blade with swept tip undergoing moderate deformations, a large number of higher order terms are generated. In order to identify and eliminate higher order terms in a consistent manner, an ordering scheme is employed. This ordering scheme is based on the assumption that the slopes

of the deformed elastic blade are moderate and of order $\epsilon(0.10 \leq \epsilon \leq 0.20)$. Orders of magnitude are then assigned to various non-dimensional physical parameters governing the rotor blade dynamic problem in terms of ϵ. In the derivation of the governing equations, higher order terms (terms of order greater than ϵ) are neglected with respect to terms of order 1, $i.e.$,

$$O(1) + O(\epsilon^3) \approx O(1) \tag{2.1}$$

The order of magnitude of various non-dimensional parameters governing this problem are given below:

Order 1:

$$\cos \phi_k, \ \sin \phi_k, \ \theta_I, \ \frac{x_k}{R} = O(1)$$

$$\frac{1}{\Omega} \frac{\partial}{\partial t}(\ ) = \frac{\partial}{\partial \psi} = O(1)$$

$$R \frac{\partial}{\partial x_k}(\ ) = \frac{\partial}{\partial x'_k} = O(1)$$

Order $\epsilon^{1/2}$:

$$\theta_G = O(\epsilon^{1/2})$$

Order ϵ:

$$\frac{a}{R}, \frac{e_1}{R}, \frac{e_2}{R}, \frac{v_k}{R}, \frac{w_k}{R} = O(\epsilon)$$

$$v'_k, w'_k, \phi, \beta_p, \beta_d, \beta_s = O(\epsilon)$$

Order $\epsilon^{3/2}$:

$$Im_{\eta\eta}, Im_{\zeta\zeta} = O(\epsilon^{3/2})$$

$$\frac{R_x}{R}, \frac{R_y}{R}, \frac{R_z}{R}, \theta_x, \theta_y, \theta_z = O(\epsilon^{3/2})$$

25

Order ϵ^2:

$$\frac{u_k}{R}, u'_k, m\eta_m, m\zeta_m \quad = \quad O(\epsilon^2)$$

It is important to note that ordering schemes are based on physical understanding of the behaviour of actual configurations. Hence, care must be exercised in deleting higher order terms, based on this ordering scheme.

In developing the equations of motion of a rotor blade, the physical quantities are nondimensionalised by the reference parameters given in Table 2.1. Nondimensional quantities are only used in the subsequent formulations.

2.3   Coordinate Systems

The description of the complex deformation of a rotor blade requires several coordinate systems. The transformation relation between quantities referred in various inertial, non-inertial coordinate systems is to be established before deriving the equations of motion of the rotor blade. The relation between two orthogonal systems X_i, Y_i, Z_i and X_j, Y_j, Z_j with $\hat{e}_{xi}, \hat{e}_{yi}$ and $\hat{e}_{zi}$ and $\hat{e}_{xj}, \hat{e}_{yj}$ and $\hat{e}_{zj}$ as unit vectors along the respective axes can be written as:

$$\left\{ \begin{array}{c} \hat{e}_{xi} \\ \hat{e}_{yi} \\ \hat{e}_{zi} \end{array} \right\} = [T_{ij}] \left\{ \begin{array}{c} \hat{e}_{xj} \\ \hat{e}_{yj} \\ \hat{e}_{zj} \end{array} \right\} \tag{2.2}$$

where the transformation matrix $[T_{ij}]$ can be obtained using the Euler angles required to rotate the $j-$system so as to make it parallel to $i-$system. The coordinate systems used in deriving the equation of motion for the rotor model are described below:

2.3.1 Hub Fixed Inertial System - R

The coordinate system - R, shown in Fig. 2.2, has its origin at the center of rotor hub O_H of the unperturbed hub. The X_R axis is pointing towards the helicopter tail, Z_R is pointing upwards and Y_R completes a right handed axis system. The unit vectors along the three axes are $\hat{e}_{xR}, \hat{e}_{yR}$ and $\hat{e}_{zR}$.

2.3.2 Hub Fixed Moving System - H

The coordinate system - H, shown in Fig. 2.3, is a body fixed system with its origin fixed at the center of rotor hub O_H of the unperturbed hub. Prior to perturbational motion of the hub, $H-$system coincides with $R-$system. If θ_z, θ_y and θ_x represents the sequential yaw-pitch-roll rotations, then the transformation matrix $[T_{HR}]$ can be defined as:

$$[T_{HR}] = \begin{bmatrix} 1 & 0 & 0 \\ 0 & \cos\theta_x & \sin\theta_x \\ 0 & -\sin\theta_x & \cos\theta_x \end{bmatrix} \begin{bmatrix} \cos\theta_y & 0 & -\sin\theta_y \\ 0 & 1 & 0 \\ \sin\theta_y & 0 & \cos\theta_y \end{bmatrix} \begin{bmatrix} \cos\theta_z & \sin\theta_z & 0 \\ -\sin\theta_z & \cos\theta_z & 0 \\ 0 & 0 & 1 \end{bmatrix}$$

$$(2.3)$$

Since θ_x, θ_y and θ_z are assumed to be of order $\epsilon^{3/2}$, sine and cosine functions can be approximated as $\sin\theta \approx \theta$ and $\cos\theta \approx 1$. By substituting this approximation, the transformation matrix in the equation, $[T_{HR}]$ can be simplified as:

$$[T_{HR}] = \begin{bmatrix} 1 & \theta_z & -\theta_y \\ \theta_x\theta_y - \theta_z & 1 & \theta_x \\ \theta_x\theta_z + \theta_y & \theta_y\theta_z - \theta_x & 1 \end{bmatrix} \qquad (2.4)$$

2.3.3 Hub Fixed Rotating System - 1

The coordinate system - 1, shown in Fig. 2.4, rotates about Z_1 axis with speed Ω of the rotor. Its origin is fixed at the center of rotor hub O_H. This system can be obtained by rotating $H-$system by an azimuthal angle ψ_k of the kth blade about Z_{1H} axis. The transformation matrix is given as:

$$[T_{1H}] = \begin{bmatrix} \cos\psi_k & \sin\psi_k & 0 \\ -\sin\psi_k & \cos\psi_k & 0 \\ 0 & 0 & 1 \end{bmatrix} \tag{2.5}$$

where, azimuthal angle of the kth blade, ψ_k, is defined as:

$$\psi_k = \psi + (k-1)\frac{2\pi}{N_b} \text{ and } \psi = \Omega t. \tag{2.6}$$

2.3.4 Rotating System - $2K$

The coordinate system - $2K$, shown in Fig. 2.5, is a hub fixed coordinate system, which rotates with k^{th} blade. The origin of the $2K$-system is at the location of the kth blade root 'A' (Fig. 2.1) which is at a distance $a\hat{e}_{y1} + e_1\hat{e}_{x1}$ from the hub center.

2.3.5 Preconed, Rotating System - $3K$

The system - $3K$, shown in Fig. 2.6a, also rotates with blade. This system is obtained by rotating $2K$-system by an angle $-\beta_p$ (precone angle) about y_{2k} axis. The transformation matrix between $2K$ and $3K$ systems is given as:

$$[T_{32}] = \begin{bmatrix} 1 & 0 & \beta_p \\ 0 & 1 & 0 \\ -\beta_p & 0 & 1 \end{bmatrix} \tag{2.7}$$

28

2.3.6 Predrooped, Preswept, Pitched, Blade-Fixed Rotating System - $4K$

The $4K$ - system, shown in Figs. 2.6(a) and 2.6(b), is blade fixed system with its origin at pitch bearing 'B' of the blade. It may be noted that the pitch axis of the blade is along $\hat{e}_{x3k}$ direction and the blade reference elastic axis is along the $\hat{e}_{x4k}$ direction. While changing the control pitch input of the blade, the elastic axis will move on the surface of a cone whose vertex angle is described by the β_s and β_d as shown in Fig. 2.6(c). The $4K$-system is obtained by the following steps:

- Translating the origin of $3K$-system by a distance 'e_2' along $\hat{e}_{x3k}$.

- Then rotating the system by an angle -β_s (presweep angle) about z_{3k} axis.

- Then rotating the system by an angle -β_d (predroop angle) about y_{3k} axis.

- Then rotating the system by an angle θ_I (pitch input) about x_{3k} axis.

The transformation matrix is given as:

$$[T_{43}] = \begin{bmatrix} 1 & -(\beta_s \cos\theta_I + \beta_d \sin\theta_I) & (\beta_d \cos\theta_I - \beta_s \sin\theta_I) \\ (\beta_s \cos\theta_I + \beta_d \sin\theta_I) & \cos\theta_I & \sin\theta_I \\ -(\beta_d \cos\theta_I - \beta_s \sin\theta_I) & -\sin\theta_I & \cos\theta_I \end{bmatrix}$$

$$(2.8)$$

2.3.7 Undeformed Element Coordinate System - e

The e - system, shown in Fig. 2.7, has its origin at the inboard node of the finite element. The axis $\hat{e}_{xe}$ is aligned with the beam element axis; while the vectors $\hat{e}_{ye}$ and $\hat{e}_{ze}$ are cross sectional coordinate axes. For the straight portion of the blade, the $(\hat{e}_{xe}, \hat{e}_{ye}$ and $\hat{e}_{ze})$ system has the same orientation as $(\hat{e}_{x4k}, \hat{e}_{y4k}$ and $\hat{e}_{z4k})$ system. For the swept-tip element, the $e-$system is oriented by rotating the $4K$-system about $\hat{e}_{y4k}$

by anhedral angle Λ_a and then about $\hat{e}_{z4k}$ by the sweep angle Λ_s. The transformation matrix between $4K$ and e - systems is given as:

$$\left\{ \begin{array}{c} \hat{e}_{xe} \\ \hat{e}_{ye} \\ \hat{e}_{ze} \end{array} \right\} = [T_{e4}] \left\{ \begin{array}{c} \hat{e}_{x4k} \\ \hat{e}_{y4k} \\ \hat{e}_{z4k} \end{array} \right\} \tag{2.9}$$

For the element in the straight portion of the blade

$$[T_{e4}] = \begin{bmatrix} 1 & 0 & 0 \\ 0 & 1 & 0 \\ 0 & 0 & 1 \end{bmatrix} \tag{2.10}$$

For the swept-tip element

$$[T_{e4}] = \begin{bmatrix} \cos\Lambda_s \cos\Lambda_a & -\sin\Lambda_s & \cos\Lambda_s \sin\Lambda_a \\ \sin\Lambda_s \cos\Lambda_a & \cos\Lambda_s & \sin\Lambda_s \sin\Lambda_a \\ -\sin\Lambda_a & 0 & \cos\Lambda_a \end{bmatrix} \tag{2.11}$$

where, Λ_s is the blade tip sweep angle, positive for backward sweep and Λ_a is the blade tip anhedral angle, positive upward.

2.3.8 Rotating, Blade-Fixed System - $5K$

The $5K$ - system, shown in Fig. 2.8, is cross-sectional coordinate system of the kth blade. In the undeformed state of the blade, both e and $5K$ - systems are parallel. But, the origin of the $5K$ - system is at a distance x_k from the origin of the e - system. During elastic deformation of the blade, the $5K$ - system translates and rotates with the cross-section. After deformation, the origin of the $5K$ - system, from the origin of $4K$ - system, is at the location given by

$$\left(\sum_{i-1}^{n-1}(l_e)_i\right)\hat{e}_{x4k} + (x_k + u_k)\hat{e}_{xe} + v_k\hat{e}_{ye} + w_k\hat{e}_{ze} \tag{2.12}$$

The transformation matrix between e and $5K$ - system is obtained following a flap-lag sequence of rotation. The Euler angles are respectively β_k and ζ_k corresponding to the local slope of the deformed blade in flap and lag directions. The transformation matrix is given by:

$$[T_{5e}] = \begin{bmatrix} \cos\zeta_k & \sin\zeta_k & 0 \\ -\sin\zeta_k & \cos\zeta_k & 0 \\ 0 & 0 & 1 \end{bmatrix} \begin{bmatrix} \cos\beta_k & 0 & \sin\beta_k \\ 0 & 1 & 0 \\ -\sin\beta_k & 0 & \cos\beta_k \end{bmatrix} \tag{2.13}$$

Since the angle β_k and ζ_k are of order $O(\epsilon)$, sine and cosine functions can be approximated as $\sin\theta \approx \theta$ and $\cos\theta \approx 1$. Euler angles can be expressed in the terms of the local slope of elastic deformation of the blade as -$\beta_k = w'_k$ and $\zeta_k = v'_k$. Substituting the above relations in the matrix $[T_{5e}]$ yields

$$[T_{5e}] = \begin{bmatrix} 1 & v'_k & -w'_k \\ -v'_k & 1 & v'_k w'_k \\ w'_k & 0 & 1 \end{bmatrix} \tag{2.14}$$

2.3.9 Coordinate System - $6K$

The $6K$ - system, shown in Fig. 2.9, represents the cross-sectional coordinate system in the deformed configuration of the blade. The term $\hat{e}_\eta - \hat{e}_\zeta$ represents the directions of the cross-sectional principal axes. $6K$ - system is obtained by rotating $5K$ - system about $\hat{e}_{x5k}$ through the angle $(\phi_k + \theta_G)$, where θ_G represents the geometric twist angle of the cross-section and ϕ_k represents the elastic twist. The transformation relation is given as:

31

$$\left\{ \begin{array}{c} \hat{e}_x \\ \hat{e}_y \\ \hat{e}_z \end{array} \right\}_{5k} = \left[\begin{array}{ccc} 1 & 0 & 0 \\ 0 & \cos(\phi_k + \theta_G) & \sin(\phi_k + \theta_G) \\ 0 & -\sin(\phi_k + \theta_G) & \cos(\phi_k + \theta_G) \end{array} \right] \left\{ \begin{array}{c} \hat{e}_x \\ \hat{e}_y \\ \hat{e}_z \end{array} \right\}_{6k} \qquad (2.15)$$

2.4 Kinematics

In this section, an expression for the absolute velocity at any arbitrary point 'p' on the blade is derived. During operation, the rotor blade undergoes lag, flap, torsion and axial modes. In addition, the hub center has both translational (R_x, R_y and R_z) and rotational (θ_x, θ_y and θ_z) motion. The formulation of inertia operator and aerodynamic operator requires a proper description of kinematics of the blade motion. It may be noted that the length quantities are nondimensional $w.r.t.$ rotor radius R and time derivatives are nondimensional $w.r.t.$ rotor angular velocity Ω.

2.4.1 Position Vector of a Point

The position vector of any arbitrary point 'p' in the nth finite element of the deformed blade with respect to the hub center O_H, is given by

$$\overrightarrow{r_p} = a\hat{e}_{y1} + e_1\hat{e}_{x2k} + (\sum_{i-1}^{n-1}(l_e)_i)\hat{e}_{x4k} + (x_k + u_k)\hat{e}_{xe} + v_k\hat{e}_{ye} + w_k\hat{e}_{ze} + \eta\hat{e}_{\eta} + \zeta\hat{e}_{\zeta} \quad (2.16)$$

Transforming all the unit vectors of Eq. 2.16 to the $4K$-system and neglecting the higher order terms, the position vector of the kth blade can be written in symbolic form as:

$$\overrightarrow{r_p} = R[r_x\hat{e}_{x4k} + r_y\hat{e}_{y4k} + r_z\hat{e}_{z4k}] \qquad (2.17)$$

2.4.2 Angular Velocity Vector

The angular velocity vector $\overrightarrow{\omega}$ of kth blade consists of three componets. They are:

- The rotational speed of the rotor (Ω).

- The rigid body angular velocity $\overrightarrow{\omega}_{rigid}$ of the hub due to perturbational rotation in roll-pitch-yaw $(\theta_x, \theta_y, \theta_z)$.

- The angular velocity contribution due to the rate of change of control pitch input $\Omega\dot{\theta}_I$ to the blade.

The net angular velocity vector can be written as:

$$\overrightarrow{\omega} = \Omega\hat{e}_{zH} + \overrightarrow{\omega}_{rigid} + \Omega\dot{\theta}_I\hat{e}_{x3k} \tag{2.18}$$

where, the rigid body angular velocity is given as:

$$\overrightarrow{\omega}_{rigid} = \Omega(\dot{\theta}_x\hat{e}_{xH} + \dot{\theta}_y\hat{e}_{yH} + \dot{\theta}_z\hat{e}_{zH}) \tag{2.19}$$

Transforming all the unit vectors of Eq. 2.18 to the $4K$-system and neglecting the higher order terms, the angular velocity of kth blade can be written in symbolic form as:

$$\overrightarrow{\omega} = \Omega(\omega_x\hat{e}_{x4k} + \omega_y\hat{e}_{y4k} + \omega_z\hat{e}_{z4k}) \tag{2.20}$$

2.4.3 Velocity at a Point 'p'

The absolute velocity vector $\overrightarrow{V}$, at a point 'p' on the deformed beam can be written as:

$$\overrightarrow{V} = \overrightarrow{V}_H + \dot{\overrightarrow{r}}_p + \overrightarrow{\omega} \times \overrightarrow{r}_p \tag{2.21}$$

where, $\overrightarrow{V}_H$ is the rigid body perturbational translation of the hub center O_H, which is given as:

$$\overrightarrow{V}_H = \Omega R(\dot{R}_x\hat{e}_{xR} + \dot{R}_y\hat{e}_{yR} + \dot{R}_z\hat{e}_{zR}) \tag{2.22}$$

Transforming all the unit vectors to $4K$-system

$$\overrightarrow{V} = \Omega R((V)_x\hat{e}_{x4k} + (V)_y\hat{e}_{y4k} + (V)_z\hat{e}_{z4k}) \tag{2.23}$$

The detailed expressions for the various quantities $(\overrightarrow{r}_p, \overrightarrow{\omega}$ and $\overrightarrow{V}_H)$ defined in Eq. 2.21

33

are given in Appendix A.

2.5   Equation of Motion for Rotor Blade

The coupled equations of motion of the rotor blade can be derived using Hamilton's principle. The mathematical form of Hamilton's principle over time t_1 to t_2 is stated as follows:

$$\int_{t_1}^{t_2} (\delta U - \delta T - \delta W_e)dt = 0 \qquad (2.24)$$

where U is the strain energy; T is kinetic energy; W_e is the work done by the non-conservative loads.

In this section, the expressions for the variation of kinetic energy and strain energy of the rotor blade are derived.

2.5.1   Kinetic Energy of the Blade

The kinetic energy of the beam, T is defined as:

$$T \;=\; \frac{1}{2}\int_V \rho \vec{V}.\vec{V}\, dV$$

The kinetic energy of the ith element is given by

$$T_i \;=\; \frac{1}{2}\int_0^{(l_e)_i} \int \int \rho \vec{V}.\vec{V}\, d\eta\; d\zeta\; dx \qquad (2.25)$$

where η, ζ blade cross-sectional principal axes coordinates.

The variation of kinetic energy of the ith element can be written as:

$$\delta T_i \;=\; \int_0^{(l_e)_i} \int \int \rho \vec{V}.\delta\vec{V}\, d\eta\; d\zeta\; dx \qquad (2.26)$$

Substituting for the velocity $\vec{V}$ from Eq. 2.21 and integrating δT by parts with respect

to time, yields

$$\delta T_i \quad = \quad \int_0^{(l_e)_i} \int \int \rho[Z_u \delta u_k + Z_v \delta v_k + Z_w \delta w_k + Z'_v \delta v'_k + Z'_w \delta w'_k + Z_\phi \delta \phi_k]d\eta \ d\zeta \ dx$$

(2.27)

where the terms Z_u, Z_v, Z_w, Z'_v, Z'_w and Z_ϕ, respectively are the coefficients of δu_k, δv_k, δw_k, $\delta v'_k$, $\delta w'_k$ and $\delta \phi_k$ in the variation of kinetic energy expression.

Integration of the expression over the cross-section yields:

$$\delta T_i \quad = \quad m_0 \Omega^2 R^3 \int_0^{(l_e)_i} [\bar{Z}_u \delta u_k + \bar{Z}_v \delta v_k + \bar{Z}_w \delta w_k + \bar{Z}'_v \delta v'_k + \bar{Z}'_w \delta w'_k + \bar{Z}_\phi \delta \phi_k]dx$$

(2.28)

The nondimensional cross-sectional integrals used in Eq. 2.28 are defined as:

$$m \quad = \quad \int \int \rho d\eta \ d\zeta$$

$$m\eta_m \quad = \quad \int \int \rho \eta d\eta \ d\zeta$$

$$m\zeta_m \quad = \quad \int \int \rho \zeta d\eta \ d\zeta$$

$$Im_{\eta\eta} \quad = \quad \int \int \rho \zeta^2 d\eta \ d\zeta$$

$$Im_{\zeta\zeta} \quad = \quad \int \int \rho \eta^2 d\eta \ d\zeta$$

$$Im_{\eta\zeta} \quad = \quad \int \int \rho \eta \zeta d\eta \ d\zeta$$

(2.29)

where m is mass per unit length of the blade; $m\eta_m$ and $m\zeta_m$ are the first moments of cross-sectional mass per unit length; $Im_{\eta\eta}$, $Im_{\zeta\zeta}$ and $Im_{\eta\zeta}$ are the cross-sectional mass moments of inertia per unit length of the beam.

2.5.2 Structural Modeling

The procedure for the mathematical formulation of the structural model for a beam, undergoing large (or moderate) deformations can be concisely described by the following sequence of steps.

1. Define the position vector of any point 'p' in the undeformed configuration of the beam $w.r.t.$ a set of coordinate system, which is rotating with the angular velocity of the rotor.

2. Evaluate the undeformed base vectors.

3. Define the position vector of point 'p' in the deformed configuration of the blade.

4. Evaluate the deformed base vectors.

5. Using the definition of strain tensor in the curvilinear coordinate system obtain the Green's strain measures.

6. Transform the strains defined in the curvilinear system to a local cartesian system to properly account for the twist and curvature in the beam

7. In moderate deflection theories, the expressions pertaining to (a) the axial strain at the elastic axis, (b) the curvature of the deformed elastic axis and (c) twist of the beam are substituted with approximate nonlinear expressions defined in terms of the physical displacements and their slopes.

Large deformation theories stop at step 6; whereas moderate deformation theories impose the approximation described in step 7. The formulation of strain energy outlined in this section essentially follows the procedure given in the Refs. [182] and [187].

2.5.3 Explicit Strain-Displacement Relations

The expressions for strain components in terms of deformations u_k, v_k, w_k, and ϕ_k can be written as (Refs. [182] and [187]):

$$
\begin{aligned}
\epsilon_{xx} \quad = \quad & \underline{u_{k,x} + \frac{1}{2}v_{k,x}^2 + \frac{1}{2}w_{k,x}^2} + \frac{1}{2}(\eta^2 + \zeta^2)\phi_{k,x}^2 + \alpha_{,x}\Psi + \alpha\tau_0(\zeta\Psi_{,\eta} - \eta\Psi_{,\zeta}) \\
& -[\eta\cos(\theta_G + \phi) - \zeta\sin(\theta_G + \phi)]v_{k,xx} \\
& -[\eta\sin(\theta_G + \phi) + \zeta\cos(\theta_G + \phi)]w_{k,xx} \\
& +\eta(\bar{\gamma}_{x\eta,x} - \tau_0\bar{\gamma}_{x\zeta}) + \zeta(\bar{\gamma}_{x\zeta,x} + \tau_0\bar{\gamma}_{x\eta})
\end{aligned}
\tag{2.30}
$$

$$
\gamma_{x\eta} \quad = \quad \bar{\gamma}_{x\eta} + \alpha\Psi_{,\eta} - \zeta(\phi_{k,x} + \phi_0)
\tag{2.31}
$$

$$
\gamma_{x\zeta} \quad = \quad \bar{\gamma}_{x\zeta} + \alpha\Psi_{,\zeta} - \eta(\phi_{k,x} + \phi_0)
\tag{2.32}
$$

$$
\epsilon_{\eta\eta} \approx 0 \quad \epsilon_{\zeta\zeta} \approx 0 \quad \gamma_{\eta\zeta} \approx 0
\tag{2.33}
$$

Where,

$$
\phi_0 \quad = \quad (v_{xx}\cos\theta_G + w_{xx}\sin\theta_G)(-v_x\sin\theta_G + w_x\cos\theta_G)
$$

These strain expressions contain seven unknowns which are functions of the axial coordinate x. The seven unknowns are respectively, three displacements u_k, v_k, w_k; elastic twist ϕ; shear strains $\bar{\gamma}_{x\eta}$, $\bar{\gamma}_{x\zeta}$ and warping amplitude α. The underlined term in ϵ_{xx} represents the axial strain at the elastic axis. τ_0 and Ψ represent initial twist rate and cross-sectional warping function of the blade, respectively. These strain expressions can be simplified using the following assumptions:

- The transverse shear at the elastic axis is assumed to be zero.

- α is assumed to be equal to $-\phi_{k,x}$.

The simplified strain components can be written as:

$$\begin{aligned}
\epsilon_{xx} &= u_{k,x} + \frac{1}{2}v_{k,x}^2 + \frac{1}{2}w_{k,x}^2 + \frac{1}{2} \\
&\quad (\eta^2 + \zeta^2)\phi_{k,x}^2 - \Psi\phi_{k,xx} - \tau_0(\zeta\Psi_{,\eta} - \eta\Psi_{,\zeta})\phi_{k,x} \\
&\quad -[\eta\cos(\theta_G + \phi) - \zeta\sin(\theta_G + \phi)]v_{k,xx} \\
&\quad -[\eta\sin(\theta_G + \phi) + \zeta\cos(\theta_G + \phi)]w_{k,xx}
\end{aligned}$$ (2.34)

$$\gamma_{x\eta} = -(\psi_\eta + \zeta)\phi_{k,x} - \zeta\phi_0$$ (2.35)

$$\gamma_{x\zeta} = -(\psi_\zeta - \eta)\phi_{k,x} + \eta\phi_0$$ (2.36)

Where,

$$\phi_0 = (v_{k,xx}\cos\theta_G + w_{k,xx}\sin\theta_G)(-v_{k,x}\sin\theta_G + w_{k,x}\cos\theta_G)$$

2.5.4 Stress-Strain Relations

Assuming that the blade is made of isotropic material, the stress-strain relationship is given by the following equations:

$$\left\{\begin{array}{c} \sigma_{xx} \\ \sigma_{x\eta} \\ \sigma_{x\zeta} \end{array}\right\} = \left[\begin{array}{ccc} E & 0 & 0 \\ 0 & G & 0 \\ 0 & 0 & G \end{array}\right] \left\{\begin{array}{c} \epsilon_{xx} \\ \gamma_{x\eta} \\ \gamma_{x\zeta} \end{array}\right\}$$ (2.37)

38

2.5.5   Strain Energy Variation

The strain energy of the beam can be written as:

$$
U \;=\; \frac{1}{2} E_0 R^3 \int_0^{l_e} \int \int
\begin{Bmatrix} \epsilon_{xx} \\ \gamma_{x\eta} \\ \gamma_{x\zeta} \end{Bmatrix}^{T}
\begin{Bmatrix} \sigma_{xx} \\ \sigma_{x\eta} \\ \sigma_{x\zeta} \end{Bmatrix}
\, d\eta \; d\zeta \; dx \tag{2.38}
$$

$$
U \;=\; \sum_i U_i \tag{2.39}
$$

The variation of strain energy of the ith element is given by

$$
\delta U_i \;=\; \frac{1}{2} E_0 R^3 \int_0^{(l_e)_i} \int \int
\begin{Bmatrix} \delta\epsilon_{xx} \\ \delta\gamma_{x\eta} \\ \delta\gamma_{x\zeta} \end{Bmatrix}^{T}
\begin{Bmatrix} \sigma_{xx} \\ \sigma_{x\eta} \\ \sigma_{x\zeta} \end{Bmatrix}
\, d\eta \; d\zeta \; dx \tag{2.40}
$$

The variation of the strain components are given as follows:

$$
\begin{aligned}
\delta\epsilon_{xx} \;=\;& \delta u_{k,x} + v_{k,x}\,\delta v_{k,x} + w_{k,x}\,\delta w_{k,x} + (\eta^2 + \zeta^2)\phi_{k,x}\,\delta\phi_{k,x} \\[4pt]
& -\Psi\delta\phi_{k,xx} - \tau_0(\zeta\Psi_{,\eta} - \eta\Psi_{,\zeta})\delta\phi_{k,x} \\[4pt]
& -[\eta\cos(\theta_G + \phi) - \zeta\sin(\theta_G + \phi)](\delta v_{k,xx} + \phi\,\delta w_{k,xx} + w_{k,xx}\,\delta\phi) \\[4pt]
& -[\eta\sin(\theta_G + \phi) + \zeta\cos(\theta_G + \phi)](\delta w_{k,xx} - \phi\,\delta v_{k,xx} - v_{k,xx}\,\delta\phi)
\end{aligned}
$$

$$
\delta\gamma_{x\eta} \;=\; -(\psi_\eta + \zeta)\delta\phi_{k,x} - \zeta\delta\phi_0 \tag{2.41}
$$

$$
\gamma_{x\zeta} \;=\; -(\psi_\zeta - \eta)\delta\phi_{k,x} + \eta\delta\phi_0 \tag{2.42}
$$

Where,

$$\begin{aligned}
\delta\phi_0 \quad = \quad & (v_{k,xx}\cos\theta_G + w_{k,xx}\sin\theta_G)(-\delta v_{k,x}\sin\theta_G + \delta w_{k,x}\cos\theta_G) \\
& (-v_{k,x}\sin\theta_G + w_{k,x}\cos\theta_G)(\delta v_{k,xx}\cos\theta_G + \delta w_{k,xx}\sin\theta_G)
\end{aligned}$$

It is assumed that the variations of strain components are of the same order as the corresponding strain components.

2.6 Finite Element Discretisation

The variational expressions associated with kinetic and potential energy of the rotor blades are nonlinear. The unknowns are the deformation function u_k, v_k, w_k and ϕ_k. These are dependent on both space and time. The spatial dependence is eliminated using finite element formulation. The blade is divided into sub-regions (finite elements) as shown in Fig. 2.10 and the total dynamic potential is calculated for each subregion. By applying Hamilton's principle to each sub-region, a discretised form of the equations of motion can be obtained. In this development, each sub-region is modeled by a straight beam type finite element. These beam elements are located along the reference elastic axis of the blade.

The discretised form of Hamilton's principle is written as:

$$\int_{t_1}^{t_2} \sum_{i=1}^{N} (\delta U_i - \delta T_i - \delta W_{ei})dt = 0 \tag{2.43}$$

Where, N is the total number of finite elements in the model. δU_i is variation of the strain energy of the ith element. δT_i is variation of the kinetic energy of the ith element. δW_{ei} is the virtual work of the loads on i^{th} element.

The deformations of a beam element are represented in space and time in the

40

following manner

$$
\left\{
\begin{array}{c}
v \\
w \\
\phi \\
u
\end{array}
\right\}
=
\left[
\begin{array}{cccc}
\{\phi_v\}^T & 0 & 0 & 0 \\
0 & \{\phi_w\}^T & 0 & 0 \\
0 & 0 & \{\phi_\phi\}^T & 0 \\
0 & 0 & 0 & \{\phi_u\}^T
\end{array}
\right]
\left\{
\begin{array}{c}
\{V\} \\
\{W\} \\
\{\Phi\} \\
\{U\}
\end{array}
\right\}
\tag{2.44}
$$

where $\{\phi_v\}^T, \{\phi_w\}^T, \{\phi_\phi\}^T$, and $\{\phi_u\}^T$ are space dependent interpolation functions. $\{V\}, \{W\}, \{\Phi\}$, and $\{U\}$ are the nodal degrees of freedom representing time dependent part of v_k, w_k, ϕ_k and u_k, respectively. These are given as follows:

$$
\left\{V\right\}
=
\left\{
\begin{array}{c}
v_1 \\
v_1' \\
v_2 \\
v_2'
\end{array}
\right\}
;
\left\{W\right\}
=
\left\{
\begin{array}{c}
w_1 \\
w_1' \\
w_2 \\
w_2'
\end{array}
\right\}
;
\left\{\Phi\right\}
=
\left\{
\begin{array}{c}
\phi_1 \\
\phi_2 \\
\phi_3
\end{array}
\right\}
;
\left\{U\right\}
=
\left\{
\begin{array}{c}
u_1 \\
u_2 \\
u_3
\end{array}
\right\}
;
\tag{2.45}
$$

The nodal coordinates are shown in Fig. 2.11. The variation of the displacement function for the beam can be written as:

$$
\left\{
\begin{array}{c}
\delta v \\
\delta w \\
\delta \phi \\
\delta u
\end{array}
\right\}
=
\left[
\begin{array}{cccc}
\{\phi_v\}^T & 0 & 0 & 0 \\
0 & \{\phi_w\}^T & 0 & 0 \\
0 & 0 & \{\phi_\phi\}^T & 0 \\
0 & 0 & 0 & \{\phi_u\}^T
\end{array}
\right]
\left\{
\begin{array}{c}
\delta\{V\} \\
\delta\{W\} \\
\delta\{\Phi\} \\
\delta\{U\}
\end{array}
\right\}
\tag{2.46}
$$

In this development, a cubic Hermite interpolation polynomial, $\{\Phi_C\}$, is used for the bending deflections (v_k, w_k) and a quadratic Lagrangian interpolation polynomial, $\{\Phi_q\}$, is used for torsional rotation (ϕ_k) and the axial deflection (u_k). The

mathematical expressions for these polynomials are given as:

$$\left\{ \ \phi_v \ \right\} = \left\{ \ \phi_w \ \right\} = \left\{ \ \Phi_C \ \right\} = \begin{Bmatrix} 1 - 3\xi^2 + 2\xi^3 \\ l_e(\xi - 2\xi^2 + \xi^3) \\ 3\xi^2 - 2\xi^3 \\ l_e(-\xi^2 + \xi^3) \end{Bmatrix} \qquad (2.47)$$

$$\left\{ \ \phi_\phi \ \right\} = \left\{ \ \phi_u \ \right\} = \left\{ \ \Phi_q \ \right\} = \begin{Bmatrix} 1 - 3\xi + 2\xi^2 \\ 4\xi - 4\xi^2 \\ -\xi + 2\xi^2 \end{Bmatrix} \qquad (2.48)$$

where $\xi = \frac{x_k}{l_e}$, x_k = span-wise coordinate of the beam element and l_e = length of the corresponding beam element.

For bending deformations, the nodal degrees of freedom are the displacements and slopes at both ends of the beam element. Therefore, the resulting elements will have inter-element continuity for both displacements and slopes. In addition, because of the cubic Hermite interpolation polynomial, bending strains vary linearly over the element length. The quadratic interpolation functions are used for torsional rotation (ϕ) and the axial deformation (u). This polynomial has the capability of modeling a linear variation of strains along the element length and therefore provides the same level of accuracy as the beam-bending element. The nodal degrees of freedom for axial and torsion deformation are chosen as the values of the displacements function at the two end nodes and at the mid-point of the element.

The resulting beam element has 14 degrees of freedom: 4 in-plane (lag) bending degrees of freedom, 4 out-of-plane (flap) bending degrees of freedom and 3 degrees of freedom each of torsion (ϕ), and axial deflection (u).

2.6.1 Element Matrices Associated with Kinetic Energy Variation

The beam element matrices associated with the kinetic energy variation are derived by substituting the assumed expressions for the displacements functions in the kinetic energy variation δT_i (Eq. 2.28) and carrying out the integration over the length of the beam element. The resulting variation of the kinetic energy can be written in the form:

$$
\begin{aligned}
\delta T_i \;=\; & -\{\delta q\}^T ([M]_{14\times14}\{\ddot{q}\} + [M^C]_{14\times14}\{\dot{q}\} + [K^{cf}]_{14\times14}\{q\} \\
& +[M^1]_{14\times3} \begin{Bmatrix} \ddot{R}_x \\ \ddot{R}_y \\ \ddot{R}_z \end{Bmatrix} + [M^2]_{14\times3} \begin{Bmatrix} \dot{R}_x \\ \dot{R}_y \\ \dot{R}_z \end{Bmatrix} + [M^3]_{14\times3} \begin{Bmatrix} \ddot{\theta}_x \\ \ddot{\theta}_y \\ \ddot{\theta}_z \end{Bmatrix} \\
& +[M^4]_{14\times3} \begin{Bmatrix} \dot{\theta}_x \\ \dot{\theta}_y \\ \dot{\theta}_z \end{Bmatrix} + \{V^I\}_{14\times1} + \{V^L\}_{14\times1} + \{V^{NL}\}_{14\times1})
\end{aligned}
\qquad (2.49)
$$

where $\{q\}$ represents the vector of unknown nodal degrees of freedom

$$
\{q\}_{14\times1} = \left\{ \begin{array}{cccccccccccccc} v_1 & v_1' & v_2 & v_2' & w_1 & w_1' & w_2 & w_2' & u_1 & u_2 & u_3 & \phi_1 & \phi_2 & \phi_3 \end{array} \right\}^T
\qquad (2.50)
$$

Detailed expressions for the various matrices defined in Eq. 2.49 are given in Appendix B.

2.6.2 Element Matrices Associated with Strain Energy Variation

The elemental matrix associated with the strain energy variation is derived by substituting the assumed expressions for the displacement function in the strain energy

43

variation δU_i (Eq. 2.40) and carrying out the integration over the length of the element. The resulting variation of the strain energy can be written in the form:

$$\delta U_i = \{\delta q\}^T([K^E]\{q\} + \{F^E\}) \tag{2.51}$$

where, $[K^E]_{14\times14}$ is the elemental stiffness matrix, $\{F^E\}_{14\times1}$ is the nonlinear stiffness vector. By linearisation of nonlinear terms associated with the axial strain at the elastic axis, the above nonlinear stiffness vector can be written in the following form as:

$$\{F^E\} = ([K^{E'}]\{q\} + \{\tilde{F}^E\}) \tag{2.52}$$

The elements of the matrices $[K^E]$ and $[K^{E'}]$, defined in Eqs. 2.51 and 2.52, respectively are given in Appendix C.

2.7 Results and Validation

The first step in the aeroelastic response study is the evaluation of natural frequencies and corresponding mode shapes of the rotating blade. Using the inertia and structural model developed here, natural frequencies and mode shapes are evaluated for different beam models namely, (i) uniform straight beam (with zero pretwist), (ii) non-uniform straight beam and (iii) non-uniform twisted beam. The equation for i^{th} finite element can be written as:

$$[M]_i\{\ddot{q}\}_i + [K]_i\{q\}_i = 0 \tag{2.53}$$

where $[M]_i$ represents the mass matrix of ith element. The stiffness matrix $[K]_i$ is a combination of three components. They are $[K^{cf}]_i$ (given in Eq. 2.49), $[K^E]_i$ (given in Eq. 2.51) and $[K^{E'}]_i$ (given in Eq. 2.52). The element matrices are assembled to form the global finite element model for the rotor blade. Imposing the root boundary conditions, the corresponding rows and columns from the global matrix are eliminated.

The resulting matrix equation can be written as:

$$[M]\{\ddot{q}\} + [K]\{q\} = 0 \qquad (2.54)$$

Performing an eigen analysis, the natural frequencies of an undamped rotating blade in vacuum can be evaluated.

2.7.1 Uniform Straight Blade

In order to validate the finite element blade model developed in this study, the results of the present analysis are compared with those available in the literature. The data shown in the Table 2.2 correspond to a uniform and untwisted hingeless blade. Using this data, the natural frequencies and mode shapes of the rotating blade are calculated. In the present formulation thirty beam elements of equal length are used. Table 2.3 shows a comparison of the natural frequencies obtained in this study with those available in the literature (Refs. [182] and [185]). It can be seen that the natural frequencies are in good agreement with each other.

2.7.2 Nonuniform Straight Blade

The mass and stiffness properties of a nonuniform rotor blade as a function of radial station are given in Tables 2.4 and 2.5, respectively. The graphical representation of these properties are shown in Figs. 2.12 and 2.13, respectively. It may be noted that the properties of the blade are given from the radial station 0.114 R. From the figures, it can be seen that both inertia and stiffness properties show large variation near the tip and root regions of the blade. Using linear interpolation of the properties within an element, the element stiffness and mass matrices are obtained. The root stiffness and mass matrices are defined for the element starting from hub centre to the radial station 0.114 R. Imposing fixed boundary condition at hub centre the root stiffness and mass matrices are obtained. The rearranged root matrices for assembly

are given below, along with degrees of freedom indicated out side the matrices. The root stiffness matrix $[K]_{root}$ is given as:

$$
\begin{bmatrix}
15.0 & 0 & 0 & 0 & 0 & 0 & 0 & 0 \\
0 & 1.0E5 & 0 & 0 & 0 & 0 & 0 & 0 \\
0 & 0 & 0.132E2 & 0 & 0 & 0 & 0 & 0 \\
0 & 0 & 0 & 0.08 & 0 & 0 & 0 & 0 \\
0 & 0 & 0 & 0 & 0.05E2 & 0 & 0 & 0 \\
0 & 0 & 0 & 0 & 0 & 0.015 & 0 & 0 \\
0 & 0 & 0 & 0 & 0 & 0 & 0.0073 & 0 \\
0 & 0 & 0 & 0 & 0 & 0 & 0 & 1.0E5
\end{bmatrix}
\begin{matrix}
\phi_{12} \\ u_{12} \\ v_2 \\ v_2' \\ w_2 \\ w_2' \\ \phi_2 \\ u_2
\end{matrix}
\qquad (2.55)
$$

The root mass matrix $[M]_{root}$ is given as:

$$
\begin{bmatrix}
2.3E-05 & 0 & 0 & 0 & 0 & 0 & 0 & 0 \\
0 & 0.12 & 0 & 0 & 0 & 0 & 0 & 0 \\
0 & 0 & 0.1 & 0 & 0 & 0 & 0 & 0 \\
0 & 0 & 0 & 2.9E-05 & 0 & 0 & 0 & 0 \\
0 & 0 & 0 & 0 & 0.076 & 0 & 0 & 0 \\
0 & 0 & 0 & 0 & 0 & 2.6E-05 & 0 & 0 \\
0 & 0 & 0 & 0 & 0 & 0 & 2.5E-05 & 0 \\
0 & 0 & 0 & 0 & 0 & 0 & 0 & 0.025
\end{bmatrix}
\begin{matrix}
\phi_{12} \\ u_{12} \\ v_2 \\ v_2' \\ w_2 \\ w_2' \\ \phi_2 \\ u_2
\end{matrix}
$$

$$(2.56)$$

(i) Nonuniform Straight Blade Configuration

The rotating natural frequencies and mode shapes for a nonuniform straight blade are evaluated. For this configuration, because of nonuniform properties, different length of beam elements are used at different spanwise locations. From the hub centre to station 0.25 R, 14 elements are used. From station 0.25 R to station 0.8 R (uniform

section) and from station 0.8 R to tip, 10 and 6 elements are used respectively. In total the rotor blade was represented by thirty beam elements. The corresponding total number of degrees of freedom are 240 (after imposing root boundary conditions).

The data shown in the Tables 2.4 and 2.5 correspond to a nonuniform blade. Using this data, the natural frequencies and mode shapes of the rotating blade are calculated. Table 2.6 shows the natural frequencies obtained in this study. Mode shapes corresponding to flap deformation can be seen in Fig. 2.14. Mode shapes of lag, torsional and axial deformation can be seen in Fig. 2.15.

(ii) Nonuniform Twisted Blade Configuration

For the twisted blade configuration, the blade pretwist starts from section 0.25 R. From hub centre to section 0.25 R, the pretwist is taken as zero. A linear pretwist of -8 deg. is taken along the span of the blade. The variation of pitch angle along the span of the blade is as follows: When the root section (0 to 0.25 R) is at zero pitch angle, the blade section at 0.25 R has a pitch angle 12 deg. and the pitch angle at the blade tip is 4 deg.

Frequencies for twisted blade configuration are evaluated and listed in Table 2.7. Corresponding mode shapes are generated and are shown in Figs. 2.16 and 2.17. From the figures, it is evident that the twist introduces coupling in flap and lag modes. The contribution of the lag in first flap mode is close to 6% (Fig. 2.16), whereas contribution of the flap in first lag mode is less than 1% (Fig. 2.17).

2.8   Summary

The coupled flap-lag-torsion-axial equations of motion of the hingeless rotor blade have been derived using Hamiltons principle. The rotor blade is modeled using beam type finite elements and each element has 14 degrees of freedom. They correspond to four lag degrees of freedom (v_1, v_1', v_2, v_2'), four flap degrees of freedom (w_1, w_1', w_2, w_2'),

three torsional (ϕ_1, ϕ_2, ϕ_3) and three axial (u_1, u_2, u_3) degrees of freedom. A cubic Hermite polynomial is used as interpolation function for the bending deflections (lag and flap) and a quadratic Lagrangian polynomial is used for torsional rotation and the axial deflection. A linear structural dynamic problem is first solved in finite element domain to obtain the rotating mode shapes and frequencies of the rotor blade.

Table 2.1: Nondimensional parameters

Physical Quantity	Reference Parameter
Length	R
Time	$1/\Omega$
Mass per unit length	m_0
Velocity	ΩR
Acceleration	$\Omega^2 R$
Force	$m_0\Omega^2\ R^2$
Moment	$m_0\Omega^2\ R^3$
Work/Energy	$m_0\Omega^2\ R^3$

Table 2.2: Data for uniform and untwisted rotor blade

$Im_{\zeta\zeta}$	0.0004
$Im_{\eta\eta}$	0.0
θ_G	0.000
m	1.0
β_s	0.0
β_d	0.0
β_p	0.0
θ_I	0.0
GJ	0.001473
EA	20.0
e_1	0.0
e_2	0.0
a	0.0
$C_0 = EAC_0/EA$	0.0
$EI_{\zeta\zeta}$	0.0301
$EI_{\eta\eta}$	0.0106

Table 2.3: Natural frequencies of uniform rotor blade

Mode	Present Study	Ref. [185]	Ref. [182]
1st Lag	0.7311	0.7311	0.732
2nd Lag	4.4530	4.4532	-
3rd Lag	11.2868	-	-
1st Flap	1.1244	1.1251	1.125
2nd Flap	3.4073	3.4266	-
3rd Flap	7.6171	7.7154	-
1st Torsion	3.2633	3.2633	3.263
1st Axial	6.9389	6.9389	-

Table 2.4: Inertia properties of nonuniform rotor blade

$\bar{r}$	m	$Im_{\eta\eta}$	$Im_{\zeta\zeta}$
0.114	1.44	5.73E-06	6.41E-05
0.121	1.35	5.41E-06	5.32E-05
0.128	1.27	5.19E-06	4.4E-05
0.135	1.21	5.76E-06	3.91E-05
0.142	1.14	6.66E-06	3.53E-05
0.148	1.07	7.58E-06	3.12E-05
0.156	1.02	8.59E-06	2.70E-05
0.164	0.993	8.94E-06	2.5E-05
0.171	0.961	8.86E-06	2.44E-05
0.179	0.928	8.78E-06	2.38E-05
0.186	0.897	8.67E-06	2.31E-05
0.194	0.866	8.56E-06	2.27E-05
0.202	0.885	8.56E-06	2.27E-05
0.209	0.905	8.29E-06	5.49E-05
0.217	0.924	8.10E-06	1.10E-04
0.224	0.943	7.91E-06	1.65E-04
0.232	0.980	7.91E-06	1.65E-04
0.247	1.03	7.34E-06	3.23E-04
0.265	1.03	7.34E-06	3.23E-04
0.295	1.02	7.34E-06	3.23E-04
0.417	1.02	7.34E-06	3.23E-04
0.477	1.01	7.34E-06	3.23E-04
0.598	1.01	7.34E-06	3.23E-04
0.629	1.00	7.34E-06	3.23E-04
0.720	0.999	7.34E-06	3.23E-04
0.750	0.996	7.34E-06	3.23E-04
0.776	0.995	7.34E-06	3.23E-04
0.800	0.994	7.34E-06	3.23E-04
0.833	0.964	6.38E-06	3.18E-04
0.879	0.927	5.08E-06	3.12E-04
0.917	0.895	3.99E-06	3.10E-04
0.924	0.854	3.78E-06	3.07E-04
0.932	0.814	3.48E-06	2.72E-04
0.955	0.594	2.500E-06	1.68E-04
0.977	0.418	1.22E-06	7.72E-05
1.000	0.249	2.72E-07	2.72E-06

Table 2.5: Stiffness properties of nonuniform rotor blade

$\bar{r}$	$EI_{\eta\eta}$	$EI_{\zeta\zeta}$	GJ
0.114	0.001990078	0.023189	0.002979
0.121	0.001863175	0.019093	0.002863
0.128	0.001892016	0.016094	0.002703
0.135	0.002220812	0.015805	0.00265
0.142	0.002549607	0.01194	0.002689
0.148	0.002884171	0.010095	0.002825
0.156	0.003189893	0.008306	0.002975
0.164	0.003143747	0.008018	0.003047
0.171	0.003091831	0.00773	0.003059
0.179	0.003034148	0.007441	0.00305
0.186	0.002976465	0.007153	0.003039
0.194	0.002901476	0.006864	0.003029
0.202	0.002838024	0.008249	0.003021
0.209	0.002878403	0.024227	0.003107
0.217	0.002918781	0.040263	0.00329
0.224	0.00295916	0.056241	0.003591
0.232	0.003016843	0.079603	0.003892
0.247	0.003057221	0.094601	0.004479
0.265	0.003057221	0.094601	0.004472
0.295	0.003057221	0.094601	0.004472
0.417	0.003057221	0.094601	0.004472
0.477	0.003057221	0.094601	0.004472
0.598	0.003057221	0.094601	0.004472
0.629	0.003057221	0.094601	0.004472
0.720	0.003057221	0.094601	0.004472
0.750	0.003057221	0.094601	0.004472
0.776	0.003057221	0.094601	0.004472
0.800	0.002861098	0.094601	0.004472
0.833	0.002388094	0.094024	0.004255
0.879	0.001897785	0.093447	0.003517
0.917	0.001626673	0.093447	0.002923
0.924	0.001511306	0.088832	0.002821
0.932	0.001222889	0.070374	0.002719
0.955	0.001176742	0.041994	0.001669
0.977	0.000152	0.012517	0.000886
1.000	0.000152	0.012517	0.002043

Table 2.6: Natural frequencies of untwisted non-uniform rotor blade

Mode	Present Study
1st Lag	0.701
2nd Lag	5.308
1st Flap	1.089
2nd Flap	2.896
3rd Flap	5.145
4th Flap	7.688
1st Torsion	4.509
1st Axial	9.155

Table 2.7: Natural frequencies of twisted non-uniform rotor blade

Mode	Present Study
1st Lag	0.701
2nd Lag	5.293
1st Flap	1.093
2nd Flap	2.822
3rd Flap	4.865
4th Flap	7.150
1st Torsion	4.508
1st Axial	9.155

a) Front view

b) Top view
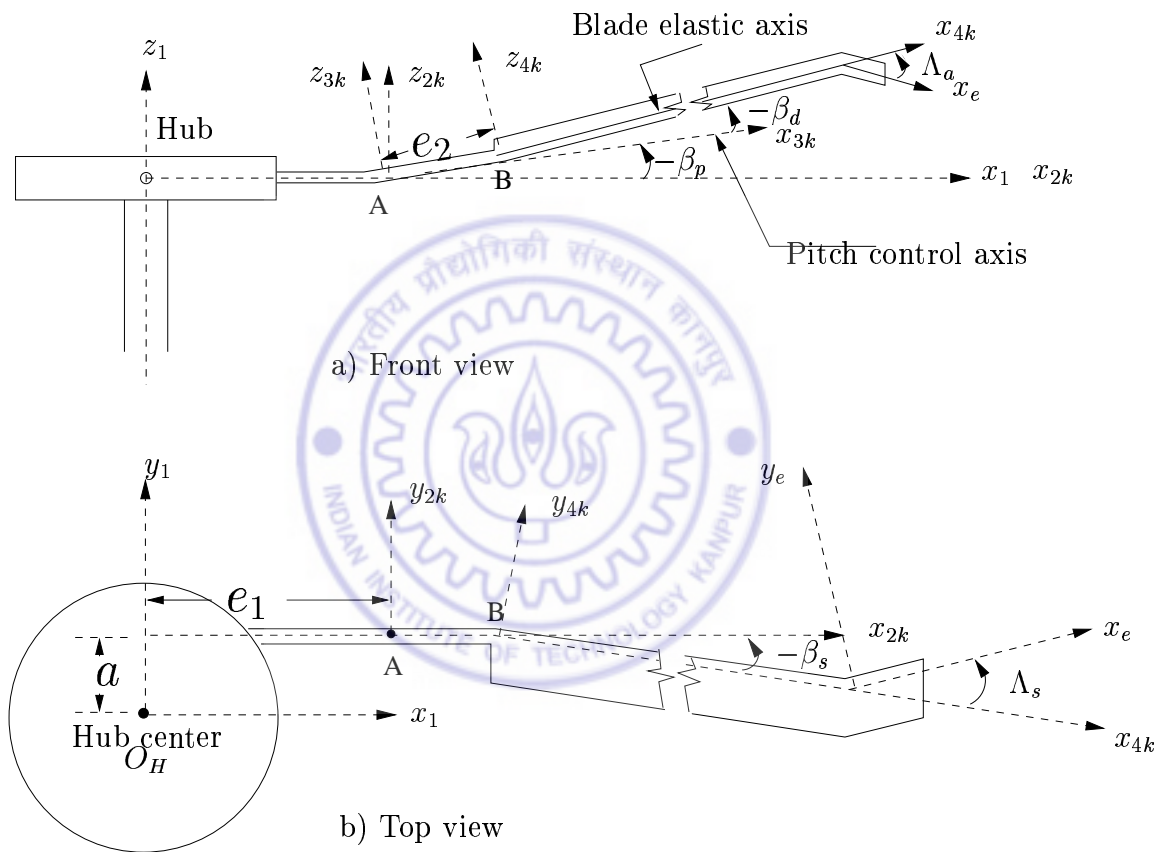
Figure 2.1: Rotor blade geometry with swept tip and anhedral
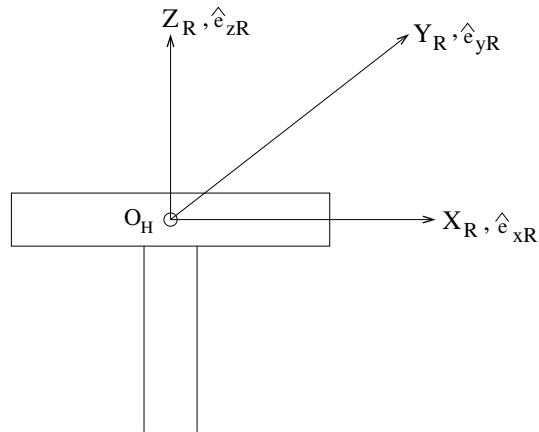
Figure 2.2: Inertial system - R
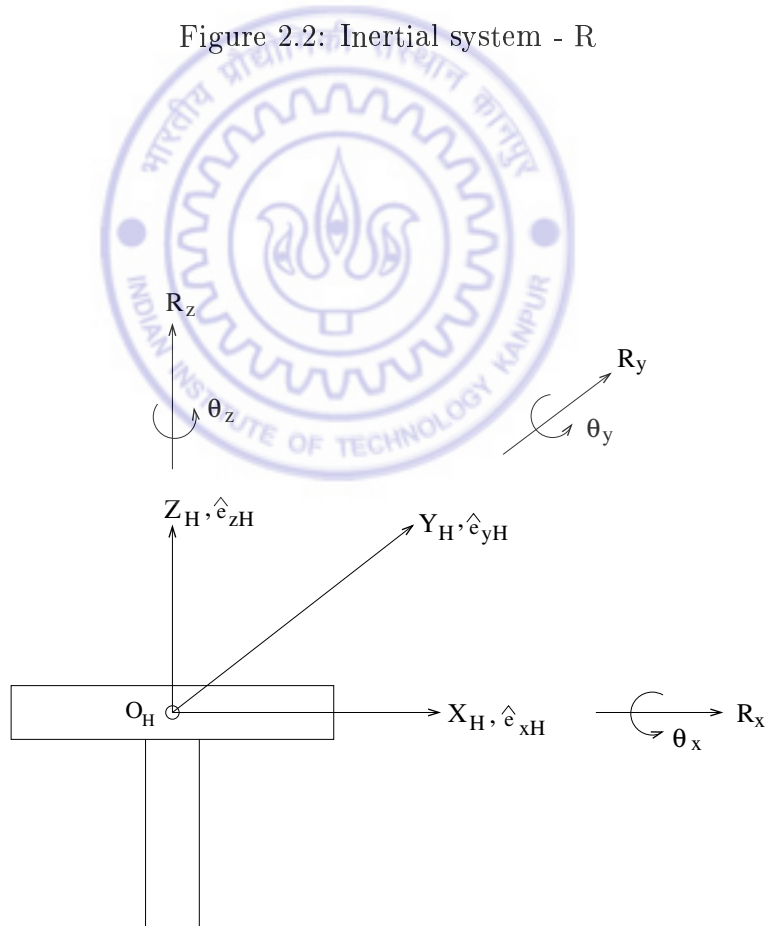
Figure 2.3: Hub fixed coordinate system - H
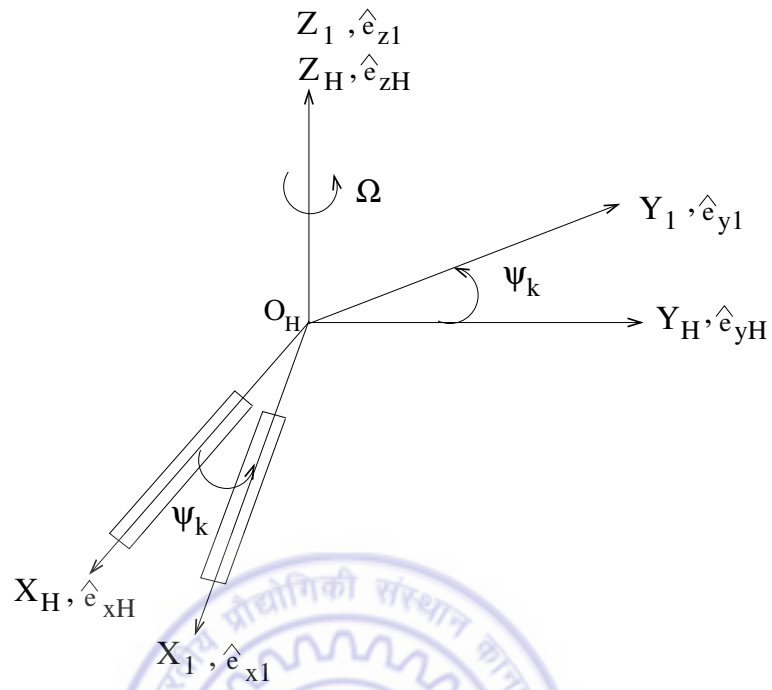
Figure 2.4: Rotating hub system - 1
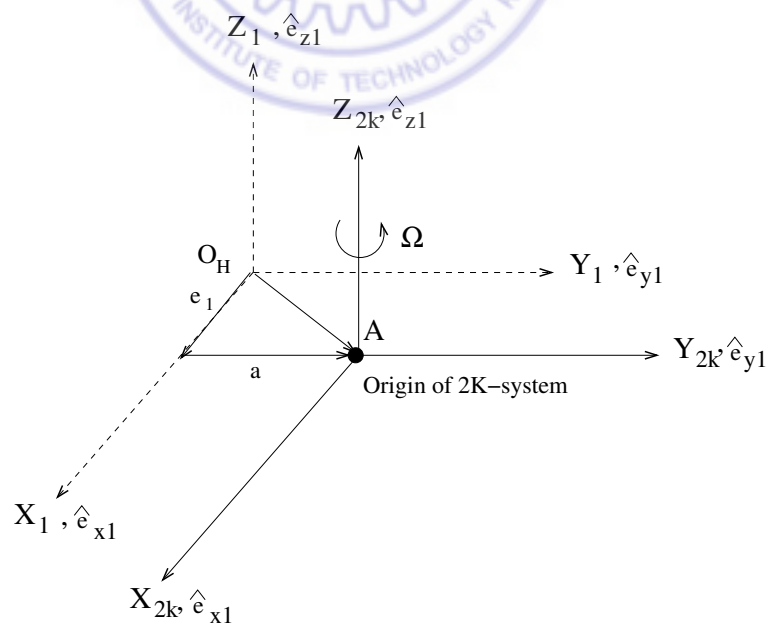
Figure 2.5: Rotating hub system - 2

a) Front view

b) Top view

c) Blade motion due to pitch input
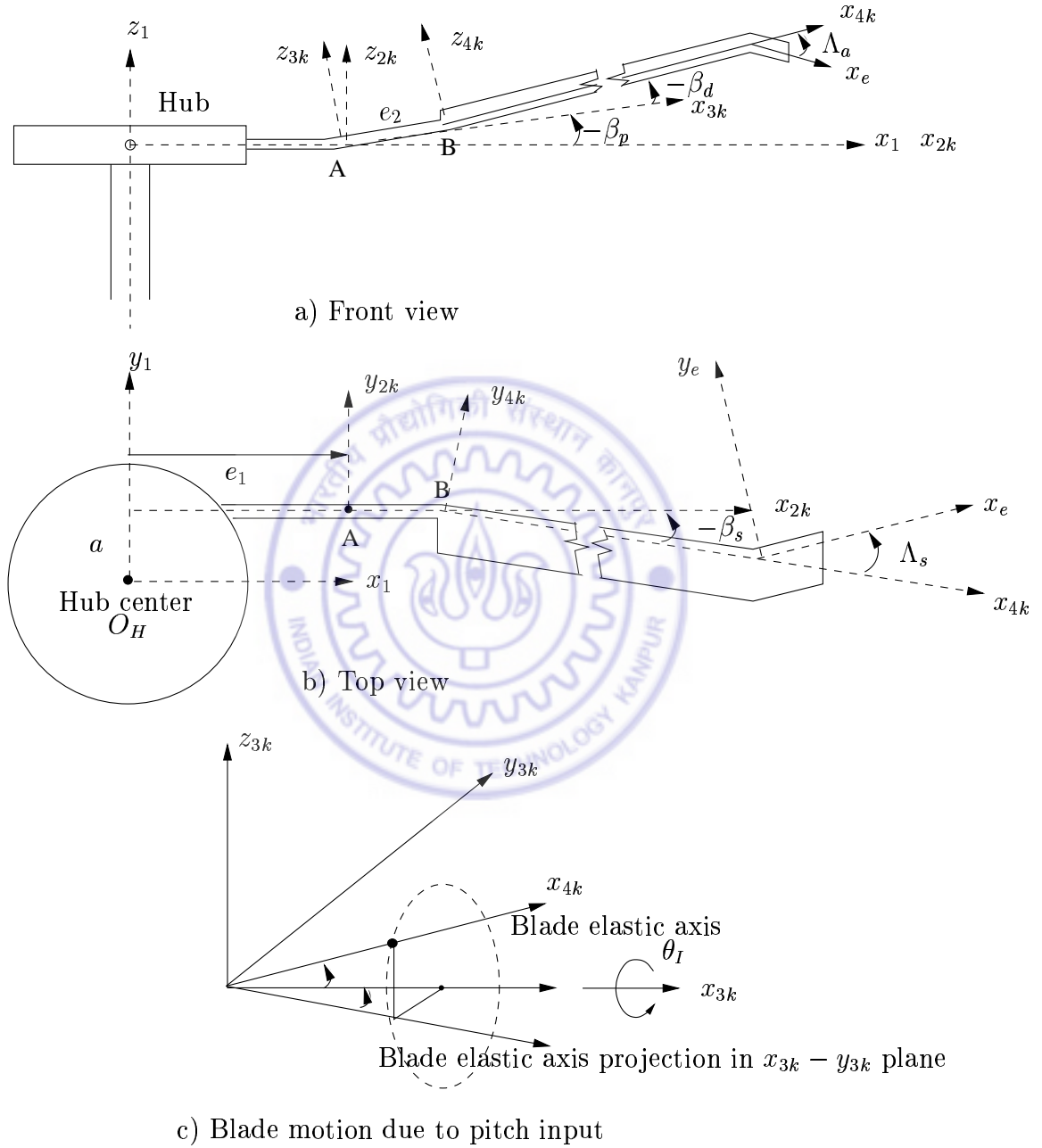
Figure 2.6: Blade coordinate system 3K and 4K
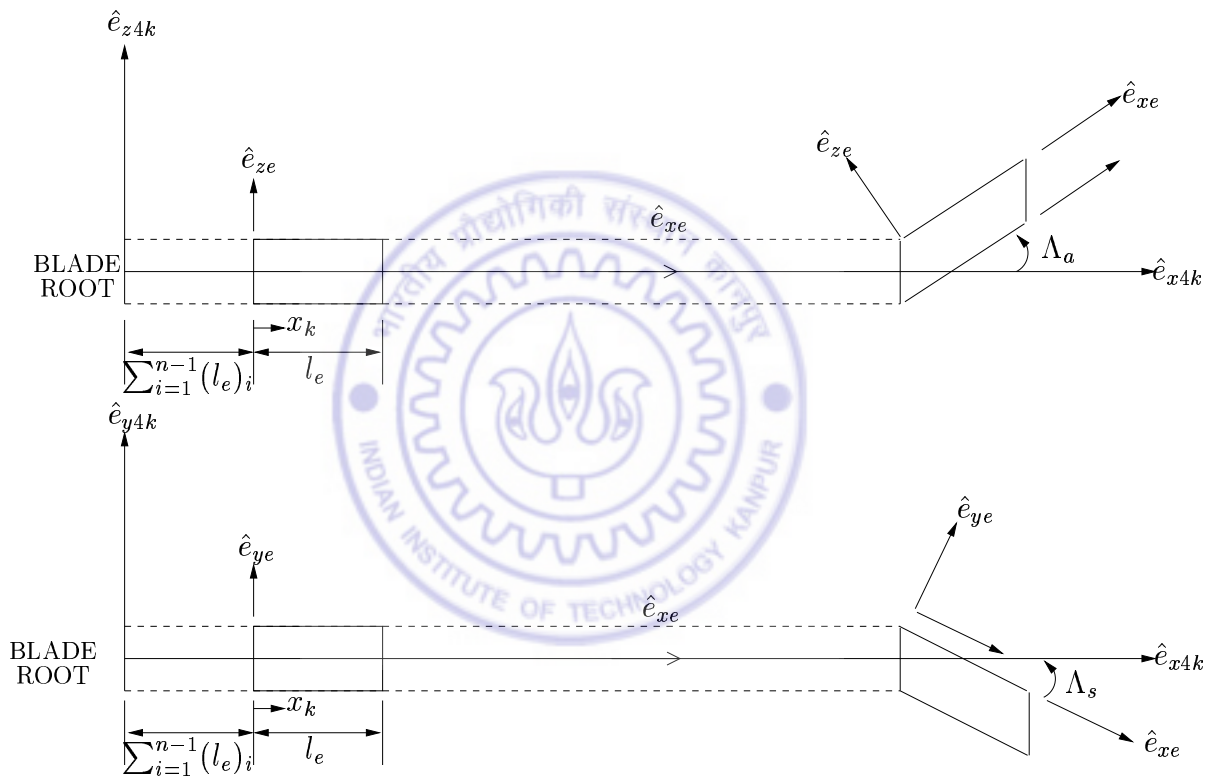
Figure 2.7: Undeformed element coordinate system
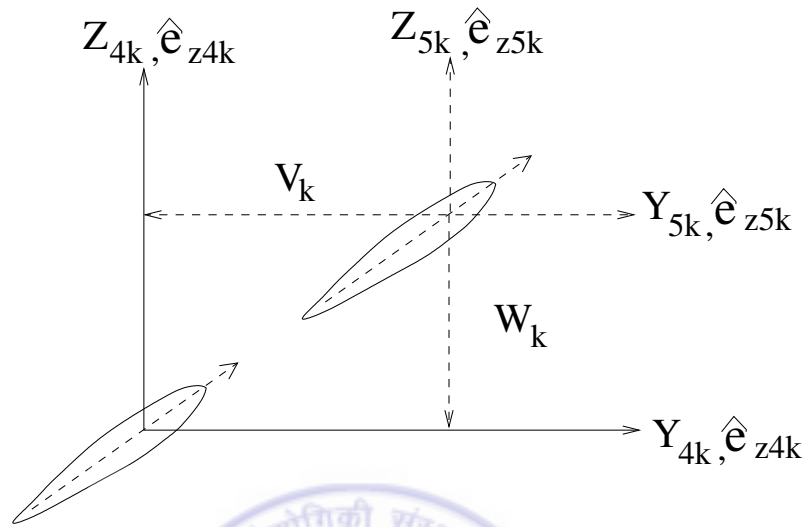
Figure 2.8: Rotating blade fixed system - 5K
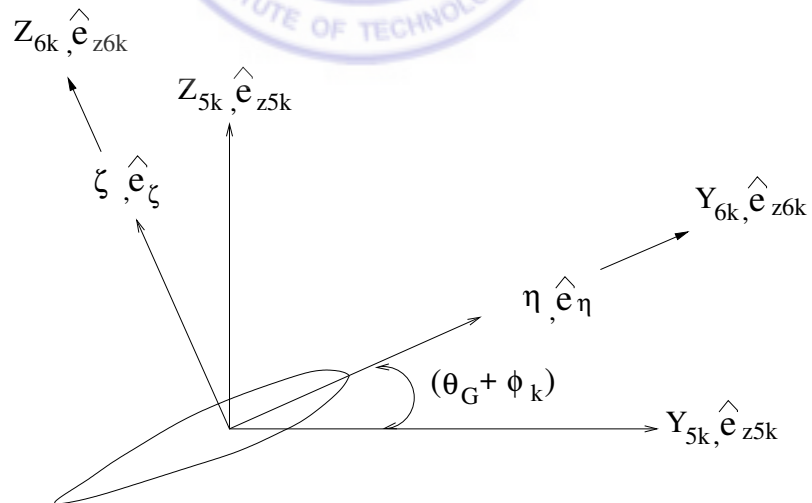
Figure 2.9: Cross-sectional principal co-ordinate system

$$(n-1)\, l_e + \, x_k$$
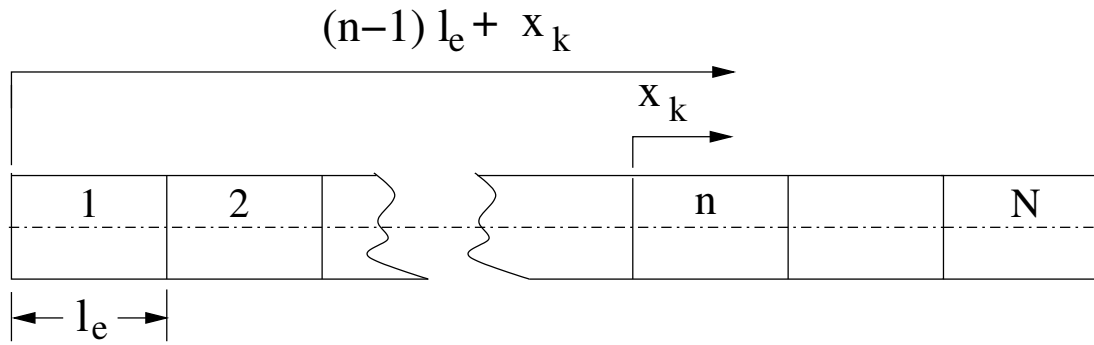
Figure 2.10: Finite element model of a blade
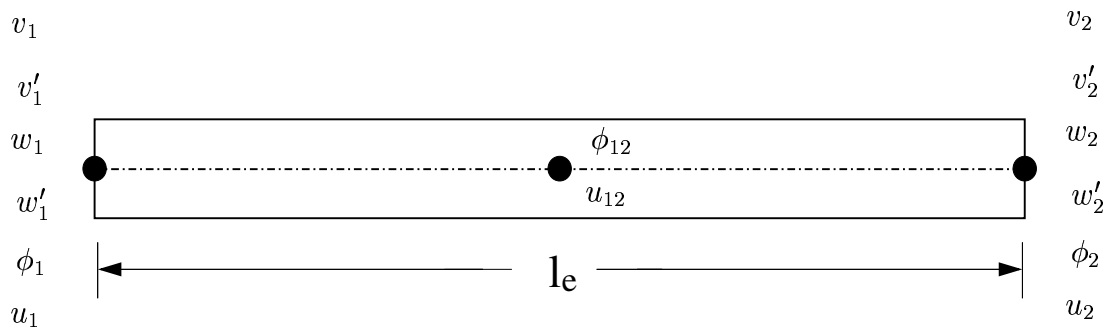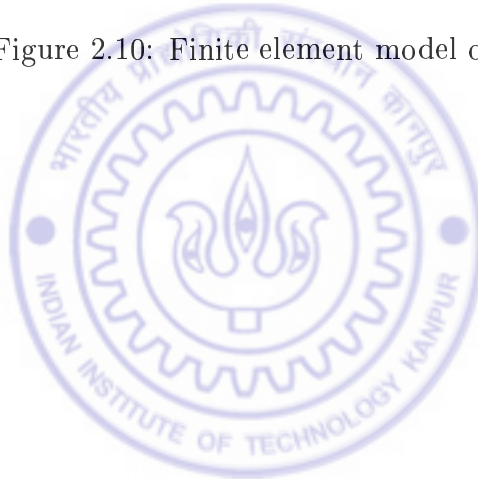
Figure 2.11: Element nodal degrees of freedom
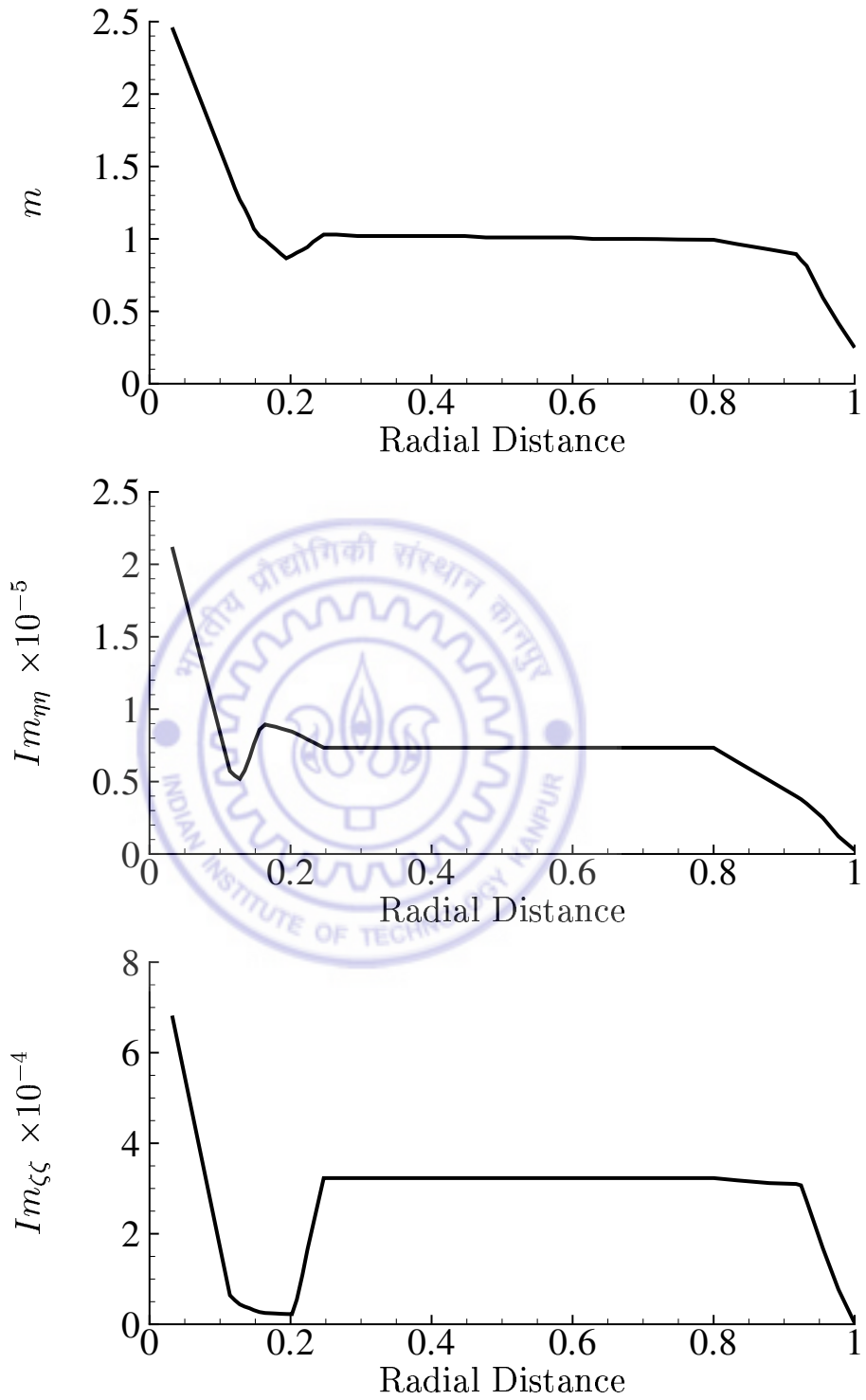
Figure 2.12: Distribution of mass and mass moment of inertia along the radius (nondimensional)
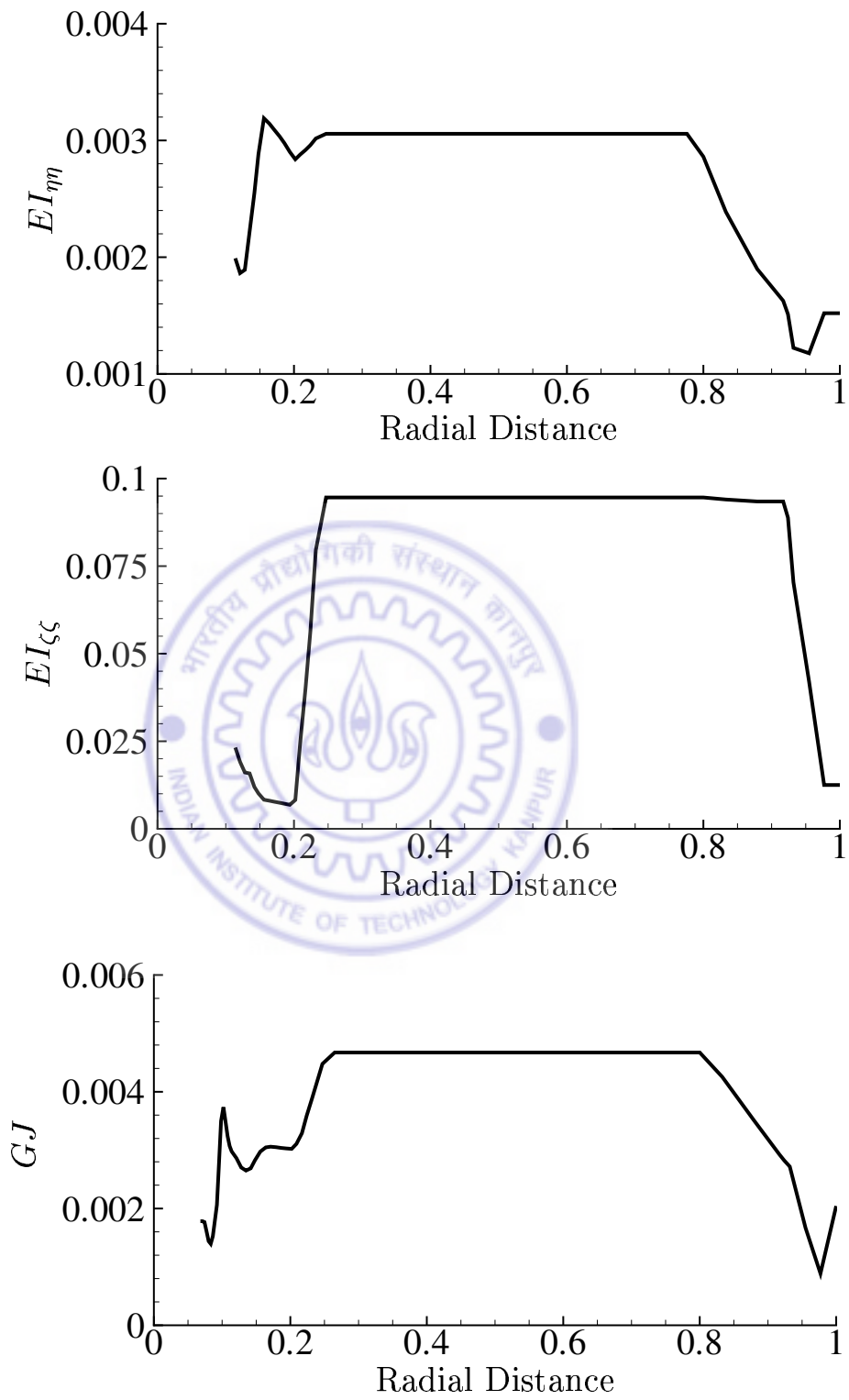
Figure 2.13: Distribution of bending and torsional stiffness along the radius (nondimensional)
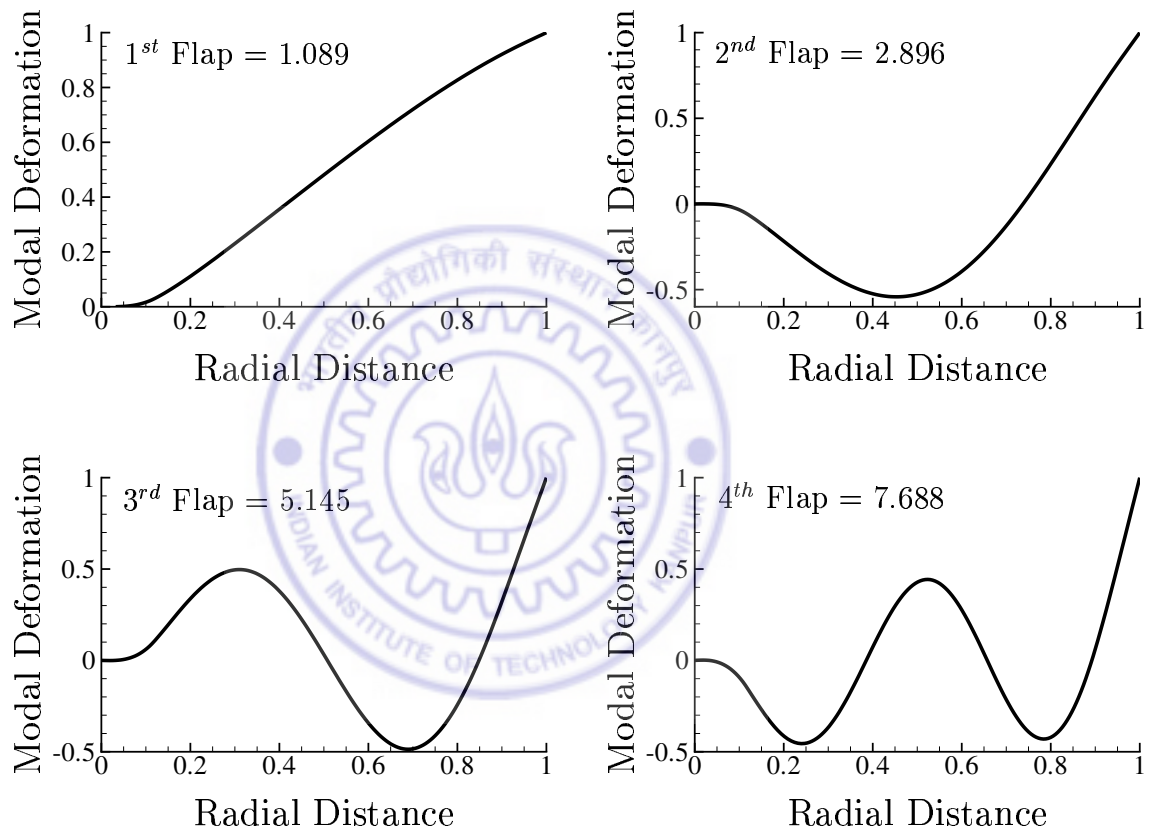
Figure 2.14: Mode shapes of straight blade in flap (out-of-plane bending) mode (nondimensional)
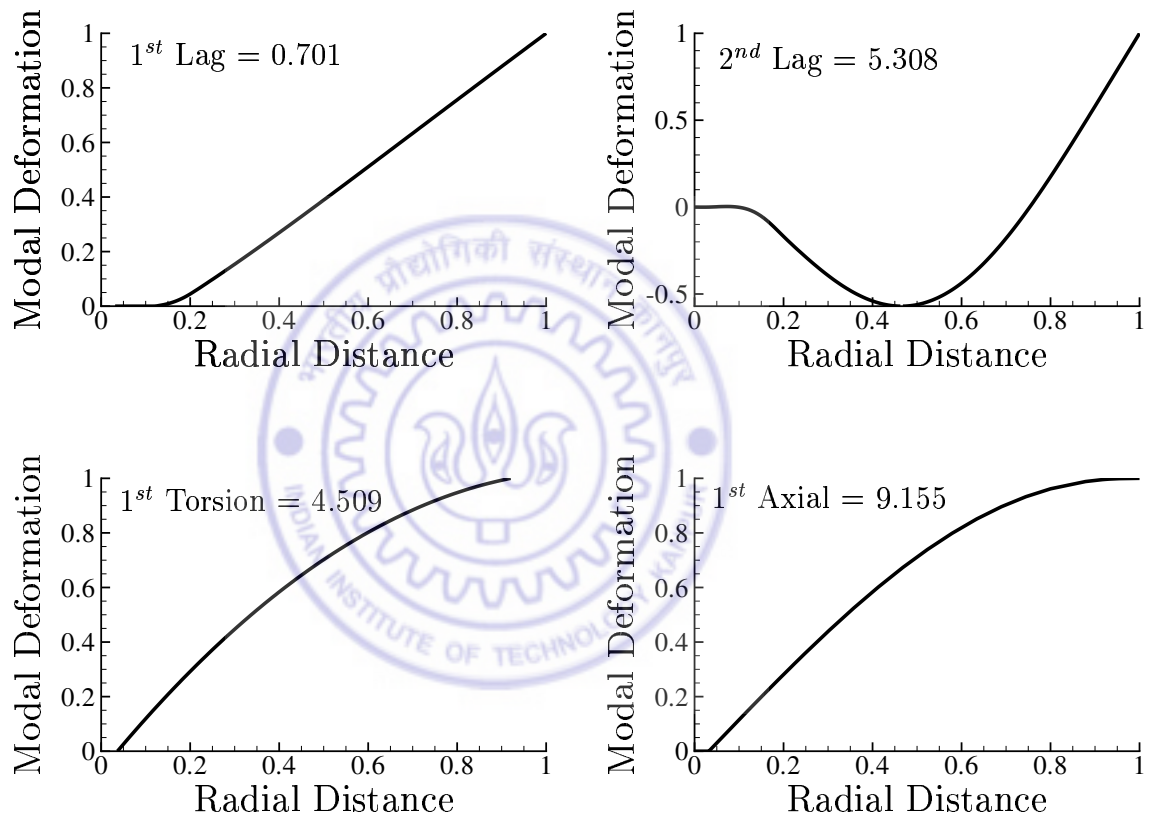
Figure 2.15: Mode shapes of straight blade in lead-lag (in-plane bending), torsional and axial mode (nondimensional)
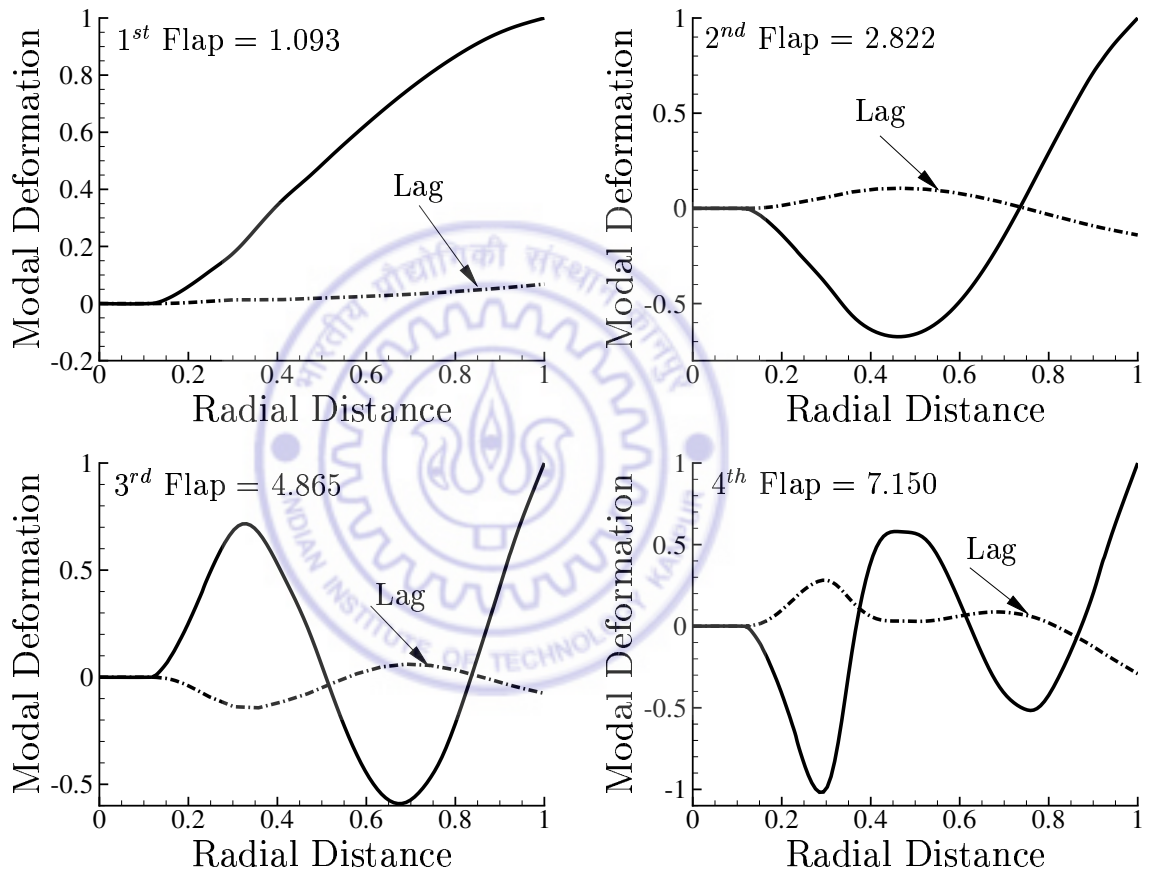
Figure 2.16: Mode shapes of twisted blade in coupled flap (out-of-plane bending) mode (nondimensional)
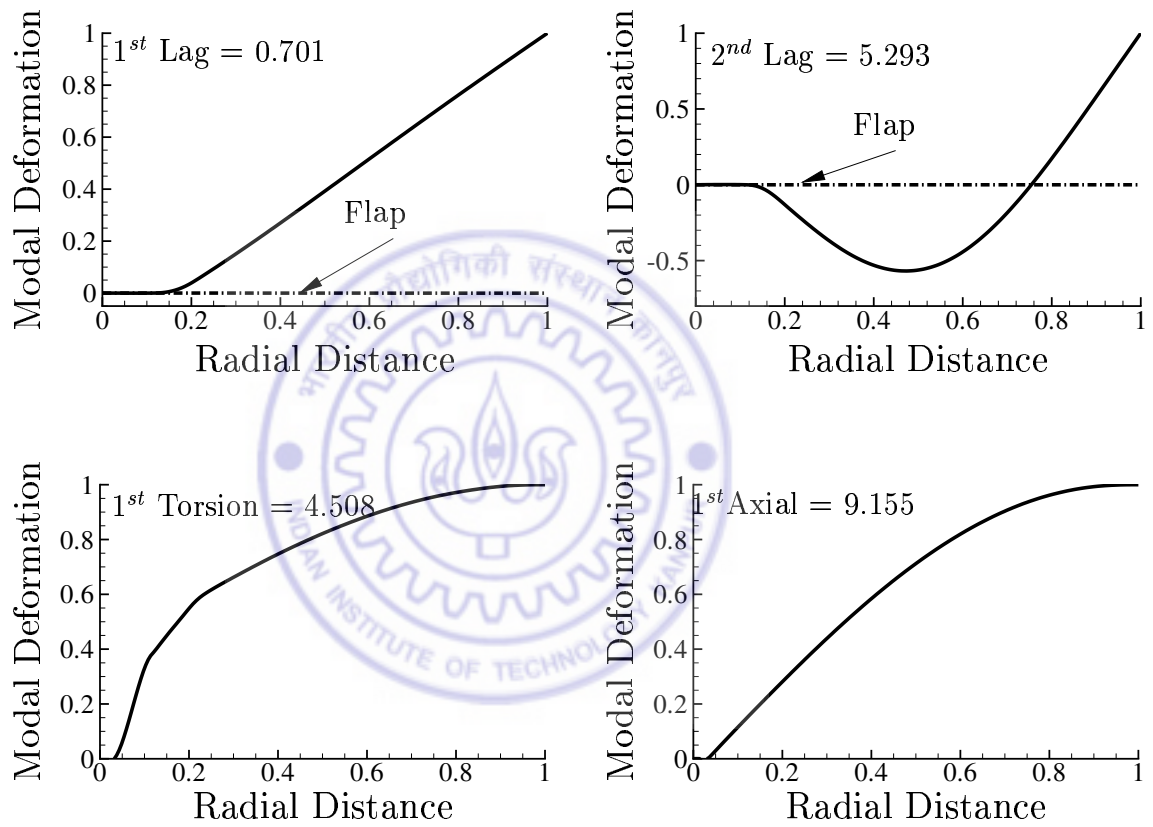
Figure 2.17: Mode shapes of twisted blade in coupled lead-lag (in-plane bending), torsional and axial mode (nondimensional)

Chapter 3

AERODYNAMIC MODELS

Modeling of rotary-wing aerodynamics requires consideration of two important aspects, namely, evaluation of inflow through rotor disc and estimation of sectional aerodynamic loads on the rotor blade. In the following, a description of the inflow models and sectional aerodynamic models is presented.

3.1   Inflow Models

The inflow models represent the rotor wake effects in a simple form. In these models, the wake-induced flow through the rotor disc is defined by a set of inflow variables. There are several inflow models available in the literature. The global inflow models are developed based on the overall rotor aerodynamic thrust, pitch moment, and roll moment. Local inflow models are developed using prescribed wake, free wake or more recently by CFD methods. In this study, the rotor inflow is represented by global models. A description of the global inflow models, starting from steady uniform inflow model to dynamic wake model is presented in the following sections.

3.1.1   Uniform Inflow Model

In this model, the total inflow through the rotor disc is assumed a constant over the rotor disc. The expression for the total inflow is obtained using the principles of

momentum theory and is given as (Refs. [56] and [189]:

$$\lambda_u = \mu \tan \alpha + \lambda_i \qquad (3.1)$$

where

$$\lambda_i = \frac{C_T}{2\sqrt{(\mu^2 + \lambda_u^2)}}$$

where μ is advance ratio and it is given as:

$$\mu = \frac{V \cos \alpha}{\Omega R}$$

C_T is thrust coefficient and λ_i is induced inflow. Flow model for momentum theory analysis of rotor in forward flight is shown in Fig. 3.1.

3.1.2 Drees Model

Drees calculated the rotor induced velocity using vortex theory. Assuming an actuator disc having radially constant but azimuthally varying $(\Gamma = \Gamma_1 - \Gamma_2 \sin \psi)$ bound circulation, he obtained an expression for the rotor inflow (Ref. [56]), which is given as:

$$\lambda(\bar{r}, \psi) = \mu \tan \alpha + \lambda_i(1 + k_x \bar{r} \sin \psi + k_y \bar{r} \cos \psi) \qquad (3.2)$$

where

$$\lambda_i = \frac{C_T}{2\sqrt{(\mu^2 + \lambda_u^2)}}$$

$$k_x = 2\mu$$

$$k_y = \frac{4}{3}[(1 - 1.8\mu^2) \csc \chi - \cot \chi]$$

where χ wake skew angle as shown in Fig. 3.2. χ is defined as $\chi = \tan^{-1}(\mu/\lambda_u)$.

In the uniform inflow model and Drees model, the rotor inflow is related to the mean thrust developed by rotor system. It is well known that rotor inflow affects the rotor thrust and vice versa. Therefore, it is reasonable to assume that whenever

68

there is a time variation in rotor thrust, the inflow also will vary with time. The formulation of a relation between time varying inflow to time varying rotor thrust forms the central idea in the development of perturbation inflow model, dynamic inflow model and dynamic wake model. For the sake of clarity, in the following the development of these models is described.

3.1.3 Perturbation Inflow Model

In perturbation inflow model, the total induced velocity on the rotor disc due to the rotor wake is assumed to consist of two parts:

1. a steady inflow, λ_0, for trim (equilibrium or mean) loadings and

2. a perturbation inflow, $\delta\lambda(t)$, for transient loadings.

Therefore, the total induced velocity normal to the rotor disc is expressed as

$$\lambda = \lambda_0 + \delta\lambda(t) \tag{3.3}$$

Assuming that the perturbation inflow, $\delta\lambda$, varies azimuthally as well as linearly along the radius, the total inflow can be written as

$$\lambda = \lambda_0 + \lambda_1 + \lambda_{1c} \ \frac{r}{R}\cos\psi + \lambda_{1s} \ \frac{r}{R}\sin\psi \tag{3.4}$$

where the inflow variables λ_1, λ_{1c} and λ_{1s} are functions of time. These inflow variables are related to the perturbational thrust, roll and pitch moment coefficients through the following relation.

$$[L]^{-1}\left\{\begin{array}{c}\lambda_1 \\ \lambda_{1s} \\ \lambda_{1c}\end{array}\right\} = \left\{\begin{array}{c}C_T \\ C_{M_x} \\ -C_{M_y}\end{array}\right\}_{PA} \tag{3.5}$$

69

where $[L]$ is called as coupling or gain matrix and subscript PA represents perturbtaional aerodynamics. The elements of $[L]$ can be obtained either theoretically by using momentum theory or experimentally. For axial flow (corresponding to hovering condition), the elements of $[L]$ can be obtained by applying momentum theory. The differential thrust on an elemental area $dA(= rdrd\psi)$ of the disc is related to the inflow by the equation

$$dT = \dot{m}2\lambda\Omega R \tag{3.6}$$

Following Johnson [72], the mass flow rate in Eq. 3.6 can be written as

$$\dot{m} = \rho\lambda_0\Omega R dA \tag{3.7}$$

In this case, the mass flow rate is defined in terms of the steady or mean value of the inflow λ_0.

The aerodynamic thrust can be obtained by integrating elemental thrust over the complete rotor disc. The aerodynamic roll and pitch moments on the rotor disc, acting at the hub, can be obtained by taking moments of the elemental thrust about the hub center and integrating over the complete rotor disc. The trust, pitch and roll moments are given, respectively as:

$$T = \int_0^R \int_0^{2\pi} dT \tag{3.8}$$

$$M_y = \int_0^R \int_0^{2\pi} -r\cos\psi dT \tag{3.9}$$

$$M_x = \int_0^R \int_0^{2\pi} r\sin\psi dT \tag{3.10}$$

Substituting Eqs. 3.4, 3.6 and 3.7 in Eqs. 3.8, 3.9 and 3.10 and integrating the thrust, pitch and roll moments are obtained. Neglecting higher order terms perturbational

quantities in thrust, roll moment and pitch moment can be written as:

$$(T)_{PA} = 2\pi\rho R^2 \lambda_0 \lambda_1 (\Omega R)^2 \tag{3.11}$$

$$-(M_y)_{PA} = \frac{\pi}{2}\rho R^3 \lambda_0 \lambda_{1c} (\Omega R)^2 \tag{3.12}$$

$$(M_x)_{PA} = \frac{\pi}{2}\rho R^3 \lambda_0 \lambda_{1s} (\Omega R)^2 \tag{3.13}$$

Nondimensionalizing Eqs. 3.11-3.13, the relation between perturbational rotor loads to perturbational rotor inflow can be expressed in matrix form as:

$$
\begin{bmatrix}
2\lambda_0 & 0 & 0 \\
0 & \frac{\lambda_0}{2} & 0 \\
0 & 0 & \frac{\lambda_0}{2}
\end{bmatrix}
\begin{Bmatrix}
\lambda_1 \\
\lambda_{1s} \\
\lambda_{1c}
\end{Bmatrix}
=
\begin{Bmatrix}
C_T \\
C_{M_x} \\
-C_{M_y}
\end{Bmatrix}_{PA}
\tag{3.14}
$$

On the other hand, if the mass flow rate $\dot{m}$ is defined with respect to the total induced velocity λ as

$$\dot{m} = \rho\lambda\Omega R \, dA \tag{3.15}$$

Then the perturbational inflow equations become

$$
\begin{bmatrix}
4\lambda_0 & 0 & 0 \\
0 & \lambda_0 & 0 \\
0 & 0 & \lambda_0
\end{bmatrix}
\begin{Bmatrix}
\lambda_1 \\
\lambda_{1s} \\
\lambda_{1c}
\end{Bmatrix}
=
\begin{Bmatrix}
C_T \\
C_{M_x} \\
-C_{M_y}
\end{Bmatrix}_{PA}
\tag{3.16}
$$

Comparing Eqs. 3.14 and 3.16, it is evident that depending on the definition of mass flow, the coefficients of the elements of $[L]^{-1}$ matrix differ by a factor of 2. These perturbational inflow models have been used in stability analysis of rotor systems by various researchers (Refs. [73], [74], [137], [138] and [140]).

Extending the perturbation inflow model to forward flight, the relation between the time varying inflow variables to time varying rotor loads is derived in Ref. [56],

71

which is given as:

$$\begin{Bmatrix} \lambda_1 \\ \lambda_{1s} \\ \lambda_{1c} \end{Bmatrix} = [L] \begin{Bmatrix} C_T \\ C_{M_x} \\ -C_{M_y} \end{Bmatrix}_{PA} \tag{3.17}$$

where gain matrix $[L]$ is given as

$$[L] = \begin{bmatrix} \dfrac{1}{2(\lambda_0 + \sqrt{\mu^2 + \lambda_0^2})} & 0 & 0 \\ 0 & \dfrac{2}{\sqrt{\mu^2 + \lambda_0^2}} & 0 \\ 0 & 0 & \dfrac{2}{\sqrt{\mu^2 + \lambda_0^2}} \end{bmatrix} \tag{3.18}$$

It may be noted that the gain matrix $[L]$ is diagonal in all the perturbation inflow models. A more general relationship will render the $[L]$ matrix fully populated.

3.1.4 Dynamic Inflow Model

The perturbation inflow model does not account for the time lag between the aerodynamic load and the time variation in inflow. The dynamic inflow models represent an extension of the perturbation inflow model by taking into account the time lag between aerodynamic loading and the inflow response.

Using potential flow theory Pitt and Peters developed [18] dynamic inflow model with three states which takes into account the time lag between inflow and rotor loads, and effect of forward flight. Pitt-Peters dynamic inflow model has been shown to provide good correlation with experimental data (Ref. [139]). The three state, dynamic inflow model in matrix form (as given in Ref. [83]) can be written as :

$$[M] \begin{Bmatrix} \dot{\lambda}_1 \\ \dot{\lambda}_{1s} \\ \dot{\lambda}_{1c} \end{Bmatrix} + [V][L]^{-1} \begin{Bmatrix} \lambda_1 \\ \lambda_{1s} \\ \lambda_{1c} \end{Bmatrix} = \begin{Bmatrix} C_T \\ C_{M_x} \\ C_{M_y} \end{Bmatrix}_{PA} \tag{3.19}$$

L-matrix is given as:

$$[L] = \begin{bmatrix} \frac{1}{2} & 0 & \frac{15\pi}{64}\tan\frac{\chi}{2} \\ 0 & \frac{-4}{1+\cos\chi} & 0 \\ \frac{15\pi}{64}\tan\frac{\chi}{2} & 0 & \frac{-4\cos\chi}{1+\cos\chi} \end{bmatrix} \tag{3.20}$$

Velocity matrix is given as:

$$[V] = \begin{bmatrix} V_T & 0 & 0 \\ 0 & V_R & 0 \\ 0 & 0 & V_R \end{bmatrix} \tag{3.21}$$

$$V_T = \sqrt{\mu^2 + \lambda^2} \tag{3.22}$$

$$V_R = \frac{\mu^2 + \lambda(\lambda + \lambda_i)}{\sqrt{\mu^2 + \lambda^2}} \tag{3.23}$$

Apparent mass matrix is given as:

$$[M] = \begin{bmatrix} \frac{8}{3\,\pi} & 0 & 0 \\ 0 & \frac{-16}{45\pi} & 0 \\ 0 & 0 & \frac{-16}{45\pi} \end{bmatrix} \tag{3.24}$$

It is observed that in the literature on dynamic inflow models, certain differences exist in the expressions for the elements V_{11} and M_{11}. In Refs. [139] and [84] the elements V_{11} and M_{11} are given as

$$V_{11} = V_R$$

$$M_{11} = \frac{128}{75\pi}$$

It is shown that the value of M_{11} as $\frac{8}{3\pi}$ in the generalised wake model developed by Peters and He (Ref. [19]). It may be noted that Carpenter and Fridovich [68] have

73

originally proposed the value for $M_{11} = \frac{8}{3\pi}$.

3.1.5 Generalised Dynamic Wake Model

Although the Pitt-Peters model has significantly improved the inflow modeling, it still has some limitations because the time varying inflow is modeled by three states. This limitation is overcome in the generalised dynamic wake theory developed by Peters and He (Refs. [19] and [77]) based on acceleration potential for an actuator disc. This model allows for arbitrary number of inflow states. A brief description of this model is provided here for continuity. Detailed derivation can be found in Ref. [77]. The inflow is represented as an infinite series in radial and harmonic functions which is expressed as:

$$\lambda(\bar{r}, \psi, t) = \sum_{p=0}^{\infty} \sum_{j=p+1, p+3, \cdots}^{\infty} \phi_j^p(\bar{r}) \left[\alpha_j^p(t) \cos(p\psi) + \beta_j^p(t) \sin(p\psi) \right] \tag{3.25}$$

where the radial function $\phi_j^p(\bar{r}) = \bar{P}_j^p(\bar{\nu})/\bar{\nu}$. $\bar{P}_j^p(\bar{\nu})/\bar{\nu}$ is Legendre polynomials and the nondimensional radial parameter $\bar{\nu} = \sqrt{1 - \bar{r}^2}$. The radial function $\phi_j^p(\bar{r})$ is given as:

$$\phi_j^p(\bar{r}) = \sqrt{(2j+1)H_j^p} \sum_{q=p, p+2, \cdots}^{j-1} \bar{r}^q \frac{(-1)^{(q-p)/2}(j+q)!!}{(q-p)!!(q+p)!!(j-q-1)!!} \tag{3.26}$$

The symbol !! is denoted as double factorial.

$$H_j^p = \frac{(j+p-1)!!(j-p-1)!!}{(j+p)!!(j-p)!!} \tag{3.27}$$

In Eq. 3.25, the parameters $\alpha_j^p(t)$ and $\beta_j^p(t)$ associated with harmonics represent the inflow states.

The inflow states are evaluated by solving a set of first order differential equations.

$$[M] \left\{ \begin{array}{c} \vdots \\ \{\dot{\alpha}_j^p\} \\ \vdots \end{array} \right\} + [V_c][\tilde{L}^c]^{-1} \left\{ \begin{array}{c} \vdots \\ \{\alpha_j^p\} \\ \vdots \end{array} \right\} = \frac{1}{2} \left\{ \begin{array}{c} \vdots \\ \{\tau_n^{mc}\} \\ \vdots \end{array} \right\} \tag{3.28}$$

$$[M] \left\{ \begin{array}{c} \vdots \\ \{\dot{\beta}_j^p\} \\ \vdots \end{array} \right\} + [V_s][\tilde{L}^s]^{-1} \left\{ \begin{array}{c} \vdots \\ \{\beta_j^p\} \\ \vdots \end{array} \right\} = \frac{1}{2} \left\{ \begin{array}{c} \vdots \\ \{\tau_n^{ms}\} \\ \vdots \end{array} \right\} \tag{3.29}$$

In the above Eqs. 3.28 and 3.29, the subscripts j, n correspond to radial functions and superscripts p, m represent the harmonics. The linear operator $[M]$ is associated with acceleration part of the induced flow, hence it can be called as the apparent mass matrix, and it is a diagonal matrix. $[\tilde{L}^c]$ and $[\tilde{L}^s]$ denote the cosine and sine influence coefficient matrices respectively and they depend on the wake skew angle χ. $[V_c]$ and $[V_s]$ represent velocity matrices. τ_n^{mc} and τ_n^{ms} represent the cosine and sine components of the aerodynamic loads acting on the rotor system. Closed-form expressions for various quantities are given below.

The apparent mass matrix is given as:

$$[M] = \begin{bmatrix} \ddots & & \\ & K_n^m & \\ & & \ddots \end{bmatrix} \tag{3.30}$$

where

$$K_n^m = \frac{2}{\pi} H_n^m \begin{cases} m = 0, 1, 2, 3, ...\text{in Eq. 3.28} \\ m = 1, 2, 3, ...\text{in Eq. 3.29} \end{cases} \tag{3.31}$$

The influence coefficient matrices are given by

$$[\tilde{L}^c] = [\tilde{L}_{jn}^{pm}]^c \quad [\tilde{L}^s] = [\tilde{L}_{jn}^{pm}]^s \tag{3.32}$$

$$[\tilde{L}_{jn}^{0m}]^c = X^m[\Gamma_{jn}^{0m}] \tag{3.33}$$

$$[\tilde{L}_{jn}^{pm}]^c = [X^{|m-p|} + (-1)^l X^{|m+p|}][\Gamma_{jn}^{pm}] \tag{3.34}$$

$$[\tilde{L}_{jn}^{pm}]^s = [X^{|m-p|} - (-1)^l X^{|m+p|}][\Gamma_{jn}^{pm}] \tag{3.35}$$

where $l = \min(p, m)$, $X = \tan(\frac{\chi}{2})$ and χ is the wake skew angle. The wake skew angle is defined as $\tan\chi = \frac{\mu}{\lambda}$. The term Γ_{jn}^{pm} is defined as

$$[\Gamma_{jn}^{pm}] = \frac{(-1)^{\frac{n+j-2p}{2}} 2\sqrt{(2n+1)(2j+1)}}{\sqrt{H_n^m H_j^p (j+n)(j+n+2)[(j-n)^2 - 1]}} \quad \text{for even } (p-m) \tag{3.36}$$

$$[\Gamma_{jn}^{pm}] = \frac{\pi \ \text{sgn}(p-m)}{2\sqrt{H_n^m H_j^p}\sqrt{(2n+1)(2j+1)}} \quad \text{for odd } (p-m) \text{ and } j = n \pm 1 \tag{3.37}$$

$$[\Gamma_{jn}^{pm}] = 0 \quad \text{for odd } (p+m) \text{ and } j \neq n \pm 1 \tag{3.38}$$

and $H_n^m = \frac{(n+m-1)!!(n-m-1)!!}{(n+m)!!(n-m)!!}$ as defined earlier in Eq. 3.27.

Velocity matrix is given as follows:

$$[V_c] = \begin{bmatrix} V_T & & & \\ & V_R & & \\ & & \ddots & \\ & & & V_R \end{bmatrix} \tag{3.39}$$

$$[V_s] = \begin{bmatrix} V_R & & & \\ & V_R & & \\ & & \ddots & \\ & & & V_R \end{bmatrix} \tag{3.40}$$

$$V_T = \sqrt{\mu^2 + \lambda^2} \qquad (3.41)$$

$$V_R = \frac{\mu^2 + \lambda(\lambda + \lambda_i)}{\sqrt{\mu^2 + \lambda^2}} \qquad (3.42)$$

where λ represents the total inflow (freestream plus thrust-induced inflow) and λ_i represents thrust induced inflow.

The cosine and sine components of the aerodynamic loads acting on the rotor system are defined in terms of blade lift weighted with radial polynomial functions $\phi_n^m(\bar{r})$. The expressions for the rotor loads are defined as:

$$\tau_n^{0c} = \frac{1}{2\pi} \sum_{k=1}^{N_b} [\int_0^1 \frac{L_k}{\rho \Omega^2 R^3} \phi_n^0(\bar{r}) d(\bar{r})] \qquad (3.43)$$

$$\tau_n^{mc} = \frac{1}{\pi} \sum_{k=1}^{N_b} [\int_0^1 \frac{L_k}{\rho \Omega^2 R^3} \phi_n^m(\bar{r}) d\bar{r}] \cos(m\psi_k) \qquad (3.44)$$

$$\tau_n^{ms} = \frac{1}{\pi} \sum_{k=1}^{N_b} [\int_0^1 \frac{L_k}{\rho \Omega^2 R^3} \phi_n^m(\bar{r}) d\bar{r}] \sin(m\psi_k) \qquad (3.45)$$

where the summation is over all the blades (N_b) in the rotor system. ψ_k represents the azimuthal location of the kth blade and is given by $\psi + \frac{2\pi(k-1)}{N_b}$. L_k represents the lift per unit span on the kth blade. The sectional blade lift can be obtained from any aerodynamic theory, say for example quasi-steady Greenberg's theory, dynamic stall theory or by CFD methods.

3.2 Sectional Aerodynamic Loads

The sectional aerodynamic loads can be evaluated by either (i) quasi-steady approximation of Greenberg's theory or (ii) dynamic stall model applicable for both attached and separated flow.

3.2.1 Greenbergs Theory

The unsteady aerodynamic lift and moment on an oscillating airfoil in pulsating oncoming stream (Fig. 3.4) is derived by Greenberg [12]. The circulatory and non-circulatory lift expressions as given by Greenberg are

$$
\begin{aligned}
L_C &= 2\pi\rho V b[V_0\theta_0 + \sigma_v V_0\theta_0 C(k_v)e^{i\omega_v t} + [b(\frac{1}{2}-a)\dot{\tilde{\theta}} + V_0\tilde{\theta}]C(k_{\tilde{\theta}}) \quad (3.46)\\
&\quad +\dot{h}C(k_h) + \sigma_v V_0\tilde{\theta}C(k_{v+\tilde{\theta}})e^{i\omega_v t}]\\
L_{NC} &= \pi\rho b^2[\ddot{h} + V\dot{\tilde{\theta}} + \dot{V}(\theta_0 + \tilde{\theta}) - ba\ddot{\tilde{\theta}}] \quad (3.47)
\end{aligned}
$$

where

b	is half-chord of the airfoil
ba	is the position of the elastic axis measured from the centre of the airfoil
$C(k)$	is Theodorsen's lift deficiency function
h	is the vertical (heaving motion) dispalcement of the airfoil
θ_0	is the constant part of angle of attack
$\tilde{\theta}$	is the time varying part of angle of attack
V_0	is the constant part of oncoming velocity, $V = V_0(1 + \sigma_v e^{i\omega_v t})$

$\sigma_v V_0 e^{i\omega_v t}$ is the time varying part of oncoming velocity, $V = V_0(1 + \sigma_v e^{i\omega_v t})$

The total moment about the axis of rotation due to both circulatory and noncirculatory parts is

$$
\begin{aligned}
M &= \pi\rho b^2[ba\ddot{h} + \dot{V}ba(\theta_0 + \tilde{\theta}) - Vb(\frac{1}{2}-a)\dot{\tilde{\theta}} - b^2(\frac{1}{8}+a^2)\ddot{\tilde{\theta}}] \quad (3.48)\\
&\quad +2\pi\rho V b^2(\frac{1}{2}+a)[V_0\theta_0 + \sigma_v V_0\theta_0 C(k_v)e^{i\omega_v t} + [(\frac{1}{2}-a)\dot{\tilde{\theta}} + V_0\tilde{\theta}]C(k_{\tilde{\theta}})\\
&\quad +\dot{h}C(k_h) + \sigma_v V_0\tilde{\theta}C(k_{v+\tilde{\theta}})e^{i\omega_v t}]
\end{aligned}
$$

For low frequency oscillations of the airfoil, the reduced frequency k is low and one can introduce assumption that the lift deficiency function $C(k)$ is equal to unity. Invoking this assumption, the circulatory and noncirculatory lift expressions can be

rewritten as:

$$L_C = 2\pi\rho V b[V_0\theta_0 + \sigma_v V_0\theta_0 e^{i\omega_v t} + [b(\frac{1}{2} - a)\dot{\tilde{\theta}} + V_0\tilde{\theta}] \quad (3.49)$$

$$+\dot{h} + \sigma_v V_0\tilde{\theta}e^{i\omega_v t}]$$

$$L_{NC} = \pi\rho b^2[\ddot{h} + V\dot{\tilde{\theta}} + \dot{V}(\theta_0 + \tilde{\theta}) - ba\ddot{\tilde{\theta}}] \quad (3.50)$$

The moment expression becomes

$$M = \pi\rho b^2[ba\ddot{h} + \dot{V}ba(\theta_0 + \tilde{\theta}) - Vb(\frac{1}{2} - a)\dot{\tilde{\theta}} - b^2(\frac{1}{8} + a^2)\ddot{\tilde{\theta}}] \quad (3.51)$$

$$+2\pi\rho V b^2(\frac{1}{2} + a)[V_0\theta_0 + \sigma_v V_0\theta_0 e^{i\omega_v t} + [b(\frac{1}{2} - a)\dot{\tilde{\theta}} + V_0\tilde{\theta}]$$

$$+\dot{h} + \sigma_v V_0\tilde{\theta}e^{i\omega_v t}]$$

Now, taking the lift and pitching moment at quarter chord i.e., $a = -1/2$ and by rearranging the terms one can get the following expressions.

$$L_C = 2\pi\rho V b[V_0(1 + \sigma_v e^{i\omega_v t})(\theta_0 + \tilde{\theta}) + \dot{h} + b\dot{\tilde{\theta}}] \quad (3.52)$$

$$L_{NC} = \pi\rho b^2[\ddot{h} + V\dot{\tilde{\theta}} + \dot{V}(\theta_0 + \tilde{\theta}) + \frac{b}{2}\ddot{\tilde{\theta}}] \quad (3.53)$$

The pitching moment due to noncirculatory term is (circulatory term goes to zero)

$$M = \pi\rho b^2[-\frac{b}{2}\ddot{h} - \dot{V}\frac{b}{2}(\theta_0 + \tilde{\theta}) - V\frac{b}{2}\dot{\tilde{\theta}} - V\frac{b}{2}\dot{\tilde{\theta}} - b^2(\frac{3}{8})\ddot{\tilde{\theta}}] \quad (3.54)$$

Above equations can be rewritten in a modified form by replacing the quantities $(\theta_0 + \tilde{\theta})$ and $V_0(1 + \sigma_v e^{i\omega_v t})$ by θ and V, respectively:

$$L_C = 2\pi\rho V b[V\theta + \dot{h} + b\dot{\theta}] \quad (3.55)$$

$$L_{NC} = \pi\rho b^2[\ddot{h} + V\dot{\theta} + \dot{V}\theta + \frac{b}{2}\ddot{\theta}] \quad (3.56)$$

$$M = \pi\rho b^2[-\frac{b}{2}(\ddot{h} + (\dot{V}\theta + V\dot{\theta}) - V\frac{b}{2}\dot{\theta} - b^2(\frac{3}{8})\ddot{\theta}] \quad (3.57)$$

79

By replacing the $V(\frac{\dot{h}}{V} + \theta)$ by W_0 and $b\dot{\theta}$ by W_1 (Refs. [85], [86] and [116]) the above equation is further modified as follows:

$$
\begin{aligned}
L_C &= 2\pi\rho V b[W_0 + W_1] \\
&= \frac{1}{2}\rho V \tilde{S}[2\pi W_0 + 2\pi W_1]
\end{aligned}
$$
(3.58)

$$
\begin{aligned}
L_{NC} &= \pi\rho b^2[\dot{W}_0 + \frac{1}{2}\dot{W}_1] \\
&= \frac{1}{2}\rho \tilde{S} b[\pi\dot{W}_0 + \frac{\pi}{2}\dot{W}_1]
\end{aligned}
$$
(3.59)

where $\tilde{S}$ ($\tilde{S} = 2b.1$) is area of the airfoil having unit width. The final form of pitching moment is

$$
\begin{aligned}
M &= \pi\rho b^2[-\frac{b}{2}(\dot{W}_0) - V\frac{1}{2}W_1 - b(\frac{3}{8})\dot{W}_1] \\
&= \frac{1}{2}\rho \tilde{S} 2b[-\frac{\pi}{4}b(\dot{W}_0) - \frac{\pi}{4}VW_1 - (\frac{3\pi}{16})b\dot{W}_1]
\end{aligned}
$$
(3.60)

The unsteady drag acting along the resultant velocity is given as:

$$
D = \frac{1}{2}\rho \tilde{S} V^2 C_{D_0}
$$
(3.61)

3.2.2 Dynamic Stall Model

It is well known that during forward flight some sections of the rotor blade undergoes stall as the blade goes around the azimuth. Hence, dynamic stall effects must be included in the aeroelastic analysis of rotor blades. In this thesis, a *modified* stall model based on the ONERA dynamic stall model has been developed. In the following, a description of the ONERA stall model and the proposed modification are presented.

3.2.3 ONERA (EDLin) Model

ONERA (EDLin) model describes the unsteady airfoil behavior in both attached flow and during dynamic stall using a set of nonlinear differential equations. An investigation on several airfoil profiles has led Petot *et al.* (Ref. [23]) to the formulation of the following mathematical model. The aerodynamic loads on a pitching airfoil (namely lift, moment and drag) can be expressed in a generic form as:

$$Q = Q_1 + Q_2 \tag{3.62}$$

$$\text{For Lift} \quad \dot{Q}_1 + \lambda Q_1 = \lambda Q_L + (\lambda s + \sigma)\dot{\theta} + s\ddot{\theta} \tag{3.63}$$

and

$$\text{For Moment or Drag} \quad Q_1 = Q_L + (s + \sigma)\dot{\theta} + s\ddot{\theta} \tag{3.64}$$

$$\ddot{Q}_2 + a\dot{Q}_2 + rQ_2 = -[r\Delta Q + E\dot{\theta}] \tag{3.65}$$

(with the condition $E = 0$ in unstalled state).

The load Q is expressed as a sum of two terms:

- Q_1 represents the load in the attached flow region. It is given interms of a first-order differential equation in the case of lift. It is an algebraic expression for the cases of moment or drag. It depends on Q_L which is the linear static aerodynamic coefficient and the pitching motion θ.

- Q_2 represents the load in the stalled region. The property $E = 0$ in unstalled state is necessary to guarantee the absence of response in Q_2. Variable $\Delta Q = Q_L - Q_s$ determines the entrance and exit from the stalled region. It is the difference between the linear static aerodynamic coefficient (Q_L) extrapolated to the stalled region to measured static coefficient (Q_s).

These equations are written in reduced time, $\tau = Vt/b$. The parameters λ, a, r, E, σ, and s have to be determined by parameter identification approach using experimental measurements on oscillating airfoils. Initial dynamic stall model developed is applicable only to pure pitching motion. Subsequently this model was extended to include heaving and oncoming velocity variations [116]. The extended stall model provides time variation of lift, drag and moment on an oscillating airfoil. A detailed discussion on this model is provided below.

The unsteady lift on the airfoil is given as:

$$L = \frac{1}{2}\rho\tilde{S}[sb\dot{W}_0 + \tilde{k}b\dot{W}_1 + V\Gamma_1 + V\Gamma_2] \qquad (3.66)$$

$$\dot{\Gamma}_1 + \lambda(\frac{V}{b})\Gamma_1 = \lambda(\frac{V}{b})\frac{\partial Cz_L}{\partial\theta}W_0 + \lambda\sigma(\frac{V}{b})W_1$$
$$+(\tilde{\alpha}\frac{\partial Cz_L}{\partial\theta} + d)\dot{W}_0 + \tilde{\alpha}\sigma\dot{W}_1 \qquad (3.67)$$

$$\ddot{\Gamma}_2 + a_l(\frac{V}{b})\dot{\Gamma}_2 + r_l(\frac{V}{b})^2\Gamma_2 = -[r_l(\frac{V}{b})^2V\Delta Cz|_{W_0/V} + E_l(\frac{V}{b})\dot{W}_0] \qquad (3.68)$$

where Γ_1 and Γ_2 are circulation per unit length corresponding to unstalled and stalled regions, respectively. $\tilde{S}$ and b are area and half-chord of the airfoil. W_0 and W_1 are defined as $W_0 = V(\frac{\dot{h}}{V} + \theta)$ and $W_1 = b\dot{\theta}$, where V is oncoming velocity, $\dot{h}$ is a heaving velocity at elastic axis and θ is pitch angle in degrees.

The various coefficients of the lift model are given by:

$$\lambda = 0.17 - 0.13M$$

$$\tilde{\alpha} = 0.53 + 0.25(\sqrt{1 - M^2} - 1)$$

$$s = (\pi + 5\pi[(1 - M^2)^{0.285} - 1])\frac{\pi}{180}$$

$$\tilde{k} = (\frac{\pi}{2} + 1.96\pi(\sqrt{(1 - M^2)} - 1))\frac{\pi}{180}$$

$$\sigma = (\frac{2\pi}{\sqrt{(1 - M^2)}})\frac{\pi}{180}$$

$$d = d_1|\Delta C_z|$$

Parameters of the dynamic stall equation (Eq. 3.68) are defined as $a_l = a_0 + a_1(\Delta C_z)^2$; $\sqrt{r_l} = r_0 + r_1(\Delta C_z)^2$ and $E_l = E_1(\Delta C_z)^2$ where ΔC_z is the difference between the linear static lift coefficient extrapolated to the stalled region to measured static coefficient (Fig. 3.3(a)). The parameters d_1, a_0, a_1, r_0, r_1, and E_1 of lift have to be determined by parameter identification approach using experimental measurements on oscillating airfoils.

The unsteady moment on the airfoil is given as:

$$
\begin{aligned}
M &= \frac{1}{2}\rho\tilde{S}2b[V^2 Cm_L|_{W_0/V} + (\overline{\sigma}_m + d_m)b\dot{W}_0 \\
&\quad + \sigma_m VW_1 + s_m b\dot{W}_1 + V\Gamma_{m2}] \quad\quad (3.69)
\end{aligned}
$$

$$
\ddot{\Gamma}_{m2} + a_m(\frac{V}{b})\dot{\Gamma}_{m2} + r_m(\frac{V}{b})^2\Gamma_{m2} = -[r_m(\frac{V}{b})^2 V\Delta Cm|_{W_0/V} + E_m(\frac{V}{b})\dot{W}_0]
$$

$$(3.70)$$

The various coefficients of the moment model are given by:

$$
\begin{aligned}
s_m &= -3\pi/16(-1.26 - 1.53\arctan[15(M - 0.7)])\frac{\pi}{180} \\
s_m + \sigma_m &= -\pi/2[1 + 1.4M^2]\frac{\pi}{180} + \sigma_{1m}|\Delta C_z| \\
d_m &= \sigma_{1m}|\Delta C_z| \\
\sigma_{1m} \;\; &\text{between} \;\; 0 \text{ and } 0.15 \\
\overline{\sigma}_m &= -\pi/4[1 + 1.4M^2]\frac{\pi}{180}
\end{aligned}
$$

where ΔC_m is the difference between the linear static moment coefficient extrapolated to the stalled region to measured static coefficient (Fig. 3.3(b)).

Parameters of the dynamic stall equation (Eq. 3.70) are defined as $a_m = a_{m0} + a_{m1}(\Delta C_z)^2$; $\sqrt{r_m} = r_{m0} + r_{m1}(\Delta C_z)^2$ and $E = E_{m1}(\Delta C_z)^2$. The parameters d_{m1}, a_{m0}, a_{m1}, r_{m0}, r_{m1} and E_{m1} of moment have to be determined by parameter identification approach using experimental measurements on oscillating airfoils.

83

The unsteady drag on the airfoil is given as:

$$D = \frac{1}{2}\rho\tilde{S}[V^2 Cd_L|_{W_0/V} + \sigma_d b\dot{W}_0 + V\Gamma_{d2}] \quad (3.71)$$

$$\ddot{\Gamma}_{d2} + a_d(\frac{V}{b})\dot{\Gamma}_{d2} + r_d(\frac{V}{b})^2\Gamma_{d2} = -[r_d(\frac{V}{b})^2 V\Delta Cd|_{W_0/V} + E_d(\frac{V}{b})\dot{W}_0] \quad (3.72)$$

where ΔC_d is the difference between the linear static drag coefficient extrapolated to the stalled region to measured static coefficient (Fig. 3.3(c)). The various coefficients of the drag model are given by:

$$\sigma_d = \sigma_{0d}\theta + \sigma_{1d}|\Delta C_z|$$

$$\sigma_{0d} = 0.003$$

$$\sigma_{1d} \quad \text{between} \quad 0 \text{ and } -0.05$$

Parameters of the dynamic stall equation (Eq. 3.72) are defined as $a_d = a_{d0} + a_{d1}(\Delta C_z)^2$; $\sqrt{r_d} = r_{d0} + r_{d1}(\Delta C_z)^2$ and $E = E_{d1}(\Delta C_z)^2$. The parameters d_{d1}, a_{d0}, a_{d1}, r_{d0}, r_{d1} and E_{d1} of drag have to be determined by parameter identification approach using experimental measurements on oscillating airfoils.

3.2.4 Development of *Modified* ONERA Stall Model

For an airfoil oscillating under unstalled conditions, Eq. 3.66 can be simplified by taking $\Gamma_2 = 0$ and $\Delta C_z = 0$ as:

$$L = \frac{1}{2}\rho\tilde{S}[sb\dot{W}_0 + \tilde{k}b\dot{W}_1] + \frac{1}{2}\rho\tilde{S}[V\Gamma_1] \quad (3.73)$$

This expression for lift can be split into two parts as:

$$L = L_{NC} + L_C \quad (3.74)$$

$$L_{NC} = \frac{1}{2}\rho\tilde{S}[sb\dot{W}_0 + \tilde{k}b\dot{W}_1] \quad (3.75)$$

$$L_C = \frac{1}{2}\rho\tilde{S}[V\Gamma_1] \quad (3.76)$$

Taking Laplace transform of Eq. 3.67 and substituting for Γ_1 in Eq. 3.76, the expression L_C can be written as (Note: $d = 0$ since $\Delta C_z = 0$):

$$L_C = \frac{1}{2}\rho\tilde{S}V\left(\frac{[\tilde{\alpha}S\frac{b}{V} + \lambda]}{[S\frac{b}{V} + \lambda]}[\frac{\partial C_{z_L}}{\partial \theta}W_0 + \sigma W_1]\right) \tag{3.77}$$

Assuming harmonic motion for the airfoil (*i.e.*, setting Laplace variable $S = i\omega$) and taking lift curve slope $\frac{\partial C_{z_L}}{\partial \theta} = 2\pi$ and substituting for W_0 and W_1, the expressions for L_{NC} and L_C for low Mach number can be written as:

$$L_{NC} = \frac{1}{2}\rho\tilde{S}\pi[(b(\ddot{h} + V\dot{\theta}) + \frac{1}{2}b^2\ddot{\theta})] \tag{3.78}$$

$$L_C = \frac{1}{2}\rho\tilde{S}V2\pi\left(\frac{[0.53\frac{i\omega b}{V} + 0.17]}{[\frac{i\omega b}{V} + 0.17]}[\dot{h} + V\theta + b\dot{\theta}]\right) \tag{3.79}$$

The expressions L_{NC} and L_C are respectively identical to the noncirculatory and circulatory parts of the unsteady lift obtained by Theodorsen [11], except for the lift deficiency function $C(k)$. In Eq. 3.79, the underlined term represents a first order rational approximation to $C(k)$, which approximately satisfies the conditions at $k = 0$, $C(k) = 1$ and $k = \infty$, $C(k) \cong 0.5$. Higher order rational functions have been shown to provide excellent correlation to lift deficiency function $C(k)$. A second order approximation [88] to Theodorsen lift deficiency function is given as:

$$C(k) \cong \frac{A_1(\frac{i\omega b}{V})^2 + A_2(\frac{i\omega b}{V}) + A_3}{(\frac{i\omega b}{V})^2 + B_2(\frac{i\omega b}{V}) + B_3} \tag{3.80}$$

where $A_1 = 0.50$, $A_2 = 0.393$, $A_3 = 0.0439425$, $B_2 = 0.5515$ and $B_3 = 0.0439075$. A comparison of first order approximation and second order approximation [88] with exact Theodorsen lift deficiency function $(C(k) = F(k) + iG(k))$ is shown in Fig. 3.5. It can be seen that second order rational approximation shows better correlation with exact $C(k)$ than the first order approximation. Replacing the first order approximation by the second order rational approximation in Eq. 3.79 and applying Laplace

inverse transform, the *modified* lift equations are obtained. They are given as:

$$L = \frac{1}{2}\rho\tilde{S}[sb\dot{W}_0 + \tilde{k}b\dot{W}_1 + V\Gamma_1 + V\Gamma_2] \tag{3.81}$$

$$\ddot{\Gamma}_1 + B_2(\frac{V}{b})\dot{\Gamma}_1 + B_3(\frac{V}{b})^2\Gamma_1 = A_3(\frac{V}{b})^2\frac{\partial C_{z_L}}{\partial\theta}W_0 + A_3\sigma(\frac{V}{b})^2W_1 + \tag{3.82}$$

$$A_2(\frac{V}{b})\frac{\partial C_{z_L}}{\partial\theta}\dot{W}_0 + A_2(\frac{V}{b})\sigma\dot{W}_1 + A_1\frac{\partial C_{z_L}}{\partial\theta}\ddot{W}_0 + A_1\sigma\ddot{W}_1$$

$$\ddot{\Gamma}_2 + a_l(\frac{V}{b})\dot{\Gamma}_2 + r_l(\frac{V}{b})^2\Gamma_2 = -[r_l(\frac{V}{b})^2V\Delta C_z|_{W_0/V} + E_l(\frac{V}{b})\dot{W}_0] \tag{3.83}$$

In the *modified* stall model, the aerodynamic state Γ_1 is given by a second order differential equation (Eq. 3.82), whereas original Petot model has a first order differential equation (Eq. 3.67). The set of Eqs. 3.81-3.83 is referred to as '*Modified stall model*' and the set of Eqs. 3.66-3.68 is denoted as Petot stall model. There is no change in the form of moment and drag equations, given by Eqs. 3.69-3.70 and Eqs. 3.71-3.72, respectively.

In the unstalled region, Petot model lift can be shown to reduce to Greenberg's theory. Replacing the first order rational function by exact lift deficiency function $C(k)$ in Eq. 3.79; and assuming $V = V_0 + \tilde{V}e^{i\omega_v t}$, $\theta = \theta_0 + \tilde{\theta}e^{i\omega_\theta t}$, $h = \tilde{h}e^{i\omega_h t}$; and substituting for W_0 and W_1, the noncirculatory and circulatory lift expressions given in Eqs. 3.78-3.79 can be written as:

$$L_{NC} = \frac{1}{2}\rho\tilde{S}[(\pi b(\dot{V}\theta + V\dot{\theta} + \ddot{h}) + \frac{\pi}{2}b^2\ddot{\theta})] \tag{3.84}$$

$$L_C = \frac{1}{2}\rho\tilde{S}V(2\pi)C(k)[V_0\theta_0 + V_0\tilde{\theta}e^{i\omega_\theta t} + \theta_0\tilde{V}e^{i\omega_v t} \tag{3.85}$$

$$+\tilde{V}\tilde{\theta}e^{i(\omega_\theta+\omega_v)t} + \dot{h} + b\dot{\theta}]$$

Replacing $C(k)$ using the frequency of the corresponding terms in Eq. 3.86 and combining with Eq. 3.84, the unsteady lift expression can be rewritten as:

$$
\begin{aligned}
L \;=\; & \frac{1}{2}\rho\tilde{S}[(\pi b(\dot{V}\theta + V\dot{\theta} + \ddot{h}) + \frac{\pi}{2}b^2\ddot{\theta})] \\
& + \frac{1}{2}\rho\tilde{S}V(2\pi)[V_0\theta_0 + (V_0\tilde{\theta}e^{i\omega_\theta t} + b\dot{\theta})C(k_\theta) \\
& + \theta_0\tilde{V}e^{i\omega_v t}C(k_v) + \tilde{V}\tilde{\theta}e^{i(\omega_\theta + \omega_v)t}C(k_{\theta+v}) + \dot{h}C(k_h)]
\end{aligned}
\tag{3.86}
$$

This lift expression is identical to the the expression derived by Greenberg [12].

3.3   Results and Discussion

The correlation of unsteady aerodynamic coefficients using the *modified* stall model with the available experimental data is discussed in the following sections. The stall equations (Eqs. 3.81-3.83, 3.69-3.70 and 3.71-3.72) are converted into state-space form and 4th order Runge-Kutta integration scheme has been used for evaluating the steady state response. The time step for integration is set at 0.00314 sec and the initial conditions for aerodynamic states are assumed to be zero. In evaluating the response, the equations corresponding to stalled domain (Eq. 3.83 for lift, Eq. 3.70 for moment and Eq. 3.72 for drag) have to be included in the solution procedure as soon as the effective pitch angle of the airfoil crosses the static stall angle during its motion.

3.3.1   Correlation of *Modified* Stall Model

Using the *modified* dynamic stall equations (Eqs. 3.81 - 3.83 for lift, Eqs. 3.69 - 3.70 for moment and Eqs. 3.71 - 3.72 for drag), time variation of the aerodynamic coefficients are generated and are compared with experimental data for three different cases, namely; (i) pure pitching motion of an airfoil, (ii) pure plunging motion of an airfoil and (iii) pitching motion of an airfoil in a pulsating oncoming flow. Results are
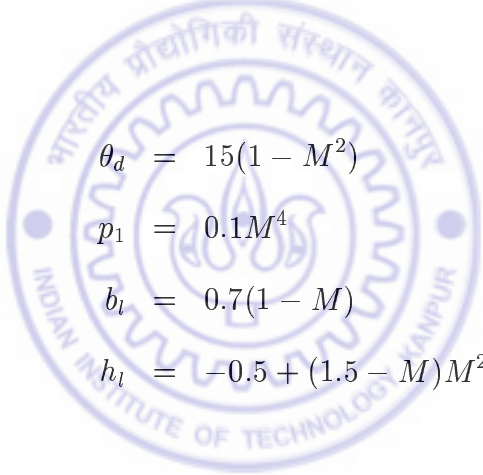
also generated for combined pitching and plunging motion in a time varying oncoming flow, simulating the cross-sectional motion of a helicopter rotor blade in operation.

The unsteady aerodynamic coefficients are generated with the following assumed static aerodynamic data for NACA 0012 airfoil, taken from Refs. [116] and [117].

Static lift data:

$$C_{z_l} = p_0 \theta \tag{3.87}$$

$$p_0 = 0.100(1 - M^8)/\sqrt{(1 - M^2)}$$

$$\Delta C_z = \begin{cases} 0 & \theta < \theta_d \\ (p_0 - p_1)(\theta - \theta_d) - b_l(\exp(h_l(\theta - \theta_d)) - 1) & \theta \geq \theta_d \end{cases}$$

where

$$\theta_d = 15(1 - M^2)$$

$$p_1 = 0.1M^4$$

$$b_l = 0.7(1 - M)$$

$$h_l = -0.5 + (1.5 - M)M^2$$

Static moment data:

$$C_{m_l} = -0.005 - 0.05 \exp(0.5(M - 1)^2) \tag{3.88}$$

$$\Delta C_m = \begin{cases} 0 & \theta < \theta_d \\ b_m(\exp(h_m(\theta - \theta_d)) - 1) & \theta \geq \theta_d \end{cases}$$

where

$$\theta_d = 15(1 - M^2)$$

$$b_m = -0.09 - 0.08 \exp(-30(M - 0.6)^2)$$

$$h_m = -0.4 - 0.21 \tan^{-1}(22(0.45 - M))$$

Static drag data:

$$C_{d_0} = 0.008 \tag{3.89}$$

$$\Delta C_d = \begin{cases} 0 & \theta < \theta_d \\ (C_{d_0} - 0.30)(1 - ((\theta_{max} - \theta)/(\theta_{max} - \theta_d))^u) & \theta \geq \theta_d \end{cases}$$

where

$$\theta_d = 15.(1 - M^2)$$

$$\theta_{max} = 25$$

$$\theta_{Mach} = 18 - 2\tan^{-1}(4M)$$

$$u = (\theta_{max} - \theta)/(\theta_{Mach} - \theta_d)$$

Parameters for lift expression (Eq. 3.83):

$$\sqrt{r_l} = 0.20 + 0.20\Delta C_z^2$$

$$a_l = 0.30 + 0.20\Delta C_z^2$$

$$E_l = -0.05\Delta C_z^2$$

Parameters for moment expression (Eq. 3.70):

$$d_m = 0$$

$$\sqrt{r_m} = 0.20 + 0.20\Delta C_z^2$$

$$a_m = 0.25 + 0.10\Delta C_z^2$$

$$E_m = 0.01\Delta C_z^2$$

Parameters for drag expression (Eq. 3.72):

$$\sigma_d = 0.003\theta - 0.04|\Delta C_z|$$

$$\sqrt{r_d} = 0.20 + 0.20\Delta C_z^2$$

$$a_d = 0.25$$

$$E_d = -0.015\Delta C_z^2$$

Blade semichord is taken as $b = 0.2$ m and the speed of sound used for calculating Mach number is assumed as 330 m/sec.

(i) *Pitching Motion*

First a comparison of the lift coefficient generated using $Modified$ dynamic stall model (Eqs. 3.81-3.83) and Petot stall model (Eqs. 3.66-3.68) is made with the experimental data of an airfoil (NACA 0012) undergoing only pitching motion. The airfoil is assumed to undergo a pitching motion $\theta = 15 + 10\cos(0.1\tau)$ deg. The Mach number is $M = 0.3$. The variation of lift coefficient for the two stall models are shown in Fig. 3.6 along with experimental data taken from Ref. [95]. The direction of variation of lift coefficient is indicated by arrows. It can be seen that the $modified$ stall model proposed in this study provides a better correlation with experimental data, particularly in the reattachment zone represented by low values of C_Z; however, it slightly underpredicts the maximum value of C_Z. It may noted that the results presented in the following are generated using the $modified$ stall model.

Keeping $M = 0.3$, the aerodynamic coefficients are generated for various reduced frequencies ($k = 0.03$, 0.05 and 0.1) of the pitching motion. The lift, moment and drag coefficients generated from the $modified$ stall model are shown in Fig. 3.7 along with the experimental data taken from Ref. [95]. The result shows that the $modified$ stall provides a reasonably good correlation with experimental data. The correlation seems to be better for the case of lift than for moment and drag, particularly for

$k = 0.1$.

(ii)   *Pitching and Plunging Motion*

For an unsymmetrical airfoil (NACA 23010), the time varying lift and moment coefficients for pure pitching and pure plunging motion in attached flow are generated. The aerodynamic static data used for this analysis are taken from Ref. [111]. A comparison of the theoretical results with the experimental data (taken from Ref. [111]) is shown in Fig. 3.8(a) for pure pitching and Fig. 3.8(b) for pure plunging motion, respectively. In the case of pure pitching motion, the pitch angle is varied as $\theta = 0.06 + 5.05 \sin(0.125\tau)$ deg. For the case of plunging motion, a mean pitch angle is set at 0.26 deg. and the effective pitch angle is given by $\theta_{eff} = 0.26 + \frac{\dot{h}}{V}$, where $h = \bar{h} \sin(0.125\tau)$. Mach number is taken as $M = 0.4$ and the reduced frequency is $k = 0.125$. The results indicate that the *modified* stall provides a reasonably good correlation with experimental data for both lift and moment coefficients.

(iii)   *Pitching Motion in Pulsating Oncoming Flow*

In Ref. [107], experimental studies have been carried out on a symmetric airfoil (NACA 0012) undergoing pitching motion in a pulsating oncoming flow. The oncoming flow velocity is given by $V = 6(1 + 0.356 \cos(0.314\tau))$ m/sec. The experiment was conducted for two pitch angle variations, one pertaining to the motion in the unstalled region, with $\theta = 6 + 6 \cos(0.314\tau + \Phi)$ deg. and the other in the stalled region given by $\theta = 12 + 6 \cos(0.314\tau + \Phi)$ deg. Φ represents the phase angle between oncoming flow velocity and the pitching motion. Results are presented for the two cases of phase angles i.e., $\Phi = 0$ deg. and $\Phi = 180$ deg. Figure 3.9 shows the comparison between experimental and theoretical stall data of unsteady lift coefficient. The results indicate that the *modified* stall model provides a better correlation with experimental data for both unstalled and stalled cases when $\Phi = 180$ deg. (Fig. 3.9(b)

and Fig. 3.9(d)). On the other hand, the correlation is not good for the case when $\Phi = 0$ deg. (Fig. 3.9(a) and Fig. 3.9(c)). The reason for the poor correlation for this case may be attributed to the deficiency of the stall model in capturing the effect of the formation of a larger leading edge bubble (Ref. [107]) as compared to the case of $\Phi = 180$ deg..

The variation of drag coefficient for pure pitching motion and pitching motion in pulsating oncoming flow is shown in Fig. 3.10(a) and Fig. 3.10(b), respectively. The theoretical results show a very good correlation with experimental data.

(iv) Combined Pitching and Plunging Motion in Pulsating Oncoming Flow

For the purpose of illustration, theoretical data is generated for an airfoil (NACA 0012) undergoing combined pitching and plunging motion in time varying oncoming flow, simulating the condition of a helicopter rotor blade cross-section in operation. The data used for this calculations are:

$$\theta = \theta_0 + \tilde{\theta}\cos(\omega t + \Phi); \qquad h = \bar{h}\,\sin(\omega t);$$

$$V = V_0 + \tilde{V}\cos(\omega t); \qquad \bar{h} = 0.42 \text{ m};$$

$$V_0 = 100 \text{ m/sec}; \quad \tilde{V} = 39.6 \text{ m/sec};$$

$$b = 0.2 \text{ m}; \quad \omega = 25 \text{ rad/sec}$$

$$k = 0.05; \qquad \Phi = 0 \text{ deg}.$$

Case(i)

$$\theta_0 = 6 \text{ deg}.$$

$$\theta_1 = 6 \text{ deg}.$$

Case (ii)

$$\theta_0 = 12 \text{ deg.}$$

$$\theta_1 = 6 \text{ deg.}$$

The results are generated for two pitch angle variations, one pertaining to low mean angle $\theta_0 = 6$ deg. and the other, corresponding to high mean angle $\theta_0 = 12$ deg. The variation of aerodynamic coefficients are shown in Fig. 3.11(a) and Fig. 3.11(b). Since there is no experimental data available for comparison, these results are presented for the sake of completeness and illustration.

3.4 Summary

In this chapter, a description of the inflow models and sectional aerodynamic models is presented. The development of global inflow models, starting from simple uniform inflow model to computationally intensive dynamic wake model, has been addressed.

ONERA (EDLin) dynamic stall model has been analysed in relation to Theodorsen's and Greenberg's unsteady aerodynamic theories. It is shown that ONERA (EDLin) dynamic stall model in the unstalled region is identical to Theodorsen's model except that lift deficiency function $C(k)$ is approximated by a first order rational approximation. Replacing the first order rational approximation by a more accurate second order rational approximation, a *modified* dynamic stall model is proposed in this study. This improved stall model is shown to provide a better correlation with experimental stall data, for pitching, plunging oscillations and pulsating oncoming flow.
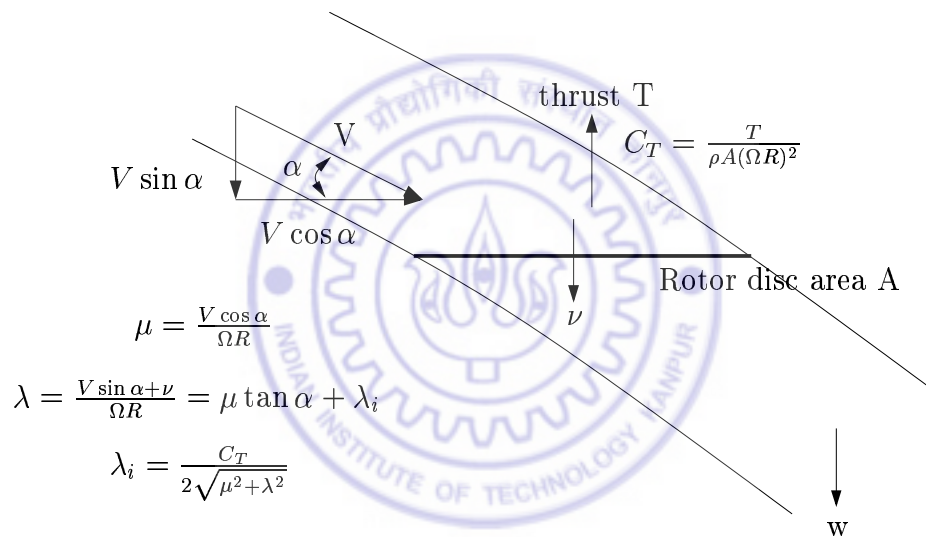
Figure 3.1: Flow model for momentum theory in forward flight

The figure contains the following labels and equations:

thrust T

$$C_T = \frac{T}{\rho A (\Omega R)^2}$$

$V \sin \alpha$

α

V

$V \cos \alpha$

Rotor disc area A

ν

$$\mu = \frac{V \cos \alpha}{\Omega R}$$

$$\lambda = \frac{V \sin \alpha + \nu}{\Omega R} = \mu \tan \alpha + \lambda_i$$

$$\lambda_i = \frac{C_T}{2\sqrt{\mu^2 + \lambda^2}}$$

w
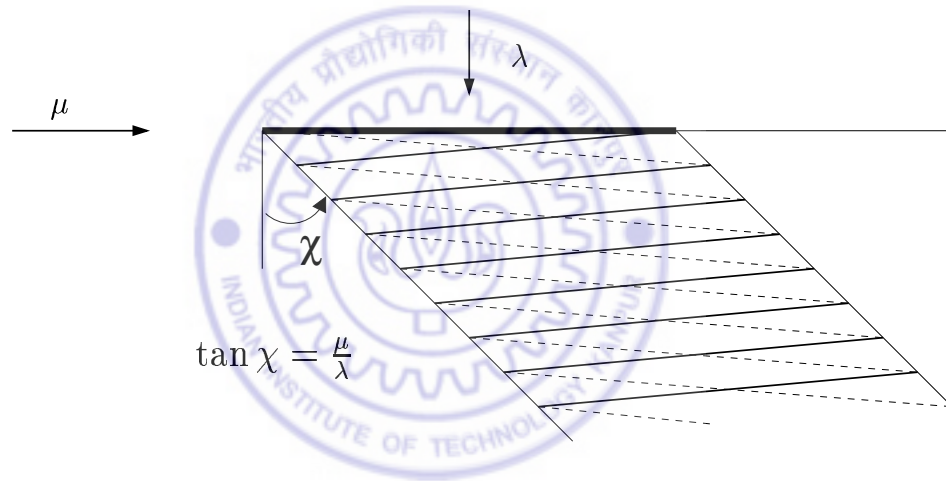
Figure 3.2: Definition of a skew angle

(a) Lift $(\theta_d$ stall angle of attack$)$

(b) Moment

(c) Drag
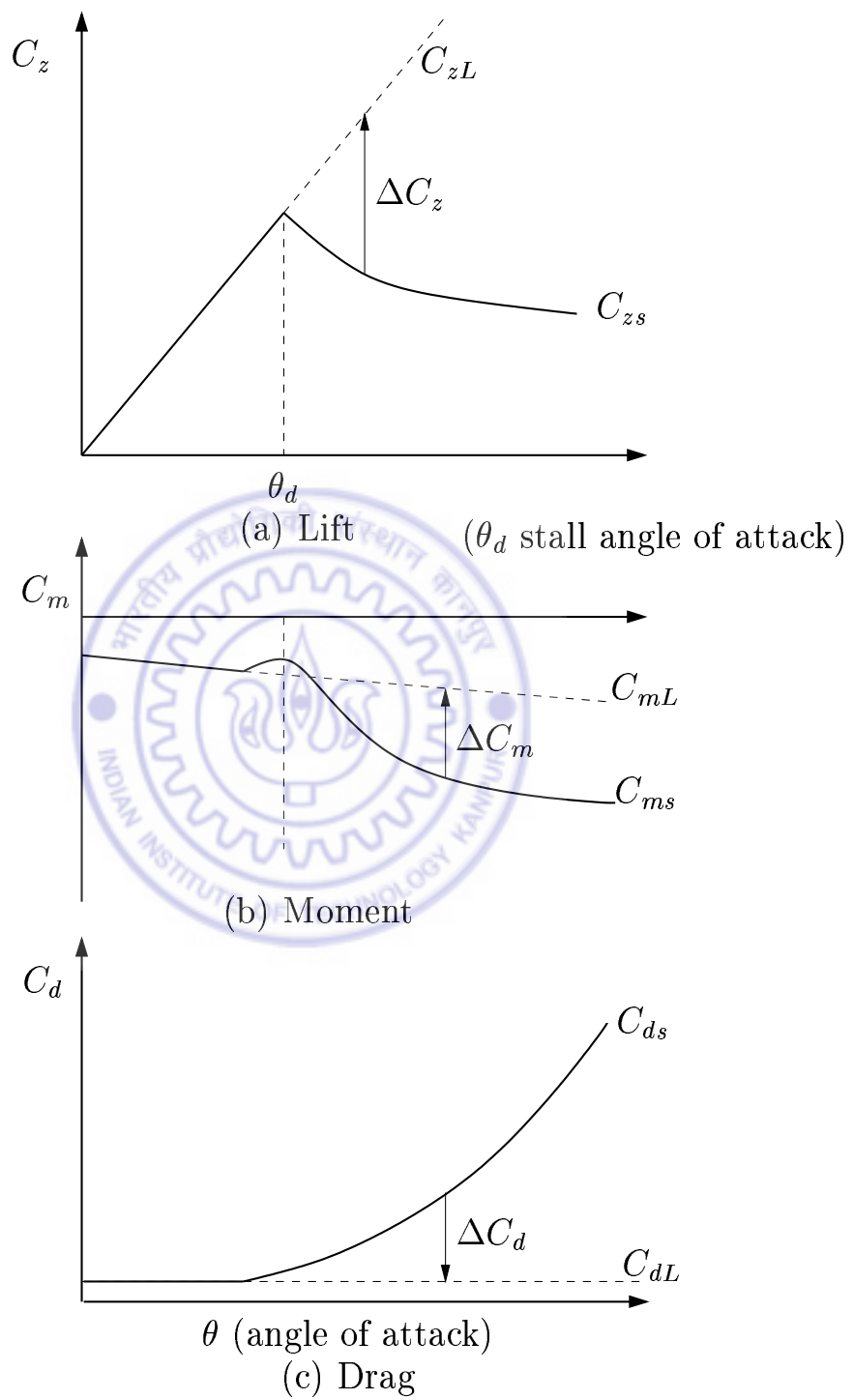
Figure 3.3: Definition of the static aerodynamic coefficients
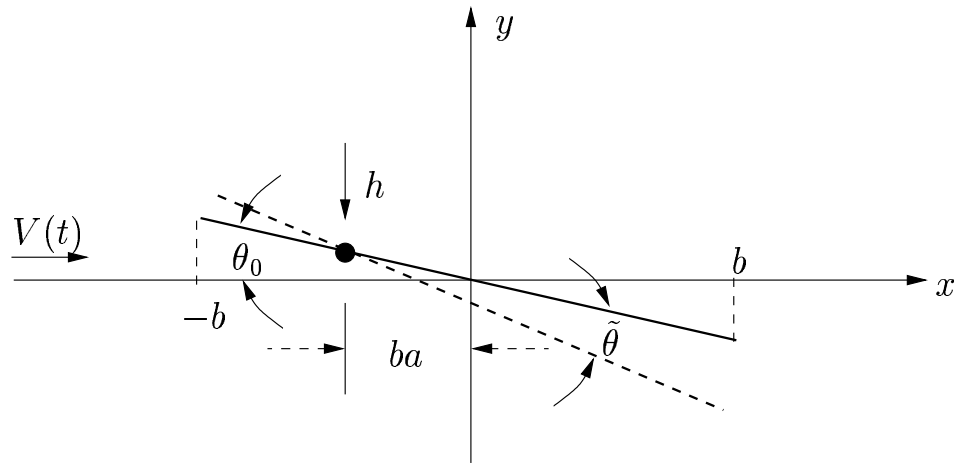
Figure 3.4: Geometry of an oscillating airfoil
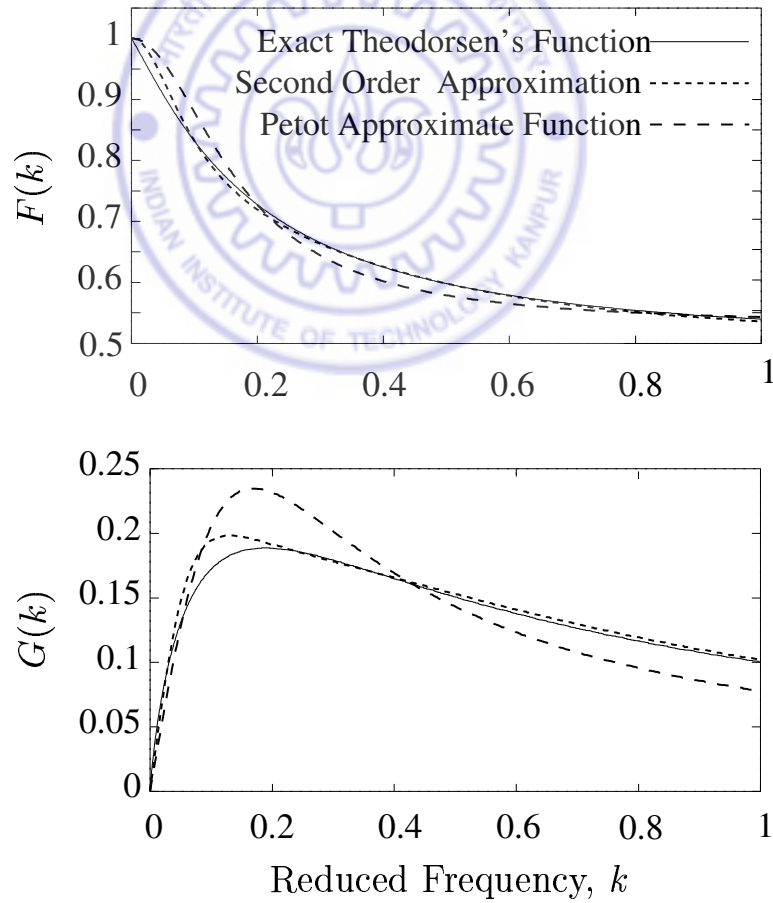
Figure 3.5: Theodorsen's lift deficiency function
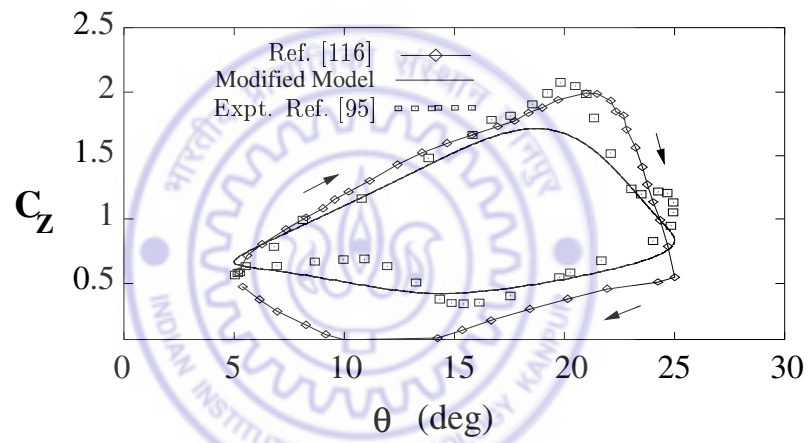
Figure 3.6: *Modified* stall model compared with experimental data and Petot Model: $\theta = 15° + 10° \cos(0.1\tau)$, $M = 0.3$
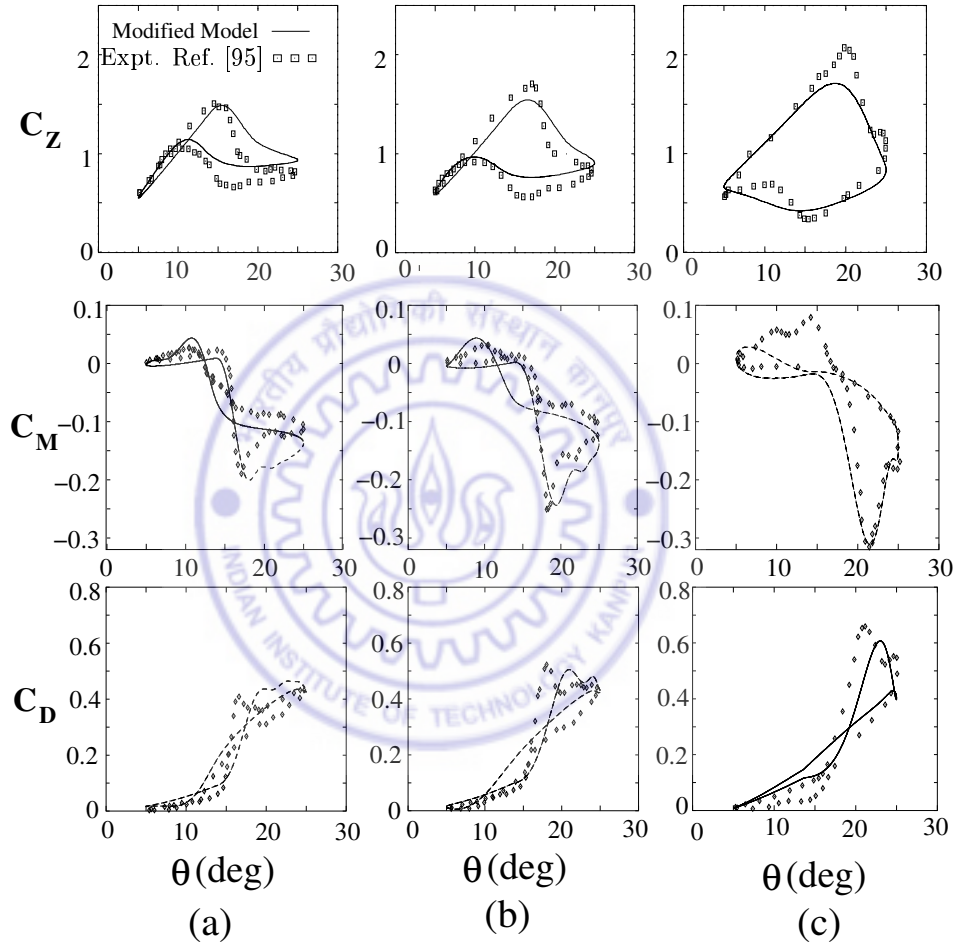
Figure 3.7: Aerodynamic hysteresis loops generated for various reduced frequencies $\theta = 15° + 10° \cos(k\tau)$, $M = 0.3$: (a) $k = 0.03$, (b) $k = 0.05$, (c) $k = 0.1$.
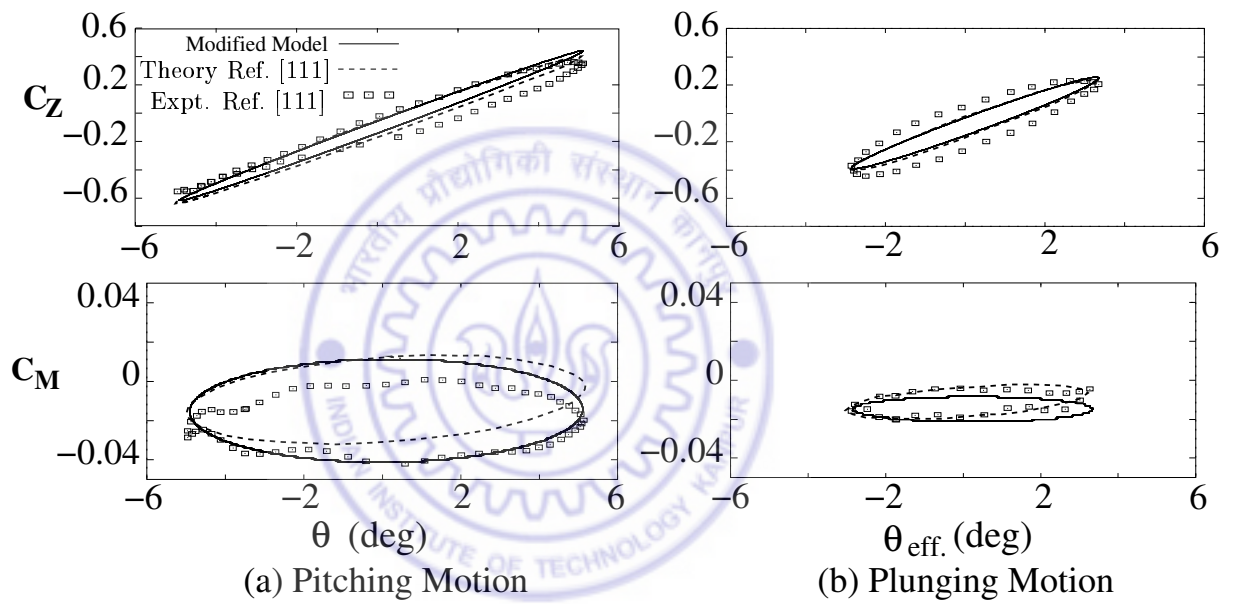
Figure 3.8: Lift and moment coefficients generated for unsymmetrical airfoil for pitch and plunge motion: Pitching motion $\theta = 0.06° + 5.05° \sin(0.125\tau)$, $M = 0.4$; Plunging motion $\theta_{eff} = 0.26° + 3.10° \sin(0.125\tau)$, $M = 0.4$.
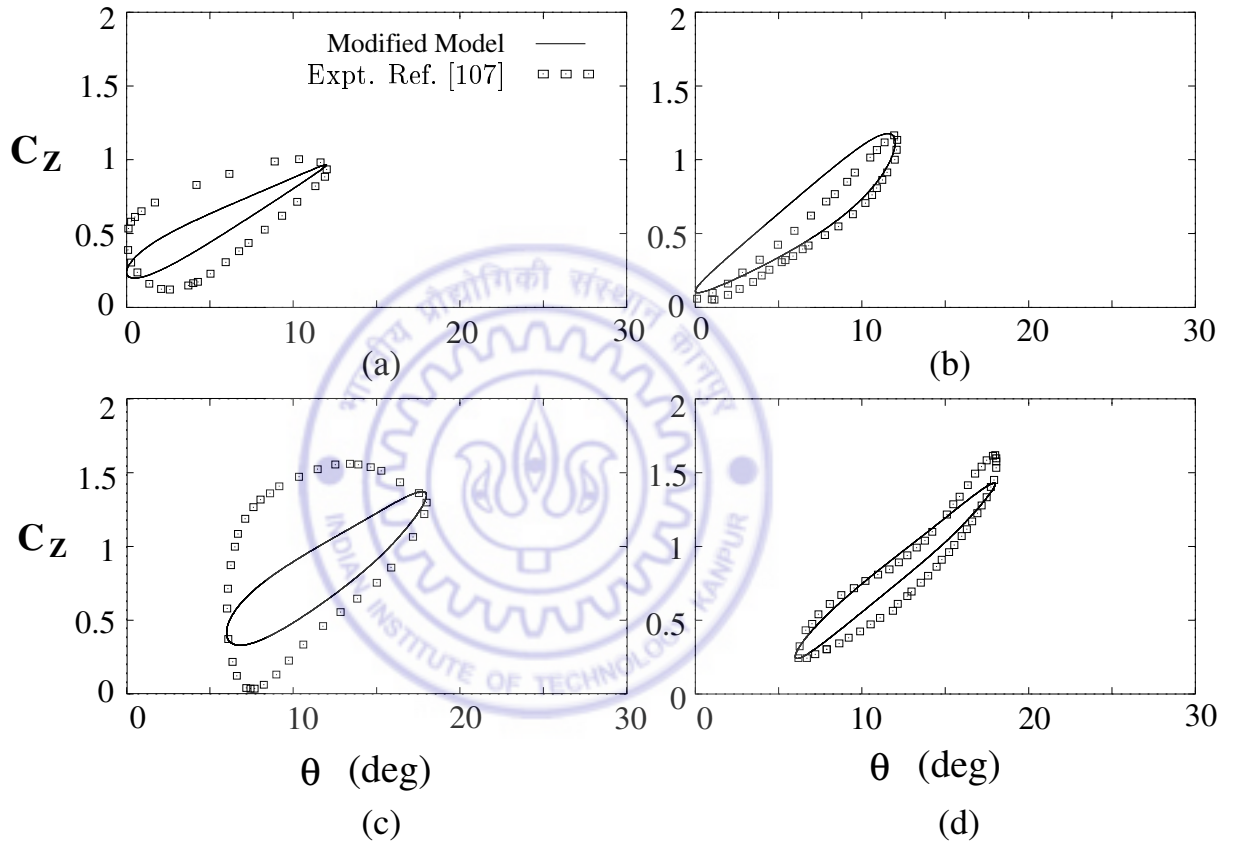
Figure 3.9: Lift coefficient generated for pitching motion ($\theta = \theta_0 + 6\cos(0.314\tau + \Phi)$deg.) in pulsating flow ($V = 6 + 2.136\cos(0.314\tau)$ m/sec.,): (a) $\theta_0 = 6°$, $\Phi = 0°$ (b) $\theta_0 = 6°$, $\Phi = 180°$ (c) $\theta_0 = 12°$, $\Phi = 0°$ (d) $\theta_0 = 12°$, $\Phi = 180°$.
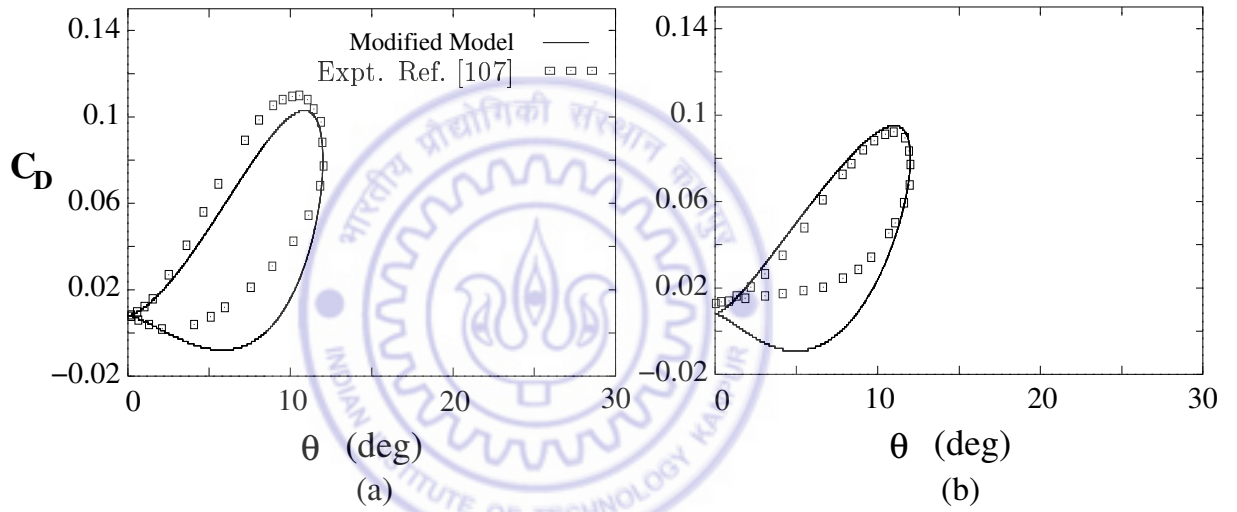
Figure 3.10: Drag coefficient generated for (a) pitching motion ($\theta = \theta_0 + 6\cos(0.314\tau + \Phi)$ deg.) and (b) pitching motion in pulsating oncoming flow ($V = 6 + 2.136\cos(0.314\tau)$ m/sec.,) with $\Phi = 0°$.
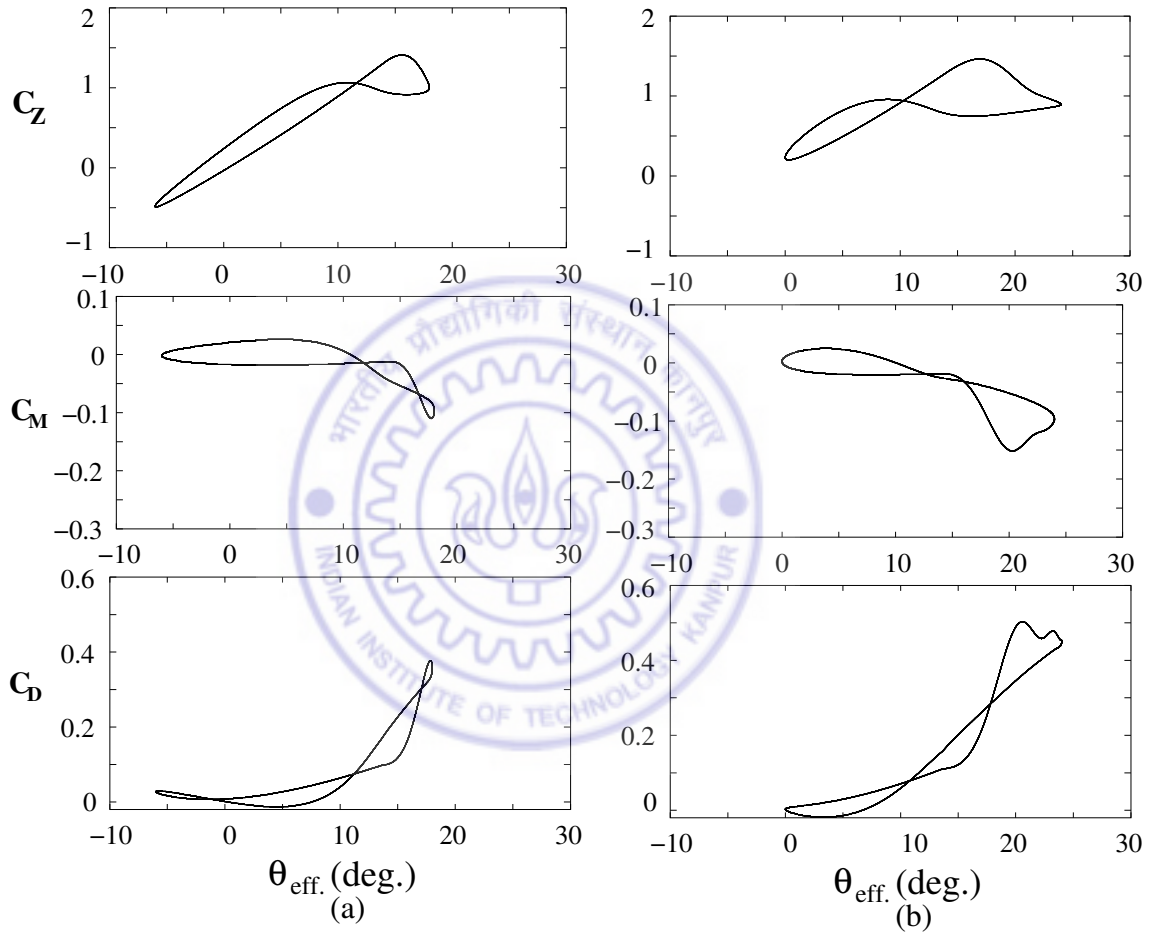
Figure 3.11: Aerodynamic hysteresis loops for combined pitching and plunging motion ($\theta_{eff} = \theta + \frac{\dot{h}}{V_0}$ in degrees) in pulsating flow: (a) $\theta_0 = 6°$, $\Phi = 0°$ (b) $\theta_0 = 12°$, $\Phi = 0°$.

Chapter 4

RESPONSE OF 2-D AIRFOIL MODEL

4.1 Introduction

In general, nonlinear effects are often cited as possible reasons for any observed difference between theory and experiment [177]. The major sources of nonlinearity in rotary wing aeroelasticity are due to: (i) geometric nonlinearity associated with moderate deformation of the rotor blade and (ii) aerodynamic nonlinearity due to dynamic stall. In this chapter an attempt has been made to understand the influence of aerodynamic nonlinearity due to dynamic stall on the response of a 2-D airfoil, by the formulation and solution of a nonlinear aeroelastic response problem. The response of a 2-D airfoil undergoing pitching and plunging motion in a pulsating flow, simulating the condition of a typical cross-section of a helicopter rotor blade in forward flight, is analysed. The modeling consists of linear structural model combined with a nonlinear aerodynamic model.

4.2 2-D Airfoil Response

Figure 4.1 shows a model of a 2-D airfoil undergoing pitching and plunging motions. The coupled equations of motion can be written as:

$$m\ddot{h} + S_\phi\ddot{\phi} + K_h h = -L \qquad (4.1)$$
$$I_\phi\ddot{\phi} + S_\phi\ddot{h} + K_\phi\phi = M$$

where S_ϕ represents the inertia coupling, ϕ represents elastic twist and h denotes the heaving motion. In Fig. 4.1, θ represents the input pitch angle and V represents the oncoming flow velocity.

The response of the airfoil is analysed for different cases to bring out: (i) the effect of dynamic stall modeling in comparison to quasi-steady approximation of Greenberg's aerodynamic theory (*i.e.*, $C(k) \simeq 1$); and (ii) influence of aeroelastic couplings (pitch-heave coupling due to S_ϕ) in association with dynamic stall. The aerodynamic loads are evaluated by using either (i) *Modified* dynamic stall model or (ii) Greenberg's quasi-steady model. For the sake of clarity, a brief mathematical description of these models is provided.

4.2.1 *Modified* ONERA Dynamic Stall Model

The unsteady lift on the airfoil is given as:

$$L = \frac{1}{2}\rho\tilde{S}[sb\dot{W}_0 + \tilde{k}b\dot{W}_1 + V\Gamma_1 + V\Gamma_2] \qquad (4.2)$$

$$\ddot{\Gamma}_1 + B_2(\frac{V}{b})\dot{\Gamma}_1 + B_3(\frac{V}{b})^2\Gamma_1 = A_3(\frac{V}{b})^2\frac{\partial C_{z_L}}{\partial\theta}W_0 + A_3\sigma(\frac{V}{b})^2 W_1 + \qquad (4.3)$$

$$A_2(\frac{V}{b})\frac{\partial C_{z_L}}{\partial\theta}\dot{W}_0 + A_2(\frac{V}{b})\sigma\dot{W}_1 + A_1\frac{\partial C_{z_L}}{\partial\theta}\ddot{W}_0 + A_1\sigma\ddot{W}_1$$

$$\ddot{\Gamma}_2 + a_l(\frac{V}{b})\dot{\Gamma}_2 + r_l(\frac{V}{b})^2\Gamma_2 = -[r_l(\frac{V}{b})^2 V\Delta C_z|_{W_0/V} + E_l(\frac{V}{b})\dot{W}_0] \qquad (4.4)$$

where $A_1 = 0.50$, $A_2 = 0.393$, $A_3 = 0.0439425$, $B_2 = 0.5515$ and $B_3 = 0.0439075$. The unsteady moment on the airfoil is given as:

$$M = \frac{1}{2}\rho \tilde{S}2b[V^2 C_{m_L}|_{W_0/V} + (\bar{\sigma}_m + d_m)b\dot{W}_0$$
$$+ \sigma_m V W_1 + s_m b\dot{W}_1 + V\Gamma_{m2}] \qquad (4.5)$$

$$\ddot{\Gamma}_{m2} + a_m(\frac{V}{b})\dot{\Gamma}_{m2} + r_m(\frac{V}{b})^2\Gamma_{m2} = -[r_m(\frac{V}{b})^2 V\Delta C_m|_{W_0/V} + E_m(\frac{V}{b})\dot{W}_0] \quad (4.6)$$

The various parameters W_0, W_1, $\dot{h}$, θ, V, $\Delta C_z|_{W_0/V}$, $\Delta C_m|_{W_0/V}$ and $C_{m_L}|_{W_0/V}$ are defined as in Chapter 3. It is to be noted that the effective angle of attack is to be specified in degrees. The various coefficients of the *modified* lift model (Eqs. 4.2 - 4.4) used in this study are given as:

$$s = (\pi + 5\pi[(1 - M_\infty^2)^{0.285} - 1])\frac{\pi}{180}$$
$$\tilde{k} = (\frac{\pi}{2} + 1.96\pi(\sqrt{(1 - M_\infty^2)} - 1))\frac{\pi}{180}$$
$$\sigma = (\frac{2\pi}{\sqrt{(1 - M_\infty^2)}})\frac{\pi}{180}$$
$$a_l = 0.30 + 0.20\Delta C_z^2$$
$$\sqrt{r_l} = 0.20 + 0.20\Delta C_z^2$$
$$E_l = -0.05\Delta C_z^2$$

The various coefficients of the moment model (Eqs. 4.5-4.6) used in this study are given as:

$$\bar{\sigma}_m = -\frac{\pi}{4}[1 + 1.4M_\infty^2]\frac{\pi}{180}$$
$$d_m = \sigma_{1m}.|\Delta C_z|, \quad (\sigma_{1m} = 0.0)$$
$$s_m = -\frac{3\pi}{16}(-1.26 - 1.53\arctan[15(M_\infty - 0.7)])\frac{\pi}{180}$$
$$\sigma_m = \sigma_{0m} + \sigma_{1m}.|\Delta C_z|$$
$$\sigma_{0m} = (\frac{3\pi}{16}(-1.26 - 1.53\arctan[15(M_\infty - 0.7)]) - \frac{\pi}{2}[1 + 1.4M_\infty^2])\frac{\pi}{180}$$

$$a_m = 0.25 + 0.10\Delta C_z^2$$

$$\sqrt{r_m} = 0.20 + 0.20\Delta C_z^2$$

$$E_m = 0.01\Delta C_z^2$$

4.2.2 Greenbergs Quasisteady Model

The quasi-steady lift and moment expressions, derived from Greenberg's theory, are given as:

$$L = \frac{1}{2}\rho\tilde{S}[\pi b(\dot{W}_0 + \frac{1}{2}\dot{W}_1) + V(2\pi W_0 + 2\pi W_1)] \tag{4.7}$$

$$M = \frac{1}{2}\rho\tilde{S}2b[-\frac{\pi b}{4} - \frac{\pi}{4}VW_1 - \frac{3\pi}{16}\dot{W}_1)] \tag{4.8}$$

4.3 Solution Procedure

The response of a 2-D airfoil undergoing pitching and plunging motion in a pulsating flow is studied to bring out the effects of dynamic stall and aeroelastic couplings. In evaluating the response of the airfoil, 4th order Runge-Kutta integration scheme with a time step $\Delta t = 0.00314$ sec., has been used. The instantaneous lift and moment acting on the airfoil are evaluated using Eqs. 4.2 - 4.4 and Eqs. 4.5 - 4.6, respectively. The response of the airfoil is calculated iteratively till steady state solution is arrived. The frequency contents of the response are obtained using Fast Fourier Transform (FFT). The data used in the calculations are: $m = 7.95$ kg; $I_\phi = 0.115$ kgm^2; $K_h = 4396.0$ N/m; $K_\phi = 734.2$ Nm; and $b = 0.209$ m. Input pitch angle θ and oncoming flow velocity are assumed to be time varying and are represented by $\theta = 12 - 6\cos(\Omega t)$ deg. and $V = 113(1 + 0.40\cos(\Omega t))$ m/sec respectively, where Ω is referred as input excitation frequency and is given as $\Omega = 22.82$ rad/sec. ($3.64Hz$). The uncoupled natural frequencies of the system are $\omega_h = 3.74$ Hz; $\omega_\phi = 12.72$ Hz.

The results pertaining to aeroelastic response of a 2-D airfoil under going pitching and plunging motion in pulsating oncoming flow are discussed in detail. The results of

this study are presented in two sections. They are: (a) Uncoupled response ($S_\phi = 0$), and (b) Coupled response ($S_\phi \neq 0$).

4.3.1 Uncoupled Response

In the uncoupled analysis, the aerodynamic center, center of mass and elastic axis are assumed to be located at the quarter chord point of a 2-D airfoil. The response of the airfoil is obtained using two aerodynamic models, namely quasi-steady aerodynamic model and $modified$ stall model. Heave and torsional responses for quasi-steady aerodynamic theory and their frequency contents are plotted in Fig. 4.2a and Fig. 4.2b, respectively. The response for $modified$ stall model and their frequency contents are plotted in Fig. 4.3a and Fig. 4.3b, respectively. From Fig. 4.2, it can be seen that the heave response obtained from the quasi-steady aerodynamic theory contains two frequencies, namely, 3.64 Hz and 7.27 Hz, whereas torsional response contains three frequencies (3.64 Hz, 7.27 Hz and 10.90 Hz), which are integer multiples of excitation frequency 3.64 Hz. For the case with $modified$ dynamic stall model, (Fig. 4.3) while the heave response contains two frequencies, pitch response has many frequencies. Table 4.1 shows the frequency contents and their magnitude of the uncoupled heave response for quasi-steady and $modified$ stall aerodynamic theory. It is observed that the amplitude of the heave response for the case of $modified$ stall model is three times greater than that for the quasi-steady model. In the case of torsional mode, $modified$ stall model introduces additional harmonics (Table 4.2), as compared to quasi-steady aerodynamics. The reason for the appearance of additional higher harmonics may be attributed to the nonlinearity of the stall model.

Lift and moment obtained from quasi-steady aerodynamics and $modified$ stall model are plotted for one cycle in Figs. 4.4a and 4.4b, respectively. The variation of lift coefficient shows that the minimum occurs at 77 deg. for quasi-steady aerodynamic theory and for $modified$ stall model, it is shifted to 95 deg. The peak value

of the lift coefficient for dynamic stall is lower than that corresponding to quasi-steady aerodynamics. The stall model also introduces additional harmonics in lift and moment coefficients.

4.3.2 Coupled Response

In the coupled analysis, heave-pitch coupling is introduced by shifting the mass centre away from the elastic axis. Elastic axis and aerodynamic centre are located at quarter chord point. The influence of aeroelastic coupling on the airfoil response has been studied for various values of S_ϕ by shifting the mass centre aft and forward of elastic axis.

Figures 4.5 - 4.10 show the response and frequency contents along with phase plane diagram for the heaving and pitching motion of the airfoil for the various aft locations of centre of mass from elastic axis, namely 3% ($S_\phi = 0.049$), 4% ($S_\phi = 0.066$) and 5% ($S_\phi = 0.083$) of the chord. A comparison of these figures show that as the pitch-heave coupling is increased (*i.e.*, by shifting the centre of mass aft of elastic axis), pitch and heave motions of airfoil become qualitatively different. Increasing the coupling seems to increase the distribution of frequency contents in the response signal, as observed in Figs. 4.5, 4.7 and 4.9. The phase plane diagrams (Figs. 4.6, 4.8 and 4.10) show that as the coupling is increased, the motion of the airfoil changes from periodic to bounded chaotic motion.

Table 4.3 shows the frequency distribution of the response and the magnitude, for different cases of centre of mass location from elastic axis of the airfoil. It can be seen that the uncoupled (0%) and the coupled (3% chord aft location of centre of mass from elastic axis) have same frequency contents but having different magnitudes. The frequencies correspond to the excitation frequency of the input 3.64 Hz and its higher harmonics. When the centre of mass location is shifted to 4% chord aft of the elastic axis, the airfoil response shows significant subharmonic (1.82 Hz which is half of

input frequency 3.64 Hz) and super harmonic frequency contents. For the case of 5% chord aft location of centre of mass from elastic axis, the response contains several frequencies which are non-integer multiple of excitation frequency, both below and above the excitation frequency. The magnitudes of these additional frequency contents are comparable to the magnitudes of the response at input excitation frequency. These results show that dynamic stall (nonlinear aerodynamics) in association with aeroelastic pitch-heave coupling above a certain level can lead to bounded chaotic motion of the airfoil. Further rearward shift of mass centre (about 7% of the chord), leads the system to become completely unstable.

In order to verify whether the motion is truly chaotic or not, computations were performed to study the effect of perturbation in initial condition on the steady state response of the system. If the steady state response is sensitive to perturbation in initial conditions, it represents chaotic motion [190] and the Liaponov exponent provides a quantitative measure of the chaotic motion. The response of the airfoil is evaluated for two different sets of initial conditions, namely (i) all initial conditions are zero and (ii) perturbed initial condition with $\phi(0) = 0.01$ and other initial conditions are set to zero. The magnitude of the difference in the response of the airfoil in pitch ($|\phi_2 - \phi_1|$) and heave ($|h_2 - h_1|$) are plotted as functions of time. (Note: Subscript 1 represents the response corresponding to all zero initial conditions, whereas subscript 2 represents the case corresponding to perturbed initial condition.) If the steady state response is independent of the perturbation in initial conditions (*i.e.*, $|\phi_2 - \phi_1|_{t\to\infty} = 0$, $|h_2 - h_1|_{t\to\infty} = 0$), then it indicates periodic response. On the other hand, if the response is sensitive to perturbations in initial conditions, it represents chaotic motion [190]. Figure 4.11 shows the sensitivity of the response to initial conditions for two cases of centre of mass locations. It is evident that the system is insensitive to initial condition for the two cases of centre of mass location, namely at 0% and 3% chord aft of elastic axis, as shown in Figs. 4.11a and 4.11b, respectively. For the case

of centre of mass location at 5% chord aft of elastic axis, the response of the system is sensitive to the perturbation in initial condition as shown in Fig. 4.12(a). The Liaponov exponent is obtained from the plots of $\ln\left|\frac{\phi_2 - \phi_1}{\delta}\right|$ and $\ln\left|\frac{h_2 - h_1}{\delta}\right|$ versus time, where δ is the perturbation in initial condition. The positive slope of the mean curve is defined as Liaponov exponent and it represents the sensitivity of the response to perturbation in initial conditions. If the mean slope reaches a steady value, it indicates a bounded chaotic motion. From Fig. 4.12(b), it can be seen that both pitch and heave motion indicate bounded chaotic motion, with Liaponov exponents 1.78 for pitch and 1.48 for heave.

Figures 4.13 - 4.18 show the response and frequency contents along with phase plane diagram for the heaving and pitching motion of the airfoil for the various forward locations of centre of mass from elastic axis, namely 5% ($S_\phi = 0.083$), 10% ($S_\phi = 0.166$) and 20% ($S_\phi = 0.332$) of the chord. Table 4.4 shows the frequency distribution of the response and the magnitude, for different cases of centre of mass location from elastic axis of the airfoil. From Figs. 4.13 - 4.18 and Table 4.4, it is evident that the forward shift of mass centre always gives rise to a stable periodic response similar to the uncoupled case.

4.4 Summary

Using the *modified* stall model, the response characteristics of a 2-D airfoil undergoing pitching and plunging motion in a pulsating oncoming flow are analysed to study the effects of dynamic stall. The results of this study show that significant difference is observed in the response of airfoil for dynamic stall and quasi-steady aerodynamic models. Dynamic stall in association with aeroelastic couplings above a certain level leads to bounded chaotic motion of the airfoil, whereas such a phenomenon is not observed with forward shift of mass centre.

Table 4.1: Uncoupled heave response for quasi-steady and *modified* stall aerodynamic theory

Frequency (Hz)	quasi-steady Magnitude (m)	Dynamic stall Magnitude (m)
3.64	0.23	0.77
7.27	0.05	0.11

Table 4.2: Uncoupled torsional response for quasi-steady and *modified* stall aerodynamic theory

Frequency (Hz)	Quasi-steady Magnitude (rad.)	Dynamic stall Magnitude (rad.)
3.64	0.008	0.048
7.27	0.005	0.028
10.90	0.001	0.021
14.53	-	0.014
18.20	-	0.005

Table 4.3: Frequency distribution of airfoil response with *modified* stall model and aeroelastic coupling

Frequency (Hz)	Magnitude of heave response (m)				Magnitude of torsional response (rad.)			
	Aft location of C.G. from E.A.				Aft location of C.G. from E.A.			
	(0%)	(3%)	(4%)	(5%)	(0%)	(3%)	(4%)	(5%)
0.40	-	-	-	0.063	-	-	-	0.009
1.59	-	-	-	0.260	-	-	-	0.013
1.82	-	-	0.213	0.016	-	-	0.019	0.002
1.89	-	-	-	0.063	-	-	-	0.003
2.18	-	-	-	0.074	-	-	-	0.003
3.08	-	-	-	0.064	-	-	-	0.003
3.64*	0.768	0.592	0.422	0.344	0.048	0.057	0.038	0.034
4.77	-	-	-	0.084	-	-	-	0.009
5.07	-	-	-	0.237	-	-	-	0.034
5.27	-	-	-	0.659	-	-	-	0.112
5.45	-	-	0.533	0.143	-	-	0.078	0.029
5.66	-	-	-	0.106	-	-	-	0.028
6.36	-	-	-	0.041	-	-	-	0.017
7.27*	0.113	0.132	0.048	0.033	0.028	0.027	0.036	0.039
7.66	-	-	-	0.030	-	-	-	0.021
8.95	-	-	-	0.036	-	-	-	0.021
9.10	-	-	0.058	0.023	-	-	0.041	0.008
10.54	-	-	-	0.008	-	-	-	0.016
10.90*	-	0.025	0.017	0.015	0.021	0.052	0.008	0.022
12.53	-	-	-	0.015	-	-	-	0.028
12.72	-	-	0.015	0.007	-	-	0.036	0.008
14.12	-	-	-	0.011	-	-	-	0.031
14.53*	-	0.008	0.006	0.003	0.014	0.024	0.007	0.020
16.35	-	-	0.004	0.002	-	-	0.020	0.013
18.20*	-	-	0.004	0.003	0.005	0.022	0.003	0.005
19.98	-	-	-	0.002	-	-	0.003	0.002

* indicates excitation frequency of the input ((3.64) Hz) and its higher harmonics.

Table 4.4: Frequency distribution of airfoil response with *modified* stall model and aeroelastic coupling

Frequency (Hz)	Magnitude of heave response (m)				Magnitude of torsional response (rad.)			
	Forward location of C.G. from E.A.				Forward location of C.G. from E.A.			
	(0%)	(5%)	(10%)	(20%)	(0%)	(5%)	(10%)	(20%)
3.64*	0.768	0.5	0.42	0.24	0.048	0.07	0.1	0.11
7.27*	0.113	0.1	0.05	0.025	0.028	0.067	0.04	0.04
10.90*	-	-	-	-	0.021	0.022	0.03	0.03
14.53*	-	-	-	-	0.014	0.012	0.016	0.018
18.20*	-	-	-	-	0.005	0.005	0.010	0.005

* indicates excitation frequency of the input ((3.64) Hz) and its higher harmonics.
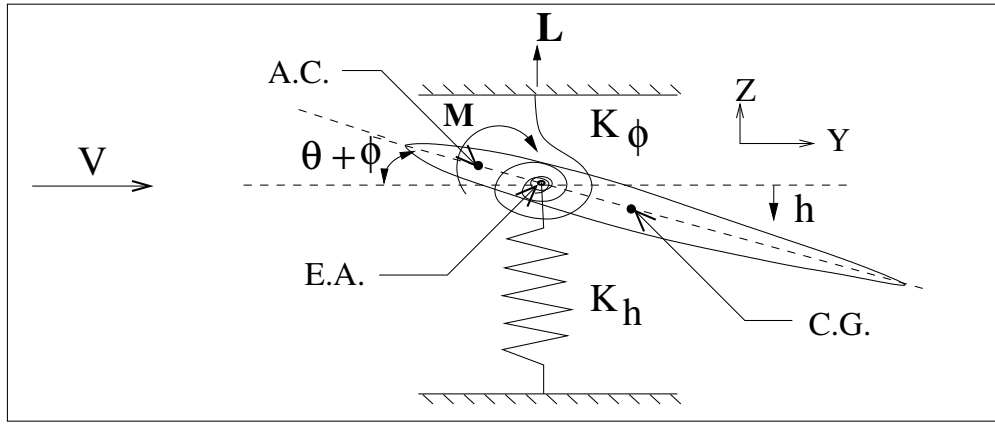
Figure 4.1: 2-D airfoil model

(a) Heave

(b) Elastic twist
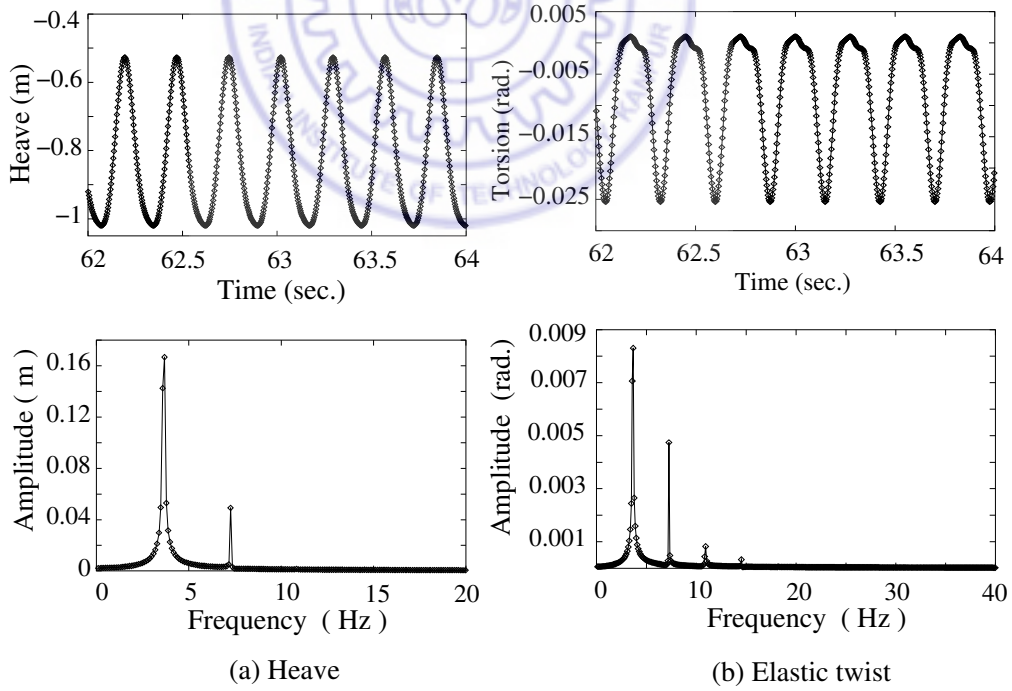
Figure 4.2: Uncoupled airfoil response for quasi-steady aerodynamic theory

(a) Heave

(b) Elastic twist
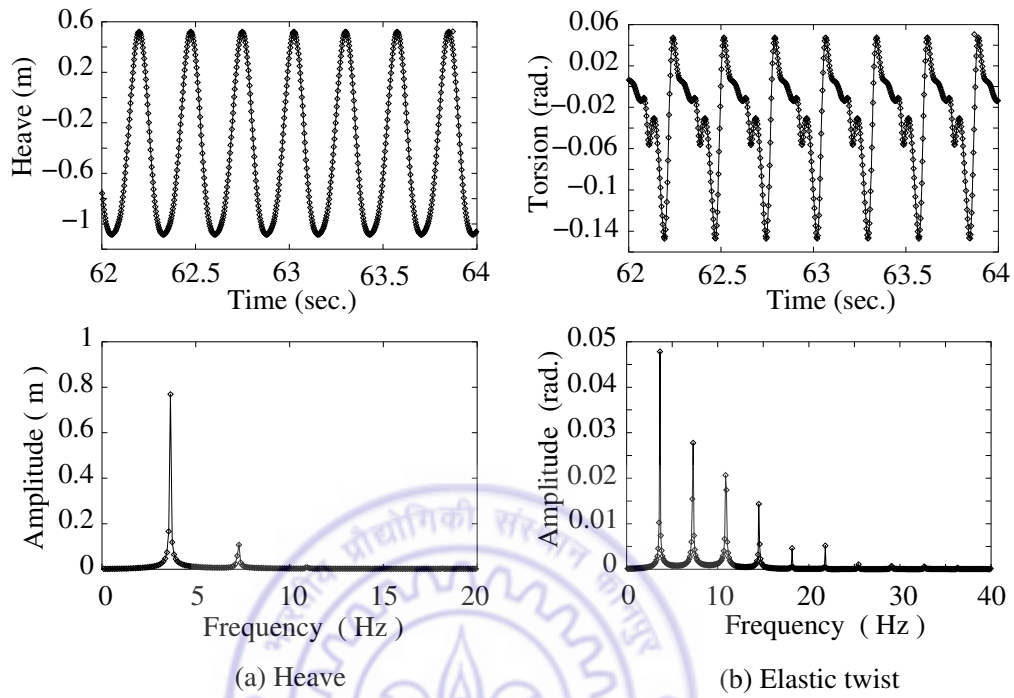
Figure 4.3: Uncoupled airfoil response for *modified* stall aerodynamic model

(a) Lift coefficient

(b) Moment coefficient
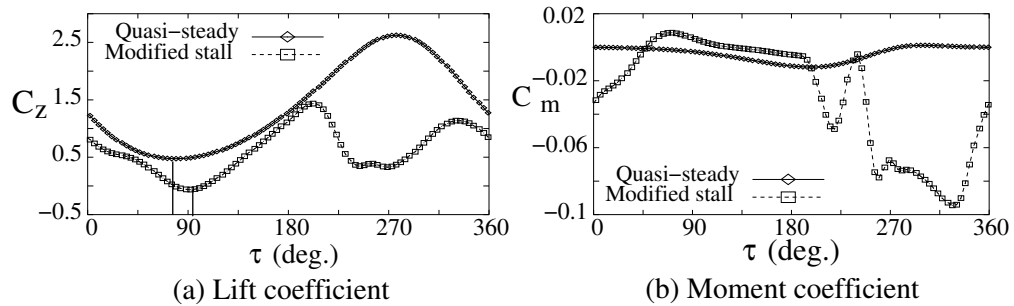
Figure 4.4: Comparison of quasi-steady lift and moment with *modified* stall model lift and moment

Figure 4.5: Airfoil response and its frequency contents generated with *modified* stall model for 3% chord aft location of C.G. from E.A.

Figure 4.6: Phase plane diagrams of airfoil response generated with *modified* stall model for 3% chord aft location of C.G. from E.A.

117

(a) Heave   (b) Elastic twist

Figure 4.7: Airfoil response and its frequency contents generated with *modified* stall model for 4% chord aft location of C.G. from E.A.

Figure 4.8: Phase plane diagrams of airfoil response generated with *modified* stall model for 4% chord aft location of C.G. from E.A.
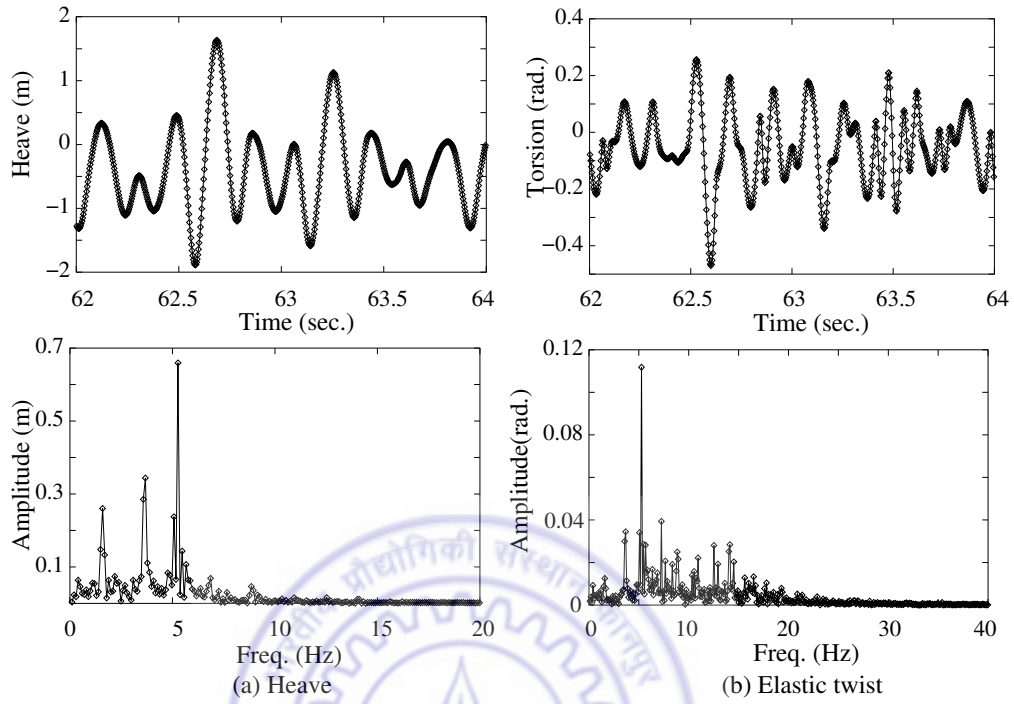
Figure 4.9: Airfoil response and its frequency contents generated with *modified* stall model for 5% chord aft location of C.G. from E.A.
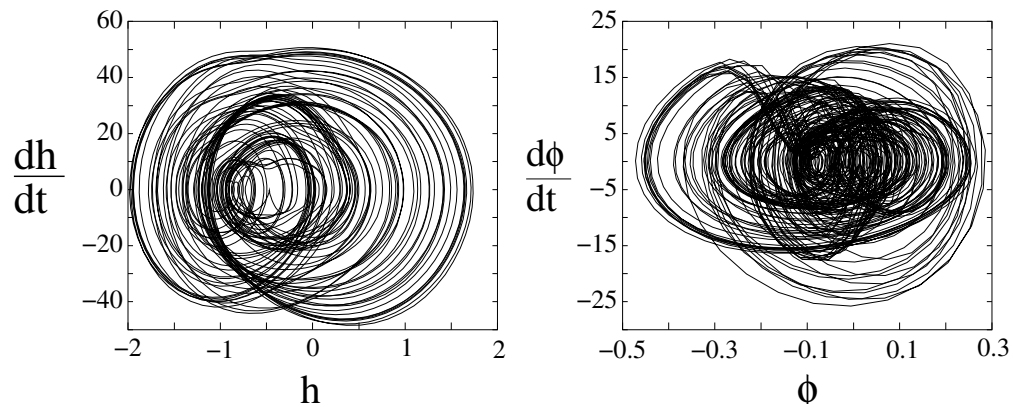
Figure 4.10: Phase plane diagrams of airfoil response generated with *modified* stall model for 5% chord aft location of C.G. from E.A.
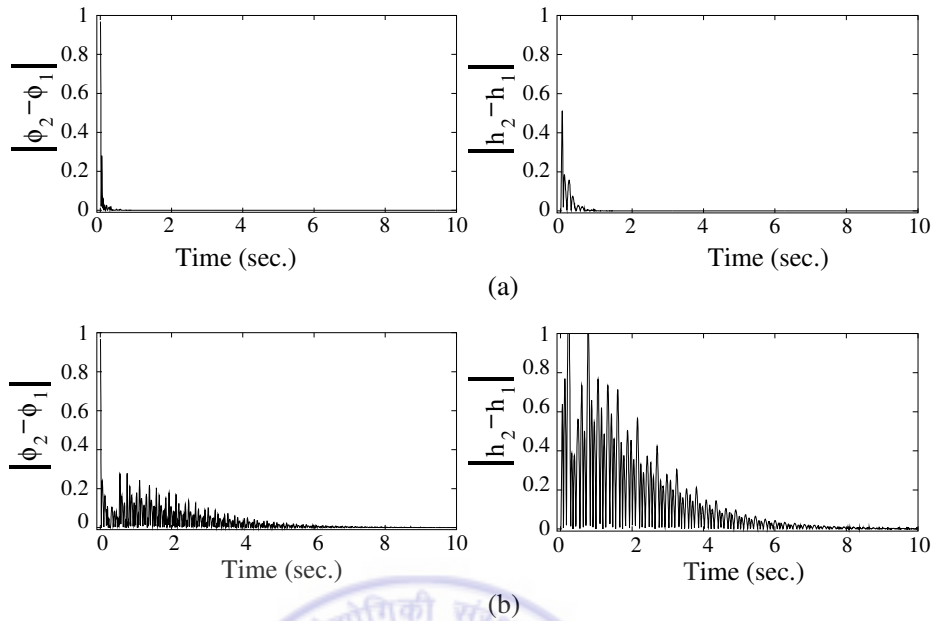
Figure 4.11: Difference of two responses generated at two different initial conditions (a) with *modified* stall model for 0% chord aft location of C.G. from E.A. (b) with *modified* stall model for 3% chord aft location of C.G. from E.A.
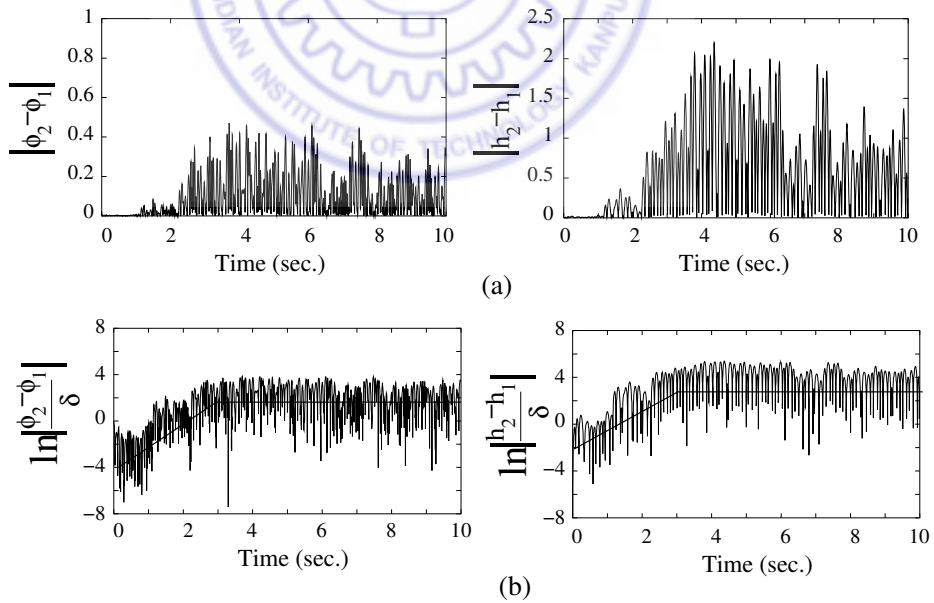
Figure 4.12: (a) Difference of two responses generated at two different initial conditions with *modified* stall model for 5% chord aft location of C.G. from E.A. (b) Liaponov exponent diagrams generated at two different initial conditions with *modified* stall model for 5% chord aft location of C.G. from E.A.
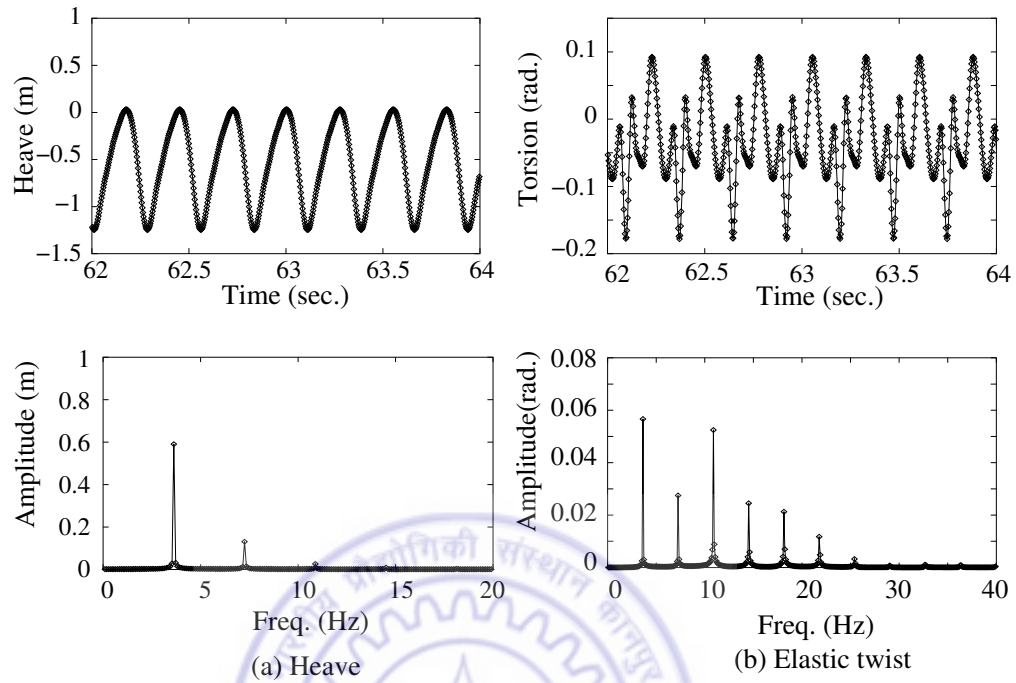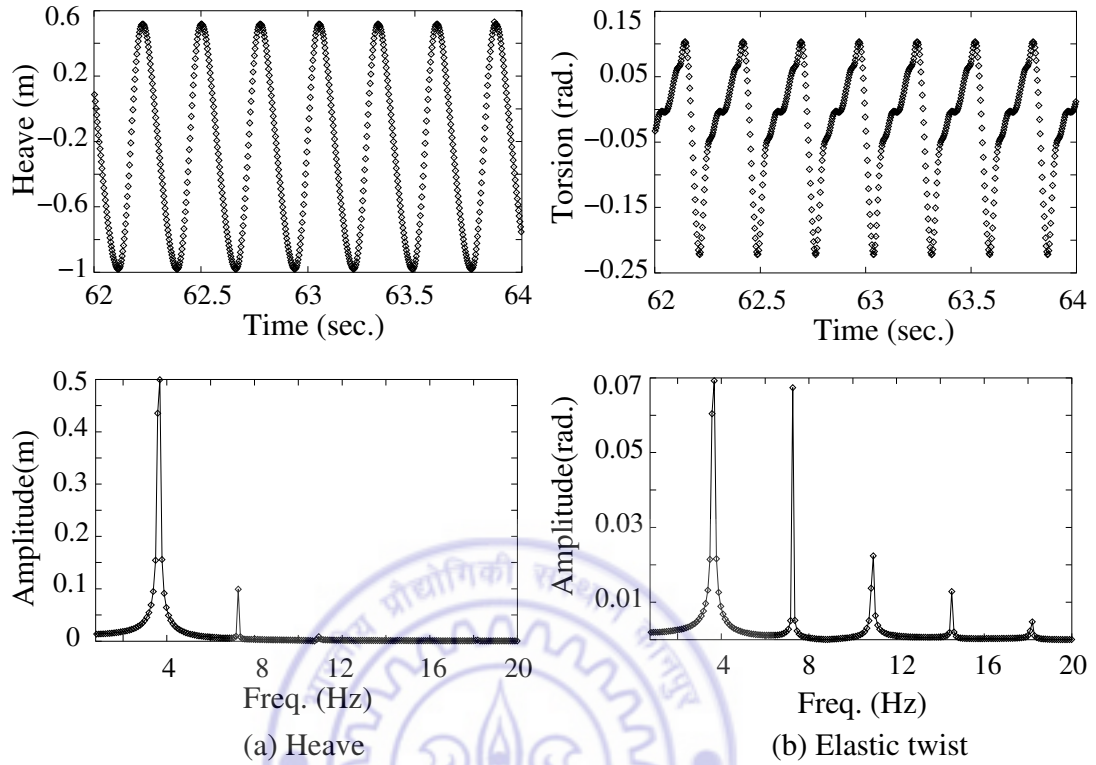
Figure 4.13: Airfoil response and its frequency contents generated with *modified* stall model for 5% chord forward location of C.G. from E.A.
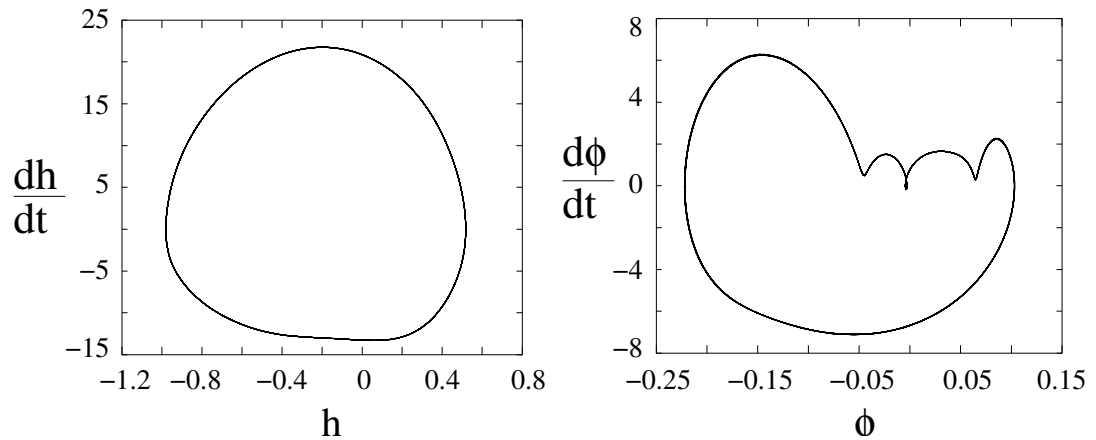
Figure 4.14: Phase plane diagrams of airfoil response generated with *modified* stall model for 5% chord forward location of C.G. from E.A.

121
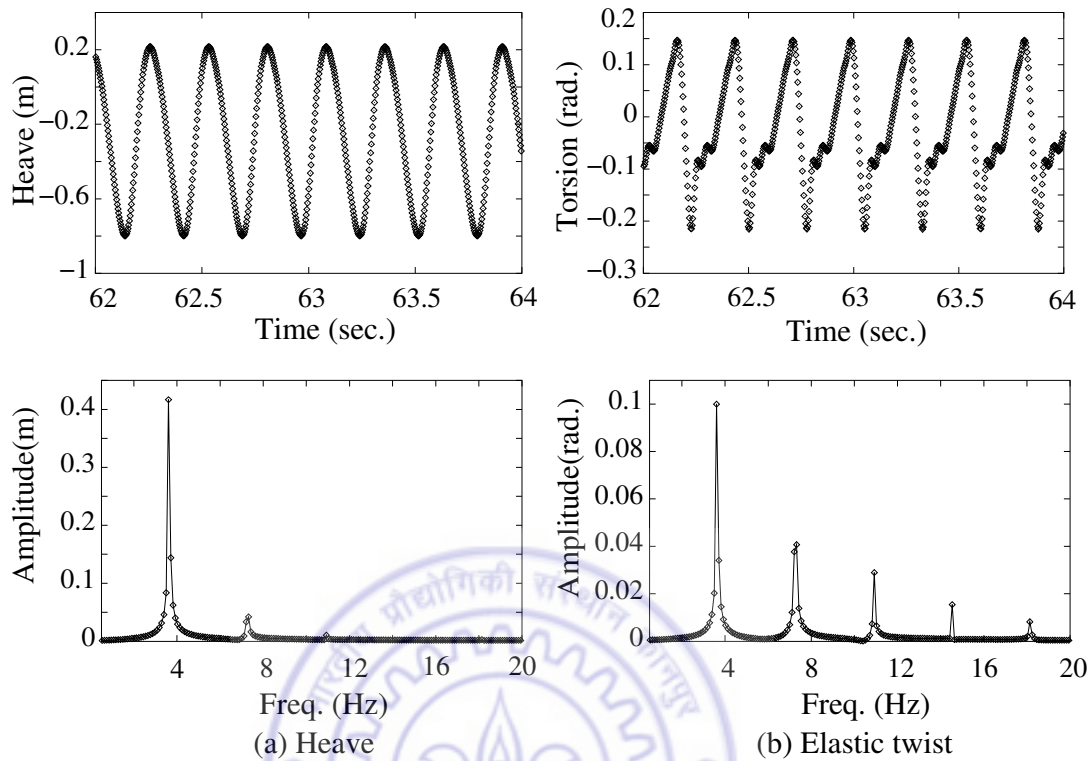
Figure 4.15: Airfoil response and its frequency contents generated with *modified* stall model for 10% chord forward location of C.G. from E.A.
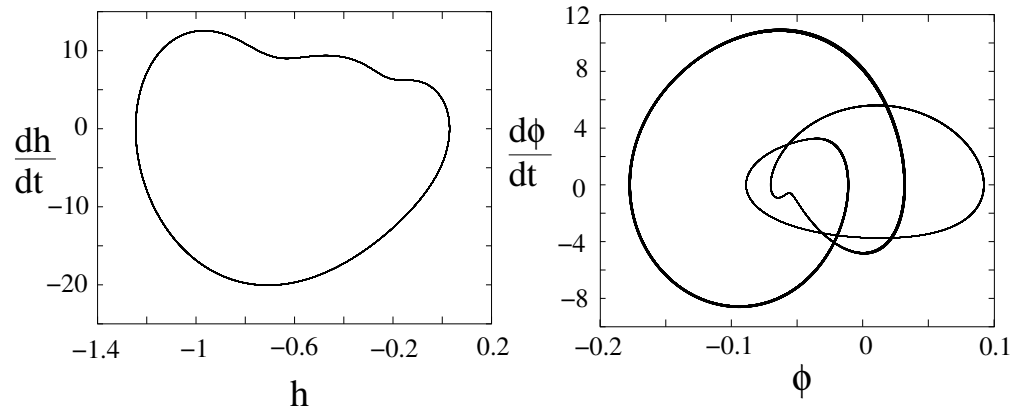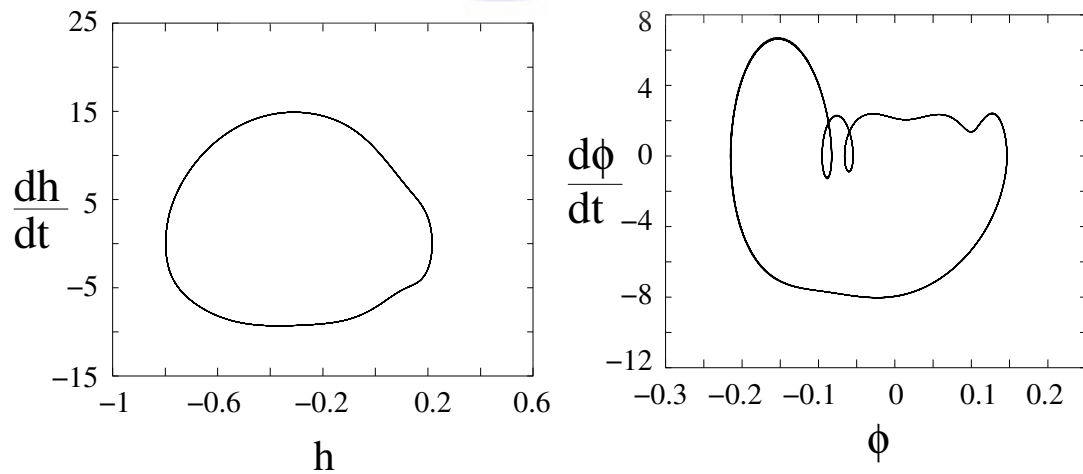

Figure 4.16: Phase plane diagrams of airfoil response generated with *modified* stall model for 10% chord forward location of C.G. from E.A.
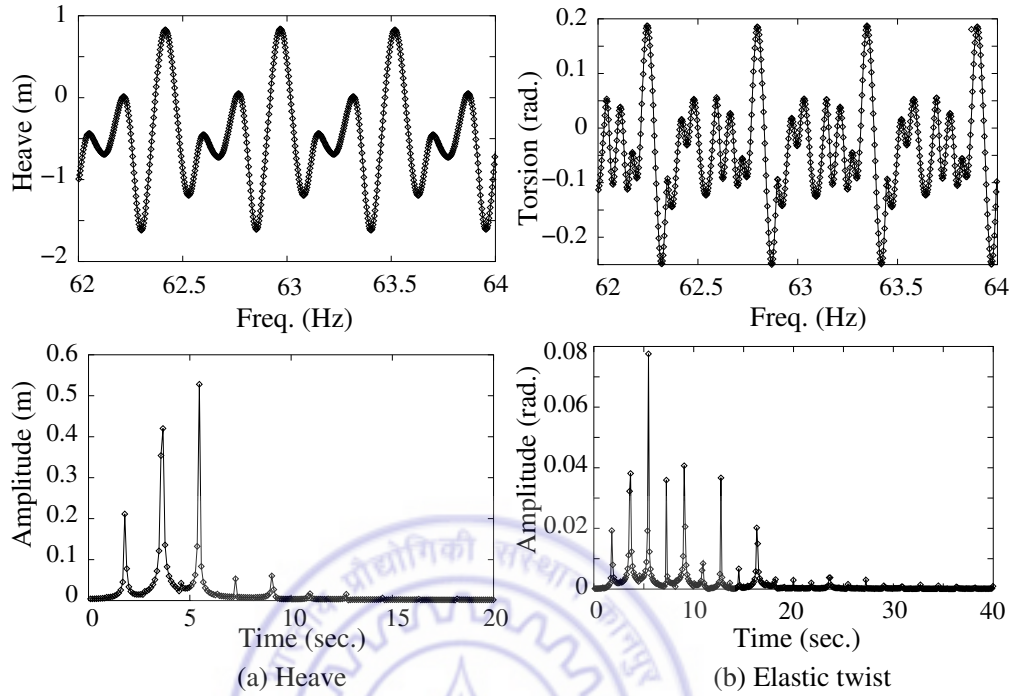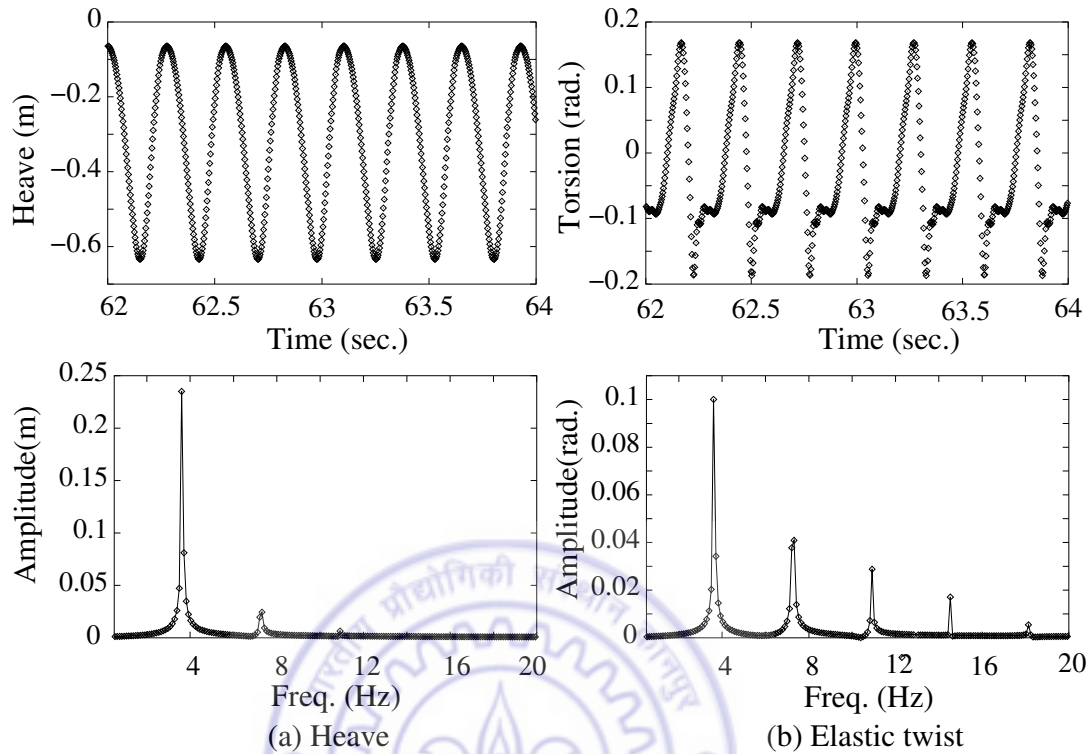
Figure 4.17: Airfoil response and its frequency contents generated with *modified* stall model for 20% chord forward location of C.G. from E.A.
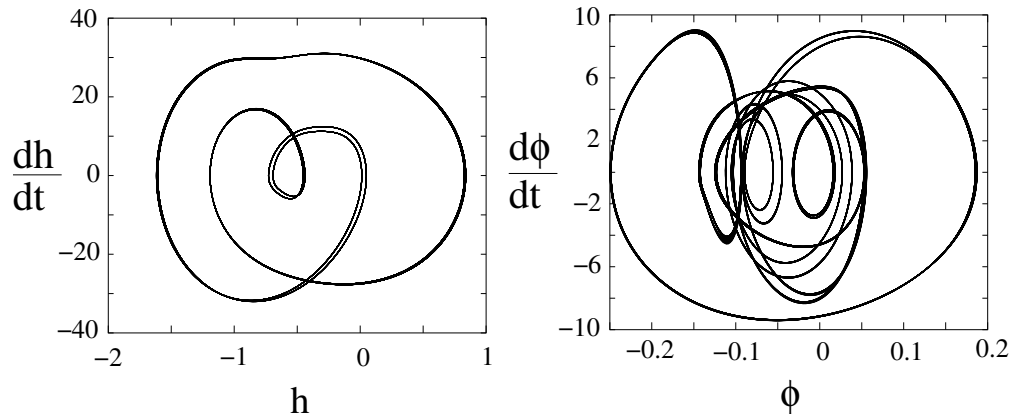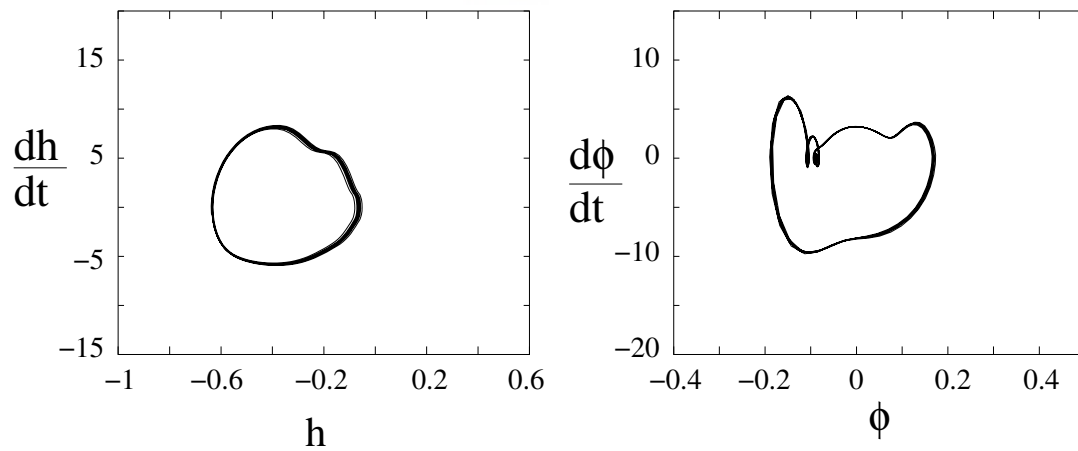

Figure 4.18: Phase plane diagrams of airfoil response generated with *modified* stall model for 20% chord forward location of C.G. from E.A.

123

Chapter 5

HELICOPTER TRIM AND ROTOR BLADE RESPONSE: SOLUTION PROCEDURE

Helicopter trim and response calculation requires all the loads acting on the helicopter system. The loads are due to (i) main rotor system (acting at the rotor hub), (ii) fuselage aerodynamic load, (iii) tail rotor hub loads, (iv) horizontal tail and vertical tail loads and (v) gravity effects. For the sake of clarity, a brief description of the loads acting on various aerodynamic surfaces is given below.

5.1   Main Rotor

Evaluation of aerodynamic loads require the motion of the blade at every instant. The blade response is evaluated in modal space in rotating system. The equations of motion in modal space can be written as:

$$\left[\bar{M}\right]\{\ddot{\eta}\} + \left[\bar{C}\right]\{\dot{\eta}\} + \left[\bar{K}\right]\{\eta\} = \{\bar{F}\} \tag{5.1}$$

where $\{\bar{F}\}$ represents the generalized aerodynamic load acting on the blade.

5.1.1 Inflow Model

The aerodynamic model requires evaluation of rotor inflow as a function of azimuth and radial distance. In this thesis, three types of global inflow models, namely, steady uniform inflow model, Drees model and dynamic wake model, are considered. A brief mathematical description of these models is provided in the following.

(i) Uniform Inflow Model

In this model, the total inflow through the rotor disc is assumed a constant and is given as:

$$\lambda_u = \mu \tan \alpha + \lambda_i \tag{5.2}$$

where

$$\lambda_i = \frac{C_T}{2\sqrt{(\mu^2 + \lambda_u^2)}}$$

(ii) Drees Model

In Drees model, the rotor inflow is a function of both azimuth and radial station. It is given as:

$$\lambda(\bar{r}, \psi) = \mu \tan \alpha + \lambda_i (1 + k_x \bar{r} \sin \psi + k_y \bar{r} \cos \psi) \tag{5.3}$$

where

$$\lambda_i = \frac{C_T}{2\sqrt{(\mu^2 + \lambda_u^2)}}$$

$$k_x = 2\mu$$

$$k_y = \frac{4}{3}[(1 - 1.8\mu^2) \csc \chi - \cot \chi]$$

where χ wake skew angle and it is defined as $\chi = \tan^{-1}(\mu/\lambda_u)$.

(iii) Dynamic Wake Model (Peters-He Model, Ref. 19)

In this model, the total inflow is a function of azimuth, time and radial station. It is given as:

$$\lambda(\bar{r}, t, \psi) = \mu \tan \alpha + \sum_{p=0}^{\infty} \sum_{j=p+1, p+3, \ldots}^{\infty} \phi_j^p(\bar{r})[\alpha_j^p(t) \sin(p\psi) + \beta_j^p(t) \cos(p\psi)] \qquad (5.4)$$

where α_j^p and $\beta_j^p(t)$ are evaluated by solving a set of differential equations.

$$[M]\{\dot{\alpha}_j^p\} + [V][\tilde{L}^c]^{-1}\{\alpha_j^p\} = \frac{1}{2}\{\tau_n^{mc}\} \qquad (5.5)$$

and

$$[M]\{\dot{\beta}_j^p\} + [V][\tilde{L}^s]^{-1}\{\beta_j^p\} = \frac{1}{2}\{\tau_n^{ms}\} \qquad (5.6)$$

In this thesis, a three term approximation (α_1^0, α_2^1 and β_2^1) has been considered.

5.1.2 Sectional Aerodynamic Loads

The sectional aerodynamic loads are evaluated by using either (i) quasi-steady approximation of Greenberg's theory or (ii) *modified* ONERA dynamic stall model applicable for both attached and separated flow. For the sake of clarity, a brief mathematical description of these models is provided.

(i) Quasisteady Greenbergs Model

The quasi-steady approximation of Greenberg's theory provides time variation of lift and moment on an oscillating airfoil. The lift, moment and drag are assumed to be acting at the quarter chord point and the expressions are given below.

Lift acting normal to the resultant flow:

$$L = \frac{1}{2}\rho \tilde{S} b [\pi \dot{W}_0 + \frac{\pi}{2} \dot{W}_1] + \frac{1}{2}\rho \tilde{S} V [2\pi W_0 + 2\pi W_1] \qquad (5.7)$$

126

Unsteady moment on the airfoil is given as:

$$M \quad = \quad \frac{1}{2}\rho\tilde{S}2b[-\frac{\pi}{4}b\dot{W}_0 - \frac{\pi}{4}VW_1 - \frac{3\pi}{16}b\dot{W}_1] \tag{5.8}$$

Drag acting along the resultant velocity:

$$D \quad = \quad \frac{1}{2}\rho\tilde{S}V^2 C_{D_0} \tag{5.9}$$

where W_0 and W_1 are defined as $W_0 = V(\theta + \dot{h}/V)$ and $W_1 = b\dot{\theta}$. The quantities $\dot{h}$, θ and V represent the heaving velocity at the elastic axis, the pitch angle and the oncoming velocity respectively.

(ii) Modified ONERA Dynamic Stall Model

The *modified* dynamic stall model provides time variation of lift, moment and drag on an oscillating airfoil. The stall model assumes that the lift, moment and drag are acting at the quarter chord point. The unsteady lift acting normal to the resultant velocity is given as:

$$L \quad = \quad \frac{1}{2}\rho\tilde{S}[sb\dot{W}_0 + kb\dot{W}_1 + V\Gamma_1 + V\Gamma_2] \tag{5.10}$$

where Γ_1, Γ_2 are evaluated using the following equations

$$\ddot{\Gamma}_1 + B_2(\frac{V}{b})\dot{\Gamma}_1 + B_3(\frac{V}{b})^2\Gamma_1 \quad = \quad A_3(\frac{V}{b})^2\frac{\partial Cz_L}{\partial\theta}W_0 + A_3\sigma(\frac{V}{b})^2W_1$$
$$+ A_2(\frac{V}{b})\frac{\partial Cz_L}{\partial\theta}\dot{W}_0 + A_2(\frac{V}{b})\sigma\dot{W}_1$$
$$+ A_1\frac{\partial Cz_L}{\partial\theta}\ddot{W}_0 + A_1\sigma\ddot{W}_1$$
$$\ddot{\Gamma}_2 + a_l(\frac{V}{b})\dot{\Gamma}_2 + r_l(\frac{V}{b})^2\Gamma_2 \quad = \quad -[r_l(\frac{V}{b})^2V\Delta Cz|_{W_0/V} + E_l(\frac{V}{b})\dot{W}_0]$$

The unsteady moment on the airfoil is given as:

$$M \quad = \quad \frac{1}{2}\rho\tilde{S}2b[V^2 C_{m_L}|_{W_0/V} + (\bar{\sigma}_m + d_m)b\dot{W}_0 + \sigma_m VW_1 + s_m b\dot{W}_1 + V\Gamma_{m2}] \tag{5.11}$$

127

where Γ_{m2} is evaluated using the following equation.

$$\ddot{\Gamma}_{m2} + a_m(\frac{V}{b})\dot{\Gamma}_{m2} + r_m(\frac{V}{b})^2\Gamma_{m2} = -[r_m(\frac{V}{b})^2 V \Delta Cm|_{W_0/V} + E_m(\frac{V}{b})\dot{W}_0]$$

The unsteady drag acting along the resultant velocity is given as:

$$D = \frac{1}{2}\rho\tilde{S}[V^2 C_{d_L}|_{W_0/V} + \sigma_d b\dot{W}_0 + V\Gamma_{d2}] \qquad (5.12)$$

where Γ_{d2} is evaluated using the following equation

$$\ddot{\Gamma}_{d2} + a_d(\frac{V}{b})\dot{\Gamma}_{d2} + r_d(\frac{V}{b})^2\Gamma_{d2} = -[r_d(\frac{V}{b})^2 V \Delta Cd|_{W_0/V} + E_d(\frac{V}{b})\dot{W}_0]$$

where $\Delta Cz|_{W_0/V}, \Delta Cm|_{W_0/V}$, and $\Delta Cd|_{W_0/V}$ are the difference between the linear static aerodynamic coefficient extrapolated to the stalled region to actual static aerodynamic coefficient of lift, moment and drag respectively, measured at an effective angle of attack W_0/V. The quantities, $C_{m_L}|_{W_0/V}$ and $C_{d_L}|_{W_0/V}$ are the static moment and drag coefficients in linear regime measured at an effective angle of attack, W_0/V. Figs. 5.1 - 5.3 provide the measured aerodynamic coefficients and the extrapolated coefficients along with the definition of $\Delta Cz|$, $\Delta Cm|$, and $\Delta Cd|$. Since, the data is given over 360 degs. angle of attack, this model can be used in reverse flow regions involving large angles of attack.

Five different combinations of aerodynamic models have been proposed and the influence of each one of these models on the trim and response characteristics of helicopter rotor in forward flight is analysed systematically. The five aerodynamic models are:

- quasi-steady aerodynamic theory (Eqs. 5.7 - 5.9) combined with uniform inflow model (Eq. 5.2) (QSUI),

- quasi-steady aerodynamic theory (Eqs. 5.7 - 5.9) combined with Drees model (Eq. 5.3) (QSDR),

128

- quasi-steady aerodynamic theory (Eqs. 5.7 - 5.9) combined with dynamic wake model (Eq. 5.4) (QSDW),

- *modified* ONERA stall model (Eqs. 5.10 - 5.12) combined with Drees model (Eq. 5.3) (DSDR); and

- *modified* ONERA stall model (Eqs. 5.10 - 5.12) combined with dynamic wake model (Eq. 5.4) (DSDW).

It may be noted that while describing the results only the abbreviations of the aerodynamic models are used for convenience.

The distributed inertia forces and moments per unit length can be obtained from Eq. 2.28. Sectional aerodynamic loads are evaluated using either Eqs. 5.7 - 5.9 or 5.10 - 5.12. By summing up all the inertia and aerodynamic loads and integrating over the length of the blade, one can obtain the root loads. The root loads of all four rotor blades are added to obtain hubloads (H, Y, T, M_x, M_y and M_z). Mean values of the hub loads are represented by $H_0, Y_0, T_0, M_{x0}, M_{y0}$ and M_{z0}.

5.1.3 Tail Rotor

The thrust generated by the tail rotor is derived using combined blade element and momentum theory. The tail rotor thrust acts normal to the tail rotor plane and in a direction providing compensation to the torque of the main rotor.

Tail rotor thrust is given by (Ref. [189]):

$$T_T \quad = \quad C_{T_t}[\rho \pi R_t^2 (\Omega_t R_t)^2] \tag{5.13}$$

where the coefficient of tail rotor thrust C_{T_t} is defined as:

$$C_{T_t} \quad = \quad \frac{\sigma_t a}{2}[\frac{\theta_{0T}}{3}(1 + \frac{3}{2}\mu^2) - \frac{\lambda_t}{2}]$$

129

and tail rotor inflow is given by

$$\lambda_t = \frac{C_{T_t}}{2\sqrt{\mu^2 + \lambda_t^2}}.$$

5.1.4 Horizontal Tail

The horizontal tail is assumed to provide only aerodynamic lift. Lift is assumed as a point load acting at the quarter chord of the horizontal tail. The lift on horizontal tail is given as:

$$T_{HT} = \frac{1}{2}\rho s_h V_{HT}^2 C_{l\theta_{ht}}\theta_{ht} \tag{5.14}$$

where s_h is surface area and V_{HT} is oncoming velocity, which is defined as:

$$V_{HT} = \begin{cases} \mu\Omega R & \mu < 0.05 \\ (\sqrt{\mu^2 + (1.8\lambda)^2})\Omega R & \mu \geq 0.05 \text{ main rotor downwash effect is added} \end{cases}$$

θ_{ht} is angle of attack and it is taken as -2 deg.

5.1.5 Vertical Tail

Vertical tail is assumed to provide a side force due to its lift. The load on vertical tail is obtained by using the static lift equation which is given below.

$$T_{VT} = \frac{1}{2}\rho s_v V_{VT}^2 C_{l\theta_{vt}}\theta_{vt} \tag{5.15}$$

where s_v is surface area and θ_{vt} is angle of attack and it is taken as 1.5 deg. The term V_{VT} it is the oncoming velocity and is defined as:

$$V_{VT} = \mu\Omega R$$

5.1.6 Fuselage Drag

Fuselage drag force is proportional to the square of the velocity and the frontal area. Fuselage drag can be evaluated by using following expression.

$$D = \frac{1}{2}\rho V_F^2 f C_d \tag{5.16}$$

where f is the equivalent frontal cross sectional area of the helicopter fuselage, C_d is drag coefficient taken as 1.0 and V_F is the oncoming velocity given as:

$$V_F = \mu \Omega R$$

Figure 5.4 shows the loads and orientation of the helicopter in flight. Transfering all the forces and moments due to main rotor, tail rotor, horizontal tail, vertical tail and fuselage drag to centre of gravity (CG) of the helicopter and equating to the components of the gravitational load, the equilibrium equations are obtained. In this thesis, only steady level flight conditions are considered; and hence inertia effects due to maneuver are not included. The force and moment equilibrium equations are given as:

$$
\begin{aligned}
H_0 + D\cos\alpha &= W\sin\Theta\cos\Phi \\
Y_0 + T_T + T_{VT} &= W\sin\Phi \\
T_0 + T_{HT} - D\sin\alpha &= W\cos\Theta\cos\Phi \\
M_{x0} - Y_0 z_{MR} + T_0 y_{MR} - (T_T z_{TR} + T_{VT} z_{VT}) + T_{HT} y_{MR} &= 0.0 \\
M_{y0} - T_0 x_{MR} + H_0 z_{MR} - T_{HT} x_{HT} &= 0.0 \\
M_{z0} + Y_0 x_{MR} - H_0 y_{MR} + (T_T x_{TR} + T_{VT} x_{VT}) &= 0.0
\end{aligned}
\tag{5.17}
$$

where $\Theta = \alpha - \theta_{FP}$. Trim variables ($\theta_0, \theta_{1c}, \theta_{1s}, \theta_{0T}, \Theta$ and Φ) can be obtained by solving the above nonlinear algebraic equations (Eq. 5.17).

5.2 Solution Procedure

The solution technique aims to obtain helicopter trim and blade response simultaneously by solving the three sets of equations in time domain, namely, (i) equations representing the elastic deformations of the rotor blade (Eq. 5.1), (ii) equations representing the inflow through the rotor disc (Eq. 5.2 or 5.3 or 5.4) and (iii) sectional aerodynamic loads representing lift, drag and moment acting on the rotor blade (Eqs. 5.7 - 5.9 or Eqs. 5.10 - 5.12). For the aerodynamic models QSUI, QSDR and QSDW, the sectional aerodynamic loads are represented by algebraic expressions given in Eqs. 5.7 - 5.9. Whereas, for the aerodynamic models DSDR and DSDW, the sectional aerodynamic loads have to be obtained by solving a set of differential equations in time domain given in Eqs. 5.10 - 5.12. Similarly for the aerodynamic models involving time varying inflow, *i.e.*, QSDW and DSDW, the inflow variables (α_1^0, α_2^1 and β_2^1) have to be obtained by solving the set of differential equations given in Eqs. 5.5 and 5.6. Of the five models used in this study, DSDW model is computationally more intensive than the other models. In this model, the time varying inflow, sectional aerodynamic loads and the blade response have to be solved by three sets of coupled ordinary differential equations, at every time step. A description on the number of variables for DSDW aerodynamic model is given in the following.

The aerodynamic loads acting on the blade are evaluated at 15 radial stations (starting from 0.25R to 0.95R with an increment of 0.05R) for each blade. Hence, there are in total 45 variables representing lift, drag and moment coefficients for one blade. It may be noted (from Eqs. 5.10-5.12) that there are four state variables for lift, two state variables each for drag and moment. Therefore, the total number of state variables representing the sectional aerodynamics for one blade is 120 (15 radial stations × 8 state variables per stations). The rotor blade structural model is represented by eight modes consisting of four flap modes, two lag modes, one torsion mode and one axial mode. Hence, the total number of state variables representing

structural modes per blade is 16. The time varying inflow is given by three state variables. Therefore, for a four bladed rotor system, there are in total 547 state variables (480 aerodynamic state variables + 64 structural state variables + three state variables for dynamic wake effects). In the present study, a four bladed system with proper spacing in the azimuth angle is considered for the analysis. By solving the response of all the blades simultaneously, one can identify the difference in the response of the blades as they go around the azimuth. Since, the response and loads of all the blades are solved at every instant of time, the time varying hub loads and the time varying inflow (dynamic wake effects) can be captured.

5.2.1 Flow Chart and Algorithm

A propulsive trim procedure has been adopted to obtain the main rotor control angles, tail rotor collective angle, fuselage roll and pitch attitudes. A fourth order Runge-Kutta integration scheme with a time step $\Delta t = 0.0025$ sec., has been used for solving the differential equations. Flow chart for calculation of helicopter trim and rotor response is shown in the Fig. 5.5. The steps involved in the evaluation of trim and response using DSDW model (which is computationally intensive as compared to other four models) are described below. These steps get simplified appropriately while using the other four models, namely, QSUI, QSDR, QSDW and DSDR.

1. For a given data including flight condition, evaluate mean rotor inflow based on all-up weight.

2. Assume initial values for trim variables ($\theta_0, \theta_{1c}, \theta_{1s}, \theta_{0T}, \Theta$ and Φ) and initial conditions for blade response.

3. Knowing rotor inflow and blade response and obtain the sectional aerodynamic loads for all the blades, by solving the dynamic stall equations.

4. Then using the sectional blade loads, the response of individual blades and rotor

133

inflow variables are obtained simultaneously for the next time step, using blade equations and dynamic wake equations respectively.

5. Next, by using the blade response and inflow, go to step 3. This iteration is performed for about 40-50 rotor revolutions till convergence in the blade response and inflow variables are obtained.

6. Using the converged blade response, the blade root loads and hub loads are obtained.

7. Then transfer the mean values of rotor hub loads, loads from horizontal tail, vertical tail, tail rotor and fuselage to the CG to satisfy the trim equations (Eq. 5.17).

8. Evaluate improved trim variables using Newton-Raphson technique.

9. Go to step 2. The iterations are continued till convergence in trim variables achieved. The convergence criterion is based on satisfying the condition that the difference in each trim setting between two successive iterations must be less than 0.002%.

5.3   Summary

In this chapter, the consolidated set of equations representing blade dynamics, rotor inflow and sectional aerodynamics are presented. Five different combinations of aerodynamic models have been proposed. The complete set of trim equations are provided. The iterative computational solution technique developed for trim and response analysis is described.
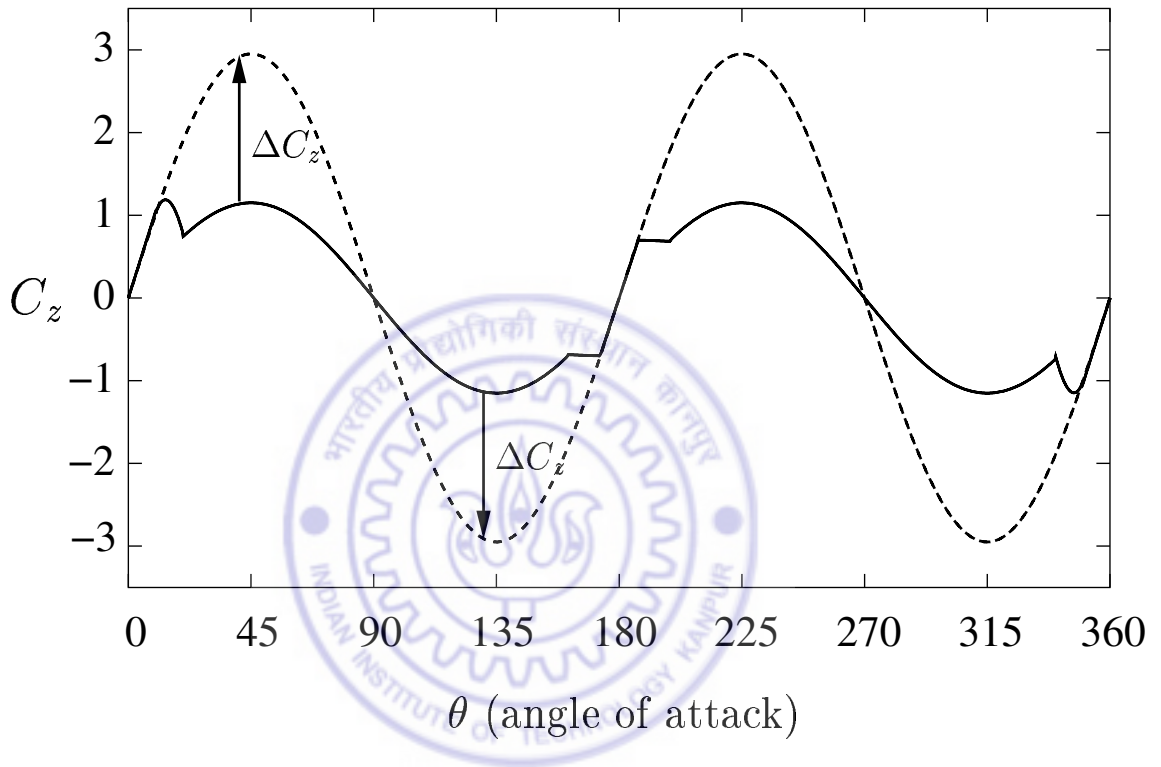
Figure 5.1: Definition of ΔC_z
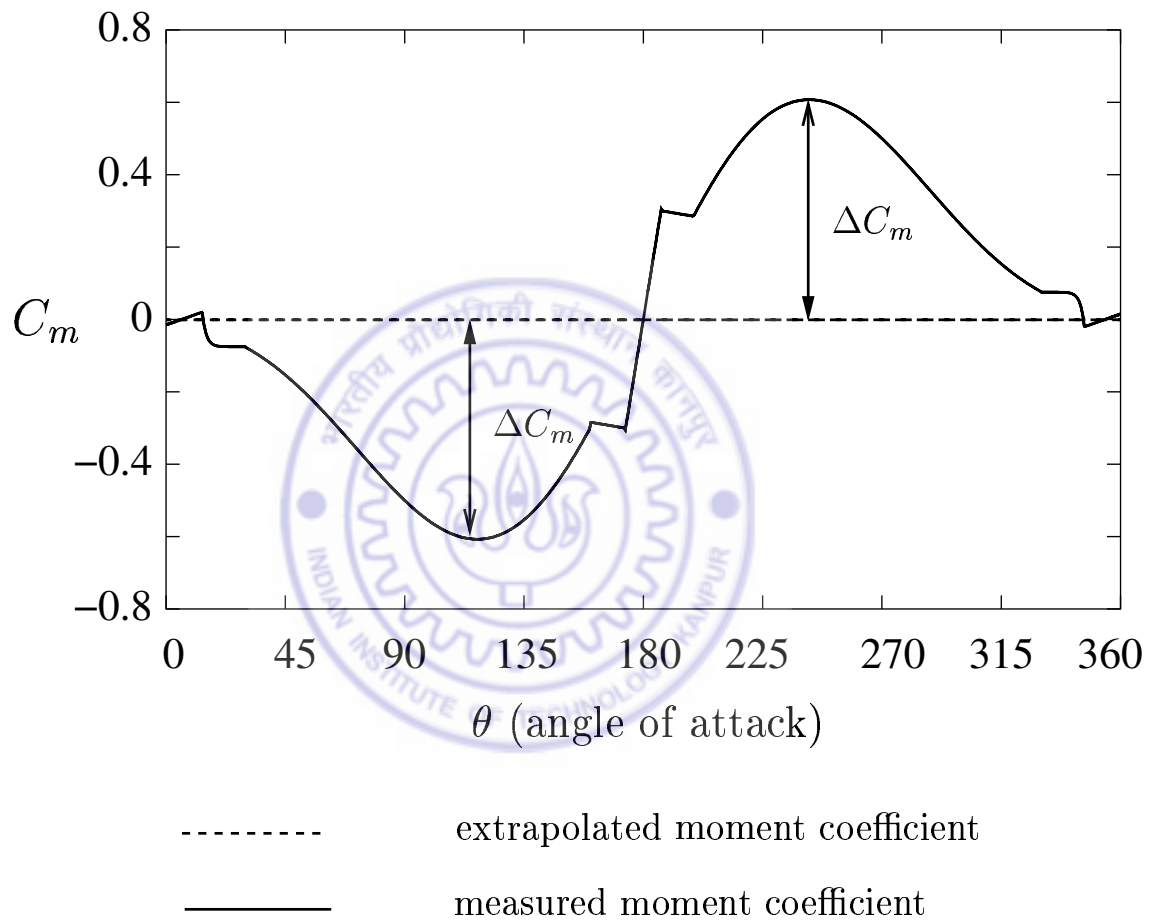
Figure 5.2: Definition of ΔC_m

Figure 5.3: Definition of ΔC_d

(a) Side view

$$\Theta = \alpha - \theta_{FP}$$

(b) Front view
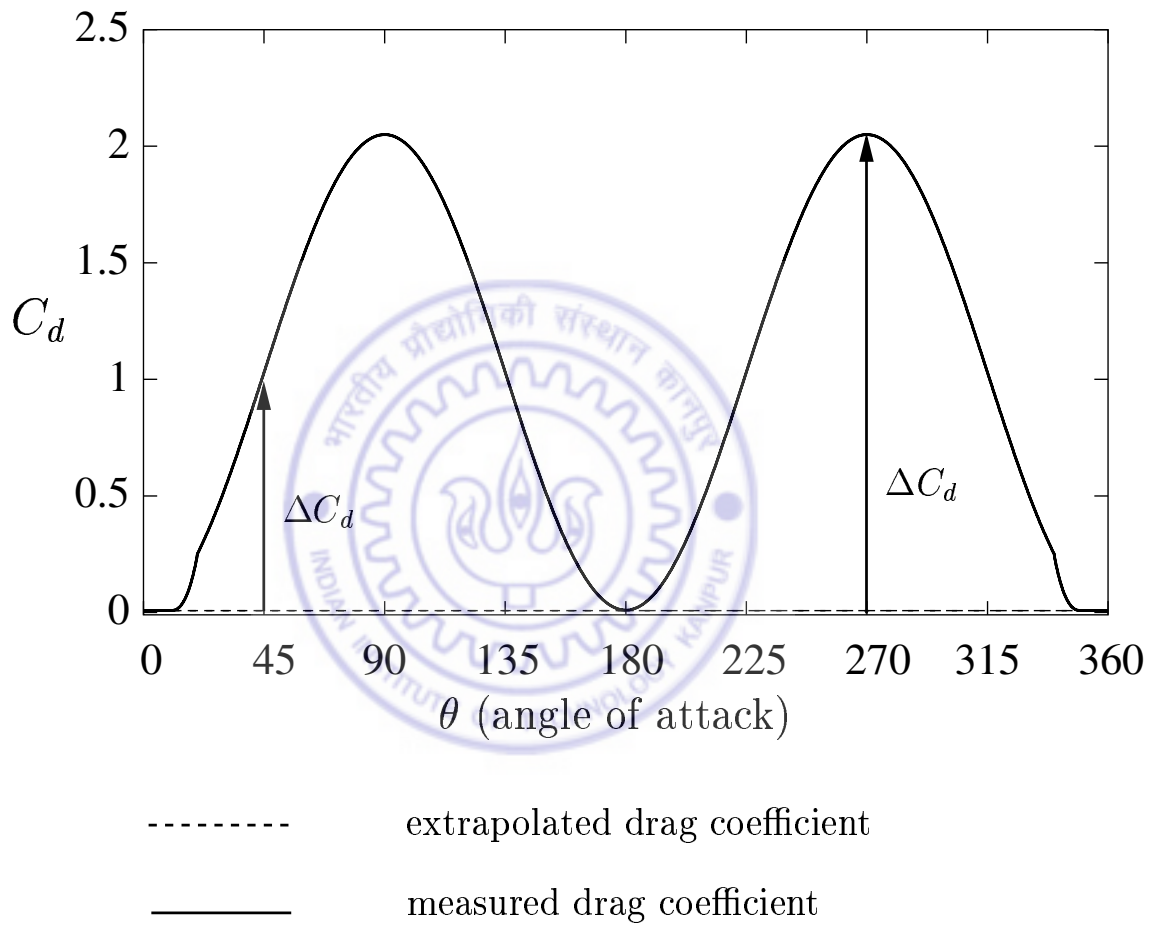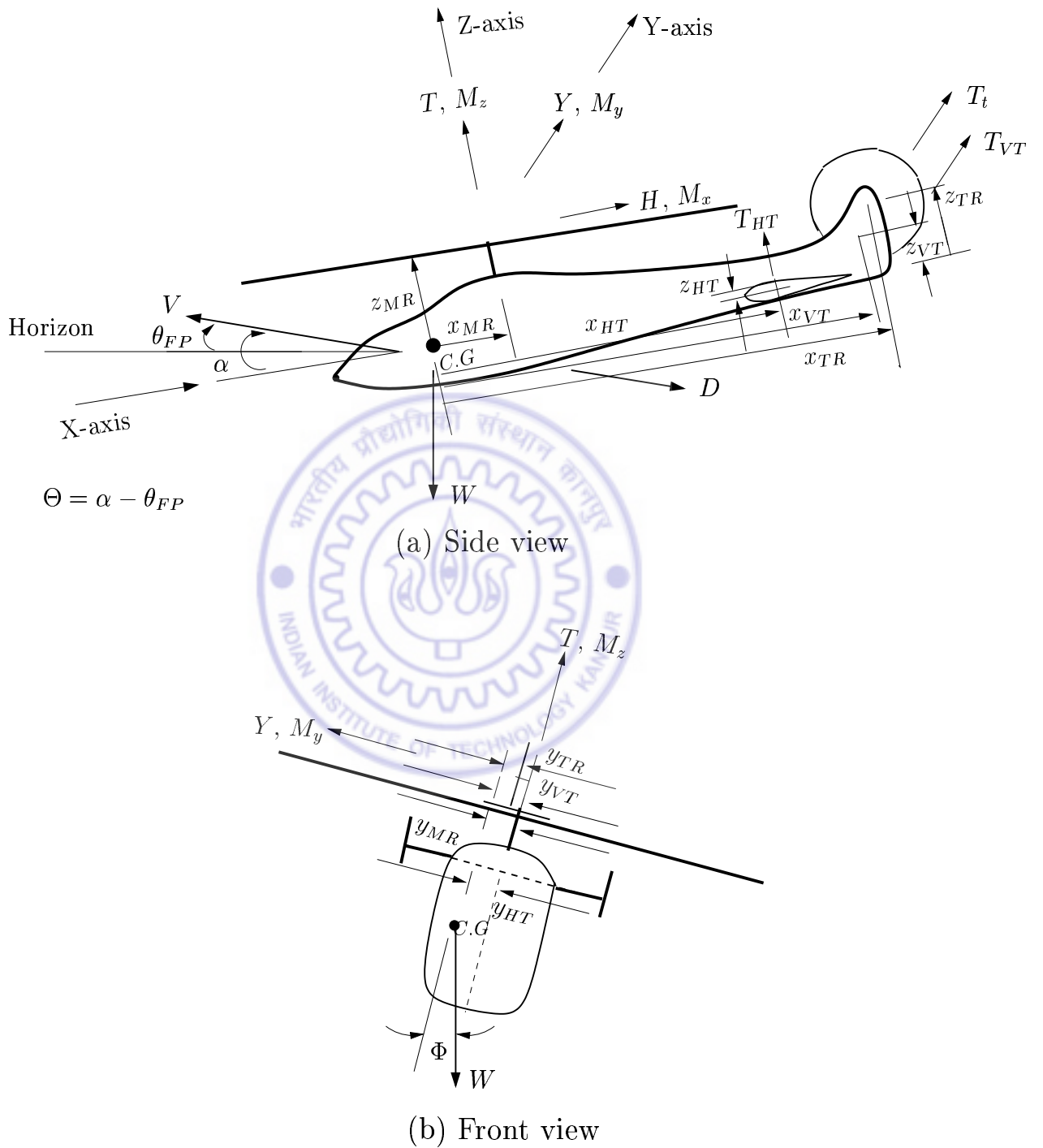
Figure 5.4: Loads and orientation of the helicopter
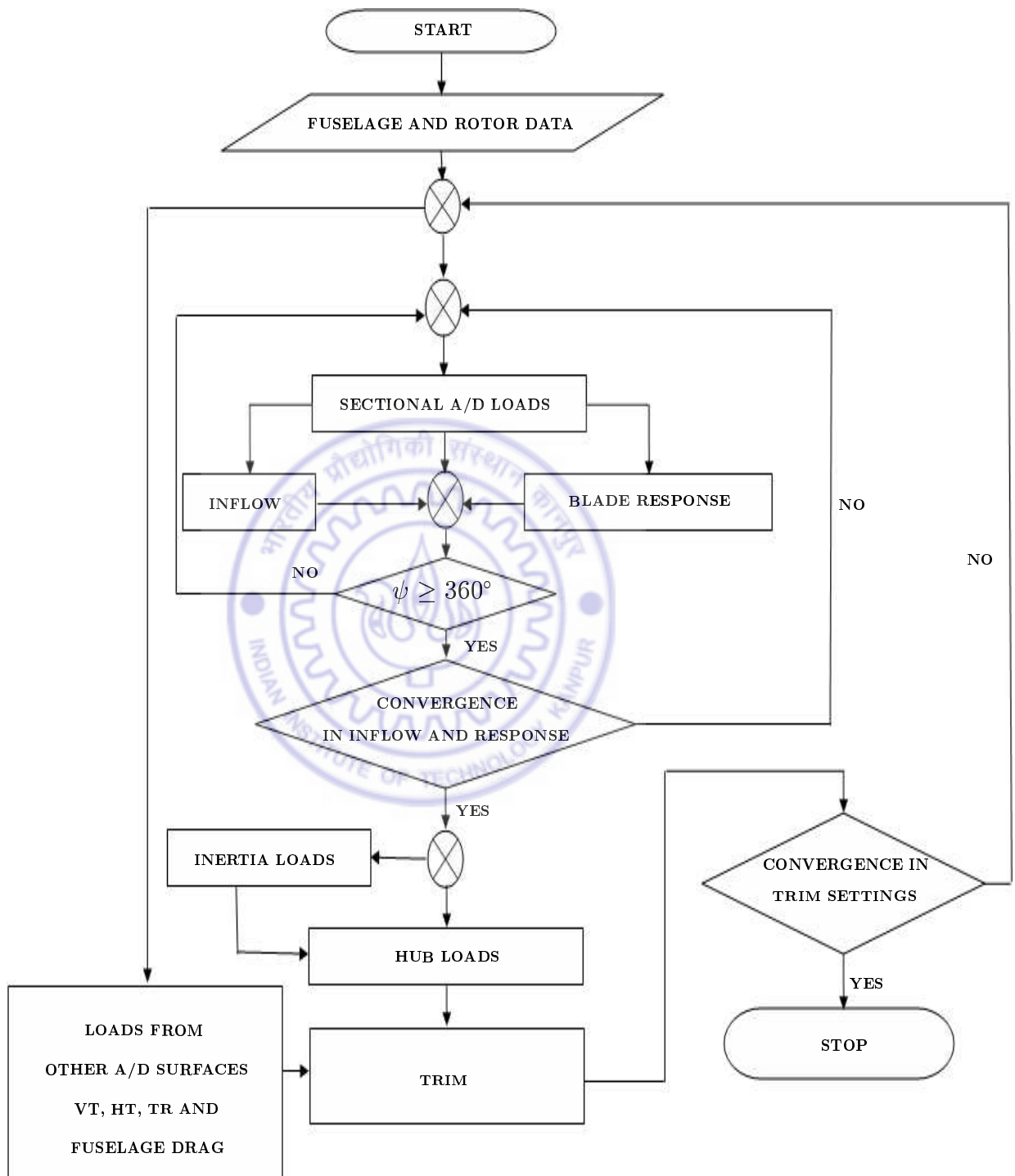
VT — Vertical Tail; HT — Horizontal Tail; TR — Tail Rotor

Figure 5.5: Flow chart for calculation of helicopter trim and rotor response

Chapter 6

HELICOPTER TRIM AND ROTOR BLADE RESPONSE: RESULTS AND DISCUSSION

6.1 Introduction

Using the solution technique described in Chapter 5, helicopter trim and aeroelastic response of the rotor blades are analysed for different cases to bring out: (i) the effect of aerodynamic modeling and (ii) the influence of structural couplings due to blade pretwist. Two sets of results are presented in the following. One set of results pertains to untwisted straight blade and the other set of results corresponds to a pretwisted blade configuration. Even though the response of all the blades in the rotor system is evaluated independently, for conciseness, in the description of the results only the response and loads of blade-1 (reference blade) are presented. The geometric description of the helicopter is shown in Fig. 6.1. The main rotor blade is modeled as a soft-in plane hingeless rotor blade with eight elastic modes representing four flap, two lag, one torsion and one axial modes. The rotor system consists of four blades. The data used in the present study are given in Tables 6.1 and 6.2.

6.1.1   Untwisted Straight Blade

Using the five different aerodynamic models (QSUI, QSDR, QSDW, DSDR and DSDW), helicopter trim and blade response are evaluated for different forward speed conditions. The variation of control angles $(\theta_0, \theta_{1c}, \theta_{1s}, \theta_{0T})$ and the fuselage attitude in pitch (Θ) and roll (Φ) with forward speed are shown in Fig. 6.2. From Fig. 6.2a, it can be seen that the magnitude of the collective pitch angle (θ_0) is affected by the aerodynamic models used in the analysis. However, at high forward speeds $(\mu > 0.25)$, the aerodynamic models do not significantly influence the collective pitch angle. It is observed that the models with dynamic wake (QSDW and DSDW) require high collective pitch setting at low forward speeds than the other aerodynamic models. For hover, the variation in the collective pitch angle for all these models is of the order 0.75 deg. A similar observation can be made for the tail rotor collective pitch (θ_{0T}) as shown in Fig. 6.2d.

The variation of the lateral cyclic control angle (θ_{1c}) with forward speed is shown in Fig. 6.2b. From the figure, it can be seen that inclusion of Drees model with quasi-steady aerodynamics (QSDR) increases the control angle in the transition zone (*i.e.*, in the range $\mu = 0.05$ to 0.075). The increase is more pronounced if dynamic wake model is used (QSDW) instead of Drees model. In this transition zone, dynamic stall model has very little effect but as μ increases dynamic stall model shows more reduction in control angle as compared to quasi-steady aerodynamics. This type of sharp rise and fall in the variation of θ_{1c} obtained with DSDW model qualitatively resembles the flight data presented in Ref. [191] (shown in Fig. 6.3). Dynamic stall models require more longitudinal cyclic control angle (θ_{1s}) at high forward speeds as can be seen in Fig. 6.2c. The equilibrium roll angle of the helicopter (as observed in Fig. 6.2e) is larger for QSUI model as compared to other four aerodynamic models. The equilibrium roll angle is the least for the two dynamic wake models DSDW and QSDW; and the roll angles are found to be almost the same for these two models. It

is interesting to note from Fig. 6.2f that the pitch attitude of the helicopter shows a monotonic increase with forward speed; but at high forward speeds there is a slight reduction in the pitch angle for the two dynamic stall models DSDR and DSDW.

The reason for the observed sharp rise and fall in lateral cyclic control angle as shown in Fig. 6.2b, can be explained by analyzing the inflow variables. For the sake of comparison, a new set of common inflow parameters λ_0, λ_{1c} and λ_{1s} has been introduced. In Drees model, these parameters denote $\lambda_0 = \lambda_i$, $\lambda_{1c} = \lambda_i k_y$ and $\lambda_{1s} = \lambda_i k_x$. In the dynamic wake model, the parameters are equal to $\lambda_0 = \sqrt{3} \, \alpha_1^0$, $\lambda_{1c} = \sqrt{15/2} \, \alpha_2^1$ and $\lambda_{1s} = \sqrt{15/2} \, \beta_2^1$. Figure 6.4 shows the variation of inflow variables for DSDR and DSDW models, in the transition zone ($\mu = 0.075$). The collective inflow (λ_0) predicted by the two models are close to each other and it is around 0.04. The lateral variation of inflow (λ_{1s}) is one order smaller than the longitudinal (λ_{1c}) and collective inflow quantities. Dynamic wake model (DSDW) predicts the longitudinal inflow as $\lambda_{1c} = 0.055$, which is much higher than that predicted by Drees model DSDR (λ_{1c}=0.03). Because of the high value of λ_{1c}, a high value of θ_{1c} is required for equilibrium with DSDW model as compared to DSDR model. The inflow variables at high forward speed ($\mu = 0.3$) are shown in Fig. 6.5 for DSDR and DSDW models. The collective inflow λ_0 predicted by the two models are almost equal and it is around 0.01. Lateral variation of inflow λ_{1s} is one order smaller than λ_0 and λ_{1c}. The inflow variable λ_{1c} is reduced as compared to the values obtained for $\mu = 0.075$. Because of the reduction in the value of λ_{1c} at high forward speeds, the lateral cyclic control angle also shows a reduction at high speeds as can be seen in Fig. 6.2b.

The variation of sectional aerodynamic loads and tip response of the rotor blades as a function of azimuth are evaluated using all the five aerodynamic models. Sectional aerodynamic loads at various radial stations are shown in Figs. 6.6 - 6.10. Sectional aerodynamic lift, moment and drag at 50%R are shown respectively in Figs. 6.6a -

142

6.6c, for one blade as it goes around the azimuth, for an advance ratio $\mu = 0.35$. From Fig. 6.6a, it can be seen that the minimum value of the sectional lift force is different in both advancing and retreating sides for quasi-steady aerodynamic model to that of dynamic stall model. Figure 6.6b shows that dynamic stall models (DSDR and DSDW) increase the variation in drag force particularly in the azimuth location $200 < \psi < 340$ deg. From Fig. 6.6c, it is observed that the sectional moment shows large variation in amplitude with dynamic stall models (DSDR and DSDW) as compared to quasi-steady aerodynamic models (QSUI, QSDR and QSDW). For the radial station $65\%R$ (Fig. 6.7), it can be seen that lift variation is not significantly influenced by aerodynamic modeling (Fig. 6.7a); however, sectional drag force shows considerable variation with respect to aerodynamic modeling (Fig. 6.7b); and torsional moment is significantly affected by dynamic stall models (Fig. 6.7c). Figure 6.8 shows the sectional lift, drag and moment at radial station $75\%R$. The variation of sectional lift (Fig. 6.8a) shows that the phase angle at which the minimum lift occurs in the advancing side, for the five aerodynamic models is: $\psi = 99$ deg. for QSUI and QSDR model, $\psi = 105$ deg. for QSDW model and $\psi = 111$ deg. for DSDR and DSDW model. This result indicates that inclusion of dynamic stall shifts the azimuth angle to a higher value in the advancing side. This observation on the occurence of minimum lift near $\psi = 115$ deg. is consistent with the flight test data presented in Ref. [176]. In the retreating side dynamic stall models (DSDR and DSDW) give a slightly higher lift force than quasi-steady models. In the case of sectional drag force (Fig. 6.8b), all the five models predict similar variation with azimuth except for the DSDR model in the azimuth range $300 < \psi < 360$ deg. From Fig. 6.8c, it can be seen that dynamic stall models provide a large variation in sectional moment compared to the other three aerodynamic models. However, in the azimuth range $300 < \psi < 360$ deg. DSDR model predicts a large value of nose-down moment compared to DSDW model. Sectional aerodynamic loads at 85%R and 95%R are

shown in Figs. 6.9 and 6.10, respectively. From Figs. 6.9a and 6.10a, it can be seen that the minimum value of the sectional lift force is almost the same in both advancing and retreating sides for those cases with dynamic stall models (DSDR and DSDW); but it is different for the quasi-steady aerodynamic models (QSUI, QSDR and QSDW). From Figs. 6.9b and 6.10b, it is observed that the sectional drag shows a large variation in retreating side ($240 < \psi < 360$ deg.) for dynamic stall models as compared to quasi-steady aerodynamic models. Figures 6.9c and 6.10c show that dynamic stall models introduce a large variation in torsional moment as compared to quasi-steady aerodynamic models.

Figure 6.11 shows the tip response of the blade in flap, lag and torsional modes in $4K$-system. It can be seen that dynamic stall models have a moderate influence on the flap response (Fig. 6.11a); and increases the lag response over the azimuth except in the range $140 < \psi < 190$ deg. (Fig. 6.11b). It may be noted that the lag response is having a positive value in the $4K$-system. If the flap and lag deformations are converted in the hub fixed rotating $1K$-system, the lag response will be a negative quantity. The torsional response of the blade significantly increases due to dynamic stall effects, as evident from Fig. 6.11c. The dynamic stall also introduces additional harmonics in the torsional response of the blade.

The variation of hub loads over one revolution is shown in the Fig. 6.12. For the sake of clarity, only the results pertaining to quasi-steady and uniform inflow (QSUI) model and more sophisticated dynamic stall and dynamic wake (DSDW) model, for an advance ratio $\mu = 0.35$ are discussed. Response of hub loads (longitudinal force (H), lateral force (Y), thrust (T), roll (Mx), pitch (My) and yaw (Mz) moments) are shown in Fig. 6.12. It can be seen that the mean values of longitudinal force (H) (Fig. 6.12a), lateral force (Y) (Fig. 6.12b) and roll moment (Mx) (Fig. 6.12d) differ by a significant amount for the two aerodynamic models. Thrust variation (Fig. 6.12c) shows that DSDW model introduces a large variation in the loads. It is observed that

DSDW model increases the magnitude of all the force and moment components of the hub loads.

A comparison of the frequency contents and their magnitudes of all the hub loads for QSUI and DSDW models are shown in Figs. 6.13 - 6.18. From these figures, it is observed that the magnitudes of the various harmonics of all the hub loads corresponding to DSDW model are larger than those obtained by QSUI model. The difference in the magnitudes is significant in the case of longitudinal force (H), lateral force (Y) and thrust (T) variation as shown in Figs. 6.13a, 6.14a and 6.15a, respectively. In the case of thrust (T) (Fig. 6.15a), it is observed that the amplitude of the 4/rev frequency (20 Hz) is around 810 N for DSDW model and it is only about 100 N for QSUI model. The enlarged figures (Figs. 6.13b - 6.18b) show that DSDW model provides a large number of harmonics including those below 20 Hz (4/rev) in all the hub loads. From these figures, it is interesting to note that even QSUI model predicts the presence of frequencies below 20 Hz (4/rev). This observation on the presence of a wide spectrum of frequencies in the hub loads is mainly due to the nonlinearity and the asymmetry associated with the aerodynamic models.

For the sake of comparison, the vertical shear force at the root of all the four blades as a function of azimuth is shown in Fig. 6.19. From the figure, it can be seen that the response of all the blades is almost identical. The frequency contents of the response are given in Table 6.3. It is evident that the magnitudes of frequency contents are slightly different for all the four blades. This difference in the magnitudes of the harmonic contents is responsible for the appearence of all harmonics in the hub loads including those corresponding to blade passage frequency N_b/rev and its integer multiples.

6.1.2 Effect of Forward Speed: Straight Blade Configuration

Using DSDW aerodynamic model, sectional aerodynamic loads at various radial stations, blade root loads and hub loads are evaluated for different forward speed conditions. The variation of sectional lift, drag and moment versus azimuth angle are shown in Figs. 6.20 - 6.22. From Fig. 6.20, it can be seen that the magnitudes of the sectional lift is affected by the forward speed. At low forward speeds $(0 < \mu < 0.1)$, sectional lift exhibits one/rev variation with small amplitude. Whereas, high forward speeds introduce large variation in the sectional lift with additional harmonics. One interesting observation from Figs. 6.20a - 6.20e is that the occurrence of minimum value of the sectional lift force in the forward speed range $0.2 < \mu < 0.3$, shifts from retreating side to advancing side as the radial station moves from in-board towards the tip. Whereas for $\mu = 0.35$, the minimum value of the sectional lift is almost the same in both advancing and retreating sides. The reason for this phenomenon can be attributed to stall in the retreating side.

Figures 6.21 and 6.22 show respectively the variation of sectional drag and moment at different radial stations. With increase in forward speed, sectional drag shows large variation in all radial stations. For the high forward speed $\mu = 0.35$, the sectional drag (Fig. 6.21) shows a large increase near the tip region ($85\%R$ and $95\%R$) in the retreating side ($230 < \psi < 360$ deg.) due to dynamic stall effects. A similar observation is also seen in the case of sectional torsional moment as shown in Fig. 6.22.

For the reference blade (blade-1), the variation of root loads and root moments with azimuth angle are shown in Figs. 6.23 and 6.24, respectively. As the forward speed increases, the amplitude of root forces and moments increase substantially.

The variation of hub forces and moments over one revolution of the rotor is shown in Figs. 6.25 and 6.26, respectively. The variations of loads show dominant $4/rev$ oscillatory component with increase in forward speed.

146

Figure 6.27 shows the tip response of the blade in flap, lag and torsional modes. In all the modes, the tip response shows a monotonic increase with increase in forward speed. For the forward speed $\mu = 0.35$, additional harmonics are introduced in torsional response due to dynamic stall effects.

6.1.3 Effect of Structural Coupling due to Pretwist

The rotor blade is assumed to have a linear pretwist of -8 deg. It may be noted that for this blade configuration, if the control pitch input is zero, then the root pitch angle of the blade is 12 deg. and the tip pitch angle is 4 deg.. The purpose of this study is to analyse the effects of the structural coupling due to pretwist on the helicopter trim and aeroelastic response of the rotor blade and hub loads. The aeroelastic analysis is performed using the DSDW aerodynamic model. In the following, a comparison of trim and response results for straight and twisted blades, is presented.

The variation of control angles $(\theta_0, \theta_{1c}, \theta_{1s}, \theta_{0T})$ and the fuselage attitude in pitch (Θ) and roll (Φ) with forward speed are shown in Fig. 6.28. The trend of all the control angles is similar for both cases of straight and twisted blade configurations. From Fig. 6.28a, it is evident that the magnitude of the collective pitch angle (θ_0) is low in the case of twisted blade as compared to the straight blade. The difference of about 6 deg. in collective pitch essentially corresponds to the pitch of the pretwisted blade at 75% radial location. The observed dip in the fuselage pitch attitude at the high advance ratio for the straight blade configuration is eliminated in the case of the twisted blade configuration (Fig. 6.28f).

The variation of hub loads for one revolution is shown in Fig. 6.29 for the two cases of straight and pretwisted configurations, for an advance ratio $\mu = 0.35$. It can be seen that the mean values of longitudinal force (H) (Fig. 6.29(a)), lateral force (Y) (Fig. 6.29(b)) and yawing moment (Mz) (Fig. 6.29(f)) differ by a significant amount for the two configurations. Whereas, the mean values remain almost the same for

thrust (T) (Fig. 6.29(c)), roll moment (Mx) (Fig. 6.29(d)) and pitch moment (My) (Fig. 6.29(e)). It is observed that blade pretwist reduces the amplitude of hub load variations. This observation can also be seen by comparing the magnitudes of harmonic contents in thrust (T), shown in Fig. 6.15 (for straight blade configuration with DSDW model) and Fig. 6.30 (for twisted blade configuration with DSDW model). It can be seen from Fig. 6.30 that the magnitudes of the various harmonics corresponding to pretwisted blade are smaller than those obtained for straight blade. The amplitude of 4/rev frequency (20 Hz) is found to be 650 N for the pretwisted blade and for the straight blade the value is 810 N.

Sectional aerodynamic lift, moment and drag at various radial stations (50%R, 65%R, 75%R, 85%R and 95%R) are shown respectively in Figs. 6.31-6.33, for one blade as it goes around the azimuth, for an advance ratio $\mu = 0.35$. From Fig. 6.31, it can be seen that for the case of straight blade configuration, the minimum value of the sectional lift force is almost the same in both advancing and retreating sides at all the radial stations. Whereas, for the case of twisted blade configuration, the occurrence of minimum value of the sectional lift force shifts from retreating side to advancing side as the radial station moves towards the tip. From Fig. 6.32, it is observed that the sectional moment shows identical variation at in-board sections (50%R and 65%R) for both twisted and straight blade configurations. At the out-board stations (85%R and 95%R), the sectional moment undergoes a large variation in the retreating side for the straight blade as compared to the twisted blade configuration. From Fig. 6.33, it is observed that at the out-board stations (85%R and 95%R), the variation in sectional drag force is considerably small for the twisted blade configuration as compared to straight blade configuration. These results show that the effect of dynamic stall is reduced in the retreating side due to blade pretwist.

The tip response of a single blade in flap, lag and torsional modes is shown in Fig. 6.34. The magnitude of the variation of the tip response is relatively small for the

case of twisted blade configuration as compared to the straight blade configuration. Figure 6.34 shows that the torsional response has more harmonics as compared to flap and lag response.

The variation of root loads for a single blade as it goes around the azimuth is shown in Fig. 6.35. From the figure, it can be seen that there is a reduction in the magnitudes of the root loads for the case of twisted blade configuration as compared to the straight blade configuration.

6.1.4   Effect of Forward Speed: Twisted Blade Configuration

For the sake of completeness, sectional aerodynamic loads, hub loads, root loads and tip response are evaluated for different forward speed conditions using DSDW model for twisted blade configuration. The variation of sectional lift, drag and moment with respect to azimuth angle are shown in Figs. 6.36 - 6.38. Comparing these figures with those shown in Figs. 6.20 - 6.22 for a straight blade configuration, it can be seen that for the case of twisted blade configuration, (i) the magnitudes of lift, drag and moment at 85 %R and 95 %R are reduced; and (ii) also the effect of stall in the retreating side is reduced.

The variation of root loads and root moments with azimuth angle are shown in Figs. 6.39 and 6.40 respectively. The variation of hub forces are shown in Fig. 6.41 and the variation of hub moments $w.r.t.$ azimuth angle is shown in Fig. 6.42. Figure 6.43 shows the flap-lag-torsion response of the blade tip. From these figures, it is evident that the increase in forward speed increases the magnitude of loads and blade response. Comparing these results with those corresponding to the straight blade configuration, it is observed that the nature of variation of the response with increase in forward speed is almost similar for both blade configurations.

6.2 Summary

A systematic study is undertaken to analyse the influence of various aerodynamic models, representing rotor inflow and sectional loads, on the helicopter trim and aeroelastic response of the rotor blades. The influence of blade pretwist on rotor loads and response is also studied.

Table 6.1: Helicopter data

Variable		Quantity
Number of blades,	N_b	4
Air density at sea level,	$\rho \ (kg/m^3)$	1.224
Weight of the Helicopter,	$W \ (N)$	45000
Radius of the main rotor blade,	$R \ (m)$	6.6
Radius of the tail rotor blade,	$R_t \ (m)$	1.3
Chord of the main rotor blade,	$C \ (m)$	0.5
Chord of the tail rotor blade,	$C_t \ (m)$	0.19
Main rotor rotating speed,	$\Omega \ (rpm)$	300
Tail rotor rotating speed,	$\Omega_t \ (rpm)$	1500
Fuselage frontal area,	$f \ (m^2)$	1.8
Horizontal tail area,	$s_h \ (m^2)$	2.24
Vertical tail area,	$s_v \ (m^2)$	2.126
Blade Frequency data (Untwisted): Nondimensional		
Flap modes		1.089
		2.896
		5.145
		7.688
Lag modes		0.701
		5.308
Torsional mode		4.509
Axial mode		9.155
Blade Frequency data (Twisted): Nondimensional		
Flap modes		1.093
		2.822
		4.865
		7.150
Lag modes		0.701
		5.293
Torsional mode		4.508
Axial mode		9.155

Table 6.2: Geometrical data of the helicopter

Variable	Quantity (m)
X_{MR}	0.0
X_{HT}	7.5
X_{VT}	7.5
X_{TR}	7.5
Y_{MR}	0.0
Y_{HT}	0.0
Y_{VT}	0.0
Y_{TR}	0.0
Z_{MR}	2.0
Z_{HT}	0.5
Z_{VT}	1.75
Z_{TR}	2.0

Table 6.3: Frequency contents of blade root shear (Fz_{1k})

| Frequency (Hz)	$1^{st}blade$	$2^{nd}blade$	$3^{rd}blade$	$4^{th}blade$
5	1633.90	1630.10	1630.20	1629.90
10	3518.80	3522.10	3522.40	3522.80
15	725.59	725.25	725.81	725.59
20	200.85	200.27	199.90	199.95
25	54.86	54.48	54.65	54.63
30	19.14	20.21	20.13	21.00
35	15.10	14.31	14.16	14.24
40	16.09	14.95	15.08	15.07
45	13.43	12.31	12.39	12.33
50	14.81	13.89	13.85	13.78
55	14.63	13.64	13.74	13.69
60	14.92	13.98	13.95	13.95
65	15.12	14.14	14.08	14.12
70	13.75	12.77	12.81	12.86
75	13.01	12.18	12.11	12.15
80	12.95	11.99	12.02	12.03
85	12.37	11.47	11.52	11.48
90	10.44	9.63	9.61	9.57
95	8.75	7.88	7.95	7.92
100	8.96	8.21	8.19	8.20
105	9.70	9.00	8.96	8.98
110	8.66	7.90	7.93	7.96
115	6.51	5.81	5.76	5.79
120	6.13	5.54	5.55	5.55
125	7.77	7.23	7.28	7.26
130	19.14	20.21	20.13	21.00
135	5.74	5.05	5.10	5.08
140	4.16	3.62	3.60	3.60
145	5.41	4.97	4.94	4.96
150	5.85	5.32	5.33	5.36
155	4.43	3.96	3.92	3.92
160	2.58	1.99	2.05	2.04
165	2.27	1.81	1.83	1.81
170	2.49	2.07	2.07	2.06
175	2.03	1.65	1.65	1.66
180	1.27	1.07	1.05	1.05
185	0.67	0.66	0.69	0.67
190	0.33	0.59	0.58	0.56
195	0.15	0.53	0.55	0.55
200	0.09	0.61	0.55	0.55

(a) Side view

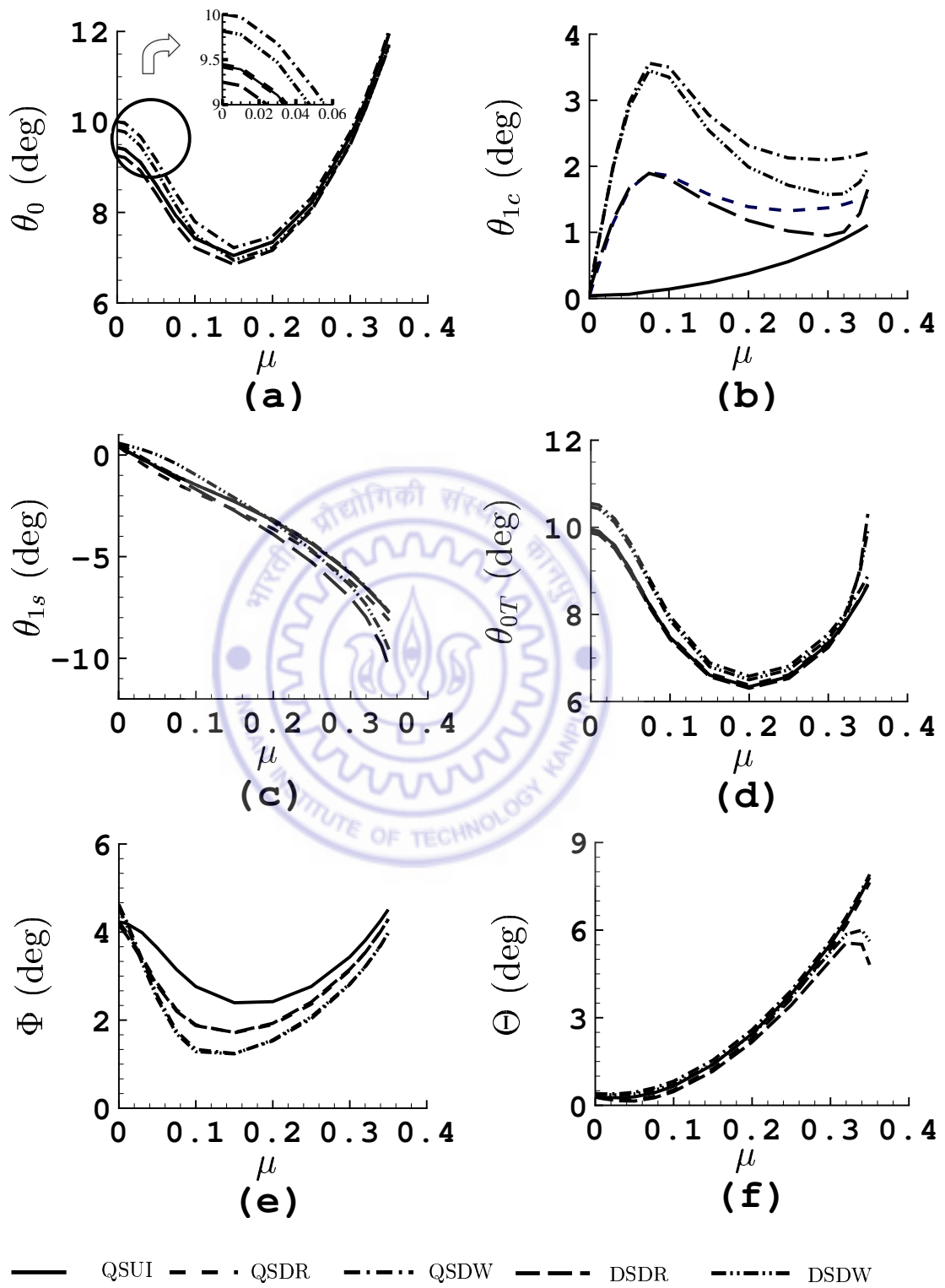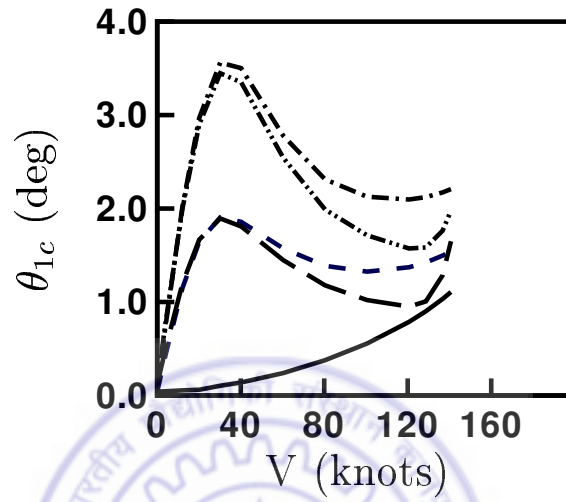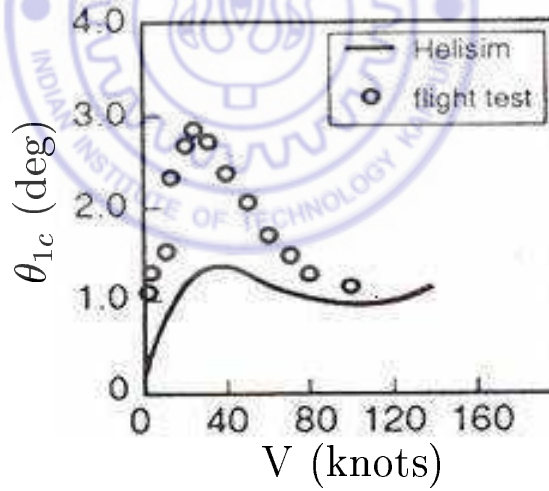(b) Front view
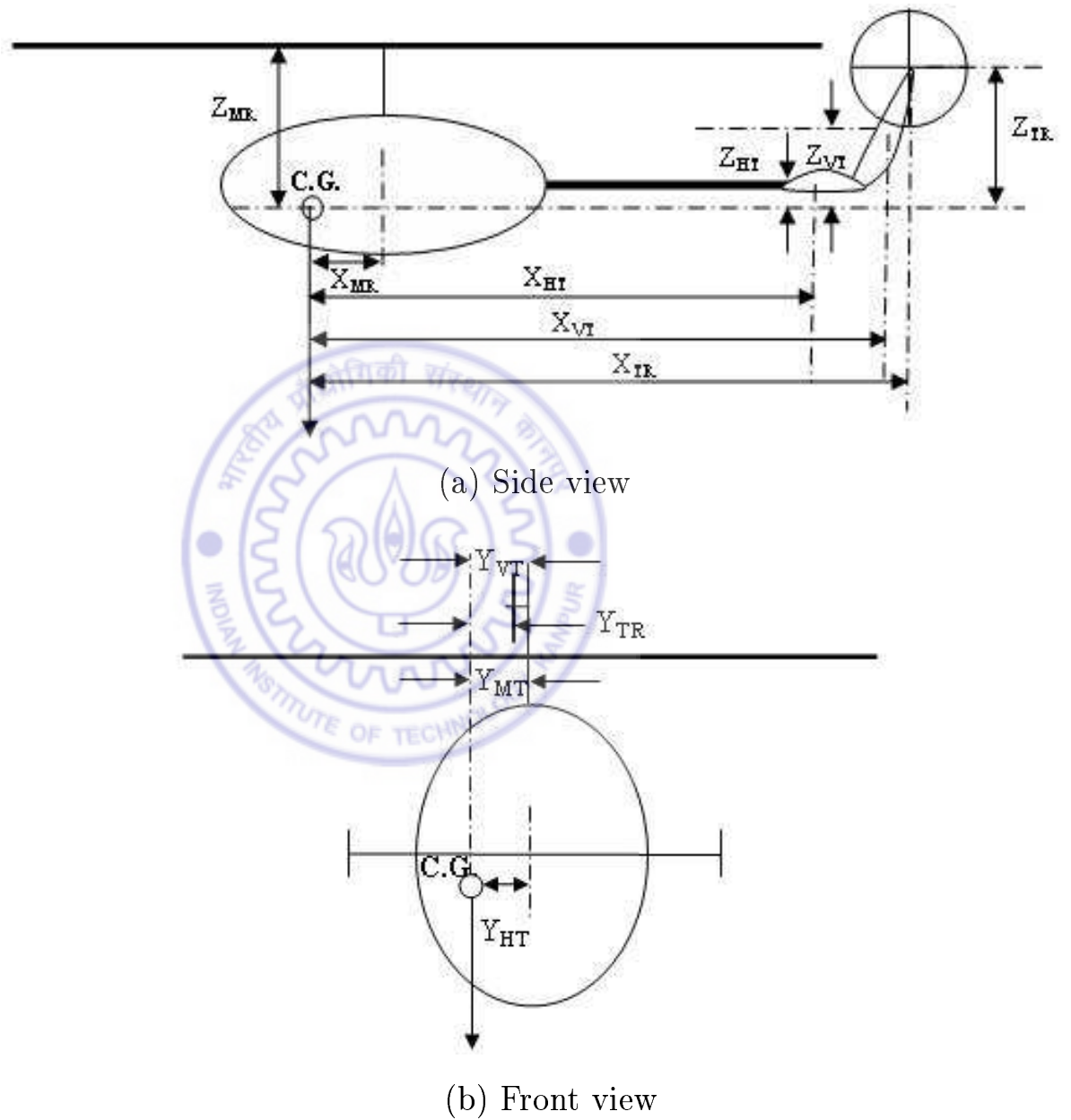
Figure 6.1: Geometric description of the helicopter

Figure 6.2: Variation of trim angles with forward speed μ

Figure 6.3: Qualitative comparison of variation of lateral pitch angle with forward speed (a) present study (b) Ref. [191]
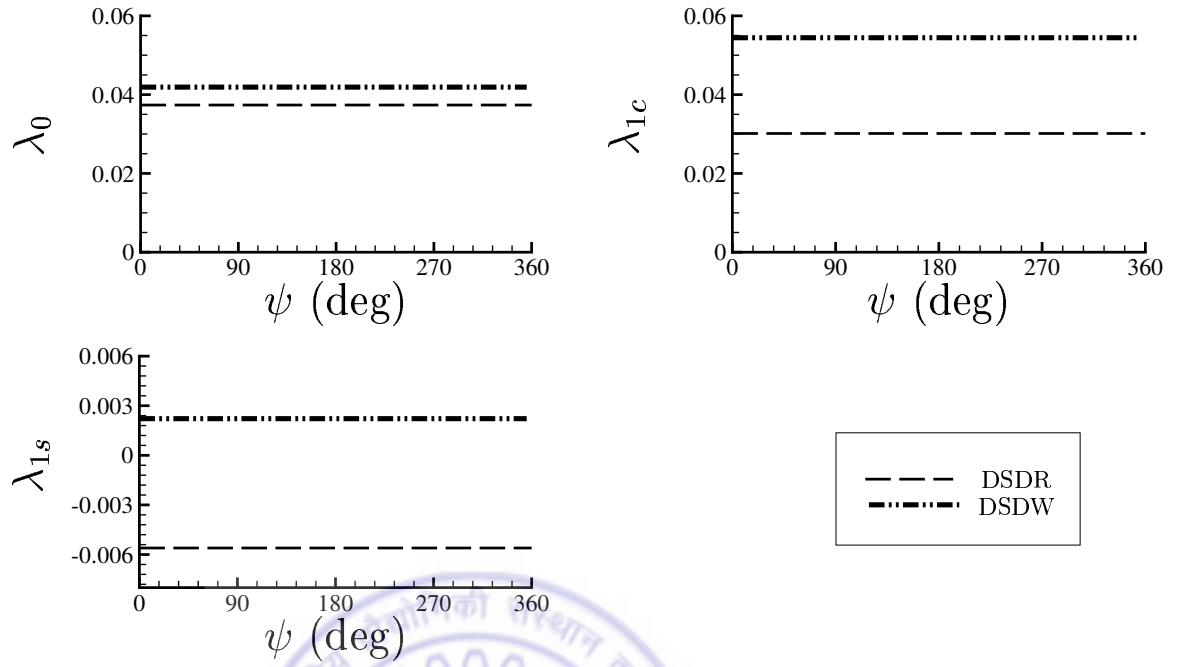
Figure 6.4: Comparison of inflow variables for Drees and dynamic wake models as a function of azimuth for $\mu = 0.075$
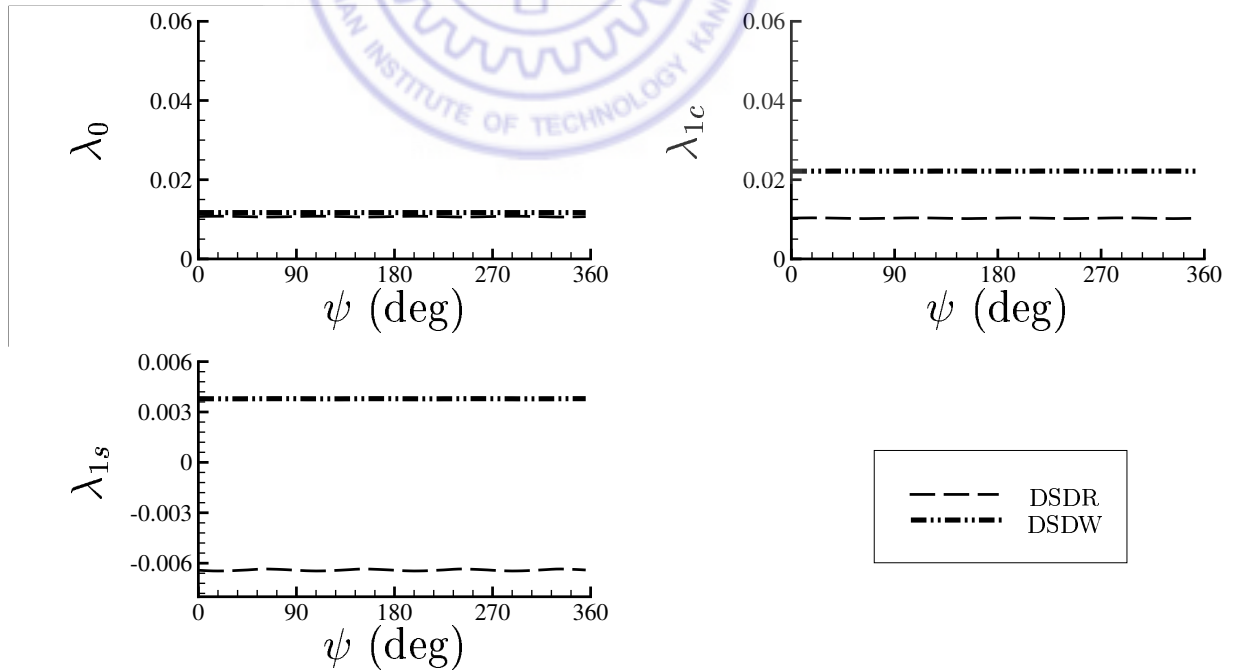

Figure 6.5: Comparison of inflow variables for Drees and dynamic wake models as a function of azimuth for $\mu = 0.30$
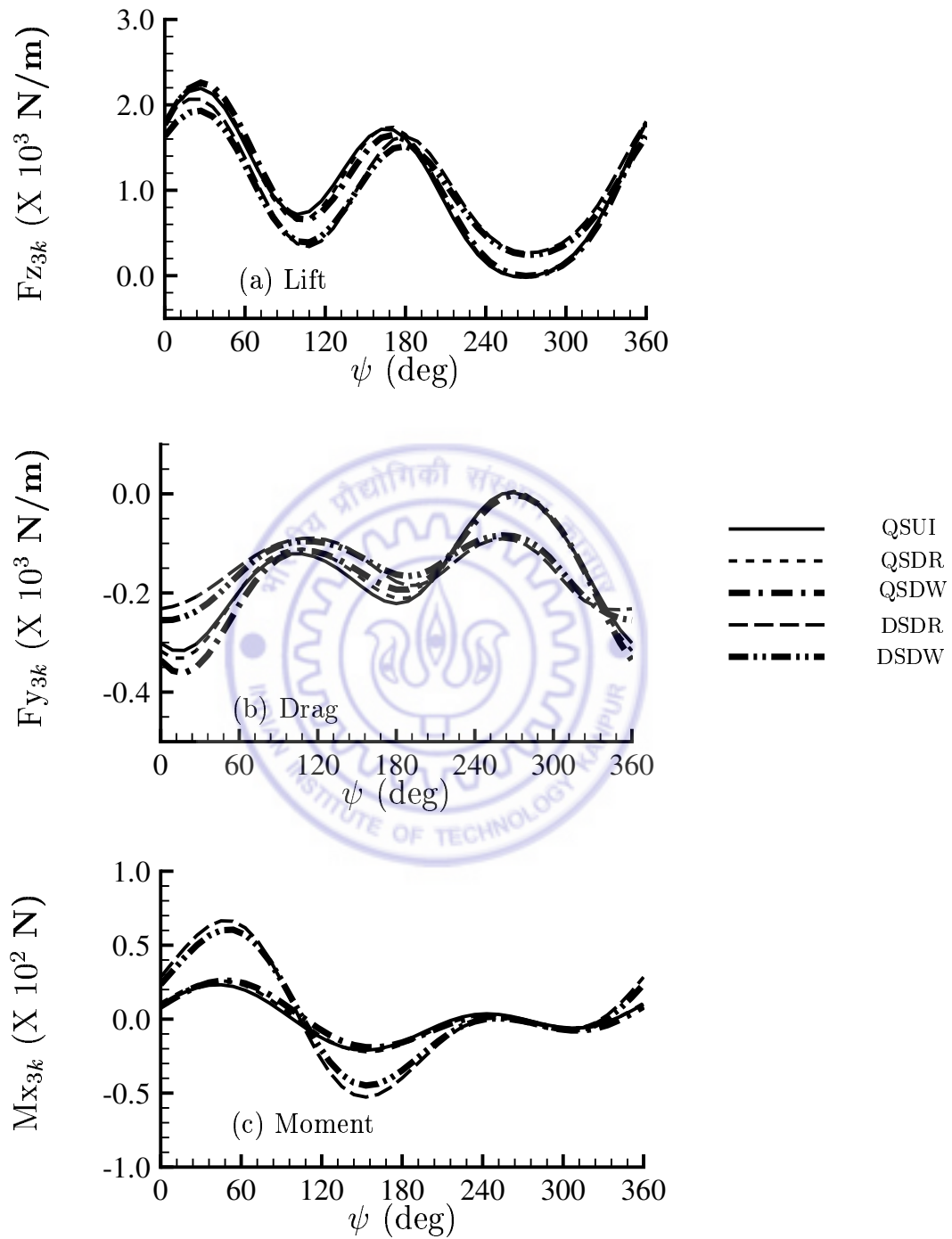
Figure 6.6: Azimuthal variation of sectional aerodynamic loads at r = 0.5 R, $\mu = 0.35$

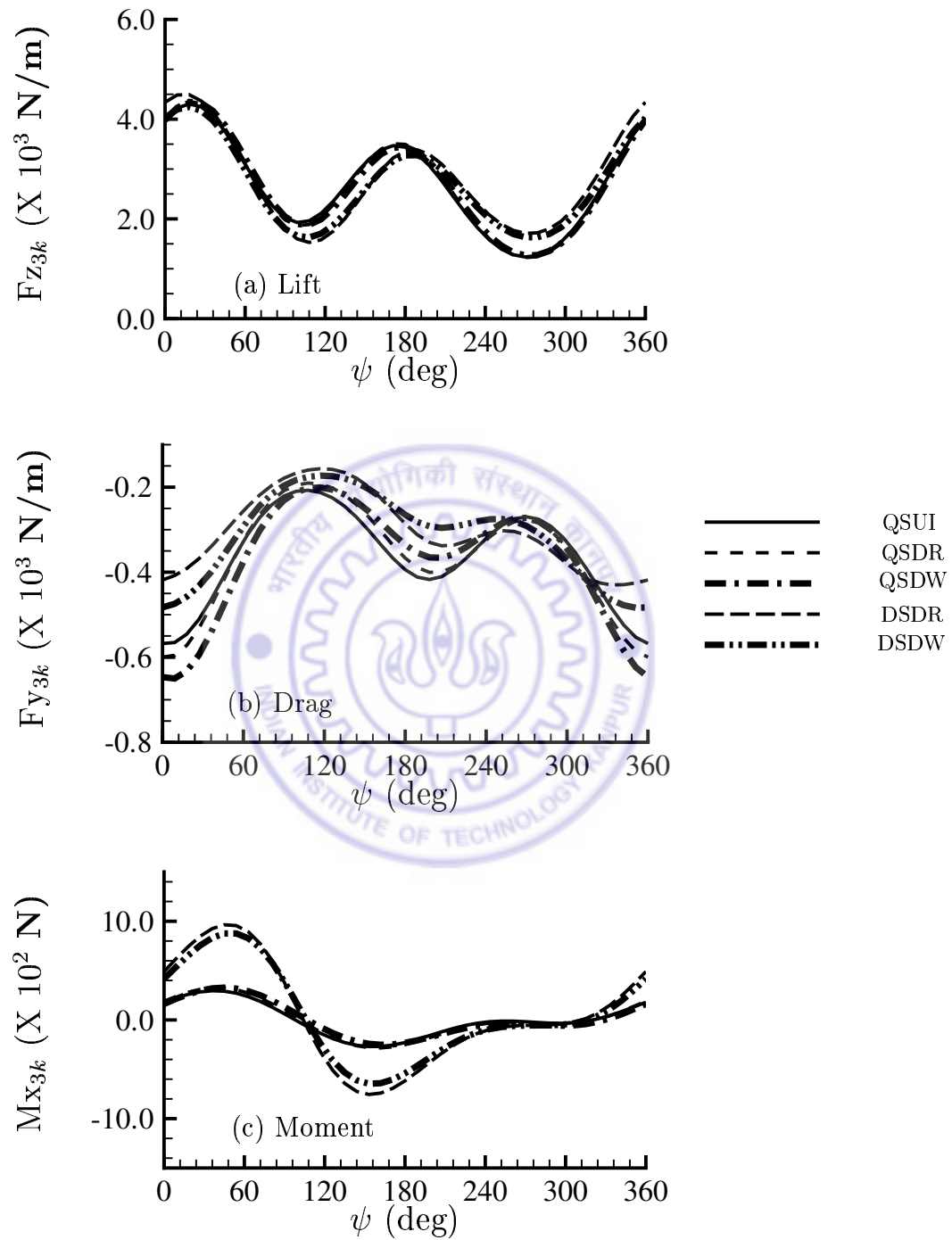Figure 6.7: Azimuthal variation of sectional aerodynamic loads at r = 0.65 R, μ = 0.35

Figure 6.8: Azimuthal variation of sectional aerodynamic loads at r = 0.75 R, $\mu = 0.35$
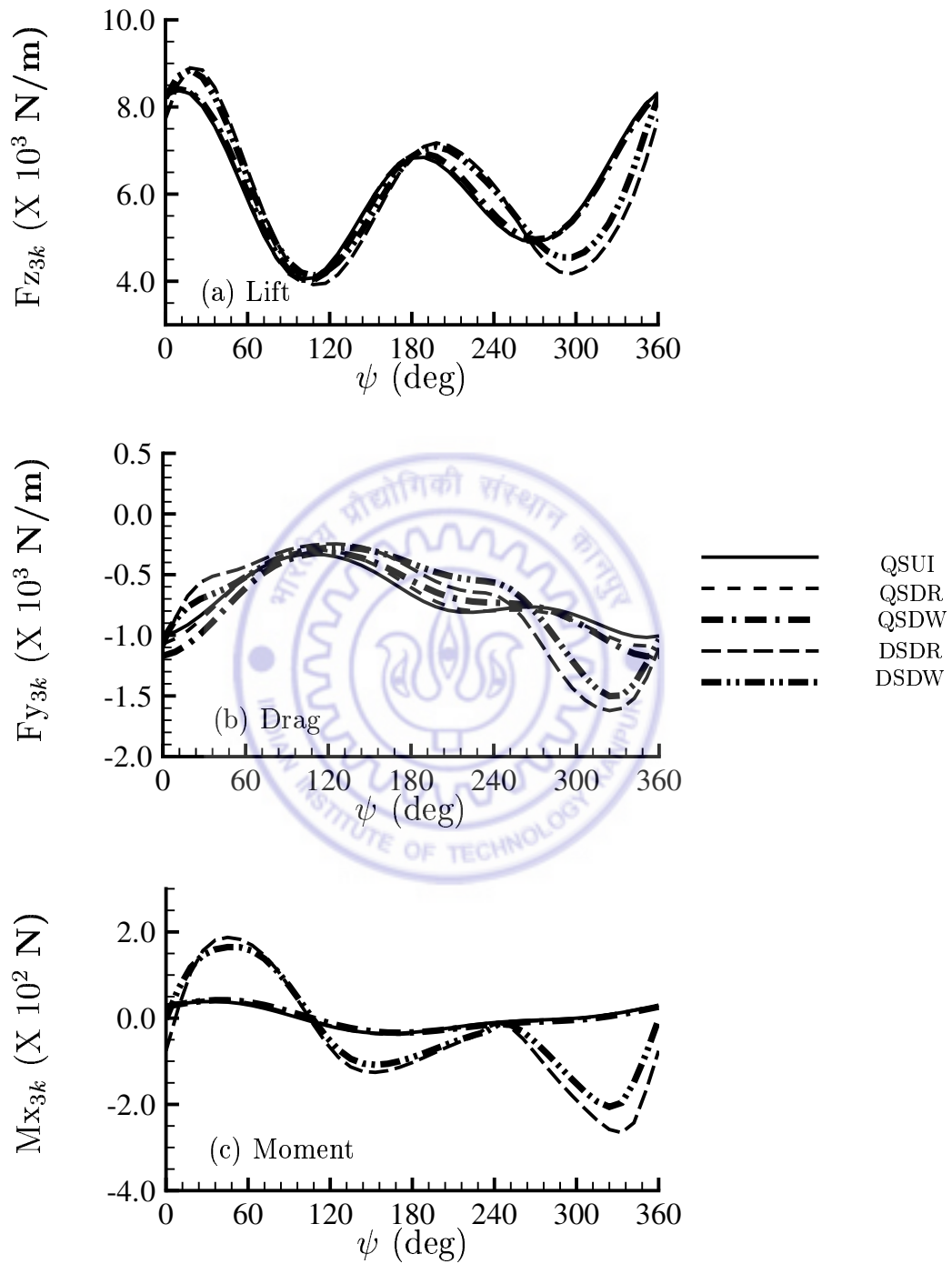
Figure 6.9: Azimuthal variation of sectional aerodynamic loads at r = 0.85 R, μ = 0.35
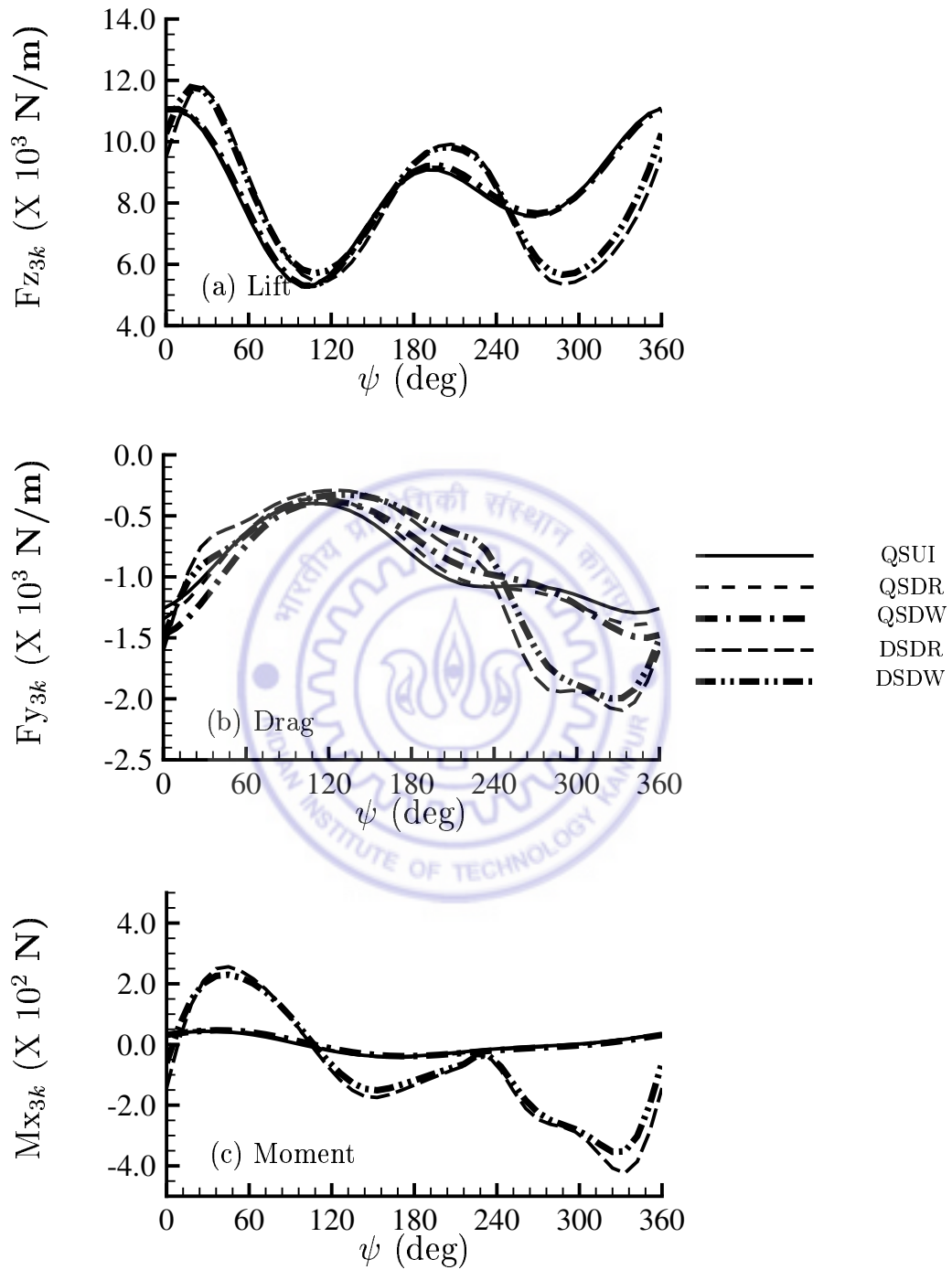
Figure 6.10: Azimuthal variation of sectional aerodynamic loads at r = 0.95 R, μ = 0.35

(a)

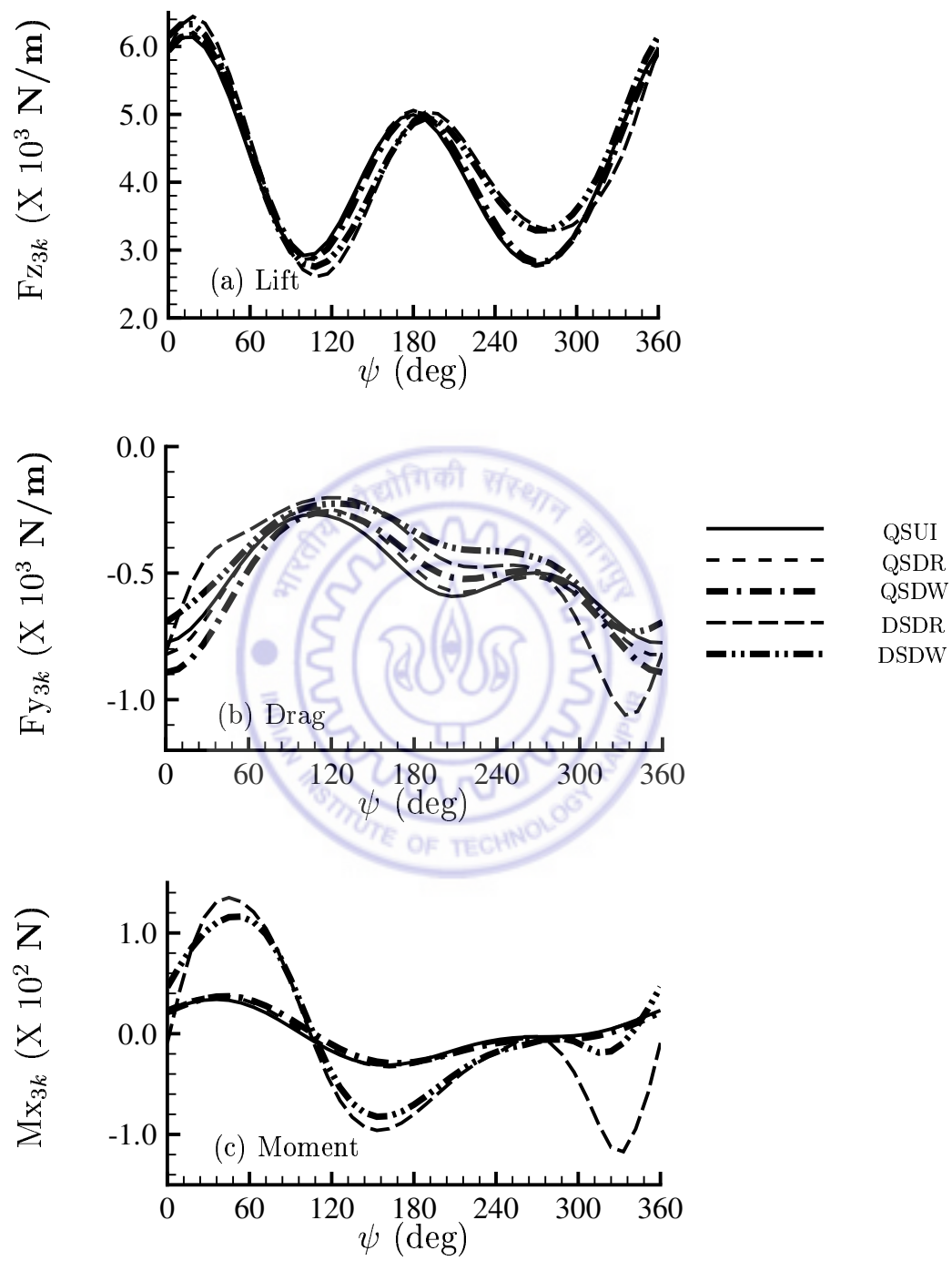**(b)**

(c)
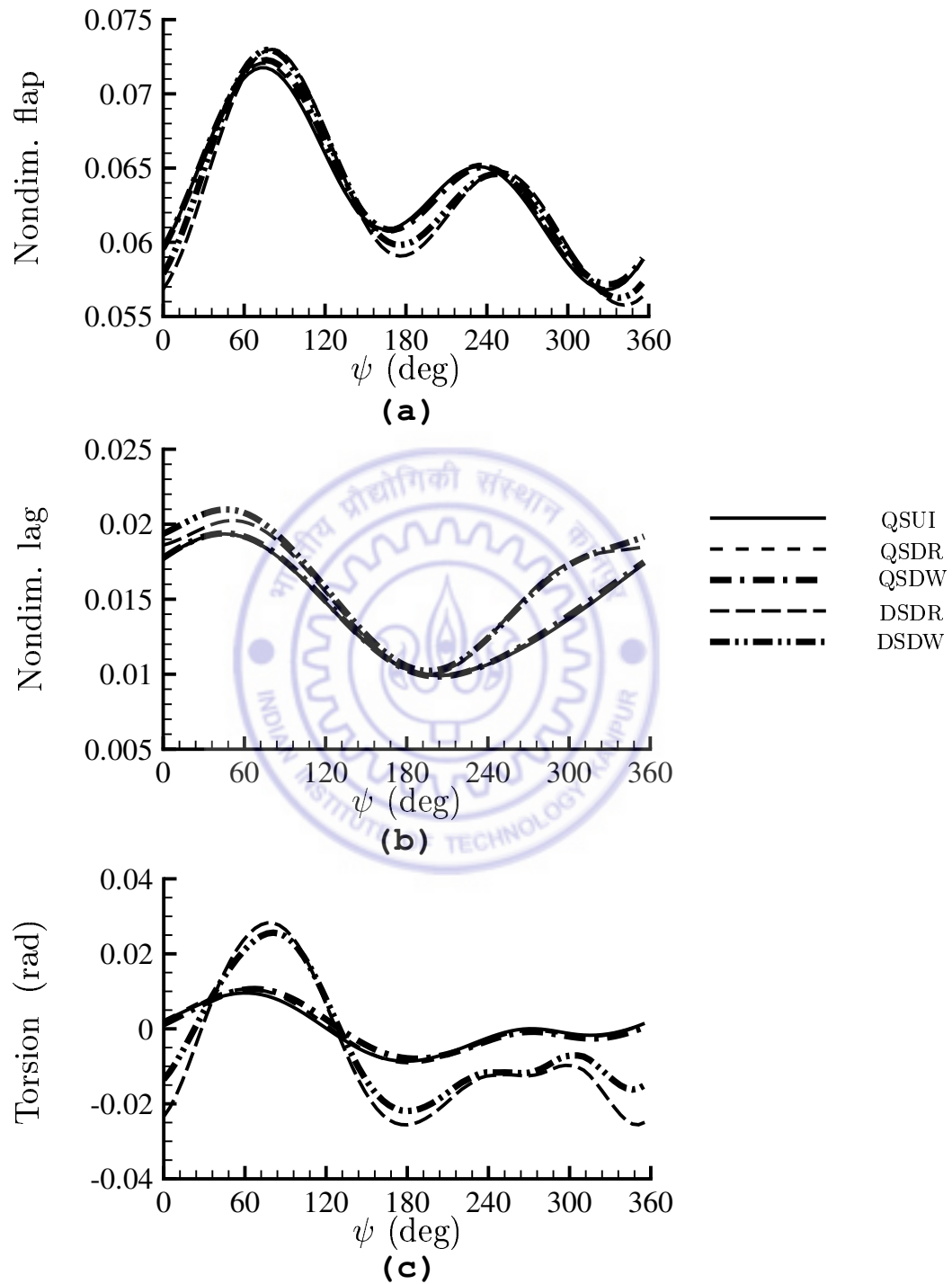
Figure 6.11: Response at the blade tip as a function of azimuth for $\mu = 0.35$

163
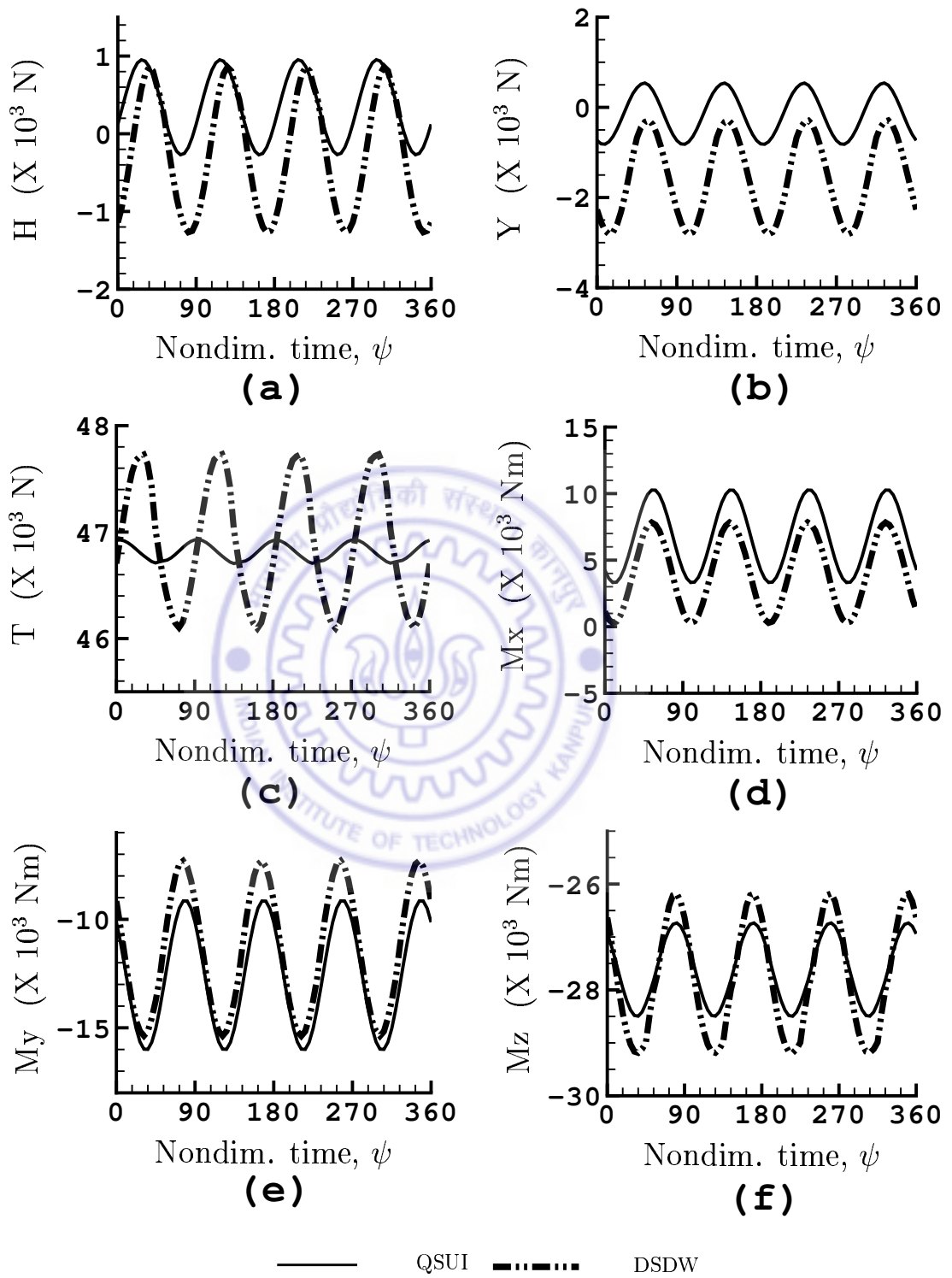
Figure 6.12: Time response of hub loads for $\mu = 0.35$
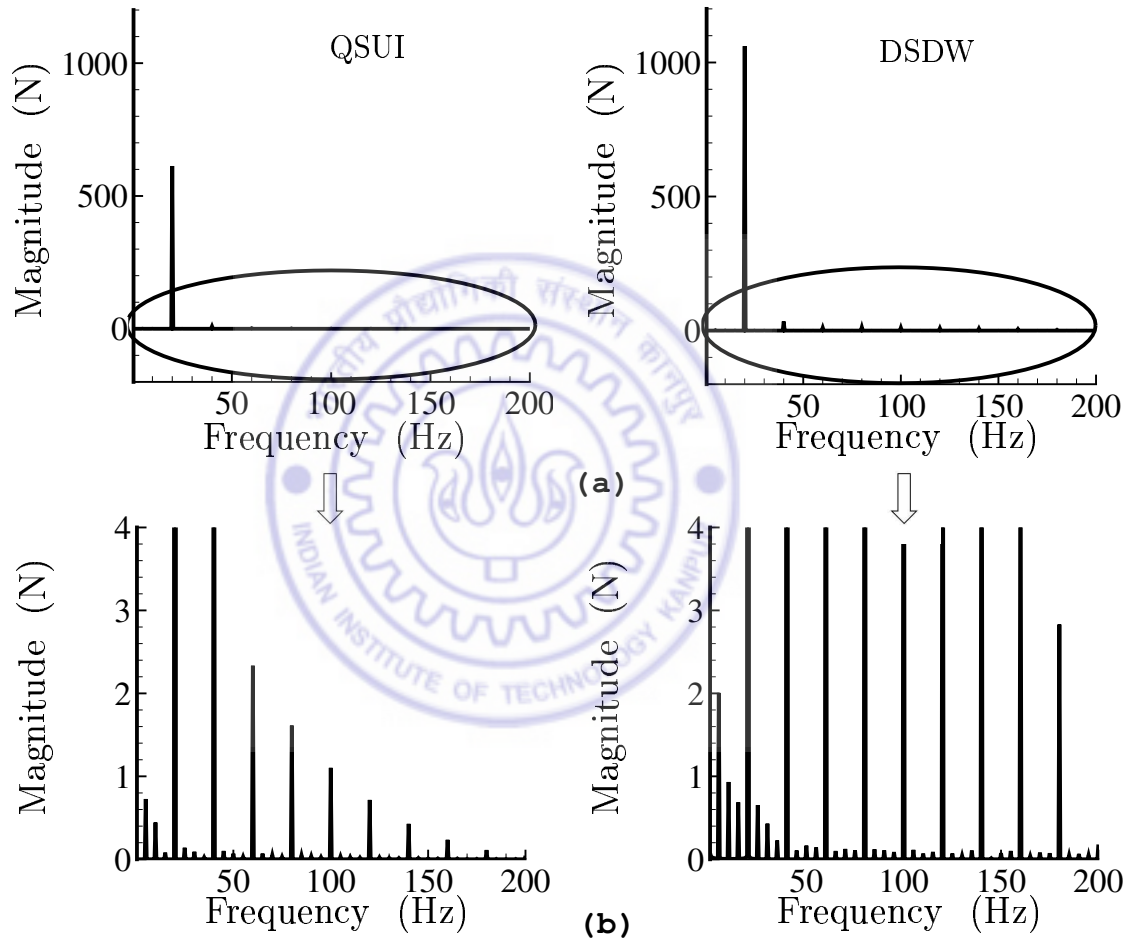
Figure 6.13: Frequency contents of longitudinal force (H) at the hub for $\mu = 0.35$
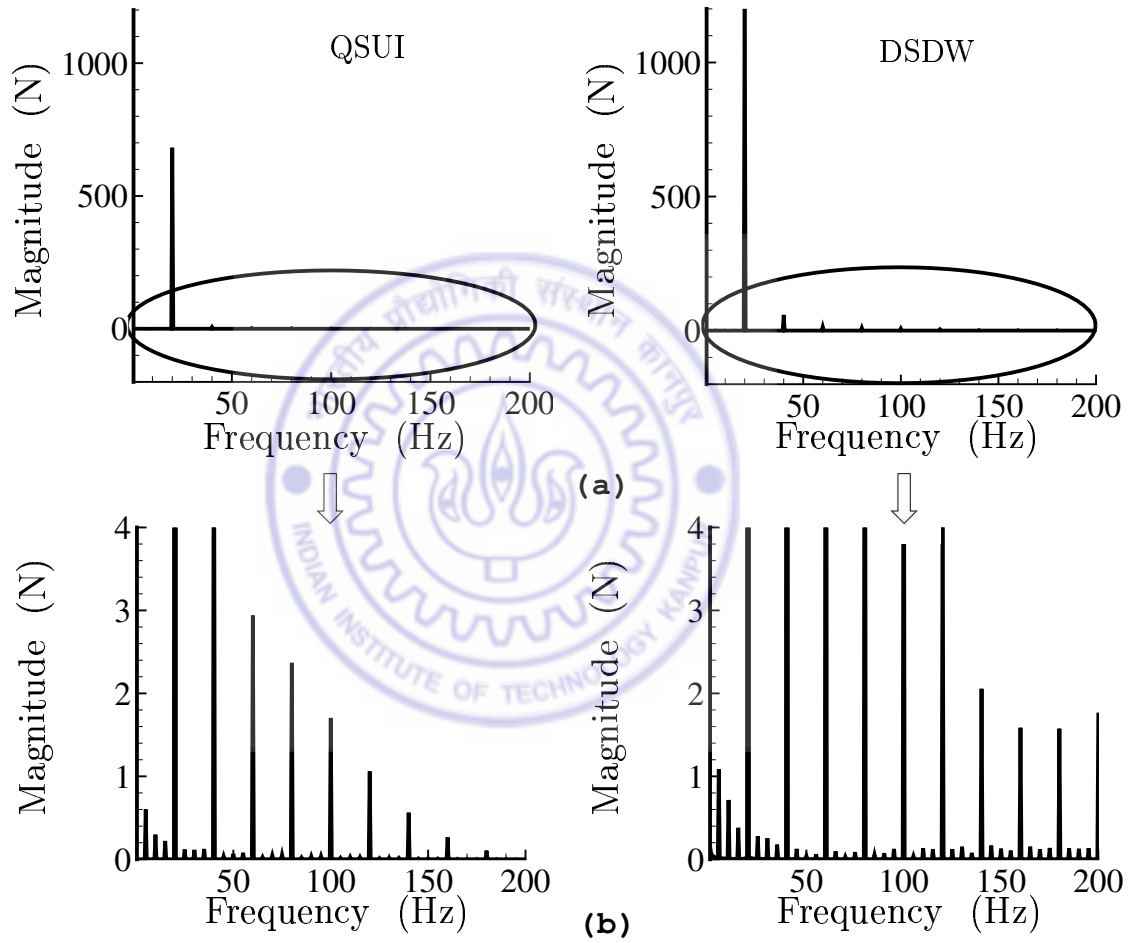
Figure 6.14: Frequency contents of lateral force (Y) at the hub for $\mu = 0.35$
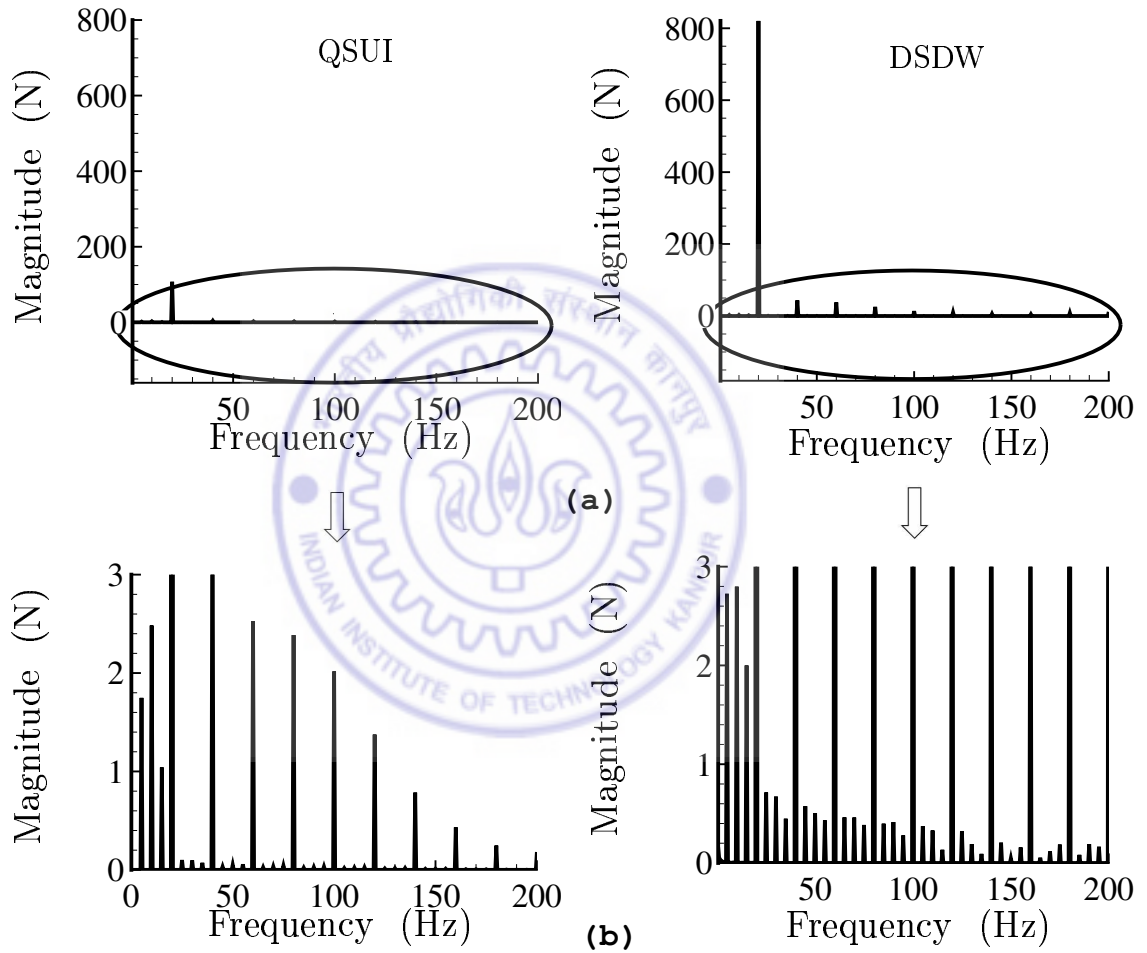
Figure 6.15: Frequency contents of vertical force (T) at the hub for $\mu = 0.35$
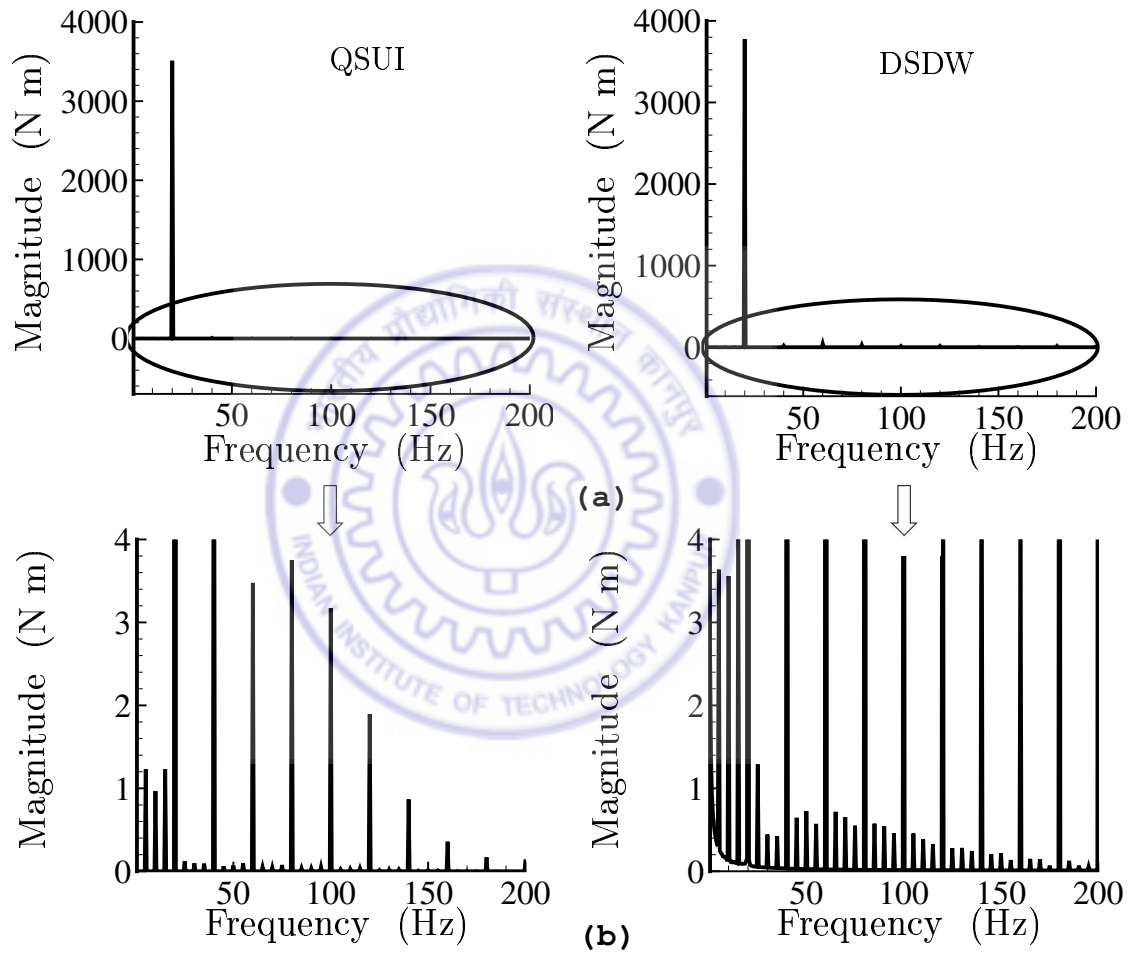
Figure 6.16: Frequency contents of rolling moment (M_x) at the hub for $\mu = 0.35$
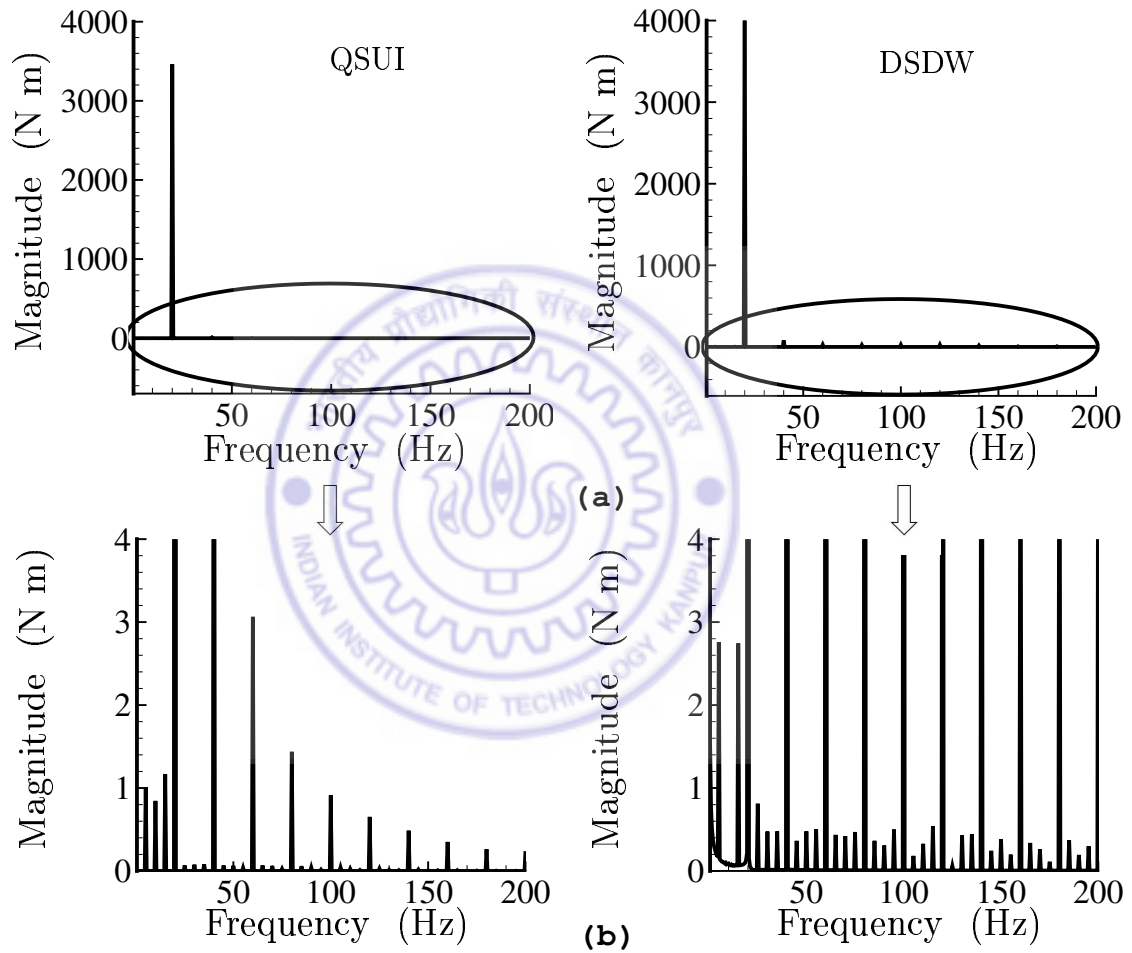
Figure 6.17: Frequency contents of pitching moment (M_y) at the hub for $\mu = 0.35$
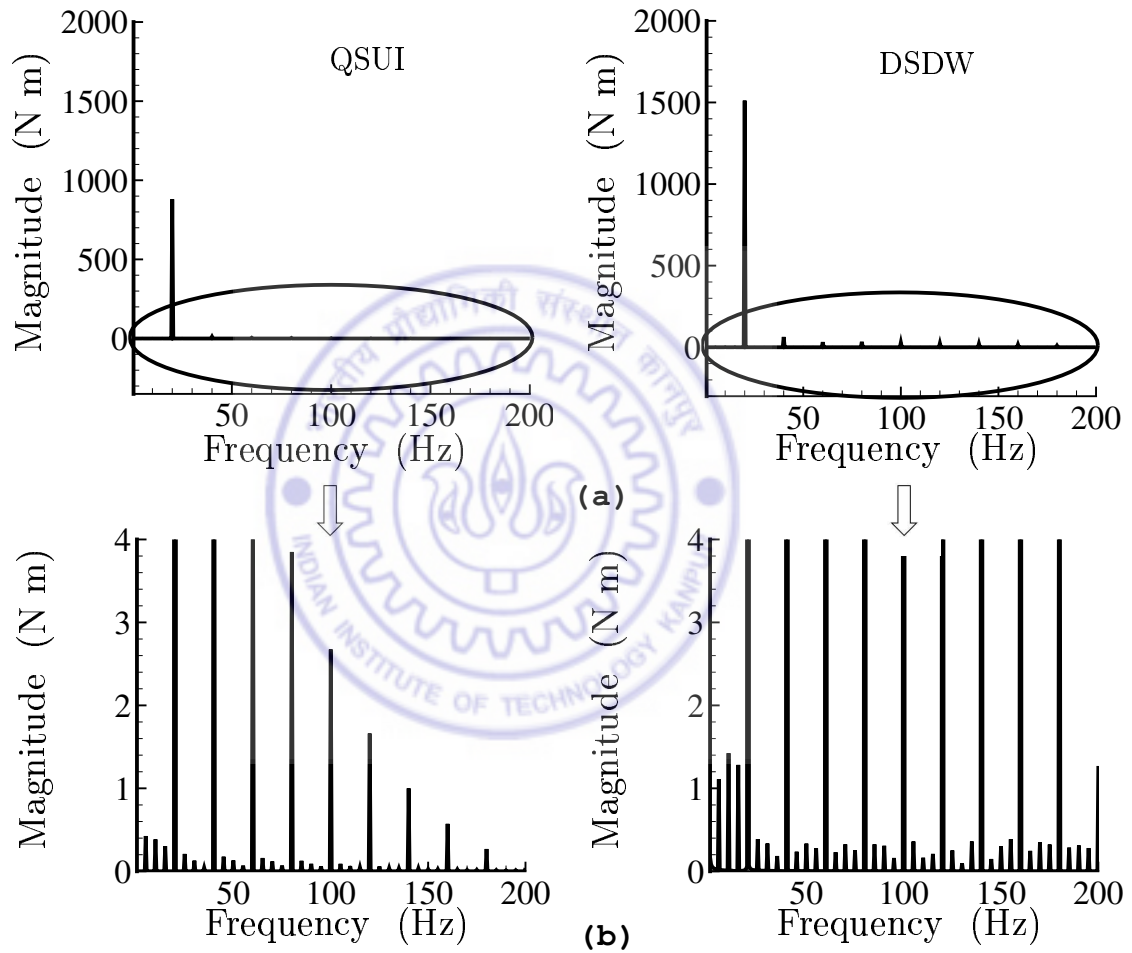
Figure 6.18: Frequency contents of yawing moment (M_z) at the hub for $\mu = 0.35$
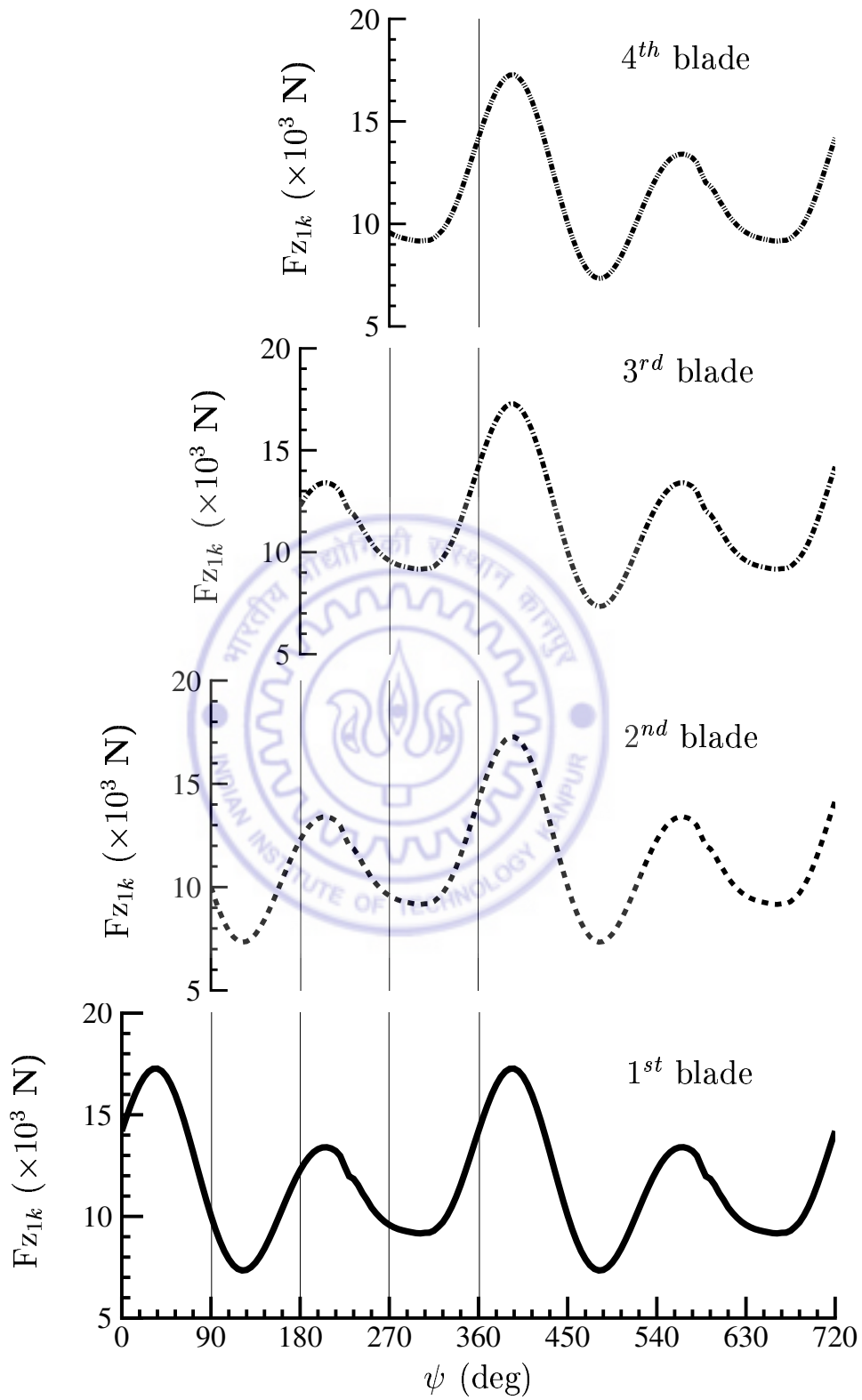
Figure 6.19: Blade vertical root shear for $\mu = 0.35$

Figure 6.20: Variation of sectional aerodynamic lift for different forward speeds
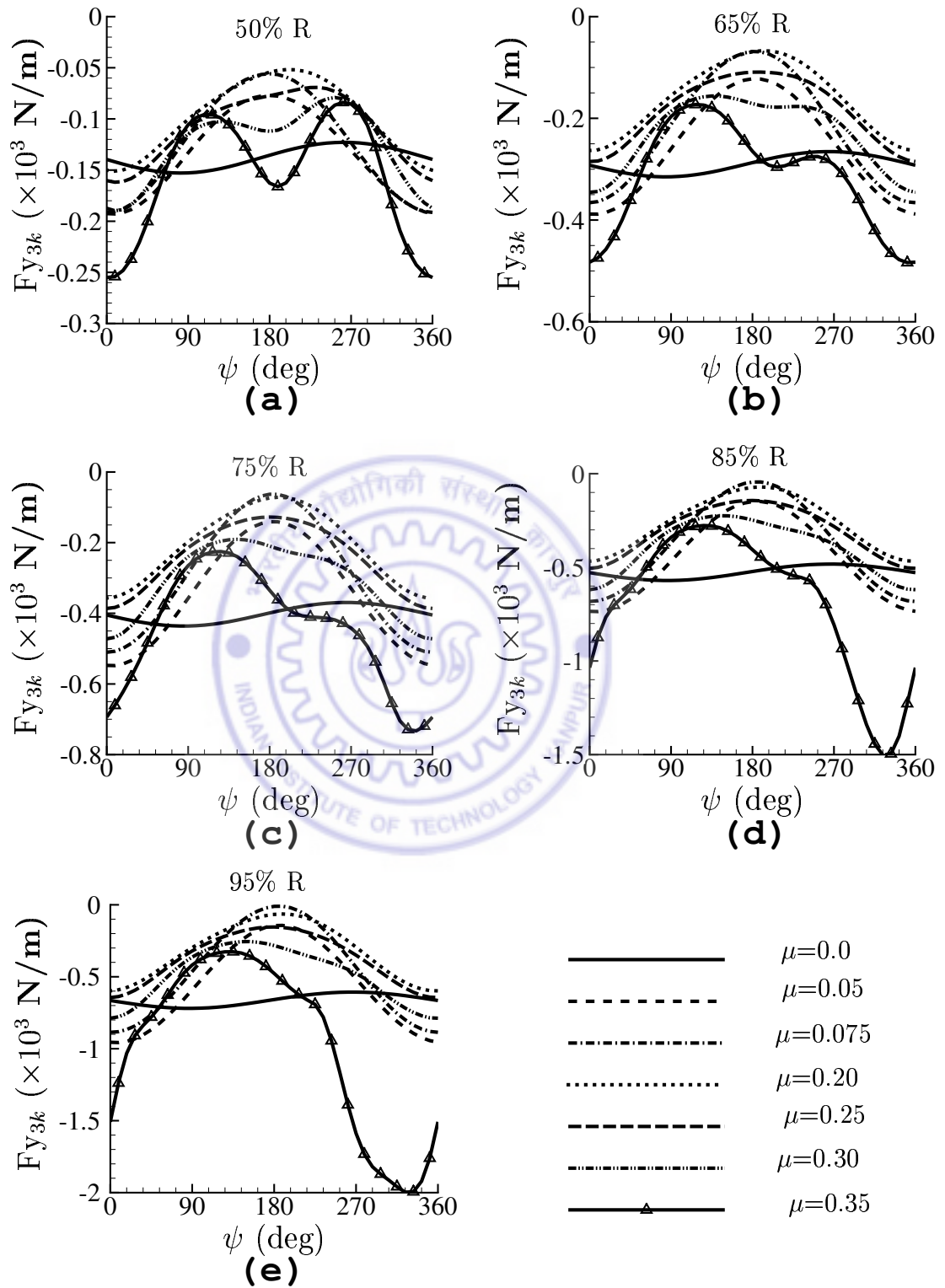
Figure 6.21: Variation of sectional aerodynamic drag for different forward speeds

Figure 6.22: Variation of sectional aerodynamic moment for different forward speeds

Figure 6.23: Blade root forces for various forward speeds

Figure 6.24: Blade root moments for various forward speeds

Figure 6.25: Hub forces for various forward speeds

Figure 6.26: Hub moments for various forward speeds
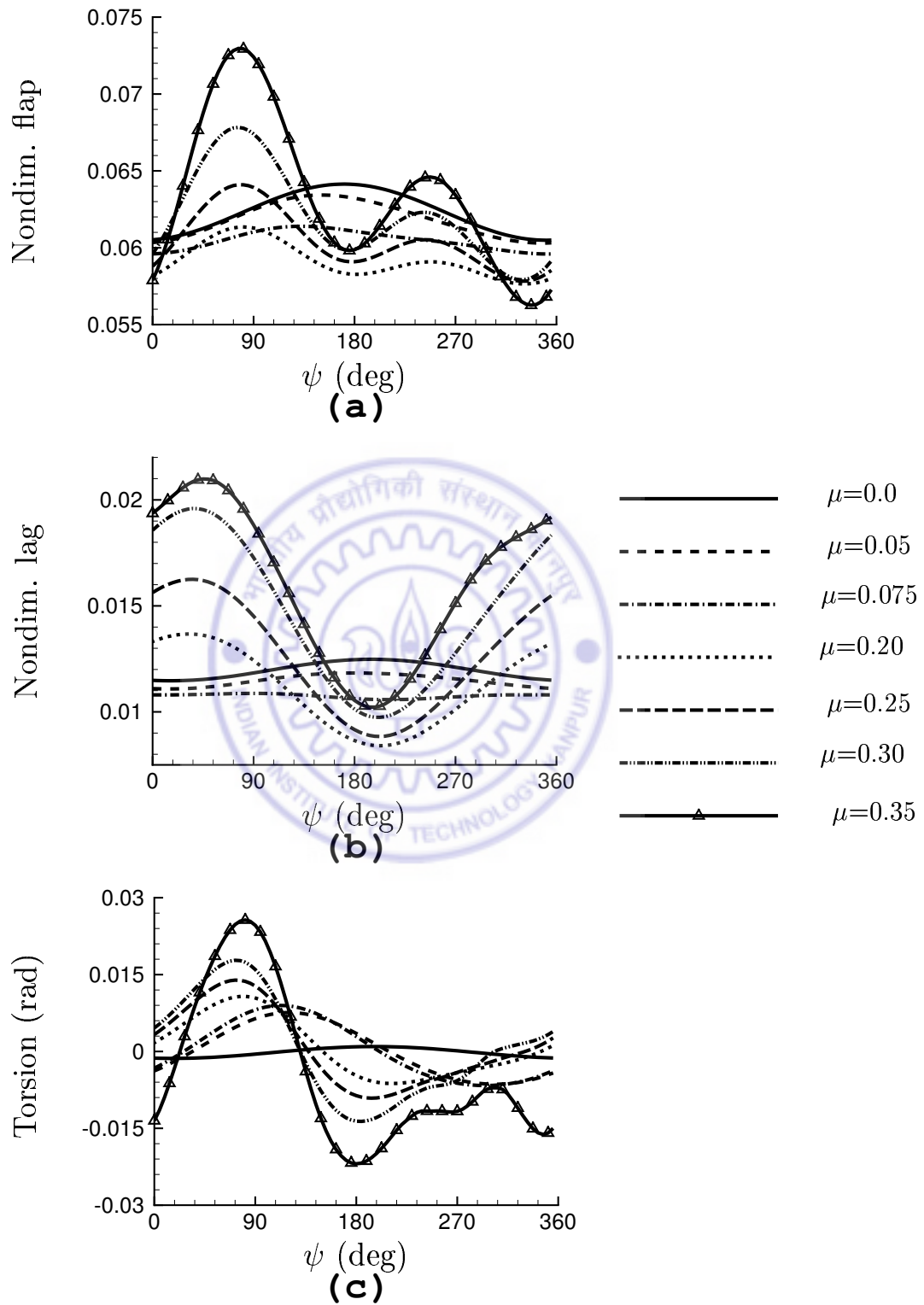
Figure 6.27: Tip response for various forward speeds
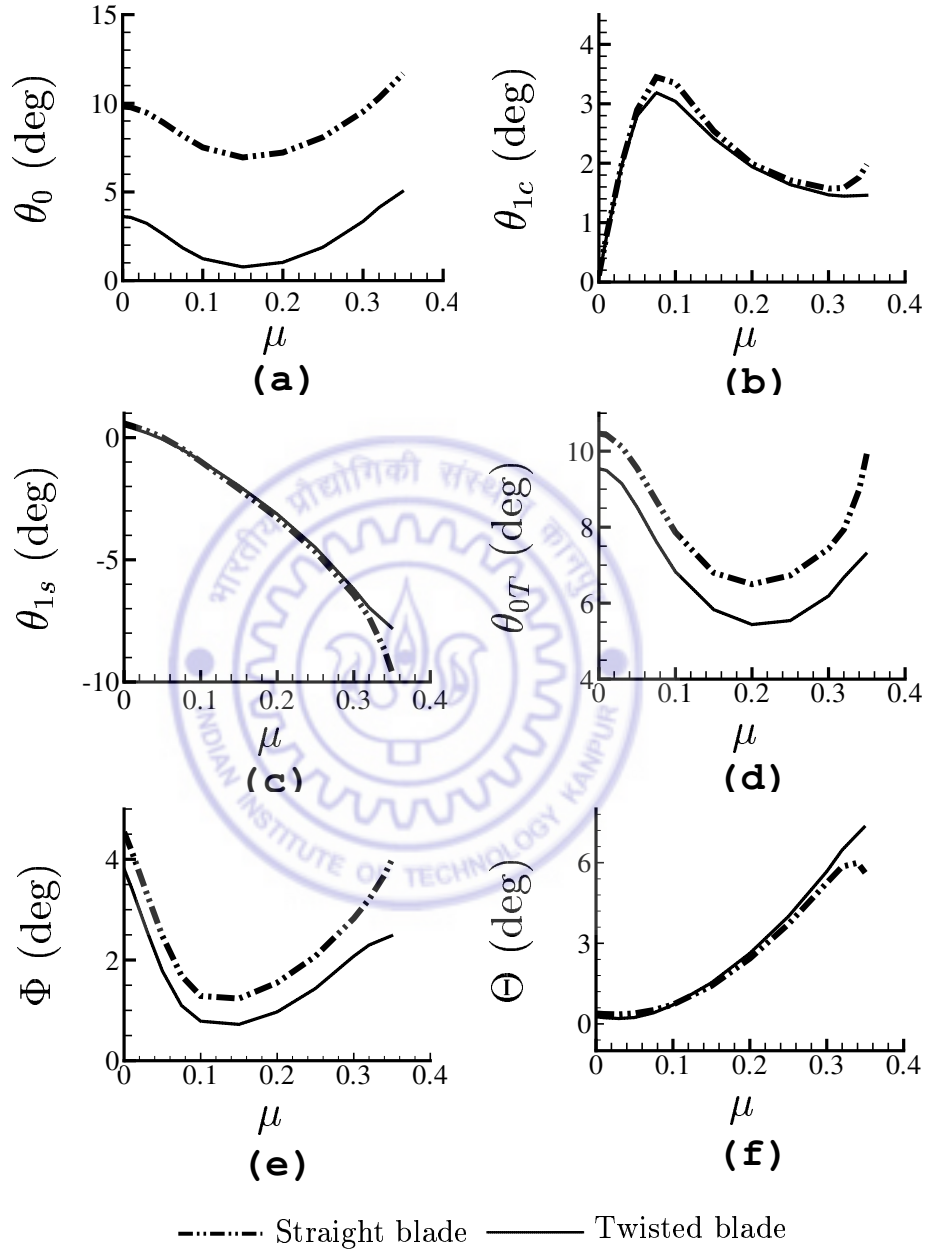
Figure 6.28: Trim variables for twisted and straight blade configuration as a function of advance ratio (μ) obtained using DSDW model
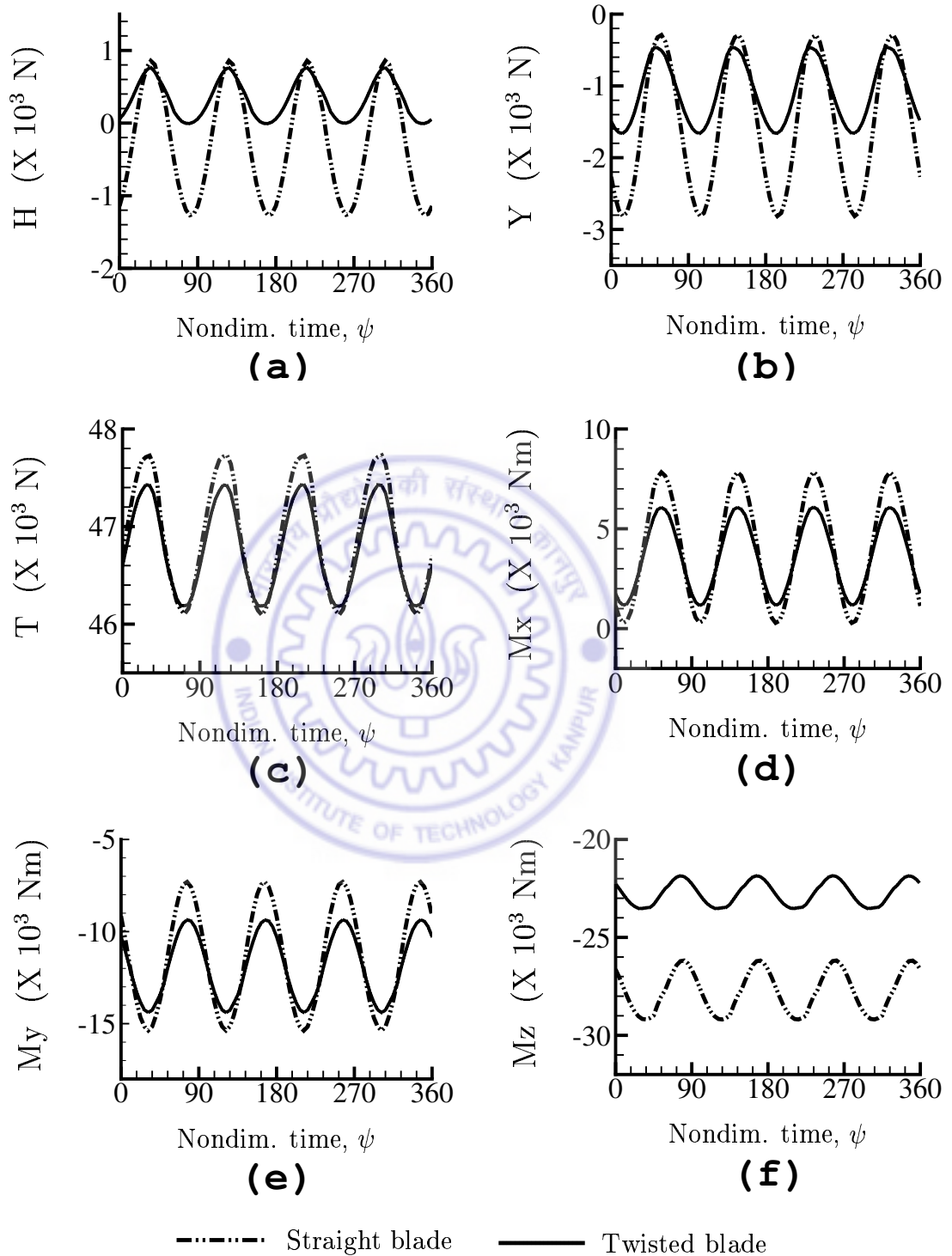
Figure 6.29: Comparison of hub loads for twisted and straight blade configuration as a function of azimuth for $\mu = 0.35$ obtained using DSDW model
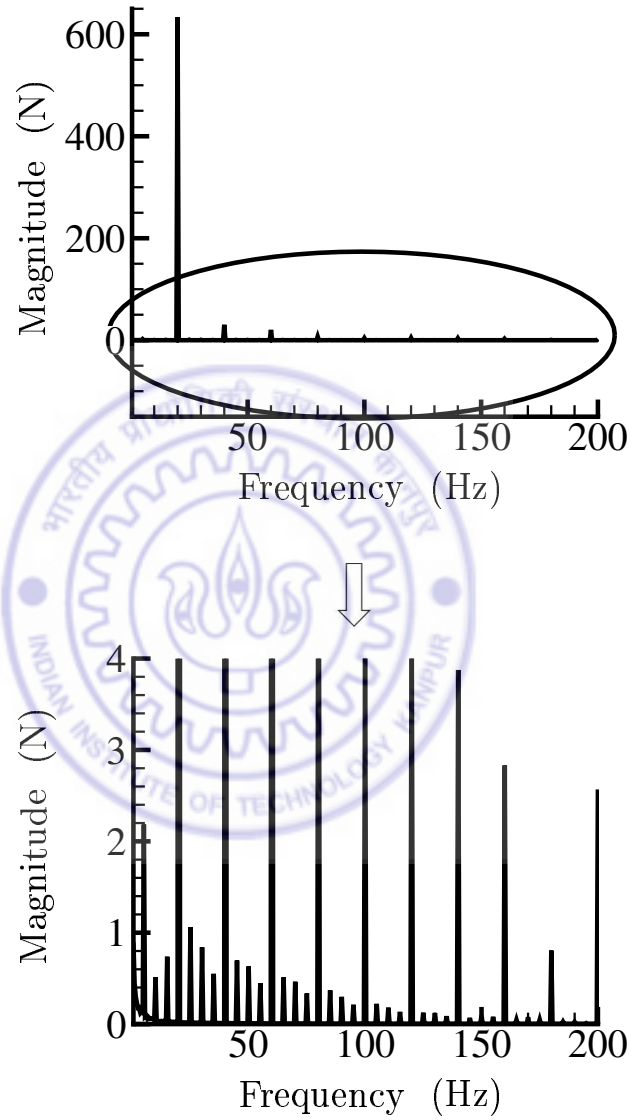
Figure 6.30: Frequency contents of vertical force at the hub obtained for twisted blade configuration for $\mu = 0.35$ obtained using DSDW model
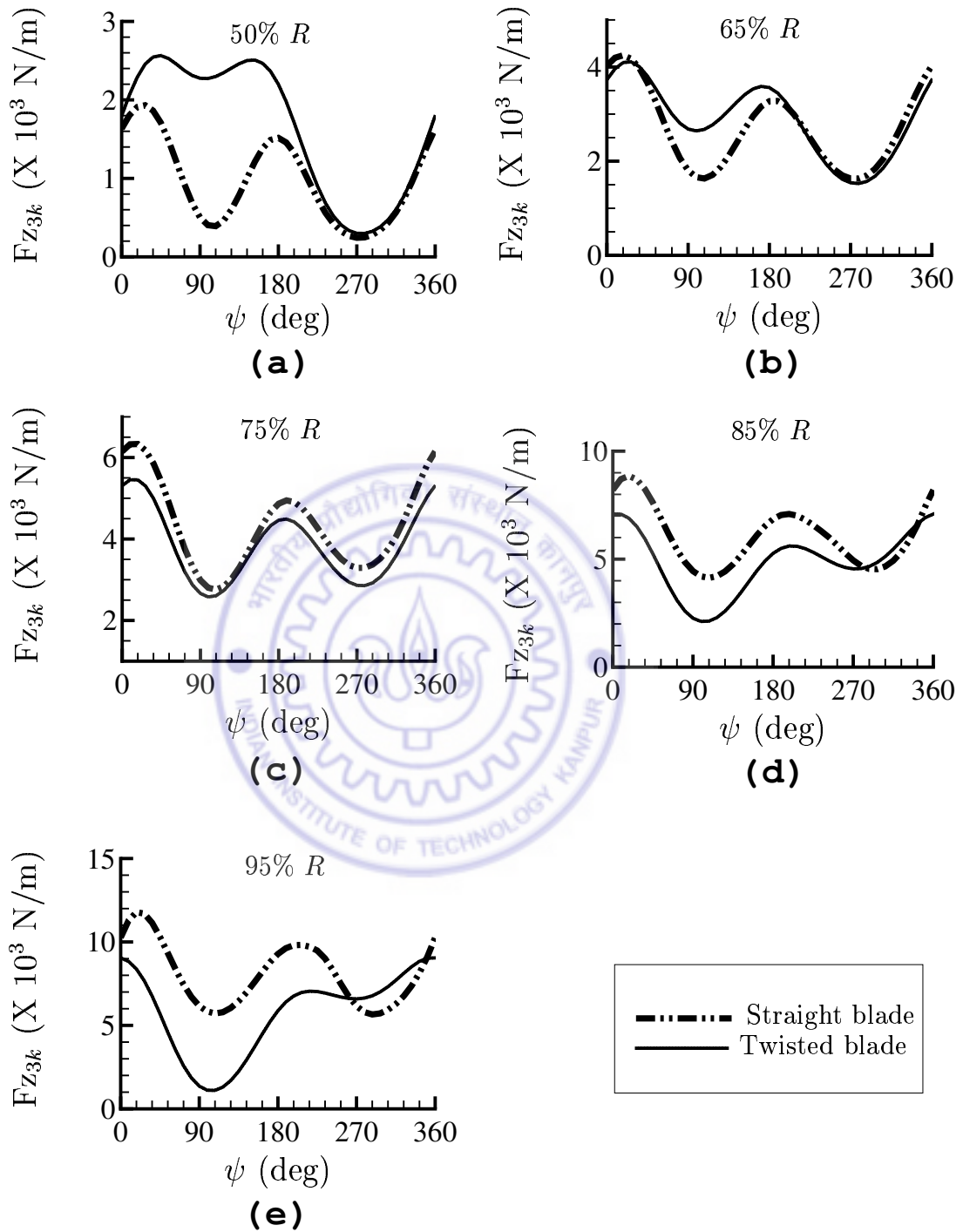
Figure 6.31: Comparison of sectional lift at various radial locations for twisted and straight blade configurations as a function of azimuth for $\mu = 0.35$, obtained using DSDW model
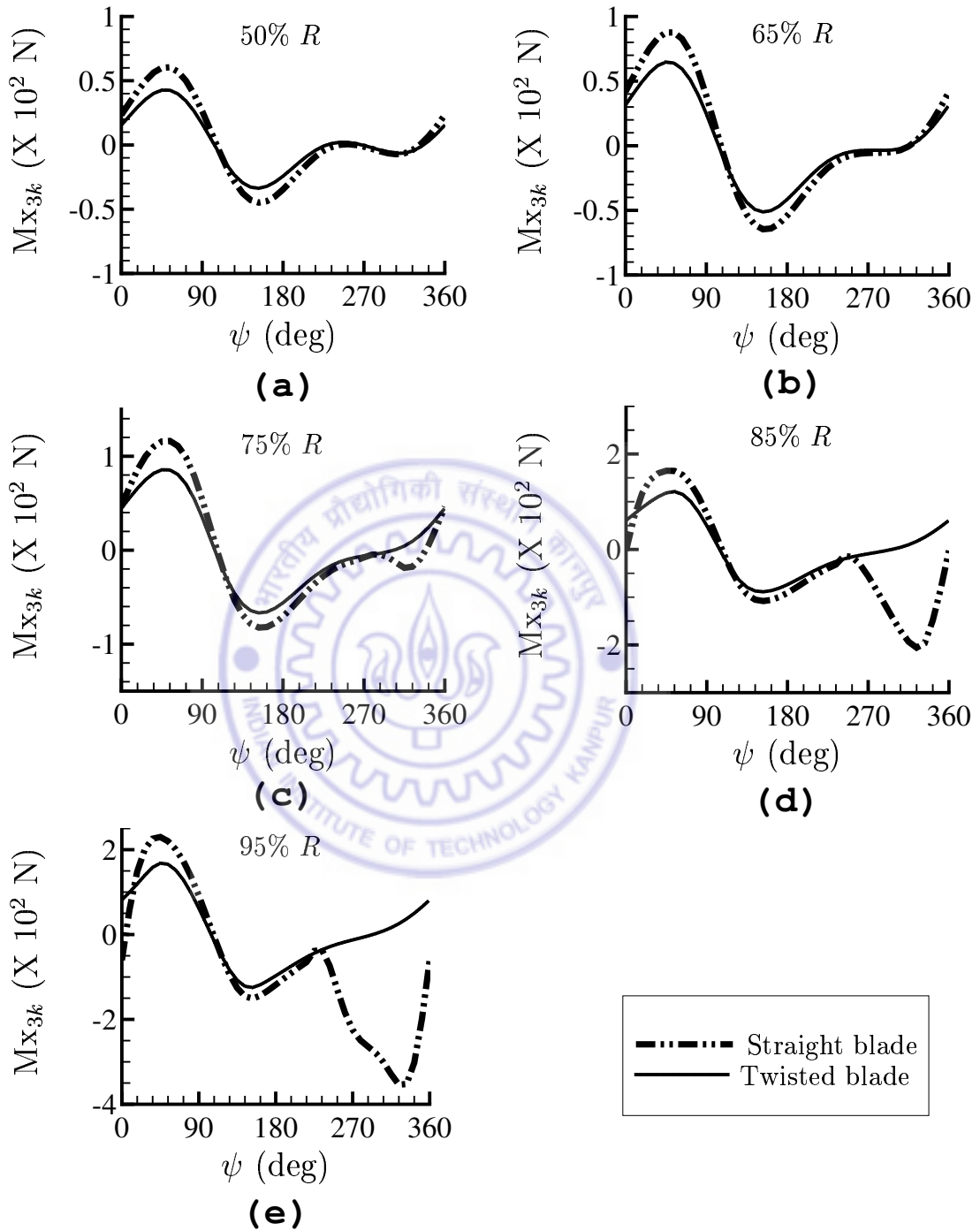
Figure 6.32: Comparison of sectional moment at various radial locations for twisted and straight blade configurations as a function of azimuth for $\mu = 0.35$, obtained using DSDW model
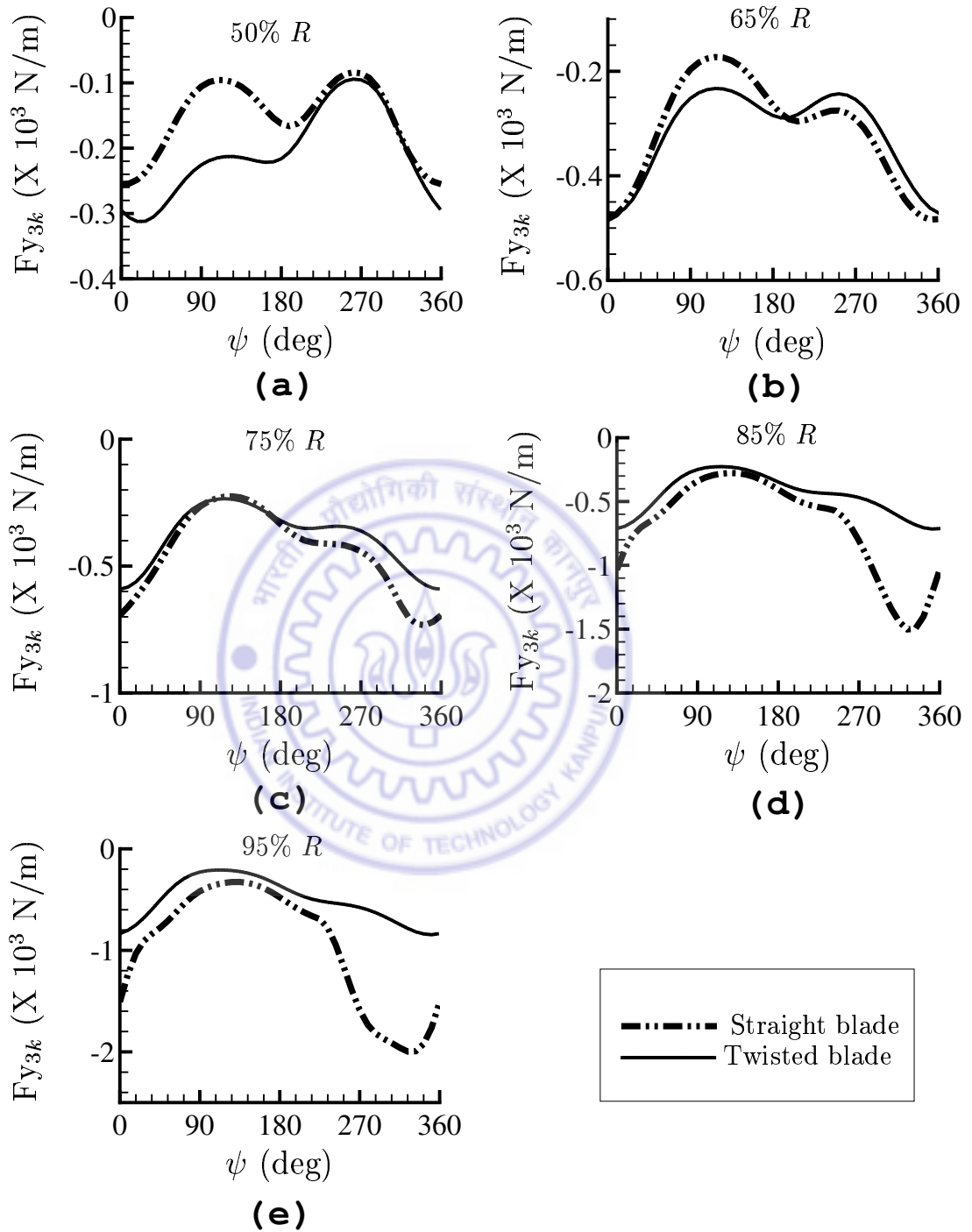
Figure 6.33: Comparison of sectional drag at various radial locations for twisted and straight blade configurations as a function of azimuth for $\mu = 0.35$, obtained using DSDW model
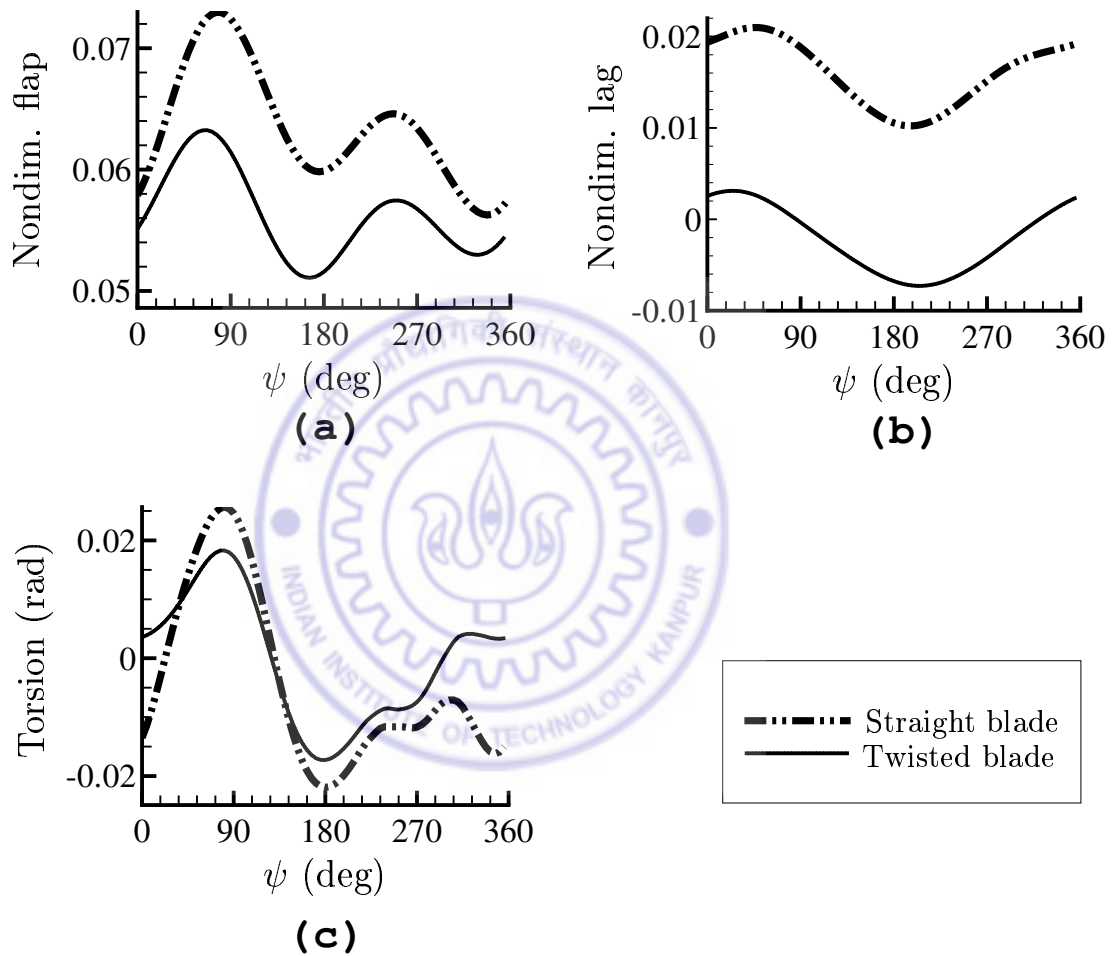
Figure 6.34: Comparison of tip deformations of the rotor blade for twisted and straight blade configurations as a function of azimuth for $\mu = 0.35$ obtained using DSDW model
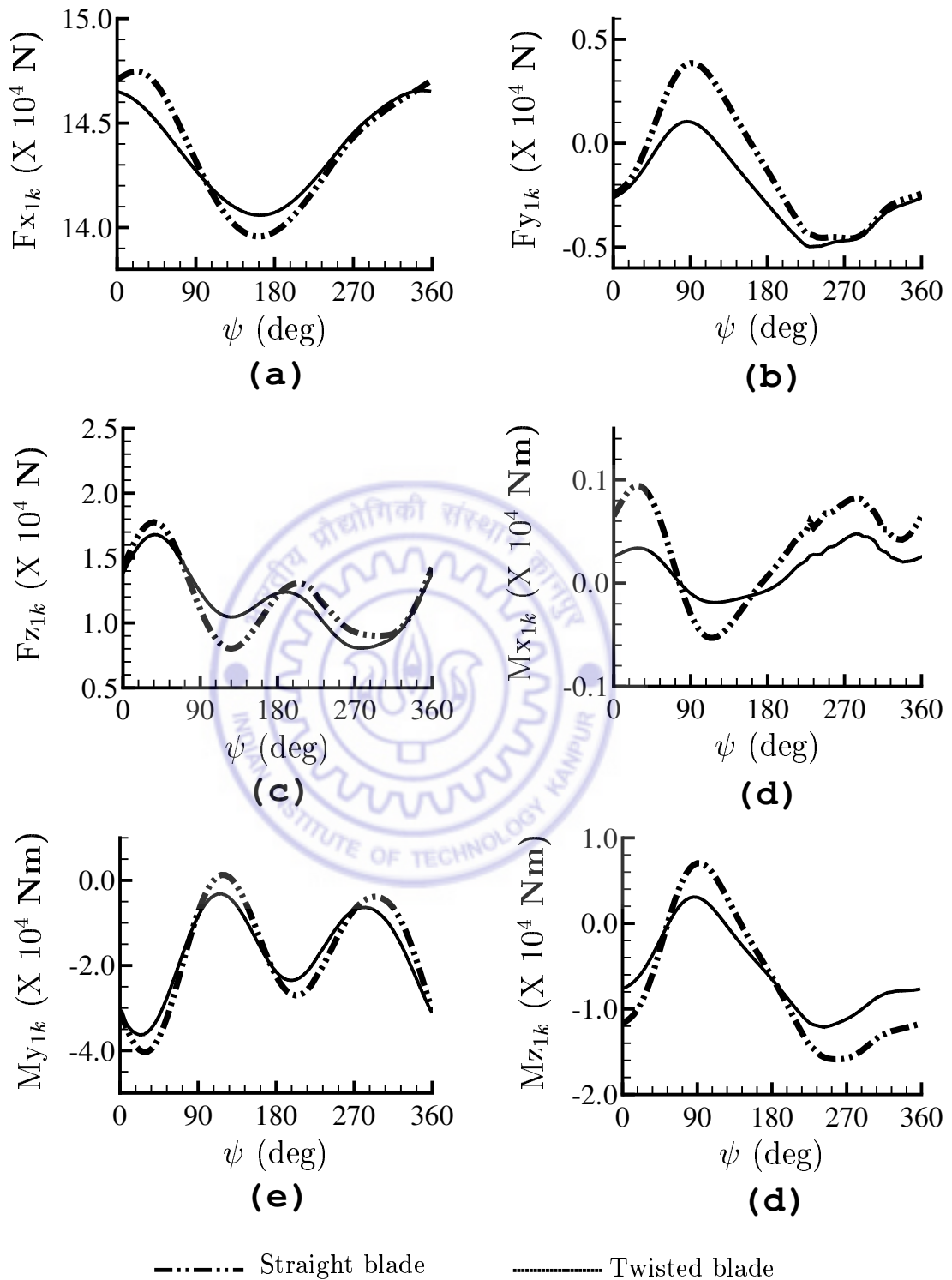
Figure 6.35: Comparison of root loads for twisted and straight blade configurations as a function of azimuth for $\mu = 0.35$ obtained using DSDW model
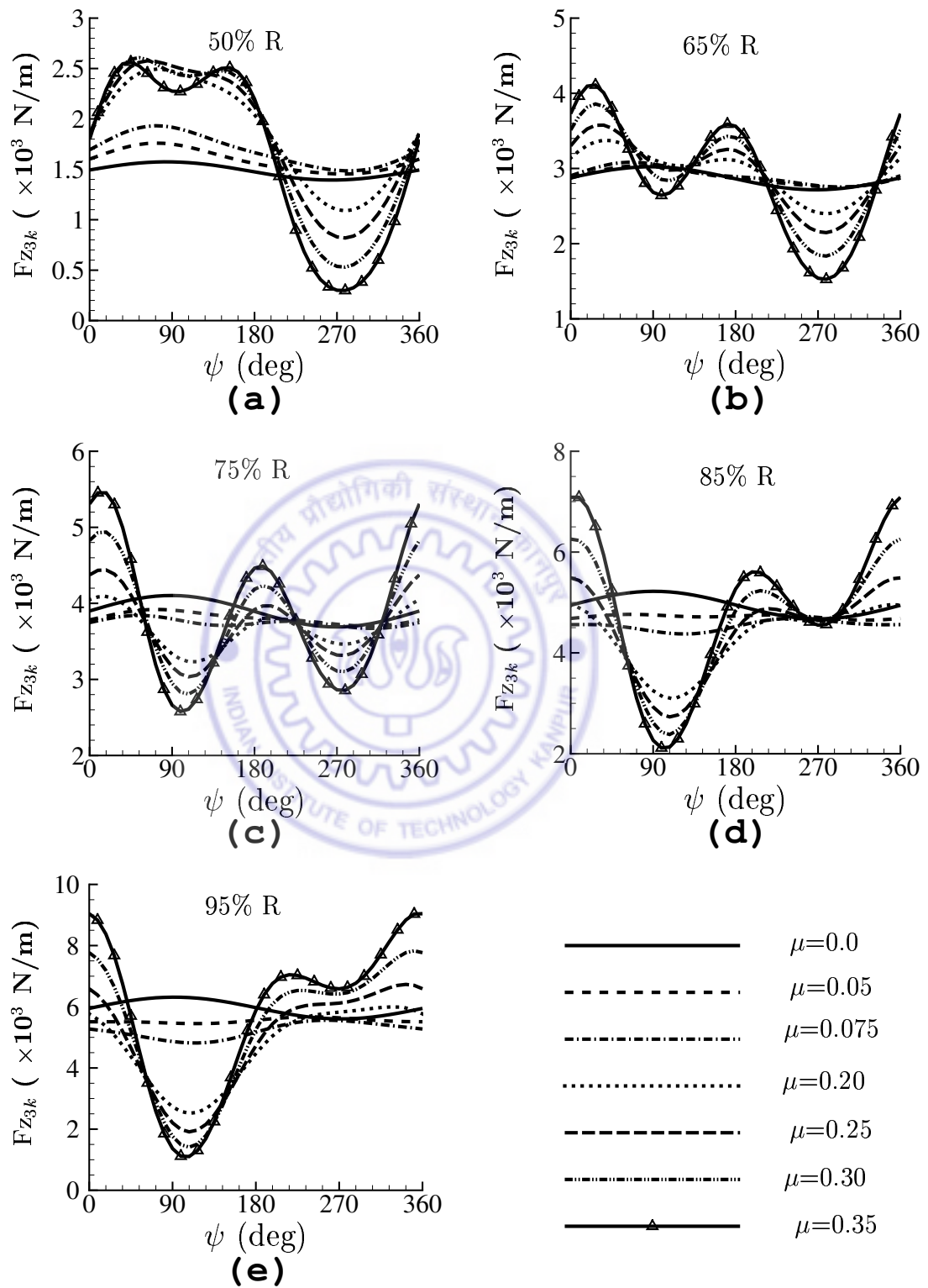
Figure 6.36: Variation of sectional aerodynamic lift for different forward speeds
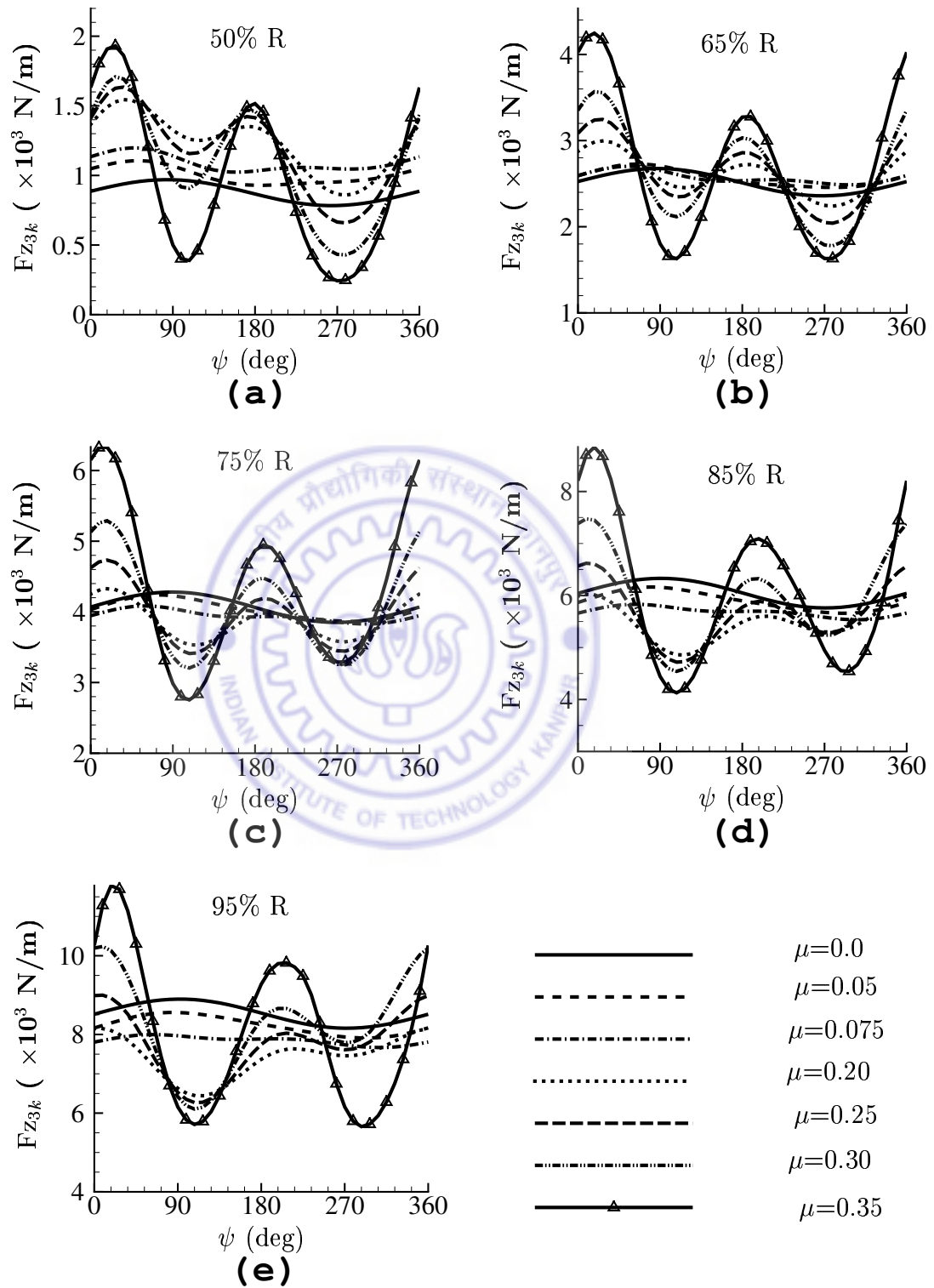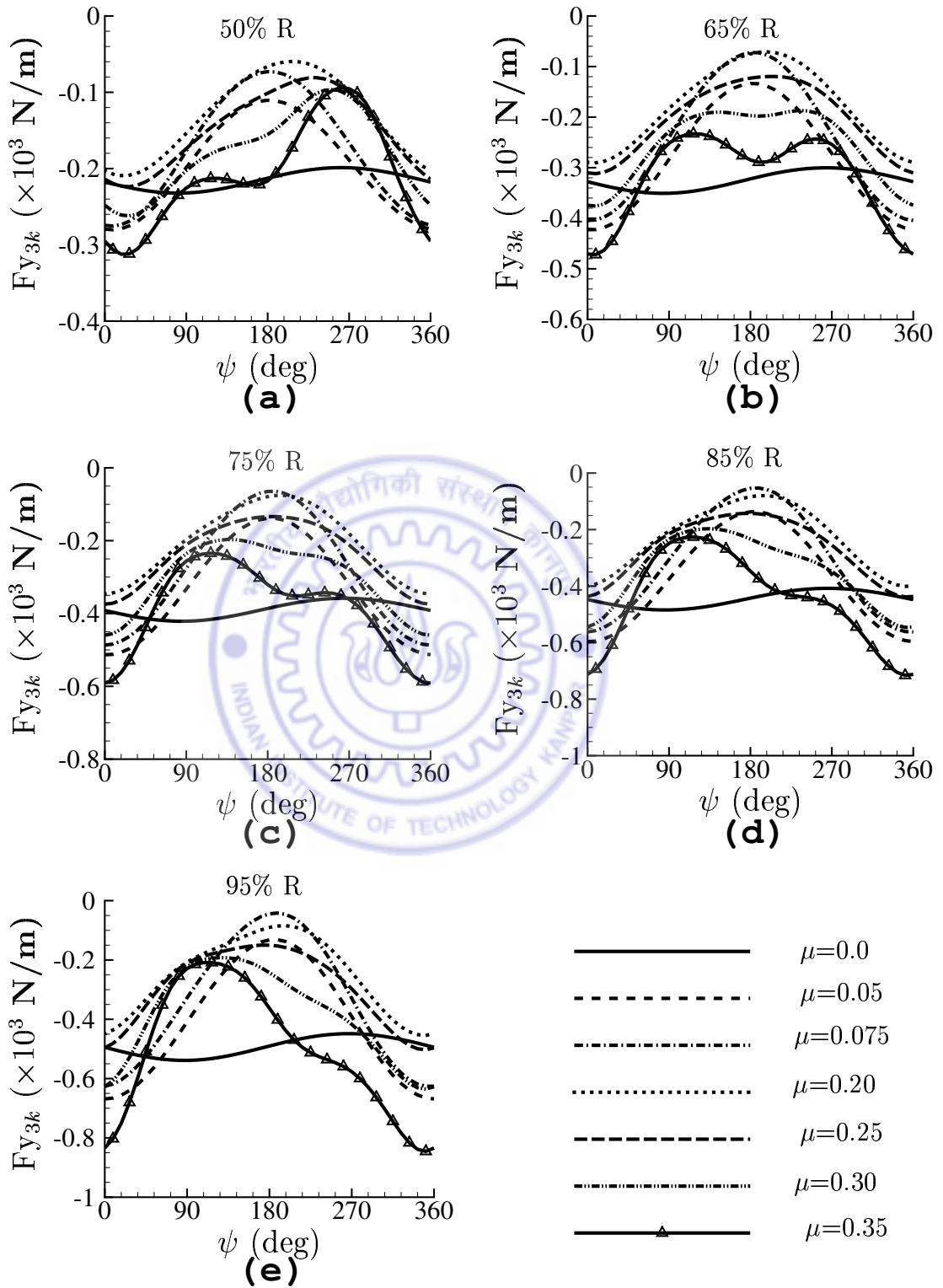
Figure 6.37: Variation of sectional aerodynamic drag for different forward speeds
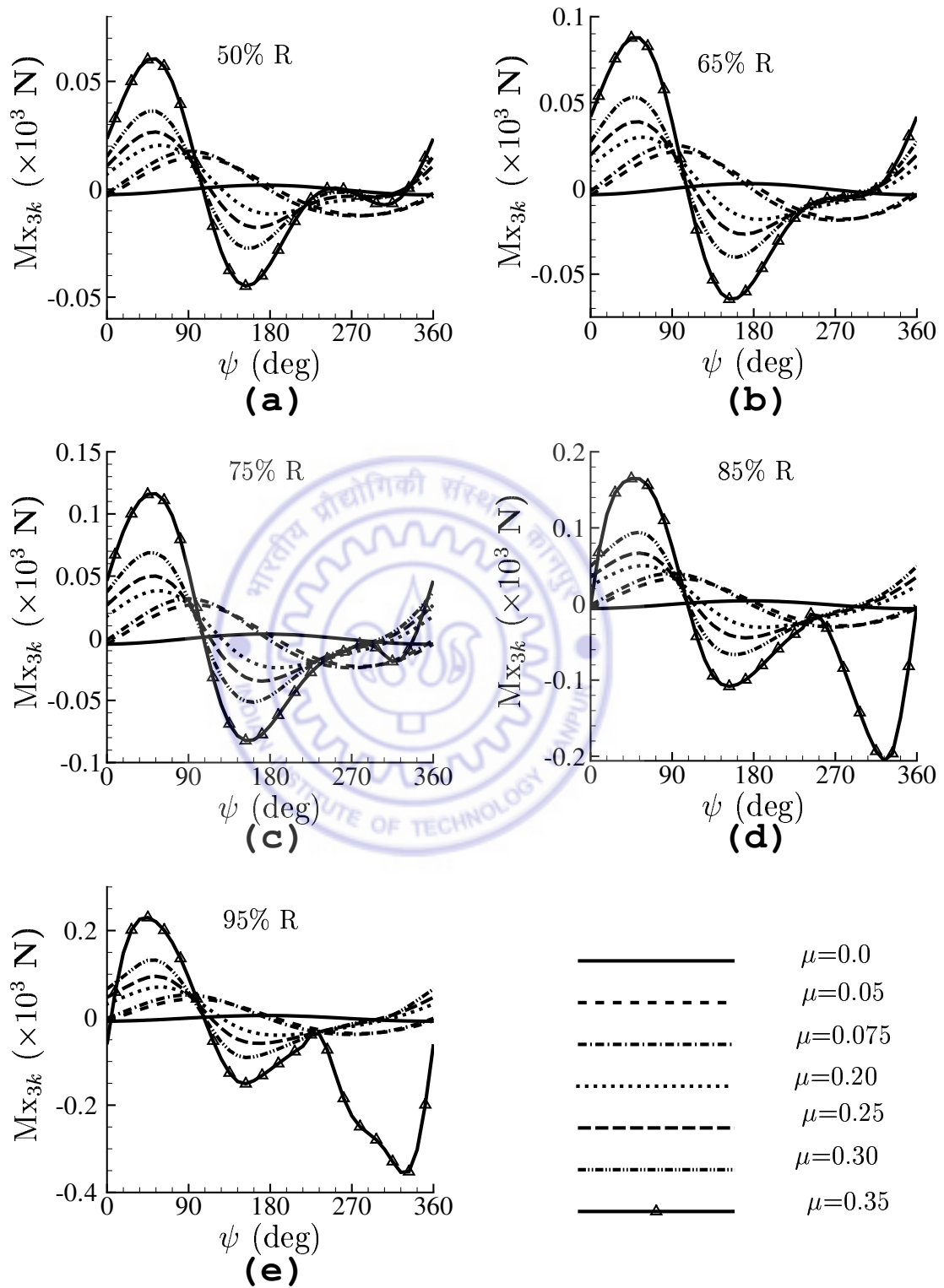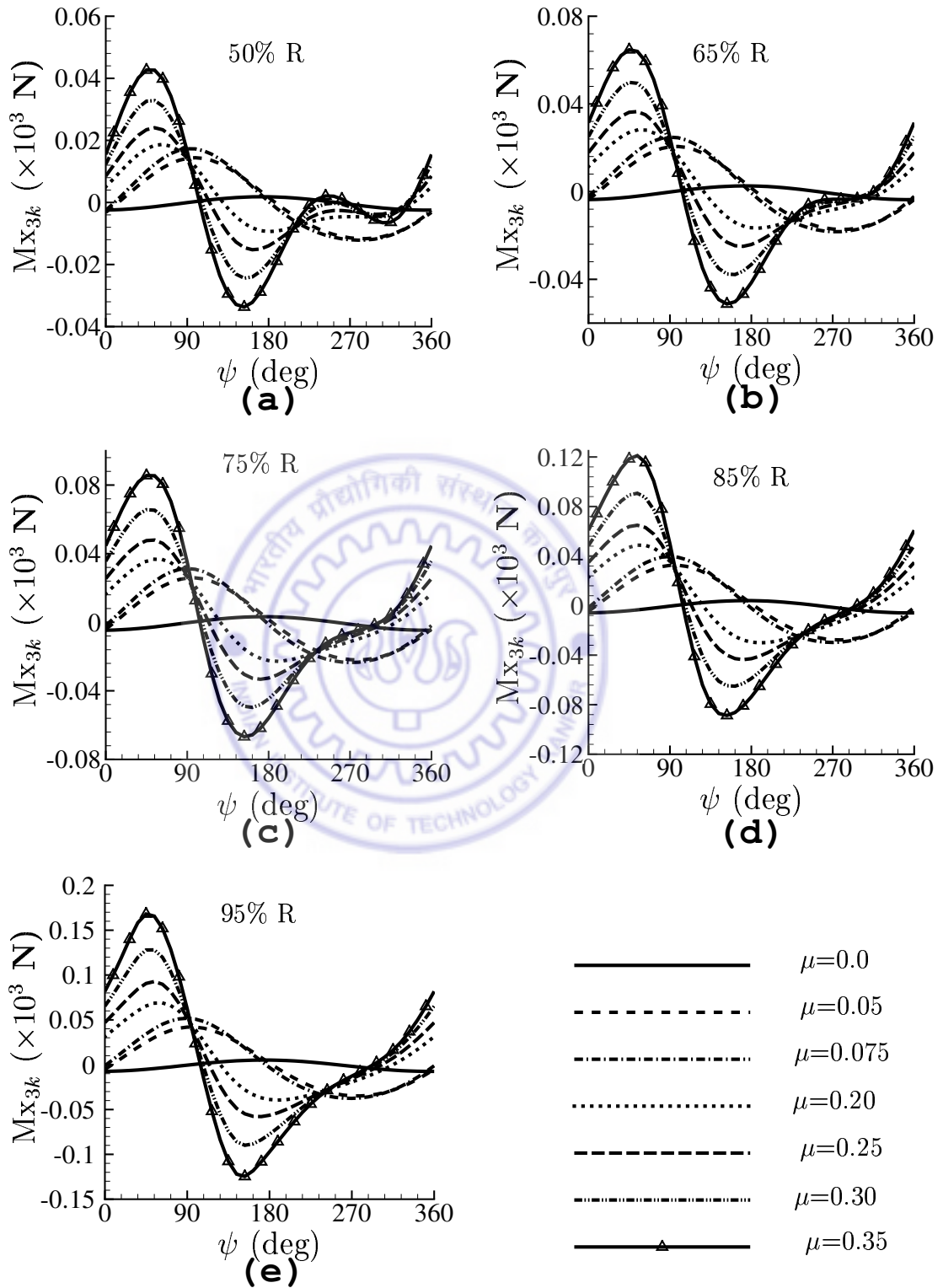
Figure 6.38: Variation of sectional aerodynamic moment for different forward speeds
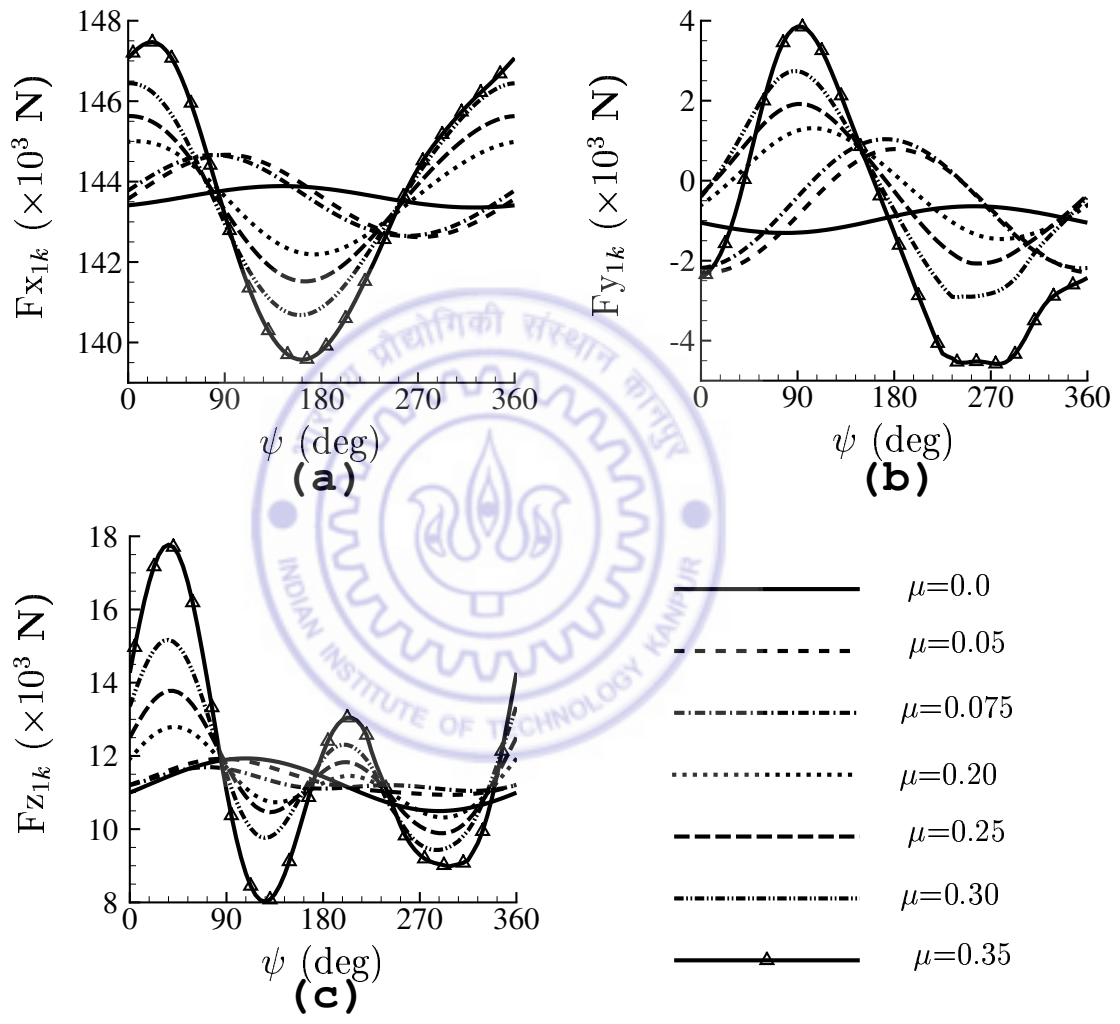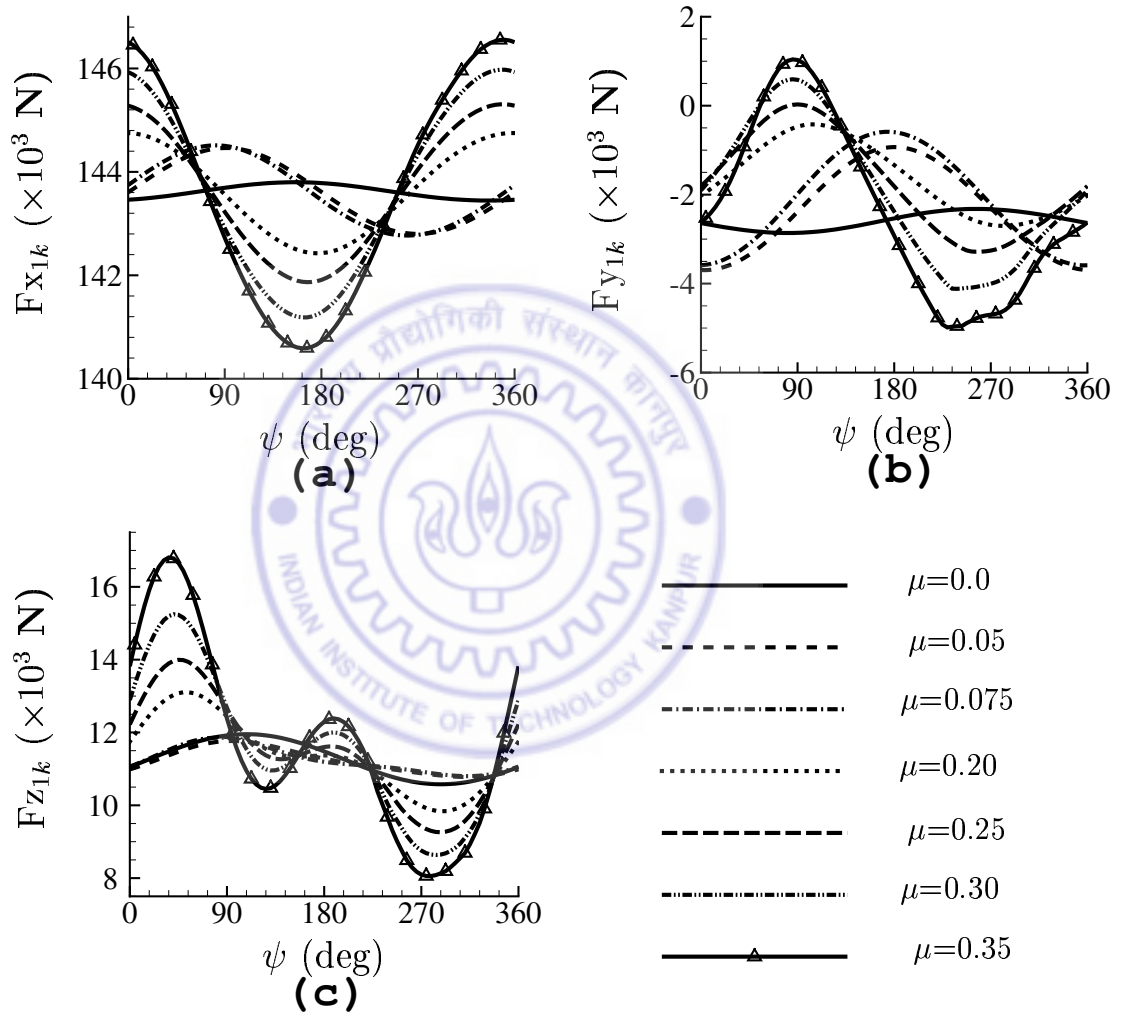
Figure 6.39: Blade root forces for various forward speeds
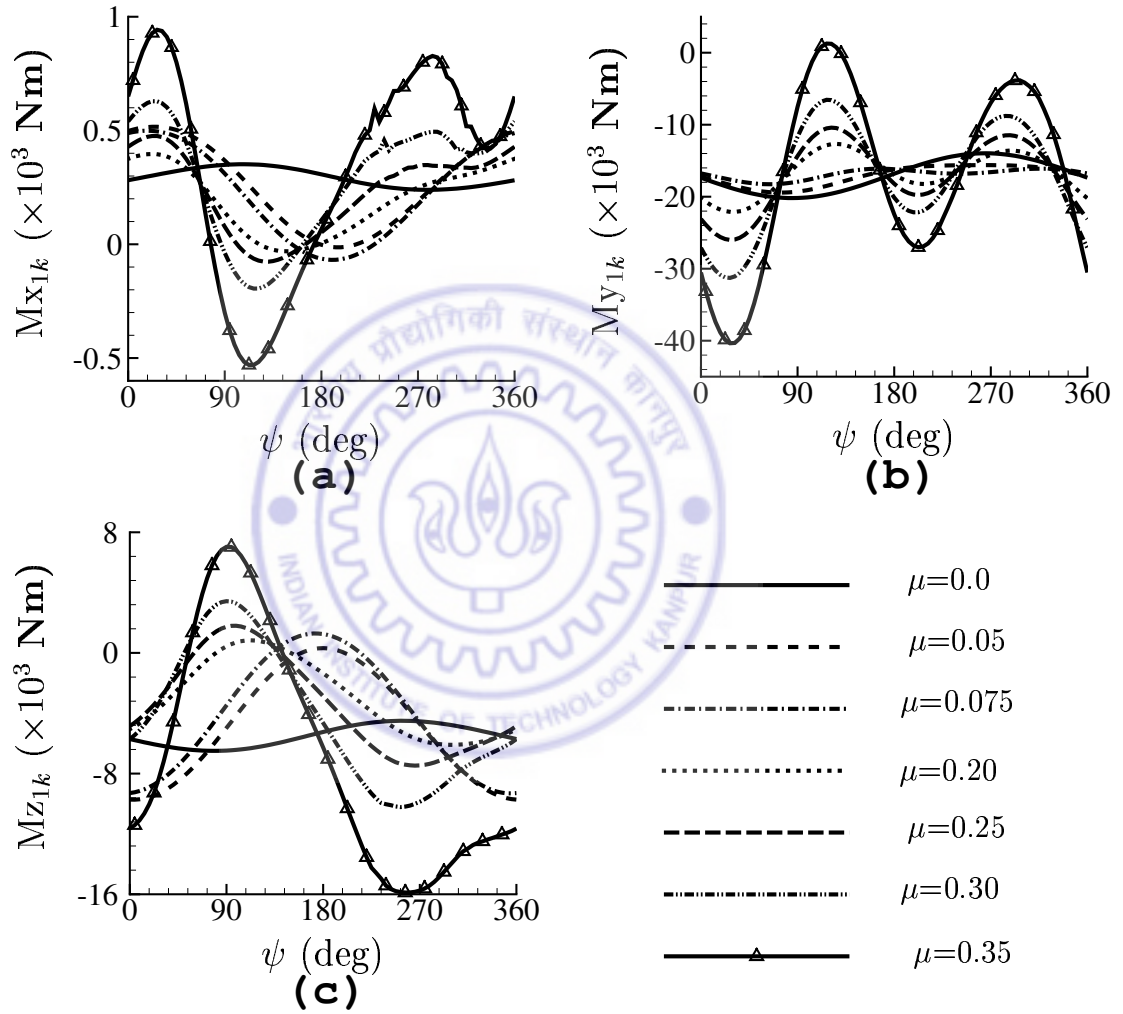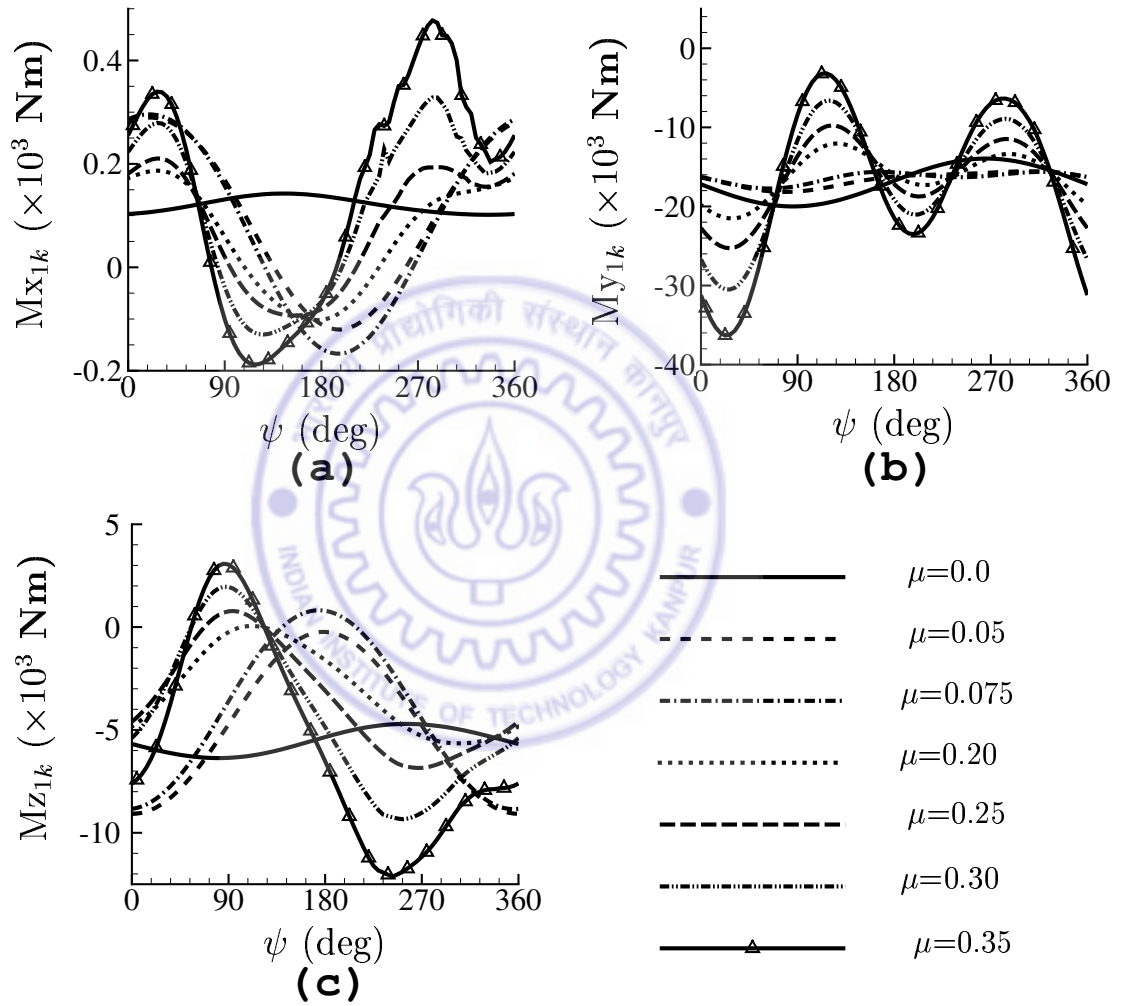
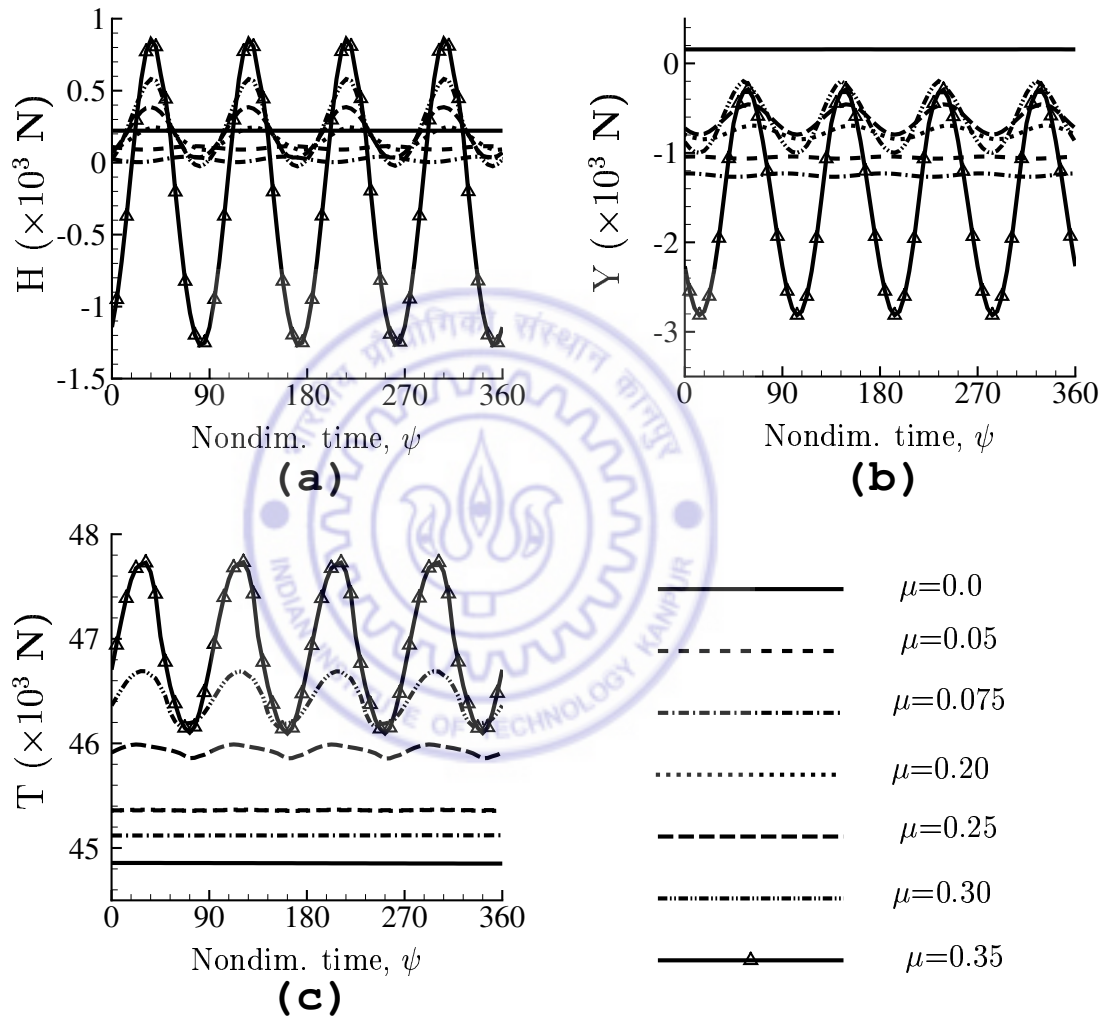Figure 6.40: Blade root moments for various forward speeds

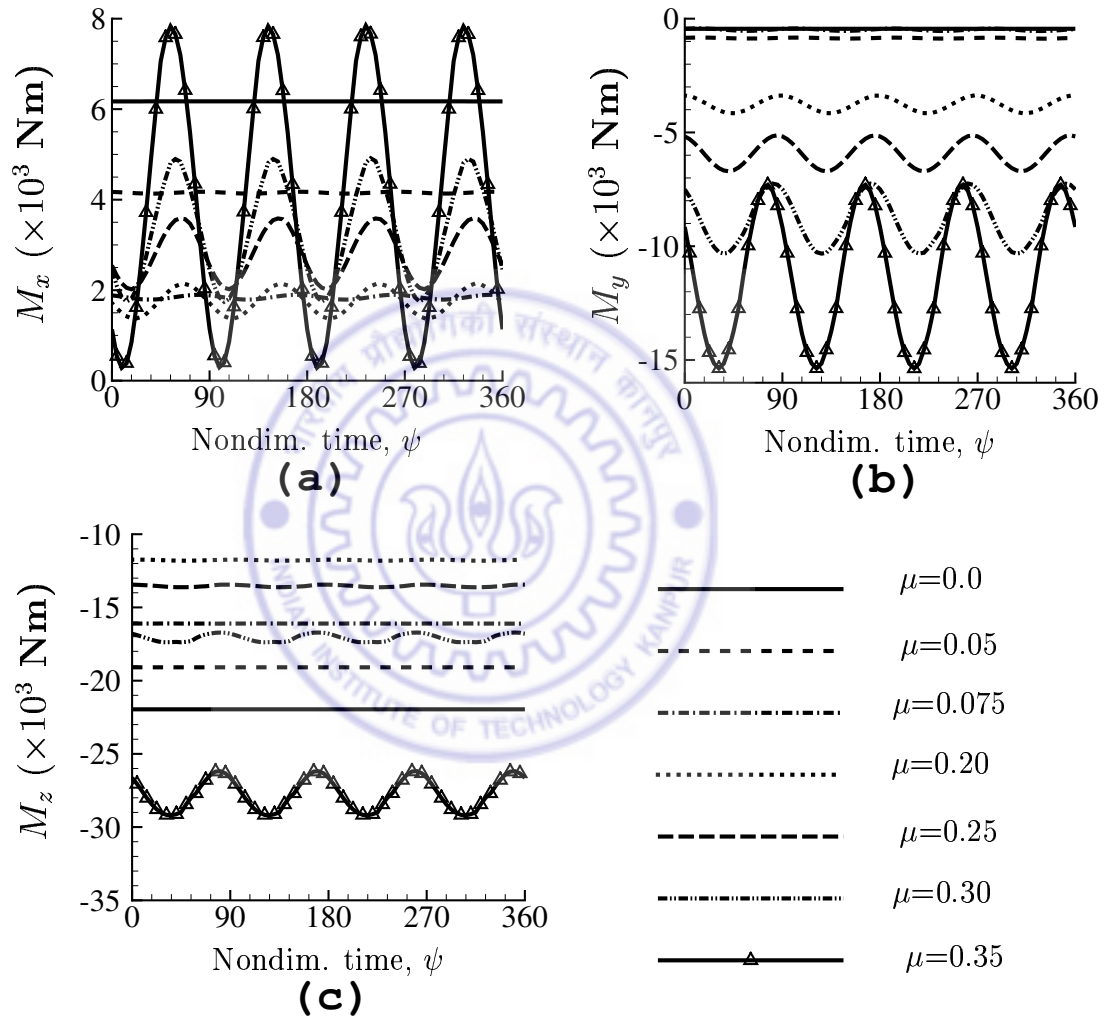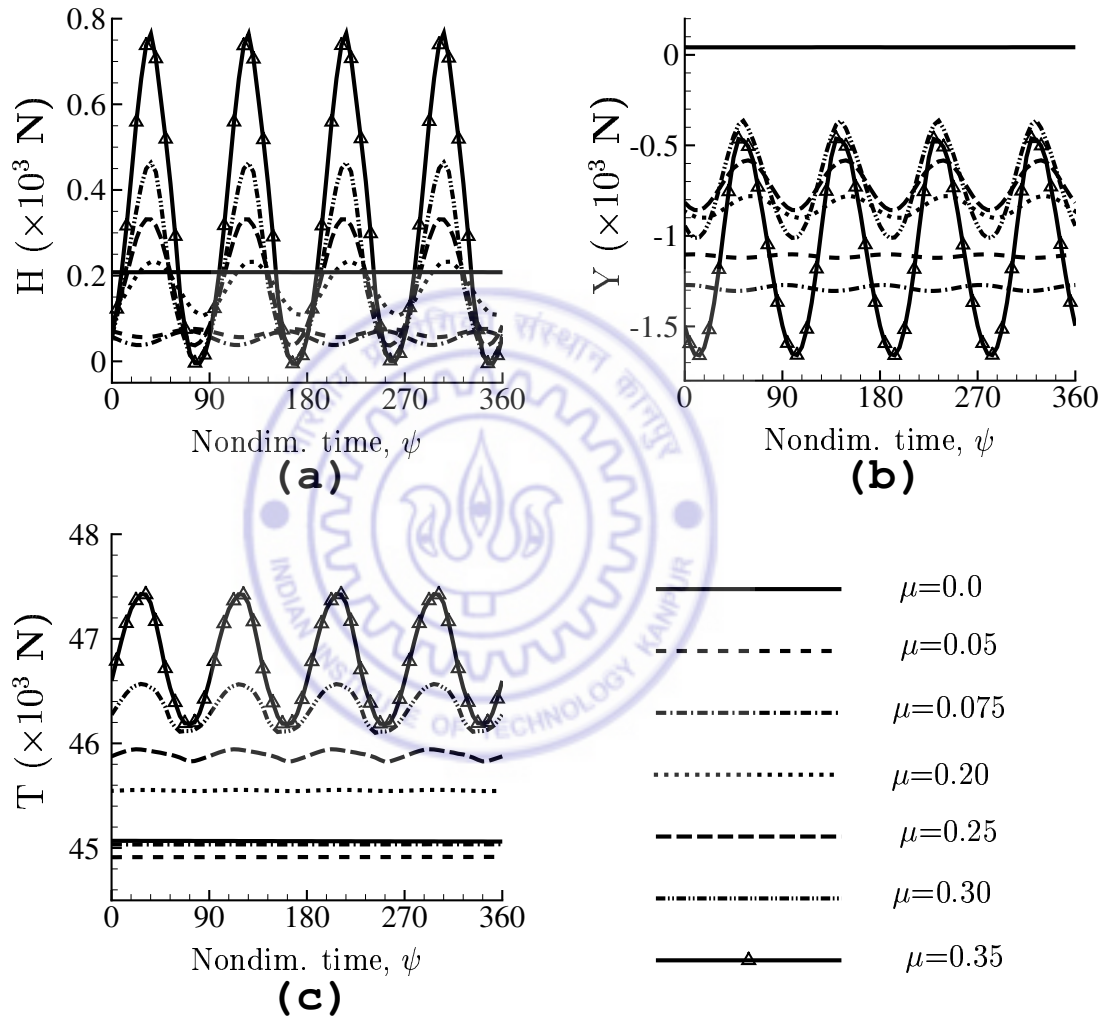Figure 6.41: Hub forces for various forward speeds
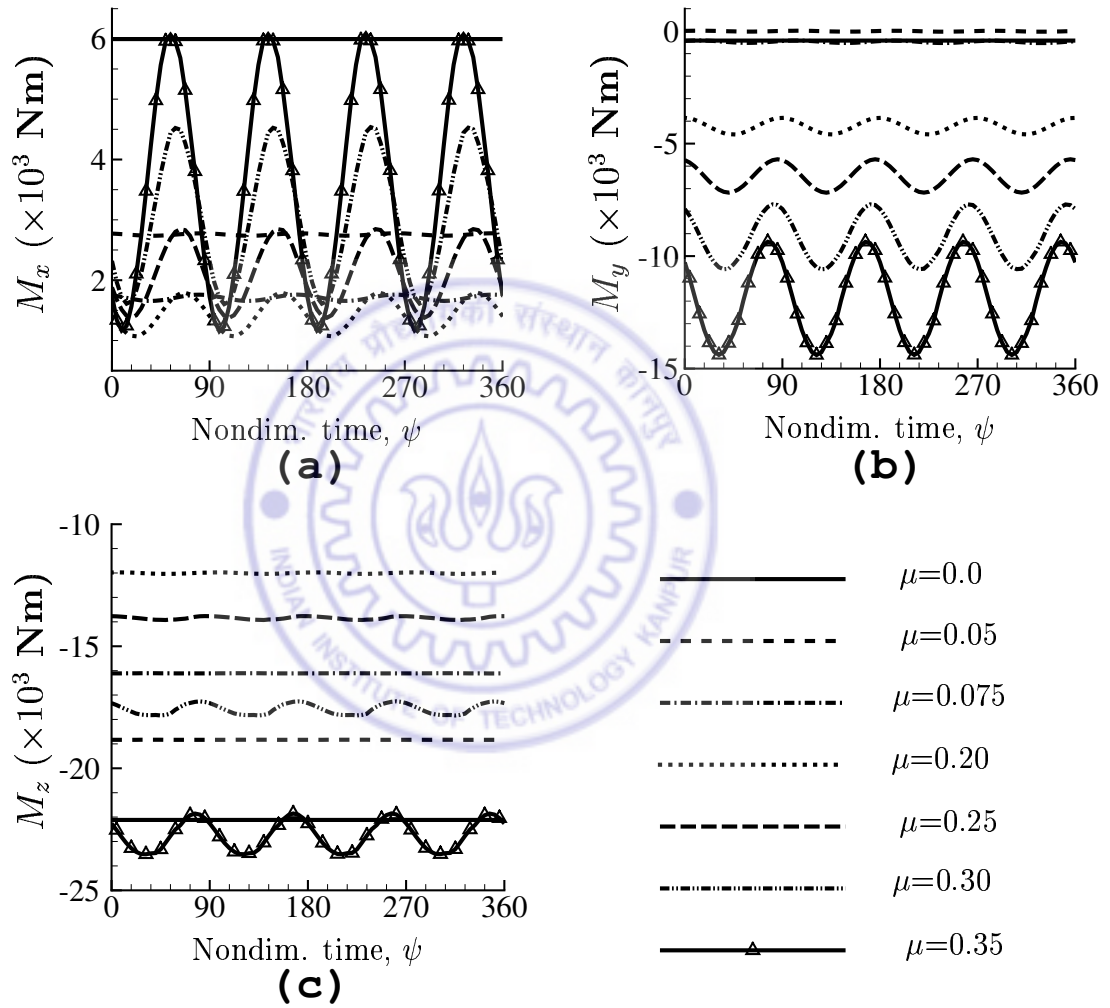
Figure 6.42: Hub moments for various forward speeds
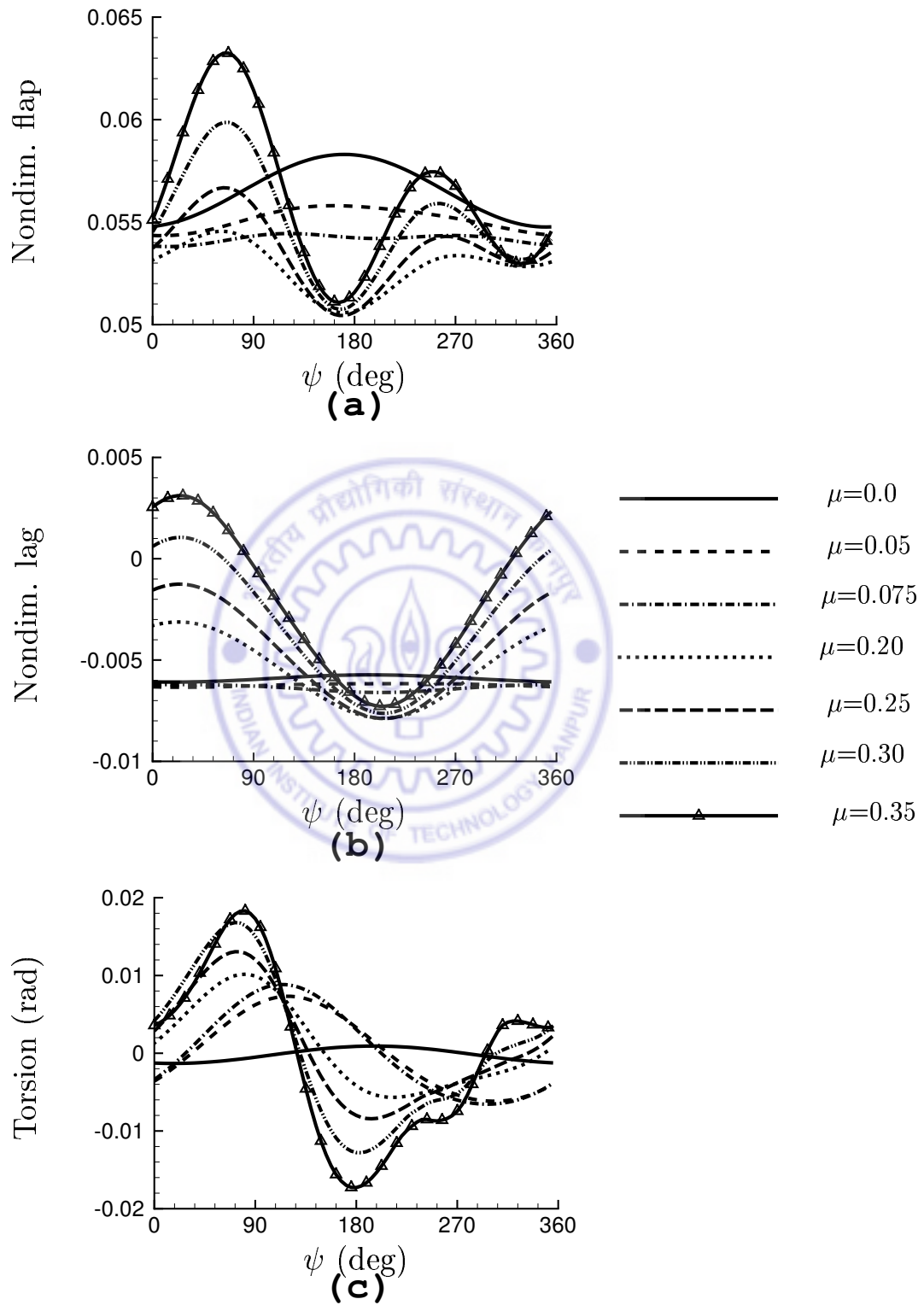
Figure 6.43: Tip response for various forward speeds

Chapter 7

CONCLUSIONS

Flight test data of helicopters indicate that vibratory levels in the fuselage exhibit a wide spectrum of frequencies including the dominant blade passage frequency and its integer multiples. The present work attempts to understand the reason for the existence of several frequencies in the response of the fuselage and possible cause for this observed phenomenon by formulating a computational aeroelastic model. In this thesis, dynamic stall and dynamic wake effects are incorporated in a coupled aeroelastic analysis to investigate blade sectional loads, hub loads and trim condition of the helicopter. The differential equations of motion are solved in time domain in a sequential manner to obtain the response of all the blades in the rotor system, the inflow variables, and the sectional loads at every time step. The influence of aerodynamic modeling on the trim condition and aeroelastic response of the rotor blade in forward flight has been brought out. The results of the study are presented in two major sections.

The first part of the work addresses a detailed study of the ONERA (EDLin) dynamic stall model. Based on this study, an improved ONERA dynamic stall model has been proposed. The response charasteristics of a 2-D airfoil undergoing pitching and plunging motion in a time varying oncoming flow, simulating the dynamics of a typical section of a rotor blade in forward flight are analysed.

The important observations of this study can be summarised as:

1. ONERA(EDLin) dynamic stall model has been analysed in relation to Theodorsen's and Greenberg's unsteady aerodynamic theory. It is shown that ONERA(EDLin) dynamic stall model in the unstalled region is identical to Theodorsen's model except that the lift deficiency function $C(k)$ is approximated by a first order rational approximation. Replacing first order rational approximation by more accurate second order rational approximation, a $modified$ dynamic stall model is proposed. This improved stall model is shown to provide a better correlation with experimental stall data.

2. Using the $modified$ stall model, the response characteristics of a 2-D airfoil undergoing pitching and plunging motion in a pulsating oncoming flow are analysed to study the effects of dynamic stall. The results of this study show that the dynamic stall in association with aeroelastic couplings above a certain level leads to bounded chaotic motion of the airfoil.

In the second part of the thesis, a computational aeroelastic model has been developed, wherein the equations representing the blade dynamics, rotor inflow and sectional aerodynamics including stall are solved in a sequential manner. A four bladed system with proper spacing in the azimuth angle has been considered for the analysis. By solving simultaneously the response of all the blades, one can identify the difference in the response of the blades as they go around the azimuth. Since the response and loads of all the blades are solved at every instant of time, the time varying hub loads and time varying inflow (dynamic wake effects) can be captured. A systematic study is undertaken to analyse the influence of five different aerodynamic models, representing rotor inflow and sectional aerodynamic loads, on the helicopter trim and aeroelastic response of the rotor blades. The influence of blade pretwist on rotor loads and response has also been studied.

The important observations of this study can be summarised as:

1. The lateral cyclic pitch (θ_{1c}) setting required for trim is significantly affected by rotor inflow at low forward speeds ($0 < \mu < 0.1$), and by dynamic stall effects at forward speeds ($\mu > 0.15$). It is also found that the aerodynamic model, incorporating dynamic wake and dynamic stall effects, predicts the trim parameter (θ_{1c}) whose variation with forward speed resembles closely to those obtained in flight test.

2. At low forward speeds ($0 < \mu < 0.1$), the sectional lift at various cross-sections of the blade, exhibits one/rev variation with small amplitude. Whereas, high forward speeds introduce large variation in the sectional lift with additional harmonics.

3. At high forward speeds, the azimuthal location in the advancing side where the minimum value of the sectional lift occurs, is influenced by dynamic stall effects.

4. At high forward speeds, dynamic stall effects significantly increase the torsional response of the rotor blade.

5. The results of this study clearly show that dynamic stall and dynamic wake model introduces large number of harmonics in the hub loads, including those below the blade passage frequency and its integer multiples.

6. The structural coupling due to blade pretwist is observed to significantly alter the time variation of the sectional loads as compared to the loads obtained for a straight untwisted blade. This result indicates that aeroelastic couplings have a significant influence on the rotor loads.

Bibliography

[1] Friedmann, P. P., "Renaissance of Aeroelasticity and Its Future," *Journal of Aircraft*, Vol. 36, No. 1, 1999, pp. 105-121.

[2] Friedmann, P. P., and Hodges, D. H., "Rotary Wing Aeroelasticity — A Historical Perspective," *Journal of Aircraft*, Vol. 40, No. 6, 2003, pp. 1019-1046.

[3] Friedmann, P. P., "Rotary Wing Aeroelasticity: Current Status and Future Trends," *AIAA Journal*, Vol. 42, No. 10, 2004, pp. 1953-1972.

[4] Lytwyn, R. T., "An Analysis of the Divergent Vertical Helicopter Oscillations Resulting from the Physical Presence of the Pilot in the Collective Control Loop," *Proceedings of the 22nd Annual Forum of the American Helicopter Society*, Washington, D.C., 1966.

[5] Bousman, W. G., "Putting the Aero Back Into Aeroelasticity," *Proceedings of the 8th Annual Workshop on Aeroelasticity of Rotorcraft Systems*, University Park, PA, USA, 1999.

[6] Prasad, C. G. N., Dwivedi, V., and Dutta, R., "Vibration Monitoring in Helicopter Structure Using Rotor Noise: Flight Test Results and Discussions," *Proceedings of the 15th National Seminar on Aerospace Structure*, Shree Maruthi Publishers, Coimbatore, India, 2007, pp. 161-165.

[7] Roget, B., and Chopra, I., "Individual Blade Control Methodology for a Rotor with Dissimilar Blades," *Journal of the American Helicopter Society*, Vol. 48, No. 3, 2003, pp. 176-185.

[8] Hodges, D. H., "Review of Composite Rotor Blade Modeling," *AIAA Journal*, Vol. 28, No. 3, 1990, pp. 561-564.

[9] Johnson, W., "Rotorcraft Dynamics Models for a Comprehensive Analysis," *Proceedings of the 54th Annual Forum of the American Helicopter Society*, Washington, D.C., 1998.

[10] Hodges, D. H., Saberi, H., and Ormiston, R. A., "Development of Nonlinear Beam Elements for Rotorcraft Comprehensive Analyses," *Journal of the American Helicopter Society*, Vol. 52, No. 1, 2007, pp. 36-48.

[11] Theodorsen, T., "General Theory of Aerodynamic Instability and the Mechanism of Flutter," *NACA Technical Report 496*, 1935.

[12] Greenberg, M. J., "Airfoil in Sinusoidal Motion in a Pulsating Stream," *NASA Technical Report 1326*, 1947.

[13] Loewy, R. G., "A Two Dimensional Approach to the Unsteady Aerodynamics of Rotor Wings," *Journal of the Aeronautical Sciences*, Vol. 24, No. 2, 1957, pp. 81-98.

[14] Friedmann, P. P., and Venkatesan. C., "Coupled Helicopter Rotor/Body Aeromechanical Stability Comparison of Theoretical and Experimental Results," *Journal of Aircraft*, Vol. 22, No. 2, 1985, pp. 148-155.

[15] Gaonkar, G. H., McNulty, M. J., and Nagabhushanam, J., "An Experimental and Analytical Investigation of Isolated Rotor Flap-Lag Stability in Forward Flight," *Journal of the American Helicopter Society*, Vol. 35, No. 2, 1990, pp. 25-34.

[16] Cernicchiaro, A., Coppotelli, G., Mastroddi, F., and Gennaretti, M. "Analysis of Helicopter Cabin Vibrations Due to Rotor Asymmetry and Gust Encounter," AIAA Paper No. 2003-1518, *Proceedings of the 44th AIAA/ASME/ASCE/AHS/ACS Structures, Structural Dynamics and Materials Conference*, Norfolk, Virginia, April 2003.

[17] Lee, H. G., Viswamurthy, S. R., and Shin, S. J., "Coupling of a Geometrically Exact Rotor Blade Analysis with Unsteady Aerodynamics and Dynamic Inflow," *American Helicopter Society Specialist's Conference on Aeromechanics*, San Francisco, CA, Jan., 2008.

[18] Pitt, D. M., and Peters, D. A., "Rotor Dynamic Inflow Derivatives and Time Constants from Various Inflow Models," *Proceedings of the 9th European Rotorcraft Forum*, Stresa, Italy, Sept. 1983.

[19] Peters, D. A., Boyd, D. D., and He, C. J., "Finite-State Induced-Flow Model for Rotors in Hover and Forward Flight," *Journal of the American Helicopter Society*, Vol. 34, No. 4, 1989, pp. 5-17.

[20] Leishman, J. G., and Crouse, G. L., "State-Space Model for Unsteady Airfoil Behavior and Dynamic Stall," AIAA Paper 89-1319, *Proceedings of the 30th AIAA/ASME/ASCE/AHS/ASC Structures, Structural Dynamics and Materials Conference*, Mobile Alabama, April 3-5, 1989.

[21] Meyer, M., and Matthies, H. G., "State-space Representation of Instationary Two-dimensional Airfoil Aerodynamics," *Journal of Wind Engineering and industrial Aerodynamics*, Vol. 92, 2004, pp. 263-274.

[22] Leishman, J. G., and Nguyen, K. Q., "State-space Representation of Unsteady Airfoil Behavior," *AIAA Journal*, Vol. 28, No. 5, 1990, pp. 836-844.

[23] Petot, D., "Progress in the Semi-Empirical Prediction of the Aerodynamic Forces due to Large Amplitude Oscillations of an Airfoil in Attached or Detached Flow," 9th *European Rotorcraft Forum*, Stresa, Italy, Sept. 13-15, 1983.

[24] Truong, V. K., "Oscillatory Behavior of Helicopter Rotor Airloads in the Blade Stall Regime," *Journal of Aircraft*, Vol. 32, No. 5, 1995, pp. 1148-1149.

[25] Srinivasan, G. R., Baeder, J. D., Obayashi, S., and McCroskey, W. J., "Flowfield of a Lifting Rotor in Hover: A Navier - Stokes Simulation," *AIAA Journal*, Vol. 30, No. 10, 1992, pp. 2371-2378.

[26] Strawn, R. C., Caradonna, F. X., and Duque, E. P. N., "30 Years of Rotorcraft Computational Fluid Dynamics Research and Development," *Journal of the American Helicopter Society*, Vol. 51, No. 1, 2006, pp. 5-21.

[27] Houbolt, J. C., and Brooks, G. W., "Differential Equations of Motion for Combined Flapwise Bending, Chordwise Bending and Torsion of Twisted Nonuniform Rotor Blades," *NACA Report 1346*, 1958.

[28] Friedmann, P. P., "Recent Developments in Rotary-wing Aeroelasticity," *Journal of Aircraft*, Vol. 14, No. 11, 1977, pp. 1027-1041.

[29] Hodges, D. H., and Dowell, E. H., "Nonlinear Equations of Motion for the Elastic Bending and Torsion of Twisted Non-uniform Rotor Blades," *NASA TN D-7818*, 1974.

[30] Kvaternik, R. G., and Kaza, K. R., "Nonlinear Curvature Expressions for Combined Flapwise Bending, Chordwise Bending, Torsion and Extension of Twisted Rotor Blades," *NASA TM-X-73997*, 1976.

[31] Kaza, K. R., and Kvaternik, R. G., "Nonlinear Aeroelastic Equations for Combined Flapwise Bending, Chordwise Bending, Torsion and Extension of Twisted Nonuniform Rotor Blades in Forward Flight," *NASA TM-74059*, 1977.

[32] Rosen, A., and Friedmann, P. P., "Nonlinear Equations of Equilibrium for Elastic Helicopter or Wind Turbine Blades Undergoing Moderate Deformation," *NASA CR-159478*, 1978.

[33] Dowell, E. H., Traybar, J., and Hodges, D. H., "An Experimental Theoretical Correlation Study of Non-linear Bending and Torsion Deformations of a Cantilever Beam," *Journal of Sound and Vibrations*, Vol. 50, No. 4, 1977, pp. 533-544.

[34] Borri, M., and Merlini, T., "A Large Displacement Formulation for Anisotropic Beam Analysis," *Meccanica*, Vol. 21, No. 1, 1986, pp. 30-37.

[35] Bauchau, O. A., "A Beam Theory for Anisotropic Materials," *Journal of Applied Mechanics*, Vol. 52, 1985, pp. 416-422.

[36] Bauchau, O. A., and Hong, C. H., "Large Displacement Analysis of Naturally Curved and Twisted Composite Beams," *AIAA Journal*, Vol. 25, No. 11, 1987, pp. 1469-1475.

[37] Minguet, P., and Dugundji, J., "Experiments and Analysis for Composite Blades under Large Deflection: Part 1 - Static Behavior," *AIAA Journal*, Vol. 28, No. 9, 1990, pp. 1573-1579.

[38] Minguet, P., and Dugundji, J., "Experiments and Analysis for Composite Blades under Large Deflection: Part 2 - Dynamic Behavior," *AIAA Journal*, Vol. 28, No. 9, 1990, pp. 1580-1588.

[39] Kalfon, J. P., and Rand, O., "Nonlinear Analysis of Composite Thin-Walled Helicopter Blades," *Computers and Structures*, Vol. 48, No. 1, 1993, pp. 51-61.

[40] Kosmatka, J. B., and Friedmann, P. P., "Vibration Analysis of Composite Turbopropellers Using a Nonlinear Beam Type Finite Element Approach," *AIAA Journal*, Vol. 27, No. 11, 1989, pp. 1606-1614.

[41] Smith, E. C., and Chopra, I., "Formulation and Evaluation of an Analytical Model for Composite Box Beams," *Journal of the American Helicopter Society*, Vol. 36, No. 3, 1991, pp. 23-35.

[42] Song, O., and Librescu, L., "Structural Modeling and Free Vibration Analysis of Rotating Composite Thin-Walled Beams," *Journal of the American Helicopter Society*, Vol. 42, No. 4, 1997, pp. 358-369.

[43] Kunz, D. L., "Survey and Comparison of Engineering Beam Theories for Helicopter Rotor Blades," *Journal of Aircraft*, Vol. 31, No. 3, 1994, pp. 473-479.

[44] Friedmann, P. P., "Helicopter Rotor Dynamics and Aeroelasticity: Some Key Ideas and Insights," *vertica*, Vol. 14, No. 1, 1990, pp. 101-121.

[45] Jung, S. N., Nagaraj, V. T., and Chopra, I., "Assessment of Composite Rotor Blade Modeling Techniques," *Journal of the American Helicopter Society*, Vol. 44, No. 3, 1999, pp. 188-205.

[46] Stemple, A. D., and Lee, S. W., "Finite Element Model for Composite Beams with Arbitrary Cross-Sectional Warping," *AIAA Journal*, Vol. 26, No. 12, 1988, pp. 1512-1520.

[47] Rehfield, L. W., Atilgan, A. R., and Hodges, D. H., "Nonclassical Behavior of Thin-Walled Composite Beams with Closed Cross Sections," *Journal of the American Helicopter Society*, Vol. 35, No. 2, 1990, pp. 42-50.

[48] Atilgan, A. R., and Hodges, D. H., "Unified Nonlinear Analysis for Nonhomogeneous Anisotropic Beams with Closed Cross Sections," *AIAA Journal*, Vol. 29, No. 11, 1991, pp. 1990-1999.

[49] Wörndle, R., "Calculation of the Cross Section Properties and the Shear Stresses of Composite Rotor Blades," *Vertica*, Vol. 6, No. 2, 1982, pp. 111-129.

[50] Cesnik, C. E. S., and Hodges, D. H., "VABS: A New Concept for Composite Rotor Blade Cross-Sectional Modeling," *Journal of the American Helicopter Society*, Vol. 42, No. 1, 1997, pp. 27-38.

[51] Panda, B., "Assembly of Moderate-Rotation Finite Elements Used in Helicopter Rotor Dynamics," *Journal of the American Helicopter Society*, Vol. 32, No. 4, 1987, pp. 63-69.

[52] Celi, R., and Friedmann, P. P., "Structural Optimization with Aeroelastic Constraints of Rotor Blades with Straight and Swept Tips," *AIAA Journal*, Vol. 28, No. 5, 1990, pp. 928-945.

[53] Kim, K. C., and Chopra, I., "Aeroelastic Analysis of Swept, Anhedral, and Tapered Tip Rotor Blades," *Journal of the American Helicopter Society*, Vol. 37, No. 1, 1992, pp. 15-30.

[54] Yuan, K. A., and Friedmann, P. P., "Aeroelasticity and Structural Optimization of Composite Helicopter Rotor Blades with Swept Tips," *NASA CR 4665*, May 1995.

[55] Kim, K. C., and Chopra, I., "The Natural Frequencies of Rotating Composite beams with Tip Sweep," *Journal of the American Helicopter Society*, Vol. 41, No. 1, 1996, pp. 29-36.

[56] Johnson, W., *Helicopter Theory*, Princeton University Press, Princeton, NJ, 1980.

[57] Coleman, R. P., Feingold, A. M., and Stempin, C. W., "Evaluation of the Induced-Velocity Field of an Idealized Helicopter Rotor," *NACA ARR L5E10*, 1945.

[58] Bramwell, A. R. S., *Helicopter Dynamics*, Edward Arnold Publishers Ltd., London, 1976.

[59] Stepniewski, W. Z., and Keys, C. N., *Rotary-wing Aerodynamics*, Dover Publications, Inc., New York, 1984.

[60] Landgrebe, A. J., "The Wake Geometry of a Hovering Helicopter Rotor and Its Influence on Rotor Performance," *Journal of the American Helicopter Society*, Vol. 17, No. 4, 1972, pp. 2-15.

[61] Kocurek J. D., Tangler J. L., "A Prescribed Wake Lifting Surface Hover Performance Analysis," *Journal of the American Helicopter Society*, Vol. 22, No. 1, 1977, pp. 24-35.

[62] Egolf, T. A., and Landgrebe, A. J., "Helicopter Rotor Wake Geometry and Its Influence in Forward Flight; Vol. 1: Generalized Wake Geometry and Wake Effect in Rotor Airloads and Performance," *NASA CR-3726*, 1983.

[63] Johnson, W., "A General Free Wake Geometry Calculation For Wings and Rotors," *Proceedings of the 51st Annual Forum of the American Helicopter Society*, Washington, D.C., 1995.

[64] Bagai, A., and Leishman, J. G., "Adaptive Grid Sequencing and Interpolation Schemes for Helicopter Rotor Wake Analyses," *AIAA Journal*, Vol. 36, No. 9, 1998, pp. 1593-1602.

[65] Gray, R. B., "Vortex Modeling for Rotor Aerodynamics — The 1991 Alexander A. Nikolsky Lecture," *Journal of the American Helicopter Society*, Vol. 37, No. 1, 1992, pp. 3-14.

[66] Leishman, J. G., *Principles of Helicopter Aerodynamics*, Cambridge University Press, Cambridge, UK, 2000.

[67] Manjunath, A. R., "Rotor Stability in Hover and Forward Flight With a Generalized Dynamic Wake," *Ph.D. Thesis*, Indian Institute of Science, May 1993.

[68] Carpenter, P. J., and Fridovitch, B., "Effect of Rapid Blade Pitch Increase on the Thrust and Induced Velocity Response of a Full Scale Helicopter Rotor," *NACA TN - 3044*, Nov. 1953.

[69] Curtiss, H. C. Jr., and Shupe, N. K., "Stability and Control Theory for Hingeless Rotors," *Annual Forum American Helicopter Society*, Nov. 1971.

[70] Ormiston, R. A., and Peters. D. A., "Hingeless Helicopter Rotor Response with Nonuniform Inflow and Elastic Blade Bending," *Journal of Aircraft*, Vol. 9, No. 10, 1972, pp. 730-736.

[71] Crews, S. T., Hohenemser, K. H., and Ormiston, R. A., "An Unsteady Wake Model for Hingeless Rotor," *Journal of Aircraft*, Vol. 10, No. 12, 1973, pp. 758-760.

[72] Johnson, W., "The Influence of Various Unsteady Aerodynamic Models on the Aeromechanical Stability of a Helicopter in Ground Resonance," *NASA TM 81302*, July 1981.

[73] Johnson, W., "The Influence of Unsteady Aerodynamics on Hingeless Rotor Ground Resonance," *Journal of Aircraft*, Vol. 19, No. 8, 1982, pp. 668-673.

[74] Friedmenn, P. P., and Venkatesan, C., "Influence of Unsteady Aerodynamic Models on Aeromechanical Stability in Ground Resonance," *Journal of the American Helicopter Society*, Vol. 31, No. 1, 1986, pp. 65-74.

[75] Chen, R. T. N., and Hindson, W. S., "Influence of Dynamic Inflow on the Helicopter Vertical Response," *Vertica*, Vol.11, No.1/2, 1987, pp. 77-91.

[76] Chen, R. T. N., "A Survey of Nonuniform Inflow Models For Rotorcraft Flight Dynamics and Control Applications", *Vertica*, Vol.14, No.2, pp. 147-184, 1990.

[77] He, Cheng Jian., "Development and Application of a Generalized Dynamic Wake Theory for Lifting Rotors," *Ph.D. Thesis*, Georgia Institute of Technology, July 1989.

[78] Peters, D. A., Karunamoorthy, S. N., and Cao, W. M., "Finite-State Induced Flow Models Part I : Two-Dimensional Thin Airfoil," *Journal of Aircraft*, Vol. 32, No. 2, 1995, pp. 313-322.

[79] Peters, D. A., and He, C. J., "Finite-State Induced Flow Models Part II : Three-Dimensional Rotor Disk," *Journal of Aircraft*, Vol. 32, No. 2, 1995, pp. 323-333.

[80] Peters, D. A., and He, C. J., "Correlation of Measured Induced Velocities with a Finite-State Wake Model," *Journal of the American Helicopter Society*, Vol. 36, No. 3, 1991, pp. 59-70.

[81] Keller, J. D., "An Investigation of Helicopter Dynamic Coupling Using an Analytical Model," *Journal of the American Helicopter Society*, Vol. 41, No. 4, 1996, pp. 322-330.

[82] Arnold, U. T. P., Keller, J. D., Curtiss, H. C., and Reichert, G., "The Effect of Inflow Models on the Predicted Response of Helicopters," *Journal of the American Helicopter Society*, Vol. 43, No. 1, 1998, pp. 25-35.

[83] Krothapalli, K. R., Prasad, J. V. R., and Peters, D. A., "Helicopter Rotor Dynamic Inflow Modeling for Maneuvering Flight," *Journal of the American Helicopter Society*, Vol. 46, No. 2, 2001, pp. 129-139.

[84] Peters, D. A., Morillo, J. A., and Nelson, A. M., "New Developments in Dynamic Wake Modeling for Dynamics Applications," *Journal of the American Helicopter Society*, Vol. 48, No. 2, 2003, pp. 120-127.

[85] Johnson, W., "Application of Unsteady Airfoil Theory to Rotary Wings," *Journal of Aircraft*, Vol. 17, No. 4, 1980, pp. 285-286.

[86] Kaza, K. R. V., and Kvaternik, R. G., "Application of Unsteady Airfoil Theory to Rotary Wings," *Journal of Aircraft*, Vol. 18, No. 7, 1981, pp. 604-605.

[87] Venkatesan, C., and Friedmann, P. P. "Aeroelastic Effects in Multi-Rotor Vehicles with Application to a Hybrid Heavy Lift System, Part-I. Formulation of Equations of Motion," *NASA CR-3822*, 1984.

[88] Venkatesan, C., and Friedmann, P. P. "A New Approach to Finite State Modelling of Unsteady Aerodynamics," *AIAA Journal*, Vol. 24, No. 12, 1986, pp. 1889-1897.

[89] Leishman, J.G., "Two-Dimensional Model for Airfoil Unsteady Drag Below Stall," *Journal of Aircraft*, Vol. 25, No. 7, 1988, pp. 665-666.

[90] Leishman, J.G., "Validation of Approximate Indicial Aerodynamic Functions for Two-Dimensional Subsonic Flow," *Journal of Aircraft*, Vol. 25, No. 10, 1988, pp. 914-922.

[91] Leishman, J.G., "Modeling of Subsonic Unsteady Aerodynamics for Rotary Wing Applications," *Journal of the American Helicopter Society*, Vol. 35, No. 1, 1990, pp. 29-38.

[92] Leishman, J.G., "Indicial Lift Approximations for Two-Dimensional Subsonic Flow as Obtained from Oscillatory Measurements," *Journal of Aircraft*, Vol. 30, No. 3, 1993, pp. 340-351.

[93] McCroskey, W. J., "Inviscid Flowfield of an Unsteady Airfoil," *AIAA Journal*, Vol. 11, No. 8, 1973, pp. 1130-1136.

[94] McCroskey, W. J., Carr, L. W., and McAlister, K. W., "Dynamic Stall Experiments on Oscillating Airfoils," *AIAA Journal*, Vol. 14, No. 1, 1976, pp. 57-63.

[95] McCroskey, W. J., McAlister, K. W., Carr, L. W., and Pucci, S. L., "An Experimental Study of Dynamic Stall on Advanced Airfoil Sections: Volume 2 - Pressure and Force Data; Volume 3 - Hot-Wire and Hot-film Measurements," *NASA TM - 84245*, July 1982.

[96] Carr, L. W., "Progress in Analysis and Prediction of Dynamic Stall," *Journal of Aircraft*, Vol. 25, No. 1, 1988, pp. 6-17.

[97] Chandrasekhara, M. S., and Carr, L. W., "Flow Visualization Studies of the Mach Number Effects on Dynamic Stall of an Oscillating Airfoil," *Journal of Aircraft*, Vol. 27, No. 6, 1990, pp. 516-522.

[98] Leishman, J.G., "Dynamic Stall Experiments on the NACA 23012 Airfoil," *Experiments in Fluids*, Vol. 9, 1990, pp. 49-58.

[99] Tang, D. M., and Dowell, E. H., "Experimental Investigation of Three-Dimensional Dynamic Stall Model Oscillating in Pitch," *Journal of Aircraft*, Vol. 32, No. 5, 1995, pp. 1062-1071.

[100] Carr, L. W., and M. S. Chandrasekhara, M. S., "Compressibility effects on dynamic stall," *Progress in Aerospace Sciences*, Vol. 32, No. 6, 1996, pp. 523-573.

[101] Carta, F.O., "A Comparison of Pitching and Plunging Response of an Oscillating Airfoil, " *NASA CR-3172*, Oct. 1979.

[102] Ericsson, L. E., and Reding, J. P., "Dynamic Stall at High Frequency and Large Amplitude," *Journal of Aircraft*, Vol. 17, No. 3, 1980, pp. 136-142.

[103] Ericsson, L. E., and Reding, J. P., "The Difference Between the Effects of Pitch and Plunge on Dynamic Airfoil Stall," 9th *European Rotorcraft Forum*, Stresa, Italy, Sept. 13-15, 1983.

[104] Ericsson, L. E., and Reding, J. P., "Unsteady Flow Concepts for Dynamic Stall Analysis," *Journal of Aircraft*, Vol. 21, No. 8, 1984, pp. 601-606.

[105] Favier, D., Rebont, J., and Maresca, C., "Large-Amplitude Fluctuations of Velocity and Incidence on an Oscillating Airfoil," *AIAA Journal*, Vol. 17, No. 11, 1979, pp. 1265-1267.

[106] Favier, D., Maresca, C., and Rebont, J., "Dynamic Stall Due to Fluctuations of Velocity and Incidence," *AIAA Journal*, Vol. 20, No. 7, 1982, pp. 865-871.

[107] Favier, D., Agnes, A., Barbi, C., and Maresca, C., "Combined Translation/Pitch Motion: A New Airfoil Dynamic Stall Simulation," *Journal of Aircraft*, Vol. 25, No. 9, 1988, pp. 805-814.

[108] Beddoes, T. S., "A Synthesis of Unsteady Aerodynamic Effects Including Stall Hysteresis," *Vertica*, Vol. 1, 1976, pp. 113-123.

[109] Gangwani, S. T., "Prediction of Dynamic Stall and Unsteady Airloads for Rotor Blades," *Proceedings of the 37th Annual National Forum of American Helicopter Society*, New Orleans, May 1981.

[110] Leishman, J. G., and Beddoes, T. S., "A generalized Model for Airfoil Unsteady Aerodynamic Behaviour and Dynamic Stall Using the Indicial Method," *Proceedings of the 42nd Annual Forum of the American Helicopter Society*, Washington D.C., June 1986.

[111] Tyler, J. C., and Leishman, J. G., "Analysis of Pitch and Plunge Effects on Unsteady Airfoil Behavior," *Journal of the American Helicopter Society*, Vol. 37, No. 3, 1992, pp. 69-82.

[112] Van der Wall, B. G., and Leishman, J. G., "On the Influence of Time-Varying Flow Velocity on Unsteady Aerodynamics," *Journal of the American Helicopter Society*, Vol. 39, No. 4, 1994, pp. 25-36.

[113] Tran, C. T., and Petot, D., "Semi-Empirical Model for the Dynamic Stall of Airfoils in View of the Application to the Calculation of the Responses of a Helicopter Blade in Forward Flight," *Vertica*, Vol. 5, 1981, pp. 35-53.

[114] McAlister, K. W., Lambert, O., and Petot, D., "Application of the ONERA Model of Dynamic Stall," *NASA Technical Paper 2399*, AVSCOM Technical Report 84-A-3, 1984.

[115] Peters, D., "Toward a Unified Lift Model for use in Rotor Blade Stability Analysis," *Journal of the American Helicopter Society*, Vol. 30, No. 3, 1985, pp. 32-42.

[116] Petot, D., "Differential Equation Modeling of Dynamic Stall," *La Reserche Aérospatiale*, No. 1989-5, 1989.

[117] Petot, D. "Errata to Differential Equation Modeling of Dynamic Stall," *Private Communication*, 2005.

[118] Truong, V. K., "A 2-D Dynamic Stall Model Based on a Hopf Bifurcation," 19th *European Rotorcraft Forum*, Cernobbio,Italy, Sept. 14-16, 1993.

208

[119] Truong, V. K., "Prediction of Helicopter Rotor Airloads Based on Physical Modeling of 3-D Unsteady Aerodynamics," 22nd *European Rotorcraft Forum*, Brighton, UK, Sept. 17-19, 1996.

[120] Petot, D., Arnaud, G., Harrison, R., Stevens. J., Dieterich, O., Van der Wall, B. G., Young, C., and Széchényi, E., "Stall Effects and Blade Torsion — An Evaluation of Predictive Tools," *Journal of the American Helicopter Society*, Vol. 44, No. 4, 1999, pp. 320-331.

[121] Srinivasan, G. R., Ekaterinaris, J. A., and McCroskey, W. J., "Evaluation of Turbulence Models for Unsteady Flows of an Oscillating Airfoil," *Computers & Fluids*, Vol. 24, No. 7, 1995, pp. 833-861.

[122] Ekaterinaris, J. A., and Platzer, M. F., "Computational Prediction of Airfoil Dynamic Stall," *Progress in Aerospace Sciences*, Vol. 33, No. 11-12, 1998, pp. 759-846.

[123] Peters, D. A., Chouchane, M., and Fulton, M., "Helicopter Trim with Flap-Lag-Torsion and Stall by an Optimized Controller," *Journal of Guidance, Control, and Dynamics*, Vol. 13, No. 5, 1990, pp. 824-834.

[124] Tang, D., and Dowell, E. H., "Damping Prediction for Hingeless Rotor Aeroelastic Stability with Experimental Correlation," *Journal of Aircraft*, Vol. 33, No. 6, 1996, pp. 1071-1078.

[125] Johnson, W., "Rotorcraft Aerodynamics Models for Comprehensive Analysis," *Proceedings of the 54th Annual Forum of the American Helicopter Society*, Washington D.C., 1998.

[126] Larsen, J. W., "Nonlinear Dynamics of Wind Turbine Wings," *Ph.D. thesis*, Dept. of Civil Engineering, Aalborg University, Denmark, July 2005.

[127] Sankar, N. L., Wake, B. E., and Lekoudis, S. G., "Solution of the Unsteady Euler Equations for Fixed and Rotor Wing Configurations," *Journal of Aircraft*, Vol. 23, No. 4, 1986, pp. 283-289.

[128] Agarwal, R. K., and Deese, J. E., "Euler Calculations for Flowfield of a Helicopter Rotor in Hover," *Journal of Aircraft*, Vol. 24, No. 4, 1987, pp. 231-238.

[129] Strawn, R. C., and Caradonna, F. X., "Conservation Full-Potential Model for Unsteady Transonic Rotor Flows," *AIAA Journal*, Vol. 25, No. 2, 1987, pp. 193-198.

[130] Ramachandran, K., Tung, C., and Caradonna, F. X., "Rotor Hover Performance Prediction Using a Free-Wake, Computational Fluid Dynamics Method," *Journal of Aircraft*, Vol. 26, No. 12, 1989, pp. 1105-1110.

[131] Srinivasan, G. R., and McCroskey, W. J., "Navier-Stokes Calculations of Hovering Rotor Flowfields," *Journal of Aircraft*, Vol. 25, No. 10, 1988, pp. 865-874.

[132] Rajagopalan, R. G., and Lim, C. K., "Laminar Flow Analysis of a Rotor in Hover," *Journal of the American Helicopter Society*, Vol. 36, No. 1, 1991, pp. 12-23.

[133] Srinivasan, G. R., and Baeder, J. D., "TURNS: A Free-Wake Euler/Navier-Stokes Numerical Method for Helicopter Rotors," *AIAA Journal*, Vol. 31, No. 5, 1993, pp. 959-962.

[134] Kang, H. J., and Kwon, O. J., "Effect of Wake Adaptation on Rotor Hover Simulations Using Unstructured Meshes," *Journal of Aircraft*, Vol. 38, No. 5, 2001, pp. 868-877

[135] Kang, H. J., and Kwon, O. J., "Unstructured Mesh Navier-Stokes Calculations of the Flow Field of a Helicopter Rotor in Hover," *Journal of the American Helicopter Society*, Vol. 47, No. 2, 2002, pp. 90-99.

[136] Strawn, R. C., and Djomehri, M. J., "Computational Modeling of Hovering Rotor and Wake Aerodynamics," *Journal of Aircraft*, Vol. 39, No. 5, 2002, pp. 786-793.

[137] Gaonkar, G. H., and Peters, D. A., "Flap-Lag Stability with Dynamic Inflow by the Method of Multiblade Coordinates," *Presented at the 20th AIAA/ASME/ASCE/AHS Structures, Structural Dynamics, and Materials Conference, AIAA Paper No. 79-0729*, St. Loiuis, Missouri, April 4-6, 1979.

[138] Gaonkar, G. H., and Peters, D. A., "Use of Multiblade Coordinates for Helicopter Flap-Lag Stability with Dynamic Inflow," *Journal of Aircraft*, Vol. 17, No. 2, 1980, pp. 112-118.

[139] Gaonkar, G. H., and Peters, D. A., "Effectiveness of Current Dynamic-Inflow Models in Hover and Forward Flight," *Journal of the American Helicopter Society*, Vol. 31, No. 2, 1986, pp. 47-57.

[140] Peters, D. A., and HaQuang, N., "Dynamic Inflow for Practical Application," *Journal of the American Helicopter Society*, Vol. 33, No. 4, 1988, pp. 64-68.

[141] Su, A., Yoo, K. M., and Peters, D. A., "Extension and Validation of an Unsteady Wake Model for Rotors," *Journal of Aircraft*, Vol. 29, No. 3, 1992, pp. 374-383.

210

[142] Peters, D. A., and Su, A., "Effect of an Unsteady Three-Dimensional Wake on Elastic Blade-Flapping Eigenvalues in Hover," *Journal of the American Helicopter Society*, Vol. 38, No. 1, 1993, pp. 45-54.

[143] Manjunath, A. R., Nagabhushanam, J., Gaonkar, G. H., Peters, D. A., and Su, A., "Flap-Lag Damping in Hover and Forward Flight With a Three-Dimensional Wake," *Journal of the American Helicopter Society*, Vol. 38, No. 4, 1993, pp. 37-49.

[144] Manjunath, A. R., Chunduru, S. J., Nagabhushanam, J., and Gaonkar, G. H., "Flap-Lag-Torsion Stability in Hover and Forward Flight With a Three-Dimensional Wake," *AIAA Journal*, Vol. 34, No. 1, 1996, pp. 18-28.

[145] Nagabushanam, J., and Gaonkar, G. H., "Hingeless Rotor Aeromechanical Stability in Axial and Forward Flight With Wake Dynamics," *Journal of the American Helicopter Society*, Vol. 44, No. 3, 1999, pp. 222-233.

[146] Tran, C. T., and Falchero, D., "Application of the ONERA Dynamic Stall Model to a Helicopter Blade in Forward Flight," *7th European Rotorcraft and Power Lift Aircraft Forum*, Garmisch-Partenkirchen, F.R.G., Sept. 8-11, 1981.

[147] Rogers, J. P., "Application of an Analytic Stall Model to Time-History and Eigenvalue Analysis of Rotor Blades," 8th *European Rotorcraft Forum*, Aix-en-Provence, France, Sept. 1982.

[148] Bergh, H., and Van der Wekken, J. P., "Comparison Between Measured and Calculated Stall-Flutter Behaviour of a One-Bladed Model Rotor," *Vertica*, Vol. 11, No. 3, 1987, pp. 447-456.

[149] Dunn, P., and Dugundji, J., "Nonlinear Stall Flutter and Divergence Analysis of Cantilevered Graphite/Epoxy Wings," *AIAA Journal*, Vol. 30, No. 1, 1992, pp. 153-162.

[150] Tang, D., and Dowell, E. H., "Comparison of Theory and Experiment For Non-linear Flutter and Stall Response of a Helicopter Blade," *Journal of Sound and Vibration*, Vol. 165, No. 2, 1993, pp. 251-276.

[151] Barwey, D., Gaonkar, G. H., and Ormiston, R. A., "Investigation of Dynamic Stall Effects on Isolated Rotor Flap-Lag Stability with Experimental Correlation," *Journal of the American Helicopter Society*, Vol. 36 No. 4, 1991, pp. 12-24.

[152] Barwey, D., and Gaonkar, G. H., "Investigation of Dynamic Stall Effects on Isolated Rotor Flap-Lag Stability with Experimental Correlation," *AIAA Journal*, Vol. 32, No. 4, 1994, pp. 811-819.

[153] Tang, D., and Dowell, E. H., "Damping Prediction for a Stalled Rotor in Flap-Lag with Experimental Correlation," *Journal of the American Helicopter Society*, Vol. 40 No. 4, 1995, pp. 79-89.

[154] Beedy, J., Barakos, G., Badcock, K. J., and Richards, B. E., "Non-linear Analysis of Stall Flutter Based on the ONERA Aerodynamic Model," *The Aeronautical Journal*, Vol. 107, 2003, pp. 495-509.

[155] Peters, D. A., Barwey, D., and Su, A., "An Integrated Airloads - Inflow Model for Use in Rotor Aeroelasticity and Control Analysis," *Mathematical and Computer Modelling*, Vol. 19, No. 3/4, 1994, pp. 109-123.

[156] Chunduru, S. J., Subramanian, S., and Gaonkar, G. H., "Dynamic Stall and Wake Effects on Trim and Stability of Hingeless Rotors with Experimental Correlation," *Journal of the American Helicopter Society*, Vol. 42, No. 4, 1997, pp. 370-382.

[157] Subramanian, S., Ma, G., Gaonkar, G. H., and Maier, T. M., "Correlation of Several Aerodynamic Models and Measurements of Hingeless - Rotor Trim and Stability," *Journal of the American Helicopter Society*, Vol. 45, No. 2, 2000, pp. 312-318.

[158] Tang, D., and Dowell, E. H., "Nonlinear Rotor Aeroelastic Analysis with Stall and Advanced Wake Dynamics," *Journal of Aircraft*, Vol. 34, No. 5, 1997, pp. 679-687.

[159] Depailler, G., and Friedmann, P. P., "Reduction of Vibration due to Dynamic stall in Helicopters Using an Actively Controlled Flap," AIAA paper 2002-1431, *Proceedings of the 43rd AIAA/ASME/ASCE/AHS/ACS Structures, Structural Dynamics and Materials Conference*, Denver, CO, April 2002.

[160] Patt, D., Liu, L., and Friedmann, P. P., "Simultaneous Vibration and Noise Reduction in Rotorcraft Using Aeroelastic Simulation," *Journal of the American Helicopter Society*, Vol. 51, No. 2, 2006, pp. 127-140.

[161] Glaz, B., Friedmann, P. P., and Liu, L., "Vibration and Noise Reduction of Helicopter Rotors Using an Active/Passive Approach," *American Helicopter Society Specialist's Conference on Aeromechanics*, San Francisco, CA, Jan., 2008.

[162] Heffernan, R. H., Yamauchi, G. K., Gaubert, M., and Johnson, W., "Hub Loads Analysis of the SA349/2 Helicopter," *Journal of the American Helicopter Society*, Vol. 35, No. 1, 1990, pp. 51-63.

[163] Lim, J. W., and Anastassiades, T., "Correlation of 2GCHAS Analysis with Experimental Data," *Journal of the American Helicopter Society*, Vol. 40, No. 4, 1995, pp. 18-33.

212

[164] Ganguly, R., Chopra, I., and Weller, W. H., "Comparison of Calculated Vibratory Rotor Hub Loads With Experimental Data," *Journal of the American Helicopter Society*, Vol. 43, No. 4, 1998, pp. 106-117.

[165] Yeo, H., and Johnson, W., "Assessment of Comprehensive Analysis Calculation of Airloads on Helicopter Rotors," *Journal of Aircraft*, Vol. 42, No. 5, 2005, pp. 1218-1228.

[166] Postsdam, M., Yeo, H., and Johnson, W., "Rotor Airloads Prediction Using Loose Aerodynamic/Structural Coupling," *Journal of Aircraft*, Vol. 43, No. 3, 2006, pp. 732-742.

[167] Datta, A., and Chopra, I., "Prediction of UH-60A Dynamic Stall Loads in High Altitude Level Flight using CFD/CSD Coupling," *Proceedings of the 61st Annual Forum of the American Helicopter Society*, Washington D.C., 2005.

[168] Datta, A., Sitaraman, J., Chopra, I., and Baeder, J, D., "CFD/CSD Prediction of Rotor Vibratory Loads in High Speed Flight," *Journal of Aircraft*, Vol. 43, No. 6, 2006, pp. 1698-1709.

[169] Datta, A., and Chopra, I., "Validation of Structural and Aerodynamic Modeling Using UH-60A Airloads Program Data," *Journal of the American Helicopter Society*, Vol. 51, No. 1, 2006, pp. 43-58.

[170] Gennaretti, M., and Bernardini, G., "Aeroelastic Response of Helicopter Rotors Using a 3D Unsteady Aeroelastic Solver," *The Aeronautical Journal*, Dec. 2006, pp. 793-801.

[171] Tanabe, Y., and Saito, S., "An Integrated Analysis Code with CFD/Rotor Dynamics Coupling Developed in JAXA," *American Helicopter Society Specialist's Conference on Aeromechanics*, San Francisco, CA, Jan., 2008.

[172] Bhagwat, M. J., Ormiston, R. A., Saberi, H. A., and Xin, H., "Application of CFD/CSD Coupling for Analysis of Rotorcraft Airloads and Blade Loads in Maneuvering Flight," *Proceedings of the 63rd Annual Forum of the American Helicopter Society*, Washington, D.C., 2007.

[173] Bhagwat, M. J., Dimanlig, A., Saberi, H., Meadowcroft, E., Panda, B., and Strawn, R., "CFD/CSD Coupled Trim Solution for the Dual-Rotor CH-47 Helicopter Including Fuselage Modeling," *American Helicopter Society Specialist's Conference on Aeromechanics*, San Francisco, CA, Jan., 2008.

[174] Silbaugh, B., and Baeder, B. D., "Coupled CFD/CSD Analysis of a Maneuvering Rotor Using Staggered Time-Accurate Coupling Schemes," *American Helicopter Society Specialist's Conference on Aeromechanics*, San Francisco, CA, Jan., 2008.

[175] Bousman, W. G., "A Qualitative Examination of Dynamic Stall from Flight Test Data," *Journal of the American Helicopter Society*, Vol. 43, No. 4, 1998, pp. 279-295.

[176] Kufeld, R. M., and Bousman, W. G., "UH-60A Airloads Program Azimuth Reference Correction," *Journal of the American Helicopter Society*, Vol. 50, No. 2, 2005, pp. 211-213.

[177] Dowell, E. H., and Ilgamav, M. *Studies in Nonlinear Aeroelasticity*, Springer-Verlag Press, New York, USA, 1988, pp. 1-3.

[178] Dowell, E. H., Edwards, J., and Strganac, T., "Nonlinear Aeroelasticity," *Journal of Aircraft*, Vol. 40, No. 5, 2003, pp. 857-874.

[179] Tang, D., and Dowell, E. H., "Chaotic Stall Response of a Helicopter Rotor in Forward Flight," *Journal of Fluids and Structures*, Vol.6, 1992, pp. 311-336.

[180] Price, S. J., and Keleris, J. P., "Non-linear Dynamics of an Airfoil Forced to Oscillate in Dynamic Stall," *Journal of Sound and Vibration*, Vol. 194, No. 2, 1996, pp. 265-283.

[181] Lee, B. H. K., Price, S. J., and Wong, Y. S., "Nonlinear Aeroelastic Analysis of Airfoils: Bifurcation and Chaos," *Progress In Aerospace Sciences*, Vol. 35, 1999, pp. 205-334.

[182] Yuan, K. A., Friedmann, P., and Venkatesan, C., "A New Aeroelastic Model for Composite Rotor Blades with Straight and Swept Tips," *AIAA Paper No. 92-2259, Proceedings of* 33rd *AIAA/ASME/ASCE/AHS/ASC Structures, Structural Dynamics and Materials Conference*, Dallas, TX, April 1992, pp. 1371-1390.

[183] Venkatesan, C., "Treatment of Axial Mode in Structural Dynamic and Aeroelastic Analysis of Rotor Blades - A Review," *National Seminar On Aerostructures*, IIT Kharagpur, India, Dec. 8-9, 1994.

[184] Gupta, P. K., "Structural Dynamics of Helicopter Rotor having Precone, Predroop, Pretwist, and Torque Offset Including Hub Motions," *M. Tech Thesis*, Department of Aerospace Engineering, IIT Kanpur, July 1996.

[185] Venu, G. M., "Structural Dynamic Analysis of Rotor Blades with Swept Tips," *M. Tech Thesis*, Dept. of Aerospace Engineering, I.I.T. Kanpur, May 1999.

[186] Uma, M. M., "Dynamic Analysis of Bearingless Rotor Blade with Swept Tips," *M. Tech Thesis*, Department of Aerospace Engineering, IIT Kanpur, May 2000.

[187] Sahu, P., and Venkatesan, C. "Modeling of the Structural Part in Aeroelastic Analysis of a Helicopter blade," *Technical Report*, July 2001.

[188] Laxman, V., "Structural Dynamic Modeling and Analysis of Hingeless Helicopter Rotor Blades," *M. Tech Thesis*, Department of Aerospace Engineering, IIT Kanpur, July 2002.

[189] Venkatesan, C., *Lecture Notes on Helicopter Technology*, Department of Aerospace Engineering, IIT Kanpur.

[190] Strogatz, S. H., *Nonlinear Dynamics and chaos*, Westview Press, USA, 1994, pp. 317-367.

[191] Padfield, G. D., *Helicopter Flight Dynamics*, Blackwell Science Ltd, 1996.

Appendix A

Components of $\overrightarrow{r_p}$, $\overrightarrow{\omega}$ and $\overrightarrow{V_H}$

Position vector at a point 'p' is given as:

$$\overrightarrow{r_p} = R\left[r_x\hat{e}_{x4k} + r_y\hat{e}_{y4k} + r_z\hat{e}_{z4k}\right]$$

where

$$
\begin{aligned}
r_x = {}& \{-a(\beta_s\cos\theta_I + \beta_d\sin\theta_I) + e_1 + e_2 + \sum_{i=1}^{n-1}(l_e)_i + \cos\Lambda_s\cos\Lambda_a(x_k + u_k) \\
& + v_k\sin\Lambda_s\cos\Lambda_a - w_k\sin\Lambda_a + \eta(-v_k'\cos\Lambda_s\cos\Lambda_a\cos(\theta_G + \phi_k) \\
& - w_k'\cos\Lambda_s\cos\Lambda_a\sin(\theta_G + \phi_k) + \sin\Lambda_s\cos\Lambda_a\cos(\theta_G + \phi_k) - \sin\Lambda_a\sin(\theta_G + \phi_k)) \\
& + \zeta(v_k'\cos\Lambda_s\cos\Lambda_a\sin(\theta_G + \phi_k) - w_k'\cos\Lambda_s\cos\Lambda_a\cos(\theta_G + \phi_k) \\
& - \sin\Lambda_s\cos\Lambda_a\sin(\theta_G + \phi_k) - \sin\Lambda_a\cos(\theta_G + \phi_k))\} \\
r_y = {}& \{a\cos\theta_I + (e_1 + e_2)(\beta_s\cos\theta_I + \beta_d\sin\theta_I) - \sin\Lambda_s(x_k + u_k) + v_k\cos\Lambda_s \\
& + \eta(v_k'\sin\Lambda_s\cos(\theta_G + \phi_k) + w_k'\sin\Lambda_s\sin(\theta_G + \phi_k) + \cos\Lambda_s\cos(\theta_G + \phi_k)) \\
& + \zeta(-v_k'\sin\Lambda_s\sin(\theta_G + \phi_k) + w_k'\sin\Lambda_s\cos(\theta_G + \phi_k) - \cos\Lambda_s\sin(\theta_G + \phi_k))\} \\
r_z = {}& \{-a\sin\theta_I + (e_1 + e_2)(\beta_s\sin\theta_I - \beta_d\cos\theta_I) + \sin\Lambda_a\cos\Lambda_s(x_k + u_k) + v_k\sin\Lambda_s\sin\Lambda_a \\
& + w_k\cos\Lambda_a + \eta(-v_k'\cos\Lambda_s\sin\Lambda_a\cos(\theta_G + \phi_k) - w_k'\cos\Lambda_s\sin\Lambda_a\sin(\theta_G + \phi_k) \\
& + \sin\Lambda_s\sin\Lambda_a\cos(\theta_G + \phi_k) + \cos\Lambda_a\sin(\theta_G + \phi_k)) + \zeta(v_k'\cos\Lambda_s\sin\Lambda_a\sin(\theta_G + \phi_k) \\
& - w_k'\cos\Lambda_s\sin\Lambda_a\cos(\theta_G + \phi_k) - \sin\Lambda_s\sin\Lambda_a\sin(\theta_G + \phi_k) + \cos\Lambda_a\cos(\theta_G + \phi_k))\}
\end{aligned}
$$

Angular velocity is given as:

$$\overrightarrow{\omega} \;=\; \Omega \left[\omega_x \hat{e}_{x4k} + \omega_y \hat{e}_{y4k} + \omega_z \hat{e}_{z4k} \right]$$

where

$$\omega_x \;=\; \left((\beta_d \cos\theta_I - \beta_s \sin\theta_I) + \dot{\theta}_x \cos\psi_k + \dot{\theta}_y \sin\psi_k + \dot{\theta}_z (\beta_d \cos\theta_I - \beta_s \sin\theta_I) + \dot{\theta}_I \right)$$

$$\omega_y \;=\; \left(\sin\theta_I - \dot{\theta}_x \sin\psi_k \cos\theta_I + \dot{\theta}_y \cos\psi_k \cos\theta_I + \dot{\theta}_z \sin\theta_I + \dot{\theta}_I (\beta_s \cos\theta_I + \beta_d \sin\theta_I) \right)$$

$$\omega_z \;=\; \left(\cos\theta_I + \dot{\theta}_x \sin\psi_k \sin\theta_I - \dot{\theta}_y \cos\psi_k \sin\theta_I + \dot{\theta}_z \cos\theta_I + \dot{\theta}_I (\beta_s \sin\theta_I - \beta_d \cos\theta_I) \right)$$

Velocity due to hub perturbations is given below:

$$\overrightarrow{V_H} \;=\; \Omega R \left[V_{H_x} \hat{e}_{x4k} + V_{H_y} \hat{e}_{y4k} + V_{H_z} \hat{e}_{z4k} \right]$$

where

$$
\begin{aligned}
V_{H_x} \;=\;& \Big(\dot{R}_x (\cos\psi_k + \sin\psi_k (\beta_s \cos\theta_I + \beta_d \sin\theta_I)) \\
& + \dot{R}_y (\sin\psi_k - \cos\psi_k (\beta_s \cos\theta_I + \beta_d \sin\theta_I)) + \dot{R}_z (\beta_d \cos\theta_I - \beta_s \sin\theta_I) \Big) \\
V_{H_y} \;=\;& \Big(\dot{R}_x (\cos\psi_k (\beta_s \cos\theta_I + \beta_d \sin\theta_I) - \sin\psi_k \cos\theta_I) \\
& + \dot{R}_y (\cos\psi_k \cos\theta_I + \sin\psi_k (\beta_s \cos\theta_I + \beta_d \sin\theta_I)) + \dot{R}_z (\sin\theta_I) \Big) \\
V_{H_z} \;=\;& \Big(\dot{R}_x (\cos\psi_k (\beta_s \sin\theta_I - \beta_d \cos\theta_I) + \sin\psi_k \sin\theta_I) \\
& + \dot{R}_y (\sin\psi_k (\beta_s \sin\theta_I - \beta_d \cos\theta_I) - \cos\psi_k \sin\theta_I) + \dot{R}_z (\cos\theta_I) \Big)
\end{aligned}
$$

Appendix B

Matrices associated with kinetic energy

Mass Matrix $[M]_{14X14}$:

$$
\begin{aligned}
[M_{11}] &= \int_0^{l_e} (m\{\Phi_c\}\{\Phi_c\}^T + (I_{\zeta\zeta}\cos^2(\theta_G + \phi_k) + I_{\eta\eta}\sin^2(\theta_G + \phi_k) \\
&\quad - I_{\eta\zeta}\sin 2(\theta_G + \phi_k))\{\Phi_c'\}\{\Phi_c'\}^T)dx \\
[M_{12}] &= \int_0^{l_e} ((\frac{1}{2})(I_{\zeta\zeta} - I_{\eta\eta})\sin 2(\theta_G + \phi_k) + I_{\eta\zeta}\cos 2(\theta_G + \phi_k))\{\Phi_c'\}\{\Phi_c'\}^T dx \\
[M_{13}] &= \int_0^{l_e} -(m\eta_m\sin(\theta_G + \phi_k) + m\zeta_m\cos(\theta_G + \phi_k))\{\Phi_c\}\{\Phi_q\}^T dx \\
[M_{14}] &= \int_0^{l_e} -(m\eta_m\cos(\theta_G + \phi_k) - m\zeta_m\sin(\theta_G + \phi_k))\{\Phi_c'\}\{\Phi_q\}^T dx \\
[M_{21}] &= \int_0^{l_e} ((\frac{1}{2})(I_{\zeta\zeta} - I_{\eta\eta})\sin 2(\theta_G + \phi_k) + I_{\eta\zeta}\cos 2(\theta_G + \phi_k))\{\Phi_c'\}\{\Phi_c'\}^T dx \\
[M_{22}] &= \int_0^{l_e} (m\{\Phi_c\}\{\Phi_c\}^T + (I_{\zeta\zeta}\sin^2(\theta_G + \phi_k) + I_{\eta\eta}\cos^2(\theta_G + \phi_k) \\
&\quad + I_{\eta\zeta}\sin 2(\theta_G + \phi_k))\{\Phi_c'\}\{\Phi_c'\}^T)dx \\
[M_{23}] &= \int_0^{l_e} (m\eta_m\cos(\theta_G + \phi_k) - m\zeta_m\sin(\theta_G + \phi_k))\{\Phi_c\}\{\Phi_q\}^T dx \\
[M_{24}] &= \int_0^{l_e} -(m\eta_m\sin(\theta_G + \phi_k) + m\zeta_m\cos(\theta_G + \phi_k))\{\Phi_c'\}\{\Phi_q\}^T dx \\
[M_{31}] &= \int_0^{l_e} -(m\eta_m\sin(\theta_G + \phi_k) + m\zeta_m\cos(\theta_G + \phi_k))\{\Phi_q\}\{\Phi_c\}^T dx \\
[M_{32}] &= \int_0^{l_e} (m\eta_m\cos(\theta_G + \phi_k) - m\zeta_m\sin(\theta_G + \phi_k))\{\Phi_q\}\{\Phi_c\}^T dx
\end{aligned}
$$

$$[M_{33}] = \int_0^{l_e} (I_{\eta\eta} + I_{\zeta\zeta})\{\Phi_q\}\{\Phi_q\}^T dx$$

$$[M_{34}] = 0.0$$

$$[M_{41}] = \int_0^{l_e} -(m\eta_m \cos(\theta_G + \phi_k) - m\zeta_m \sin(\theta_G + \phi_k))\{\Phi_q\}\{\Phi_c'\}^T dx$$

$$[M_{42}] = \int_0^{l_e} -(m\eta_m \sin(\theta_G + \phi_k) + m\zeta_m \cos(\theta_G + \phi_k))\{\Phi_q\}\{\Phi_c'\}^T dx$$

$$[M_{43}] = 0.0$$

$$[M_{44}] = \int_0^{l_e} m\{\Phi_q\}\{\Phi_q\}^T dx$$

Damping Matrix $\left[M^C\right]_{14X14}$:

$$\left[M_{11}^C\right] = \int_0^{l_e} 2[-(m\eta_m \cos(\theta_G + \phi_k) - m\zeta_m \sin(\theta_G + \phi_k))\cos(\theta_I)\{\Phi_c\}\{\Phi_c'\}^T$$
$$+ (m\eta_m \cos(\theta_G + \phi_k) - m\zeta_m \sin(\theta_G + \phi_k))\cos(\theta_I)\{\Phi_c'\}\{\Phi_c\}^T]dx$$

$$\left[M_{12}^C\right] = \int_0^{l_e} 2[-m(\beta_p + \dot{\theta}_I + \beta_d \cos(2\theta_I))\{\Phi_c\}\{\Phi_c\}^T$$
$$- (m\eta_m \sin(\theta_G + \phi_k) + m\zeta_m \cos(\theta_G + \phi_k))\cos(\theta_I)\{\Phi_c\}\{\Phi_c'\}^T$$
$$- (m\eta_m \cos(\theta_G + \phi_k) - m\zeta_m \sin(\theta_G + \phi_k))\sin(\theta_I)\{\Phi_c'\}\{\Phi_c\}^T]dx$$

$$\left[M_{13}^C\right] = \int_0^{l_e} 2[-\dot{\theta}_I(m\eta_m \cos(\theta_G + \phi_k) - m\zeta_m \sin(\theta_G + \phi_k))\{\Phi_c\}\{\Phi_q\}^T + (-\cos(\theta_I)$$
$$((\frac{1}{2})(I_{\zeta\zeta} - I_{\eta\eta})\sin 2(\theta_G + \phi_k) + I_{\eta\zeta}\cos 2(\theta_G + \phi_k)) - \sin(\theta_I)$$
$$(I_{\zeta\zeta}\cos^2(\theta_G + \phi_k) + I_{\eta\eta}\sin^2(\theta_G + \phi_k) - I_{\eta\zeta}\sin 2(\theta_G + \phi_k)))\{\Phi_c'\}\{\Phi_q\}^T]dx$$

$$\left[M_{14}^C\right] = \int_0^{l_e} 2m\cos(\theta_I)\{\Phi_c\}\{\Phi_q\}^T dx$$

$$\left[M_{21}^C\right] = \int_0^{l_e} 2[m(\beta_p + \dot{\theta}_I + \beta_d \cos(2\theta_I))\{\Phi_c\}\{\Phi_c\}^T$$
$$+ (m\eta_m \sin(\theta_G + \phi_k) + m\zeta_m \cos(\theta_G + \phi_k))\cos(\theta_I)\{\Phi_c'\}\{\Phi_c\}^T$$
$$+ (m\eta_m \cos(\theta_G + \phi_k) - m\zeta_m \sin(\theta_G + \phi_k))\sin(\theta_I)\{\Phi_c\}\{\Phi_c'\}^T]dx$$

$$\left[M_{22}^C\right] = \int_0^{l_e} 2[(m\eta_m \sin(\theta_G + \phi_k) + m\zeta_m \cos(\theta_G + \phi_k))\sin(\theta_I)\{\Phi_c\}\{\Phi_c'\}^T$$
$$- (m\eta_m \sin(\theta_G + \phi_k) + m\zeta_m \cos(\theta_G + \phi_k))\sin(\theta_I)\{\Phi_c'\}\{\Phi_c\}^T]dx$$

$$\left[M_{23}^C\right] = \int_0^{l_e} 2[-\dot{\theta}_I(m\eta_m\sin(\theta_G+\phi_k)+m\zeta_m\cos(\theta_G+\phi_k))\{\Phi_c\}\{\Phi_q\}^T +$$

$$(-\sin(\theta_I)((\frac{1}{2})(I_{\zeta\zeta}-I_{\eta\eta})\sin 2(\theta_G+\phi_k)+I_{\eta\zeta}\cos 2(\theta_G+\phi_k))-\cos(\theta_I)$$

$$(I_{\zeta\zeta}\sin^2(\theta_G+\phi_k)+I_{\eta\eta}\cos^2(\theta_G+\phi_k)+I_{\eta\zeta}\sin 2(\theta_G+\phi_k)))\{\Phi_c'\}\{\Phi_q\}^T]dx$$

$$\left[M_{24}^C\right] = \int_0^{l_e} -2m\sin(\theta_I)\{\Phi_c\}\{\Phi_q\}^Tdx$$

$$\left[M_{31}^C\right] = \int_0^{l_e} 2[\dot{\theta}_I(m\eta_m\cos(\theta_G+\phi_k)-m\zeta_m\sin(\theta_G+\phi_k))\{\Phi_q\}\{\Phi_c\}^T +$$

$$(\cos(\theta_I)((\frac{1}{2})(I_{\zeta\zeta}-I_{\eta\eta})\sin 2(\theta_G+\phi_k)+I_{\eta\zeta}\cos 2(\theta_G+\phi_k))+\sin(\theta_I)$$

$$(I_{\zeta\zeta}\cos^2(\theta_G+\phi_k)+I_{\eta\eta}\sin^2(\theta_G+\phi_k)-I_{\eta\zeta}\sin 2(\theta_G+\phi_k)))\{\Phi_q\}\{\Phi_c'\}^T]dx$$

$$\left[M_{32}^C\right] = \int_0^{l_e} 2[\dot{\theta}_I(m\eta_m\sin(\theta_G+\phi_k)+m\zeta_m\cos(\theta_G+\phi_k))\{\Phi_q\}\{\Phi_c\}^T +$$

$$(\sin(\theta_I)((\frac{1}{2})(I_{\zeta\zeta}-I_{\eta\eta})\sin 2(\theta_G+\phi_k)+I_{\eta\zeta}\cos 2(\theta_G+\phi_k))+\cos(\theta_I)$$

$$(I_{\zeta\zeta}\sin^2(\theta_G+\phi_k)+I_{\eta\eta}\cos^2(\theta_G+\phi_k)+I_{\eta\zeta}\sin 2(\theta_G+\phi_k)))\{\Phi_q\}\{\Phi_c'\}^T]dx$$

$$\left[M_{33}^C\right] = 0.0$$

$$\left[M_{34}^C\right] = \int_0^{l_e} -2[\cos(\theta_I)(m\eta_m\sin(\theta_G+\phi_k)+m\zeta_m\cos(\theta_G+\phi_k))$$

$$+\sin(\theta_I)(m\eta_m\cos(\theta_G+\phi_k)-m\zeta_m\sin(\theta_G+\phi_k))\{\Phi_q\}\{\Phi_q\}^T]dx$$

$$\left[M_{41}^C\right] = \int_0^{l_e} -2m\cos(\theta_I)\{\Phi_q\}\{\Phi_c\}^Tdx$$

$$\left[M_{42}^C\right] = \int_0^{l_e} 2m\sin(\theta_I)\{\Phi_q\}\{\Phi_c\}^Tdx$$

$$\left[M_{43}^C\right] = \int_0^{l_e} 2[\cos(\theta_I)(m\eta_m\sin(\theta_G+\phi_k)+m\zeta_m\cos(\theta_G+\phi_k))+\sin(\theta_I)$$

$$(m\eta_m\cos(\theta_G+\phi_k)-m\zeta_m\sin(\theta_G+\phi_k))\{\Phi_q\}\{\Phi_q\}^T]dx$$

$$\left[M_{44}^C\right] = 0.0$$

Stiffness Matrix $\left[M^{cf}\right]_{14X14}$:

$$\left[M_{11}^{cf}\right] = \int_0^{l_e} [m\left(-\cos^2(\theta_I)-\dot{\theta}_I^2-2\beta_p\dot{\theta}_I+2\beta_d\dot{\theta}_I\left(\cos(\theta_I)-\cos(2\theta_I)\right)\right)\{\Phi_c\}\{\Phi_c\}^T$$

$$-2\dot{\theta}_I\sin(\theta_I)(m\eta_m\cos(\theta_G+\phi_k)-m\zeta_m\sin(\theta_G+\phi_k))\{\Phi_c'\}\{\Phi_c\}^T$$

$$-(I_{\zeta\zeta}\cos^2(\theta_G+\phi_k)+I_{\eta\eta}\sin^2(\theta_G+\phi_k)-I_{\eta\zeta}\sin 2(\theta_G+\phi_k))\{\Phi_c'\}\{\Phi_c'\}^T]dx$$

$$\left[M_{12}^{cf}\right] = \int_0^{l_e} [m\left(-\beta_d\dot\theta_I\sin(\theta_I) + 2\beta_d\sin(2\theta_I)\dot\theta_I + \sin(\theta_I)\cos(\theta_I) - \ddot\theta_I\right)\{\Phi_c\}\{\Phi_c\}^T$$
$$- 2\dot\theta_I\cos(\theta_I)(m\eta_m\cos(\theta_G + \phi_k) - m\zeta_m\sin(\theta_G + \phi_k))\{\Phi_c'\}\{\Phi_c\}^T$$
$$- ((\frac{1}{2})(I_{\zeta\zeta} - I_{\eta\eta})\sin 2(\theta_G + \phi_k) + I_{\eta\zeta}\cos 2(\theta_G + \phi_k))\{\Phi_c'\}\{\Phi_c'\}^T]dx$$

$$\left[M_{13}^{cf}\right] = 0.0$$

$$\left[M_{14}^{cf}\right] = 0.0$$

$$\left[M_{21}^{cf}\right] = \int_0^{l_e} [m\left(-\beta_d\dot\theta_I\sin(\theta_I) - 2\beta_d\sin(2\theta_I)\dot\theta_I + \sin(\theta_I)\cos(\theta_I) + \ddot\theta_I\right)\{\Phi_c\}\{\Phi_c\}^T$$
$$- 2\dot\theta_I\sin(\theta_I)(m\eta_m\sin(\theta_G + \phi_k) + m\zeta_m\cos(\theta_G + \phi_k))\{\Phi_c'\}\{\Phi_c\}^T$$
$$- ((\frac{1}{2})(I_{\zeta\zeta} - I_{\eta\eta})\sin 2(\theta_G + \phi_k) + I_{\eta\zeta}\cos 2(\theta_G + \phi_k))\{\Phi_c'\}\{\Phi_c'\}^T]dx$$

$$\left[M_{22}^{cf}\right] = \int_0^{l_e} [m\left(-\sin^2(\theta_I) - \dot\theta_I^2 - 2\beta_p\dot\theta_I - 2\beta_d\dot\theta_I\cos(2\theta_I)\right)\{\Phi_c\}\{\Phi_c\}^T$$
$$- 2\dot\theta_I\cos(\theta_I)(m\eta_m\sin(\theta_G + \phi_k) + m\zeta_m\cos(\theta_G + \phi_k))\{\Phi_c'\}\{\Phi_c\}^T$$
$$- (I_{\zeta\zeta}\sin^2(\theta_G + \phi_k) + I_{\eta\eta}\cos^2(\theta_G + \phi_k) + I_{\eta\zeta}\sin 2(\theta_G + \phi_k))\{\Phi_c'\}\{\Phi_c'\}^T]dx$$

$$\left[M_{23}^{cf}\right] = 0.0$$

$$\left[M_{24}^{cf}\right] = 0.0$$

$$\left[M_{31}^{cf}\right] = \int_0^{l_e} [[(\dot\theta_I^2 + \cos^2(\theta_I))(m\eta_m\sin(\theta_G + \phi_k) + m\zeta_m\cos(\theta_G + \phi_k))$$
$$+ (\ddot\theta_I + \cos(\theta_I)\sin(\theta_I))(m\eta_m\cos(\theta_G + \phi_k) - m\zeta_m\sin(\theta_G + \phi_k))]\{\Phi_q\}\{\Phi_c\}^T$$
$$+ (\dot\theta_I\sin(\theta_I)((I_{\zeta\zeta} - I_{\eta\eta})\sin 2(\theta_G + \phi_k) + 2I_{\eta\zeta}\cos 2(\theta_G + \phi_k)) + 2\dot\theta_I\cos(\theta_I)$$
$$(I_{\zeta\zeta}\sin^2(\theta_G + \phi_k) + I_{\eta\eta}\cos^2(\theta_G + \phi_k) + I_{\eta\zeta}\sin 2(\theta_G + \phi_k)))\{\Phi_q\}\{\Phi_c'\}^T]dx$$

$$\left[M_{32}^{cf}\right] = \int_0^{l_e} [[-(\dot\theta_I^2 + \sin^2(\theta_I))(m\eta_m\cos(\theta_G + \phi_k) - m\zeta_m\sin(\theta_G + \phi_k))$$
$$+ (\ddot\theta_I - \cos(\theta_I)\sin(\theta_I))(m\eta_m\sin(\theta_G + \phi_k) + m\zeta_m\cos(\theta_G + \phi_k))]\{\Phi_q\}\{\Phi_c\}^T$$
$$- (\dot\theta_I\cos(\theta_I)((I_{\zeta\zeta} - I_{\eta\eta})\sin 2(\theta_G + \phi_k) + 2I_{\eta\zeta}\cos 2(\theta_G + \phi_k)) + 2\dot\theta_I\sin(\theta_I)$$
$$(I_{\zeta\zeta}\cos^2(\theta_G + \phi_k) + I_{\eta\eta}\sin^2(\theta_G + \phi_k) - I_{\eta\zeta}\sin 2(\theta_G + \phi_k)))\{\Phi_q\}\{\Phi_c'\}^T]dx$$

$$\left[M_{33}^{cf}\right] = \int_0^{l_e} [((I_{\eta\eta} - I_{\zeta\zeta})\cos 2(\theta_G - \theta_I) + 2I_{\eta\zeta}\sin 2(\theta_G - \theta_I) - 2(I_{\eta\eta} - I_{\zeta\zeta})\beta_d$$
$$\dot\theta_I\sin 2(\theta_I)\sin(\theta_I) - 4I_{\eta\zeta}\beta_d\dot\theta_I\sin(\theta_I)\cos 2(\theta_G))\{\Phi_q\}\{\Phi_q\}^T]dx$$

$$\left[M_{34}^{cf}\right] = 0.0$$

$$\left[M_{41}^{cf}\right] = \int_0^{l_e} [m(\sin(\theta_I)(\beta_p + 2\dot{\theta}_I + \beta_d\cos(2\theta_I)) + \beta_d\ddot{\theta}_I)\{\Phi_q\}\{\Phi_c\}^T$$
$$+ (m\eta_m\cos(\theta_G + \phi_k) - m\zeta_m\sin(\theta_G + \phi_k))\{\Phi_q\}\{\Phi_c'\}^T]dx$$

$$\left[M_{42}^{cf}\right] = \int_0^{l_e} [m(\cos(\theta_I)(\beta_p + 2\dot{\theta}_I + \beta_d\cos(2\theta_I)))\{\Phi_q\}\{\Phi_c\}^T +$$
$$(m\eta_m\sin(\theta_G + \phi_k) + m\zeta_m\cos(\theta_G + \phi_k))\{\Phi_q\}\{\Phi_c'\}^T]dx$$

$$\left[M_{43}^{cf}\right] = 0.0$$

$$\left[M_{44}^{cf}\right] = \int_0^{l_e} -m\{\Phi_q\}\{\Phi_q\}^T dx$$

Fuselage Matrix $[M^1]_{14X3}$:

$$\left[M_{11}^1\right] = \int_0^{l_e} [-m(\cos(\theta_I)\sin(\psi_k))\{\Phi_c\}$$
$$- \cos(\psi_k)(m\eta_m\cos(\theta_G + \phi_k) - m\zeta_m\sin(\theta_G + \phi_k))\{\Phi_c'\}]dx$$

$$\left[M_{12}^1\right] = \int_0^{l_e} [m(\cos(\theta_I)\cos(\psi_k))\{\Phi_c\}$$
$$- \sin(\psi_k)(m\eta_m\cos(\theta_G + \phi_k) - m\zeta_m\sin(\theta_G + \phi_k))\{\Phi_c'\}]dx$$

$$\left[M_{13}^1\right] = \int_0^{l_e} [m\sin(\theta_I)\{\Phi_c\}]\,dx$$

$$\left[M_{21}^1\right] = \int_0^{l_e} [m(\sin(\theta_I)\sin(\psi_k))\{\Phi_c\}$$
$$- \cos(\psi_k)(m\eta_m\sin(\theta_G + \phi_k) + m\zeta_m\cos(\theta_G + \phi_k))\{\Phi_c'\}]dx$$

$$\left[M_{22}^1\right] = \int_0^{l_e} [-m(\sin(\theta_I)\cos(\psi_k))\{\Phi_c\}$$
$$- \sin(\psi_k)(m\eta_m\sin(\theta_G + \phi_k) + m\zeta_m\cos(\theta_G + \phi_k))\{\Phi_c'\}]dx$$

$$\left[M_{23}^1\right] = \int_0^{l_e} [m\cos(\theta_I)\{\Phi_c\}]dx$$

$$\left[M_{31}^1\right] = \int_0^{l_e} [[\cos(\theta_I)\sin(\psi_k)(m\eta_m\sin(\theta_G + \phi_k) + m\zeta_m\cos(\theta_G + \phi_k) +$$
$$\sin(\theta_I)\sin(\psi_k)(m\eta_m\cos(\theta_G + \phi_k) - m\zeta_m\sin(\theta_G + \phi_k))]\{\Phi_q\}]dx$$

$$\left[M_{32}^1\right] = \int_0^{l_e} [[-\cos(\theta_I)\cos(\psi_k)(m\eta_m\sin(\theta_G + \phi_k) + m\zeta_m\cos(\theta_G + \phi_k)$$
$$- \sin(\theta_I)\cos(\psi_k)(m\eta_m\cos(\theta_G + \phi_k) - m\zeta_m\sin(\theta_G + \phi_k))]\{\Phi_q\}]dx$$

$$\left[M_{33}^1\right] = \int_0^{l_e} [[\cos(\theta_I)(m\eta_m\cos(\theta_G + \phi_k) - m\zeta_m\sin(\theta_G + \phi_k))$$
$$- \sin(\theta_I)(m\eta_m\sin(\theta_G + \phi_k) + m\zeta_m\cos(\theta_G + \phi_k))]\{\Phi_q\}]dx$$

$$\left[M_{41}^1\right] \;=\; \int_0^{l_e} [m\cos(\psi_k)\{\Phi_q\}]\,dx$$

$$\left[M_{42}^1\right] \;=\; \int_0^{l_e} [m\sin(\psi_k)\{\Phi_q\}]\,dx$$

$$\left[M_{43}^1\right] \;=\; [m(\beta_p + \beta_d\cos(2\theta_I))\{\Phi_q\}]\,dx$$

Fuselage Matrix $[M^2]_{14X3}$:

$$\left[M_{11}^2\right] \;=\; \int_0^{l_e}\left[m(-\beta_d\dot\theta_I\cos(\psi_k) - \beta_p\sin(\theta_I)\sin(\psi_k) - \beta_d\cos(2\theta_I)\sin(\theta_I)\sin(\psi_k))\{\Phi_c\}\right]dx$$

$$\left[M_{12}^2\right] \;=\; \int_0^{l_e}\left[m(-\beta_d\dot\theta_I\sin(\psi_k) + \beta_p\sin(\theta_I)\cos(\psi_k) + \beta_d\cos(2\theta_I)\sin(\theta_I)\cos(\psi_k))\{\Phi_c\}\right]dx$$

$$\left[M_{13}^2\right] \;=\; 0.0$$

$$\left[M_{21}^2\right] \;=\; \int_0^{l_e} [m(-\beta_p\cos(\theta_I)\sin(\psi_k) - \beta_d\cos(2\theta_I)\cos(\theta_I)\sin(\psi_k))\{\Phi_c\}]\,dx$$

$$\left[M_{22}^2\right] \;=\; \int_0^{l_e} [m(\beta_p\cos(\theta_I)\cos(\psi_k) + \beta_d\cos(2\theta_I)\cos(\theta_I)\cos(\psi_k))\{\Phi_c\}]\,dx$$

$$\left[M_{23}^2\right] \;=\; 0.0$$

$$\left[M_{31}^2\right] \;=\; 0.0$$

$$\left[M_{32}^2\right] \;=\; 0.0$$

$$\left[M_{33}^2\right] \;=\; 0.0$$

$$\left[M_{41}^2\right] \;=\; 0.0$$

$$\left[M_{42}^2\right] \;=\; 0.0$$

$$\left[M_{43}^2\right] \;=\; \left[-m(2\beta_d\dot\theta_I\sin(2\theta_I))\{\Phi_q\}\right]dx$$

Fuselage Matrix $[M^3]_{14X3}$:

$$\begin{aligned}
\left[M_{11}^3\right] \;=\; \int_0^{l_e} & [(m(-\beta_d\cos(\psi_k)(\textstyle\sum(le)_i + x_k) - \beta_p\cos(\theta_I)\cos(\psi_k)(\textstyle\sum(le)_i + x_k) \\
& + a\sin(\theta_I)\cos(\psi_k) + \sin(\theta_I)\sin(\psi_k)(e_1 + e_2 + \textstyle\sum(le)_i + x_k)) \\
& - (m\eta_m\sin(\theta_G + \phi_k) + m\zeta_m\cos(\theta_G + \phi_k))\cos(\psi_k))\{\Phi_c\} + (\cos(\theta_I)\sin(\psi_k) \\
& ((\tfrac{1}{2})(I_{\zeta\zeta} - I_{\eta\eta})\sin 2(\theta_G + \phi_k) + I_{\eta\zeta}\cos 2(\theta_G + \phi_k)) + \sin(\theta_I)\sin(\psi_k) \\
& (I_{\zeta\zeta}\cos^2(\theta_G + \phi_k) + I_{\eta\eta}\sin^2(\theta_G + \phi_k) - I_{\eta\zeta}\sin 2(\theta_G + \phi_k)))\{\Phi_c'\}]dx
\end{aligned}$$

223

$$\left[M_{12}^3\right] \;=\; \int_0^{l_e} [(m(-\sin(\theta_I)\cos(\psi_k)(e_1 + e_2 + \sum (le)_i + x_k)) - \beta_d \sin(\psi_k)$$
$$(\sum (le)_i + x_k) - \beta_p \cos(\theta_I)\sin(\psi_k)(\sum (le)_i + x_k) + a\sin(\theta_I)\sin(\psi_k))$$
$$- (m\eta_m \sin(\theta_G + \phi_k) + m\zeta_m \cos(\theta_G + \phi_k))\sin(\psi_k))\{\Phi_c\} + (-\cos(\theta_I)$$
$$\cos(\psi_k)((\frac{1}{2})(I_{\zeta\zeta} - I_{\eta\eta})\sin 2(\theta_G + \phi_k) + I_{\eta\zeta}\cos 2(\theta_G + \phi_k)) - \sin(\theta_I)$$
$$\cos(\psi_k)(I_{\zeta\zeta}\cos^2(\theta_G + \phi_k) + I_{\eta\eta}\sin^2(\theta_G + \phi_k) - I_{\eta\zeta}\sin 2(\theta_G + \phi_k)))\{\Phi_c'\}]dx$$

$$\left[M_{13}^3\right] \;=\; \int_0^{l_e} [m(\cos(\theta_I)(e_1 + e_2 + \sum (le)_i + x_k))\{\Phi_c\} +$$
$$(\cos(\theta_I)((\frac{1}{2})(I_{\zeta\zeta} - I_{\eta\eta})\sin 2(\theta_G + \phi_k) + I_{\eta\zeta}\cos 2(\theta_G + \phi_k))$$
$$+ \sin(\theta_I)(I_{\zeta\zeta}\cos^2(\theta_G + \phi_k) + I_{\eta\eta}\sin^2(\theta_G + \phi_k) - I_{\eta\zeta}\sin 2(\theta_G + \phi_k)))\{\Phi_c'\}]dx$$

$$\left[M_{21}^3\right] \;=\; \int_0^{l_e} [(m(\cos(\theta_I)\cos(\psi_k)(e_1 + e_2 + \sum (le)_i + x_k))$$
$$+ \beta_p \sin(\theta_I)\cos(\psi_k)(\sum (le)_i + x_k) + a\cos(\theta_I)\cos(\psi_k))$$
$$+ (m\eta_m \cos(\theta_G + \phi_k) - m\zeta_m \sin(\theta_G + \phi_k))\cos(\psi_k))\{\Phi_c\} + (\cos(\theta_I)\sin(\psi_k)$$
$$(I_{\zeta\zeta}\sin^2(\theta_G + \phi_k) + I_{\eta\eta}\cos^2(\theta_G + \phi_k) + I_{\eta\zeta}\sin 2(\theta_G + \phi_k))$$
$$+ \sin(\theta_I)\sin(\psi_k)((\frac{1}{2})(I_{\zeta\zeta} - I_{\eta\eta})\sin 2(\theta_G + \phi_k) + I_{\eta\zeta}\cos 2(\theta_G + \phi_k)))\{\Phi_c'\}]dx$$

$$\left[M_{22}^3\right] \;=\; \int_0^{l_e} [(m(-\cos(\theta_I)\cos(\psi_k)(e_1 + e_2 + \sum (le)_i + x_k))$$
$$+ \beta_p \sin(\theta_I)\sin(\psi_k)(\sum (le)_i + x_k) + a\cos(\theta_I)\sin(\psi_k))$$
$$+ (m\eta_m \cos(\theta_G + \phi_k) - m\zeta_m \sin(\theta_G + \phi_k))\sin(\psi_k))\{\Phi_c\} - (\cos(\theta_I)\cos(\psi_k)$$
$$(I_{\zeta\zeta}\sin^2(\theta_G + \phi_k) + I_{\eta\eta}\cos^2(\theta_G + \phi_k) + I_{\eta\zeta}\sin 2(\theta_G + \phi_k))$$
$$+ \sin(\theta_I)\cos(\psi_k)((\frac{1}{2})(I_{\zeta\zeta} - I_{\eta\eta})\sin 2(\theta_G + \phi_k) + I_{\eta\zeta}\cos 2(\theta_G + \phi_k)))\{\Phi_c'\}]dx$$

$$\left[M_{23}^3\right] \;=\; \int_0^{l_e} [(m(-\sin(\theta_I)(e_1 + e_2 + \sum (le)_i + x_k)))\{\Phi_c\}$$
$$+ (-\sin(\theta_I)(I_{\zeta\zeta}\sin^2(\theta_G + \phi_k) + I_{\eta\eta}\cos^2(\theta_G + \phi_k) + I_{\eta\zeta}\sin 2(\theta_G + \phi_k))$$
$$+ \cos(\theta_I)((\frac{1}{2})(I_{\zeta\zeta} - I_{\eta\eta})\sin 2(\theta_G + \phi_k) + I_{\eta\zeta}\cos 2(\theta_G + \phi_k)))\{\Phi_c'\}]dx$$

$$\left[M_{31}^3\right] \;=\; \int_0^{l_e} [((I_{\eta\eta} + I_{\zeta\zeta})\cos(\psi_k) + \cos(\theta_I)\sin(\psi_k)(\sum (le)_i + x_k)$$
$$(m\eta_m \cos(\theta_G + \phi_k) - m\zeta_m \sin(\theta_G + \phi_k)) - (\sum (le)_i + x_k)$$
$$\sin(\theta_I)\sin(\psi_k)(m\eta_m \sin(\theta_G + \phi_k) + m\zeta_m \cos(\theta_G + \phi_k)))\{\Phi_q\}]dx$$

$$[M_{32}^3] = \int_0^{l_e} [((I_{\eta\eta} + I_{\zeta\zeta})\sin(\psi_k) + \sin(\theta_I)\cos(\psi_k)(\sum (le)_i + x_k)$$
$$(m\eta_m \sin(\theta_G + \phi_k) + m\zeta_m \cos(\theta_G + \phi_k)) - (\sum (le)_i + x_k)$$
$$\cos(\theta_I)\cos(\psi_k)(m\eta_m \cos(\theta_G + \phi_k) - m\zeta_m \sin(\theta_G + \phi_k)))\{\Phi_q\}]dx$$

$$[M_{33}^3] = \int_0^{l_e} [(-\cos(\theta_I)(\sum (le)_i + x_k)(m\eta_m \sin(\theta_G + \phi_k) + m\zeta_m \cos(\theta_G + \phi_k))$$
$$- \sin(\theta_I)(\sum (le)_i + x_k)(m\eta_m \cos(\theta_G + \phi_k) - m\zeta_m \sin(\theta_G + \phi_k)))\{\Phi_q\}]dx$$

$$[M_{41}^3] = \int_0^{l_e} [(-\cos(\theta_I)\sin(\psi_k)(m\eta_m \sin(\theta_G + \phi_k) + m\zeta_m \cos(\theta_G + \phi_k))$$
$$- \sin(\theta_I)\sin(\psi_k)(m\eta_m \cos(\theta_G + \phi_k) - m\zeta_m \sin(\theta_G + \phi_k)))\{\Phi_q\}]dx$$

$$[M_{42}^3] = \int_0^{l_e} [(\cos(\theta_I)\cos(\psi_k)(m\eta_m \sin(\theta_G + \phi_k) + m\zeta_m \cos(\theta_G + \phi_k))$$
$$+ \sin(\theta_I)\cos(\psi_k)(m\eta_m \cos(\theta_G + \phi_k) - m\zeta_m \sin(\theta_G + \phi_k)))\{\Phi_q\}]dx$$

$$[M_{43}^3] = \int_0^{l_e} [(ma + \sin(\theta_I)(m\eta_m \sin(\theta_G + \phi_k) + m\zeta_m \cos(\theta_G + \phi_k))$$
$$- \cos(\theta_I)(m\eta_m \cos(\theta_G + \phi_k) - m\zeta_m \sin(\theta_G + \phi_k)))\{\Phi_q\}]dx$$

Fuselage Matrix $[M^4]_{14X3}$:

$$[M_{11}^4] = \int_0^{l_e} [m(\beta_d \sin(\psi_k)(\sum (le)_i + x_k) - 2a\sin(\psi_k)\sin(\theta_I)$$
$$+ 2\sin(\theta_I)\cos(\psi_k)(e_1 + e_2 + \sum (le)_i + x_k)$$
$$- \beta_d \cos(2\theta_I)\cos(\theta_I)\sin(\psi_k)(\sum (le)_i + x_k))\{\Phi_c\}]dx$$

$$[M_{12}^4] = \int_0^{l_e} [m(2\sin(\theta_I)\sin(\psi_k)(e_1 + e_2 + \sum (le)_i + x_k) - \beta_d \cos(\psi_k)(\sum (le)_i + x_k)$$
$$+ 2a\cos(\psi_k)\sin(\theta_I) + \beta_d \cos(2\theta_I)\cos(\theta_I)\cos(\psi_k)(\sum (le)_i + x_k))\{\Phi_c\}]dx$$

$$[M_{13}^4] = \int_0^{l_e} [m(\beta_p \sin(\theta_I)(\sum (le)_i + x_k) - 2a\cos(\theta_I)$$
$$+ \beta_d \cos(2\theta_I)\sin(\theta_I)(\sum (le)_i + x_k))\{\Phi_c\}]dx$$

$$[M_{21}^4] = \int_0^{l_e} [m(2\cos(\theta_I)\cos(\psi_k)(e_1 + e_2 + \sum (le)_i + x_k) - 2a\sin(\psi_k)\cos(\theta_I)$$
$$+ \beta_d \cos(2\theta_I)\sin(\theta_I)\sin(\psi_k)(\sum (le)_i + x_k))\{\Phi_c\}]dx$$

$$\left[M_{22}^4\right] \;=\; \int_0^{l_e} [m(2a\cos(\psi_k)\cos(\theta_I) + 2\cos(\theta_I)\sin(\psi_k)(e_1 + e_2 + \sum(le)_i + x_k)$$
$$- \beta_d\cos(2\theta_I)\sin(\theta_I)\cos(\psi_k)(\sum(le)_i + x_k))\{\Phi_c\}]dx$$

$$\left[M_{23}^4\right] \;=\; \int_0^{l_e} [m(\beta_p\cos(\theta_I)(\sum(le)_i + x_k) + 2a\sin(\theta_I)$$
$$+ \beta_d\cos(2\theta_I)\cos(\theta_I)(\sum(le)_i + x_k))\{\Phi_c\}]dx$$

$$\left[M_{31}^4\right] \;=\; 0.0$$

$$\left[M_{32}^4\right] \;=\; 0.0$$

$$\left[M_{33}^4\right] \;=\; 0.0$$

$$\left[M_{41}^4\right] \;=\; \int_0^{l_e} \left[m(\beta_d\cos(\theta_I)\cos(\psi_k)(\sum(le)_i + x_k) + \beta_p\cos(\psi_k)(\sum(le)_i + x_k))\{\Phi_q\}\right]dx$$

$$\left[M_{42}^4\right] \;=\; \int_0^{l_e} \left[m(\beta_d\cos(\theta_I)\sin(\psi_k)(\sum(le)_i + x_k) + \beta_p\sin(\psi_k)(\sum(le)_i + x_k))\{\Phi_q\}\right]dx$$

$$\left[M_{43}^4\right] \;=\; \int_0^{l_e} \left[-m(e_1 + e_2 + \sum(le)_i + x_k)\{\Phi_q\}\right]dx$$

Vector $\left[V^I\right]_{14X1}$:

$$\left[V_{11}^I\right] \;=\; \int_0^{l_e} [m(a\beta_d(\dot\theta_I - 2\dot\theta_I\cos(2\theta_I)\cos(\theta_I) + \dot\theta_I\cos^2(\theta_I)$$
$$- 2\dot\theta_I\cos(\theta_I)) - a\cos(\theta_I) - \beta_d\cos(\theta_I)\sin(\theta_I)(e_1 + e_2)$$
$$- \beta_d(\sum(le)_i + x_k)\ddot\theta_I + \beta_p\sin(\theta_I)(e_1 + e_2 + \sum(le)_i + x_k)$$
$$+ \beta_d\cos(2\theta_I)\sin(\theta_I)(e_1 + e_2 + \sum(le)_i + x_k))\{\Phi_c\}]dx$$

$$\left[V_{21}^I\right] \;=\; \int_0^{l_e} [m(a\sin(\theta_I) + a\beta_d(2\dot\theta_I\cos(2\theta_I)\sin(\theta_I) - \dot\theta_I\cos(\theta_I)\sin(\theta_I)$$
$$- 2\dot\theta_I\sin(\theta_I)) + \beta_d\sin^2(\theta_I)(e_1 + e_2) - \beta_d(\sum(le)_i + x_k)\dot\theta_I{}^2$$
$$+ (\beta_p + \beta_d\cos(2\theta_I))\cos(\theta_I)(e_1 + e_2 + \sum(le)_i + x_k)$$
$$- (\sum(le)_i + x_k)(\beta_p\beta_d\dot\theta_I + \beta_d^2\dot\theta_I\cos(2\theta_I))\{\Phi_c\}]dx$$

$$\left[V_{31}^I\right] \;=\; 0.0$$

$$\left[V_{41}^I\right] \;=\; \int_0^{l_e} [m(a\beta_d(-2\ddot\theta_I\cos(2\theta_I) + 4\dot\theta_I{}^2\sin(2\theta_I) + \ddot\theta_I\cos(\theta_I)$$
$$- \dot\theta_I{}^2\sin(\theta_I)) - \beta_d\dot\theta_I\cos(\theta_I)(e_1 + e_2 + \sum(le)_i + x_k)$$
$$- (e_1 + e_2 + \sum(le)_i + x_k) + a\beta_d\sin(2\theta_I))\{\Phi_q\}]dx$$

Vector $\left[V^L\right]_{14X1}$:

$$
\begin{aligned}
\left[V_{11}^L\right] \;=\; & \int_0^{l_e} [(-\cos^2(\theta_I)(m\eta_m \cos(\theta_G + \phi_k) - m\zeta_m \sin(\theta_G + \phi_k)) \\
& + (\cos(\theta_I)\sin(\theta_I) - \ddot{\theta}_I)(m\eta_m \sin(\theta_G + \phi_k) + m\zeta_m \cos(\theta_G + \phi_k)))\{\Phi_c\} \\
& + ((m\eta_m \cos(\theta_G + \phi_k) - m\zeta_m \sin(\theta_G + \phi_k))(\sum (le)_i + x_k) \\
& + (I_{\zeta\zeta}\cos^2(\theta_G + \phi_k) + I_{\eta\eta}\sin^2(\theta_G + \phi_k) - I_{\eta\zeta}\sin 2(\theta_G + \phi_k)) \\
& (-2\sin(\theta_I)\dot{\theta}_I - \beta_d\ddot{\theta}_I - \sin(\theta_I)(\beta_p + \beta_d \cos(2\theta_I))) \\
& + ((\tfrac{1}{2})(I_{\zeta\zeta} - I_{\eta\eta})\sin 2(\theta_G + \phi_k) + I_{\eta\zeta}\cos 2(\theta_G + \phi_k)) \\
& (-2\cos(\theta_I)\dot{\theta}_I - \cos(\theta_I)(\beta_p + \beta_d \cos(2\theta_I))))\{\Phi_c'\}]dx \\
\left[V_{21}^L\right] \;=\; & \int_0^{l_e} [((\cos(\theta_I)\sin(\theta_I) + \ddot{\theta}_I)(m\eta_m \cos(\theta_G + \phi_k) - m\zeta_m \sin(\theta_G + \phi_k)) \\
& - \sin^2(\theta_I)(m\eta_m \sin(\theta_G + \phi_k) + m\zeta_m \cos(\theta_G + \phi_k)))\{\Phi_c\} \\
& + ((m\eta_m \sin(\theta_G + \phi_k) + m\zeta_m \cos(\theta_G + \phi_k))(\sum (le)_i + x_k) \\
& + (I_{\zeta\zeta}\sin^2(\theta_G + \phi_k) + I_{\eta\eta}\cos^2(\theta_G + \phi_k) + I_{\eta\zeta}\sin 2(\theta_G + \phi_k)) \\
& (-2\cos(\theta_I)\dot{\theta}_I - \cos(\theta_I)(\beta_p + \beta_d \cos(2\theta_I))) \\
& + ((\tfrac{1}{2})(I_{\zeta\zeta} - I_{\eta\eta})\sin 2(\theta_G + \phi_k) + I_{\eta\zeta}\cos 2(\theta_G + \phi_k)) \\
& (-2\sin(\theta_I)\dot{\theta}_I - \beta_d\ddot{\theta}_I - \sin(\theta_I)(\beta_p + \beta_d \cos(2\theta_I))))\{\Phi_c'\}]dx \\
\left[V_{31}^L\right] \;=\; & \int_0^{l_e} [((I_{\eta\eta} + I_{\zeta\zeta})(\ddot{\theta}_I - 2\beta_d \sin(2\theta_I)\dot{\theta}_I) \\
& - (\tfrac{1}{2})(I_{\eta\eta} - I_{\zeta\zeta})\sin 2(\theta_G + \theta_I) + I_{\eta\zeta}\cos 2(\theta_G + \theta_I) + \\
& (\beta_d\dot{\theta}_I \sin(\theta_I))((I_{\eta\eta} - I_{\zeta\zeta})\cos 2(\theta_G) + 2I_{\eta\zeta}\sin 2(\theta_G)))\{\Phi_q\}]dx \\
\left[V_{41}^L\right] \;=\; & \int_0^{l_e} [(2\sin(\theta_I)\dot{\theta}_I(m\eta_m \cos(\theta_G + \phi_k) - m\zeta_m \sin(\theta_G + \phi_k)) + \\
& 2\cos(\theta_I)\dot{\theta}_I(m\eta_m \sin(\theta_G + \phi_k) + m\zeta_m \cos(\theta_G + \phi_k)))\{\Phi_q\}]dx
\end{aligned}
$$

The detailed expressions can be found in Ref. [188].

Appendix C

Matrices associated with strain energy

Stiffness Matrix $\left[K^E\right]_{14X14}$:

$$\left[K_{11}^E\right] = \int_0^{l_e} ((\overline{EI_{\zeta\zeta}}\cos\theta_G - \overline{EI_{\eta\zeta}}\sin\theta_G)\{\Phi_c''\}\{\Phi_c''\}^T)dx$$

$$\left[K_{12}^E\right] = \left[K_{21}^E\right] = \int_0^{l_e} ((\overline{EI_{\zeta\eta}}\cos\theta_G - \overline{EI_{\eta\eta}}\sin\theta_G)\{\Phi_c''\}\{\Phi_c''\}^T)dx$$

$$\left[K_{13}^E\right] = \left[K_{31}^E\right] = \int_0^{l_e} (\overline{EAD_1}\{\Phi_c''\}\{\Phi_q''\}^T + \tau_0\overline{EAD_1'}\{\Phi_c''\}\{\Phi_q'\}^T)dx$$

$$\left[K_{14}^E\right] = \left[K_{41}^E\right] = \int_0^{l_e} (-\overline{EA\eta_a}\{\Phi_c''\}\{\Phi_q'\}^T)dx$$

$$\left[K_{22}^E\right] = \int_0^{l_e} ((\overline{EI_{\eta\eta}}\cos\theta_G + \overline{EI_{\zeta\eta}}\sin\theta_G)\{\Phi_c''\}\{\Phi_c''\}^T)dx$$

$$\left[K_{23}^E\right] = \left[K_{32}^E\right] = \int_0^{l_e} (\overline{EAD_2}\{\Phi_c''\}\{\Phi_q''\}^T + \tau_0\overline{EAD_2'}\{\Phi_c''\}\{\Phi_q'\}^T)dx$$

$$\left[K_{24}^E\right] = \left[K_{42}^E\right] = \int_0^{l_e} (-\overline{EA\zeta_a}\{\Phi_c''\}\{\Phi_q'\}^T)dx$$

$$\left[K_{33}^E\right] = \int_0^{l_e} (EAD_3\{\Phi_q''\}\{\Phi_q''\}^T + \tau_0 EAD_5\{\Phi_q''\}\{\Phi_q'\}^T$$
$$+ (\tau_0^2 EAD_3' - GJ)\{\Phi_q'\}\{\Phi_q'\}^T)dx$$

$$\left[K_{34}^E\right] = \left[K_{43}^E\right] = \int_0^{l_e} (-\overline{EAD_0}\{\Phi_q''\}\{\Phi_q'\}^T - \tau_0\overline{EAD_0'}\{\Phi_q'\}\{\Phi_q'\}^T)dx$$

$$\left[K_{44}^E\right] = \int_0^{l_e} (EA\{\Phi_q'\}\{\Phi_q'\}^T)dx$$

Stiffness Matrix $\left[K^{E'}\right]_{14X14}$:

$$K_{1\times1}^{E'} = \frac{12}{35l_e}a_1 + \frac{3}{5l_e}a_2 + \frac{6}{5l_e}a_3$$

$$K_{1\times2}^{E'} = K_{2\times1}^{E'} = \frac{1}{14}a_1 + \frac{1}{10}a_2 + \frac{1}{10}a_3$$

$$K_{1\times3}^{E'} = K_{3\times1}^{E'} = -\frac{12}{35l_e}a_1 - \frac{3}{5l_e}a_2 - \frac{6}{5l_e}a_3$$

$$K_{1\times4}^{E'} = K_{4\times1}^{E'} = -\frac{1}{35}a_1 + \frac{1}{10}a_3$$

$$K_{2\times2}^{E'} = \frac{2l_e}{105}a_1 + \frac{l_e}{30}a_2 + \frac{2l_e}{15}a_3$$

$$K_{2\times3}^{E'} = K_{3\times2}^{E'} = -\frac{1}{14}a_1 - \frac{1}{10}a_2 - \frac{1}{10}a_3$$

$$K_{2\times4}^{E'} = K_{4\times2}^{E'} = -\frac{l_e}{70}a_1 + \frac{l_e}{60}a_2 + \frac{l_e}{30}a_3$$

$$K_{3\times3}^{E'} = \frac{12}{35l_e}a_1 + \frac{3}{5l_e}a_2 + \frac{6}{5l_e}a_3$$

$$K_{3\times4}^{E'} = K_{4\times3}^{E'} = \frac{1}{35}a_1 - \frac{1}{10}a_3$$

$$K_{4\times4}^{E'} = \frac{3l_e}{35}a_1 + \frac{l_e}{10}a_2 + \frac{2l_e}{15}a_3$$

$$K_{5\times5}^{E'} = K_{1\times1}^{E'}$$

$$K_{5\times6}^{E'} = K_{6\times5}^{E'} = K_{1\times2}^{E'}$$

$$K_{5\times7}^{E'} = K_{7\times5}^{E'} = K_{1\times3}^{E'}$$

$$K_{5\times8}^{E'} = K_{8\times5}^{E'} = K_{1\times4}^{E'}$$

$$K_{6\times6}^{E'} = K_{2\times2}^{E'}$$

$$K_{6\times7}^{E'} = K_{7\times6}^{E'} = K_{2\times3}^{E'}$$

$$K_{6\times8}^{E'} = K_{8\times6}^{E'} = K_{2\times4}^{E'}$$

$$K_{7\times7}^{E'} = K_{3\times3}^{E'}$$

$$K_{7\times8}^{E'} = K_{8\times7}^{E'} = K_{3\times4}^{E'}$$

$$K_{8\times8}^{E'} = K_{4\times4}^{E'}$$

$$K_{9\times9}^{E'} = \frac{EAC_0}{EA}\left(\frac{1}{5l_e}a_1 + \frac{1}{3l_e}a_2 + \frac{7}{3l_e}a_3\right)$$

$$\begin{aligned}
K_{9\times10}^{E'} &= K_{10\times9}^{E'} = & \frac{EAC_0}{EA}\left(-\frac{2}{5l_e}a_1 - \frac{2}{3l_e}a_2 - \frac{8}{3l_e}a_3\right) \\
K_{9\times11}^{E'} &= K_{11\times9}^{E'} = & \frac{EAC_0}{EA}\left(\frac{1}{5l_e}a_1 + \frac{1}{6l_e}a_2 + \frac{1}{3l_e}a_3\right) \\
K_{10\times10}^{E'} &= & \frac{EAC_0}{EA}\left(\frac{32}{15l_e}a_1 + \frac{8}{3l_e}a_2 + \frac{16}{3l_e}a_3\right) \\
K_{10\times11}^{E'} &= K_{11\times10}^{E'} = & \frac{EAC_0}{EA}\left(-\frac{26}{15l_e}a_1 - \frac{2}{l_e}a_2 - \frac{8}{l_e}a_3\right) \\
K_{11\times11}^{E'} &= & \frac{EAC_0}{EA}\left(\frac{23}{15l_e}a_1 + \frac{11}{6l_e}a_2 + \frac{7}{3l_e}a_3\right)
\end{aligned}$$

The detailed expressions can be found in Ref. [188].